Where and when Star Formation Occurs in Main Sequence Galaxies at Cosmic Noon

by

Shannon H. MacFarland

A Thesis Submitted to Saint Mary's University, Halifax, Nova Scotia in Partial Fulfillment
of the Requirements for the Degree of MSc in Astronomy
(Department of Astronomy and Physics)

August 2024, Halifax, Nova Scotia

Approved: _____

Dr. Marcin Sawicki
Supervisor

Approved: _____

Dr. Vincent Hénault-Brunet
Committee Member

Approved: _____

Dr. Robert Thacker
Committee Member

Date: August 8, 2024.

Acknowledgements

Firstly, I would like to thank my supervisor, Dr. Marcin Sawicki, for the support and guidance he provided throughout this journey.

Thank you to the CANUCS collaboration and especially Yoshihisa Asada and Ghassan Sarrouh for processing the photometric data required for this work. I am also grateful to Angelo George and Lamiya Mowla for providing the morphology fitting. I am also deeply grateful to Kartheik Iyer for providing his guidance on the spatially resolved fits.

Thank you to the entire Extragalactic Group here at SMU for encouraging me to learn and ask questions. Thank you to my committee members, Dr. Robert Thacker and Dr. Vincent Hénault-Brunet, for reviewing my thesis and especially to Dr. Hénault-Brunet for being a supportive and reassuring figure throughout this process. I am also extremely grateful to all the other grad students, especially Margaret, Nolan, Fraser, Maigan, and Peter for providing so much support throughout classes and research, and for being my first friends when I decided to move across the country.

I am grateful to my family for constantly encouraging me, especially my parents. Thank you to my friends, for giving me a life outside of work and for being a constant source of laughter in my life. Finally, thank you to my partner, Cindy, your patience, understanding, and love has gotten me through this entire journey. Thank you for convincing me to get Artemis (who is the only one that physically got me to stop working by pushing my laptop off of my lap) - in this way we're bringing a piece of Nova Scotia back with us.

Contents

List of Figures

List of Tables

Abstract

Where and when Star Formation Occurs in Main Sequence Galaxies at Cosmic Noon

by Shannon H. MacFarland

We perform spatially resolved pixel-by-pixel Spectral Energy Distribution (SED) fitting on 166 disky star-forming galaxies between $0.7 < z < 3$. Due to the incredible spatial resolution of the Near Infrared Camera on board the James Webb Space Telescope, we are able to probe down to $\sim$0.75 kpc at z=1. From the 2D property maps made from SED fitting with `Dense Basis`, we extract property radial profiles such as the stellar mass, star formation rate, and dust. We find that massive galaxies above the star-forming main sequence have dusty, star-forming centers, and galaxies below the star-forming main sequence have centrally-depressed star formation, indicating the inside-out growth of galaxies. Additionally, the star formation rate radial profile is not uniformly smooth, but concentrated in star-forming regions. Overall, our results show when galaxies burst above the main sequence, they add new stars in the disk through spatially inhomogeneous star formation, and in their cores through dusty starbursts.

Date: August 8, 2024

Chapter 1

Introduction

Galaxies are gravitationally bound collections of dust, gas, stars and dark matter. The diversity of galaxies in their shapes, sizes, and colours shows that galaxies evolve differently throughout their lifetime. Due to the timescales over which galaxies evolve, the relative contributions of different physical processes to galaxy formation still lack a detailed understanding from an observational perspective. This chapter provides a broad overview of the terminology and processes involved when discussing galaxy evolution, as well as important discoveries that have occurred in the field.

1.1 Galaxy Classification, Formation and Evolution

Galaxy morphology has been studied since the first observations of galaxies (Hubble, 1926). The most popular classification scheme is the Hubble "tuning fork" (Hubble, 1936) with revisions made throughout the decades (Kormendy & Bender, 1996; de Vaucouleurs, 1959). Broadly, there are two classes of galaxies. *Spirals* consist of a disk and spiral arm structure and are on average bluer, with younger stellar populations, and recent star formation. Conversely, *elliptical* galaxies have no clearly defined structure, are typically redder, and have older stellar populations with no ongoing star formation. Figure 1.1 shows the original Hubble tuning fork and classification scheme depicting the differences in morphology between elliptical and spiral galaxies.

A surface brightness profile is a fundamental way of characterizing these differences in the morphology. The surface brightness profile can be made by calculating the azimuthally averaged surface brightness at different radii within a galaxy. The most well studied radial surface

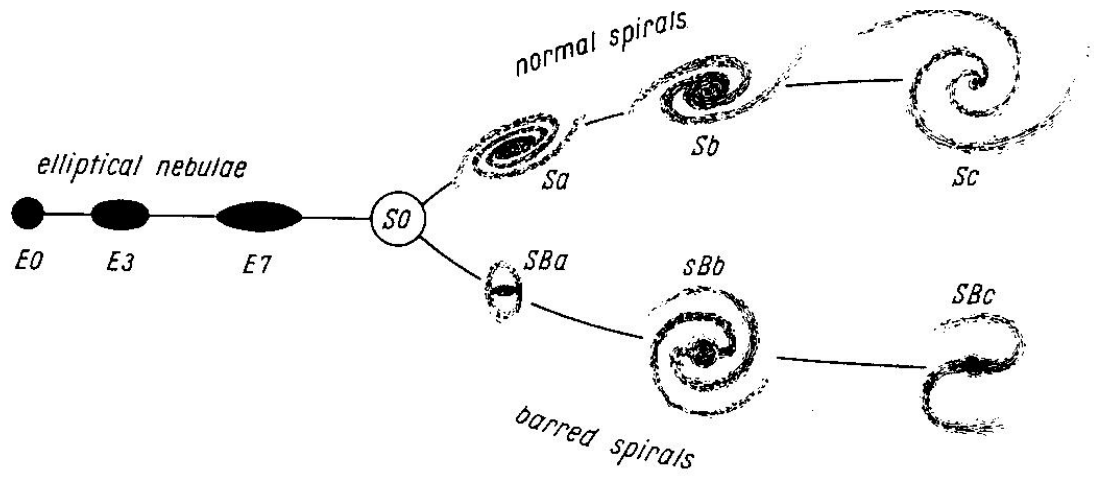

Figure 1.1: The original tuning fork diagram from Hubble (1936). This diagram illustrates the morphological differences between elliptical/bulge dominated early-type galaxies and spiral/disk dominated late-type galaxies.

brightness profile is the Sérsic profile (Sersic, 1968). Also known as a generalized de Vaucouleurs profile, it is defined as

$$\log\left(\frac{\mathrm{I(R)}}{\mathrm{I_e}}\right) = -\mathrm{b_n}\left[\left(\frac{\mathrm{R}}{\mathrm{R_e}}\right)^{1/\mathrm{n}} - 1\right] \tag{1.1}$$

where I_e is the surface brightness at R_e, and R_e is the effective radius, the projected radius where half of the galaxy's luminosity is emitted. The coefficient b_n is chosen such that the region within $1\mathrm{R}_e$ emits half the luminosity, and to good approximation $\mathrm{b}_n \approx 1.999\mathrm{n}\text{-}0.327$. Finally n is the Sérsic index, where for the bulges of spiral galaxies and elliptical galaxies n=4, and for n=1 one recovers an exponential surface brightness profile, characteristic of a disky galaxy.

A luminosity function describes the relative number of galaxies that we expect to find at different luminosities, and it has been shown that the ultraviolet (UV) and infrared (IR) luminosity functions evolve with cosmic time. For a typical initial mass function (IMF, the initial distribution of masses for a stellar population), the total luminosity of a galaxy is dominated by UV emission from young, massive stars. Additionally, these stars have short lifespans, as such the UV emission fades quickly, making UV luminosity (at wavelengths of ~ 1500 Å) a good indicator of the star formation rate (SFR) of a galaxy over a timescale of 100 Myr. This wavelength range is accessible with ground-based optical observations of galaxies at $\mathrm{z} \gtrsim 1$, and observations at lower redshifts require space-based UV data (Madau & Dickinson, 2014). From these observations, we see that at $\mathrm{z} > 2$ the characteristic luminosity is three magnitudes brighter than the local UV-luminosity (Schneider, 2006). However, UV photons are heavily affected by dust attenuation, and the SFR

observed must be corrected by a dust extinction factor, which requires a sufficient model of the dust extinction of a galaxy. The UV energy that the dust absorbs is re-radiated in the IR, making the IR flux an indicator for star formation in galaxies as well, and the IR luminosity function shows a large increase in the number density of luminous sources compared to the local universe; although, older stellar populations can also heat dust and contribute to IR emission. Overall, the cosmic star formation must be uncovered by utilizing multiple indicators of SFR, and doing so depicts the same story since the global SFR was first studied (Lilly et al., 1996; Sawicki et al., 1997): galaxies were actively forming more stars between $1 < z < 3$, a period of time colloquially known as "cosmic noon". An example of the cosmic star formation history is shown in Figure 1.2 using far-UV and IR rest frame measurements. There is a rising phase from $3 \lesssim z \lesssim 8$, with a peak between $z = 1.5$-2 followed by an exponentially declining phase to present day.

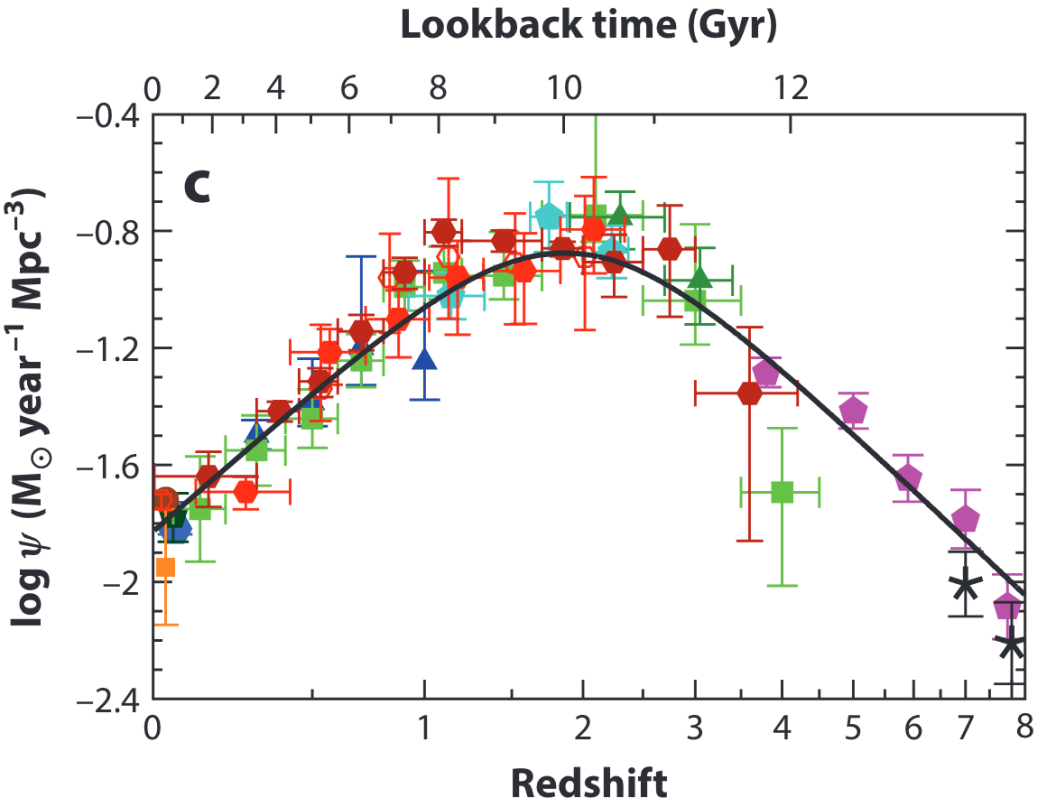

Figure 1.2: Figure 9c from Madau & Dickinson (2014). The comoving star formation rate density as a function of redshift. Warmer symbols (red, orange) show data from UV surveys, and cooler symbols (green, blue) are from IR surveys (references in Table 1 from Madau & Dickinson (2014)). The solid curve shows the best fit to the data.

Since this trend was uncovered, a large amount of research has been conducted to explain how

a galaxy transitions from star-forming to quiescent, a process that is known as *quenching*. There have been several theoretical methods proposed (see review by Man & Belli 2018); however, in general, stars form out of cool gas accreted onto the galaxy, and quenching is an interruption of the gas conditions needed to form stars. Unfortunately, the timescales on which galaxies evolve are so long that one cannot directly observe the star formation and quenching processes, and instead inferences are made based on observing galaxies across cosmic time and linking the physical properties of a galaxy to a theoretical quenching model. At the very least, from observations it appears that the cessation of star formation correlates with both galaxy mass and environment (Peng et al., 2010). In fact, the massive star-forming galaxies at $z \sim 2$ must quench soon after to account for the mass function that is observed at $z = 0$, and quiescent galaxies have been observed as early as 1.5 Gyr after the Big Bang (Carnall et al., 2023; Looser et al., 2024; Strait et al., 2023).

The separation of red and blue galaxies we observe in colour-space emerges again in other physical properties. Observations have shown that there is a near-linear correlation between the integrated SFR and stellar mass of star-forming galaxies known as the star-forming main sequence (SFMS, or simply 'main sequence' (MS)). This relation has been shown to hold at high redshifts with a low degree of scatter ($\sim$ 0.3 dex); (Abdurro'uf & Akiyama, 2018; Speagle et al., 2014), with the normalization decreasing with time reflecting the decline in the star formation rates of star-forming galaxies with cosmic time (Schreiber et al., 2015; Speagle et al., 2014). The growing population of galaxies below this main sequence tend to be quiescent with higher Sérsic indices (Wuyts et al., 2012), and the small population of galaxies above the main sequence are undergoing a period of rapid star formation or "starbursting". There is also emerging evidence that star-forming galaxies grow their mass through bursts, particularly at $z>2$ (Tacchella et al., 2016) and in low mass systems (Asada et al., 2024; Looser et al., 2023), rather than evolving steadily on the main sequence. These periods of intense star formation may even be followed by periods of quiescence, a so called "mini-quenching" event (Dome et al., 2024). Looser et al. (2023) describe these episodes of mini-quenching as the inflow of gas into the galaxy being disrupted, leading to a temporary halt in star formation for a few tens to a hundred million years. Following mini-quenching, the galaxy would find itself in a period of rejuvenation, characterized by old stellar populations and strong nebular emission lines. Observational evidence for bursty star formation remains sparse, since it is difficult to disentangle multiple episodes of star formation,

and therefore to differentiate between mini-quenched and permanently quenched galaxies.

Zolotov et al. (2015) and Tacchella et al. (2016) explored the physical mechanisms that confined star-forming galaxies to a narrow main sequence through cosmological simulations. They deduce that galaxies oscillate along the main sequence, reaching the upper ridge of the MS when there is an intense gas inflow event, perhaps driven by minor mergers, which funnel gas towards the galaxy center in a phase known as 'compaction'. These events build the central regions of galaxies and leads to a central starburst, also known as a 'blue nugget' phase. This phase is followed by a central gas depletion phase, from a combination of stellar feedback and outflows, the galaxy experiences inside-out quenching, this quenching attempt may fail for low halo masses at high redshifts due to the inflow of gas being able to recover and the cycle may repeat again.

What remains unknown are the processes that drive star formation and what moves galaxies off the SFMS and into the quenched population. What is crucial to disentangling the star formation history (SFH) of galaxies are high spatial resolution maps of both SFR and stellar mass, to determine where galaxy star formation occurs when a galaxy is on, above, or below the main sequence. This data would provide a test of how galaxies grow and insight into a galaxy's assembly history.

1.2 Features of a Galaxy's Spectrum

A galaxy's spectrum is the flux density emitted by the galaxy at different wavelengths, and since a galaxy is made of a collection of stars, its spectrum can be thought of as a superposition of all the stars within a galaxy. This is the basis of the theory of stellar population synthesis, which is discussed in depth in Section 3.3.1. This section provides an overview of the various features in a given galaxy's spectrum, and the differences between the spectrum of a star-forming galaxy and a quiescent one.

Figure 1.3 shows multiple spectra for different galaxies ordered by their Hubble type. There is a clear trend in multiple features; first, star-forming galaxies have strong emission lines and elliptical galaxies have stronger absorption features. These strong emission lines originate from the regions of fully ionized hydrogen (HII) around young hot stars that photoionize the gas. As a byproduct of this ionizing radiation, these regions emit nebular emission lines such as [OII]

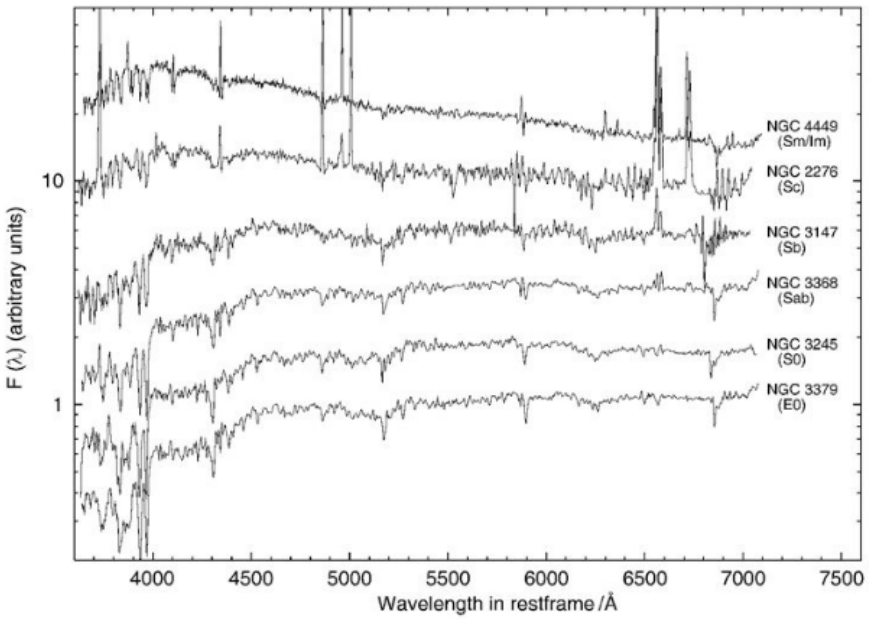

Figure 1.3: Figure 3.36 from Schneider (2006), created using data from Kennicutt (1992). Spectra from galaxies ordered by their Hubble types, as given in Figure 1.1. Spiral galaxies are at the top, and elliptical galaxies are at the bottom.

and the Hydrogen recombination lines (Hα, Hβ, etc.). However, after 10 Myr depending on the strength of the emission from these lines they may only contribute to the broad-band photometry a little, so spectral fitting softwares must rely on the rest-frame UV continuum flux as mentioned earlier to deduce star formation rates, which varies on timescales of 100 Myr.

This leads to a common issue when using the limited information available from broad-band colours. As mentioned before, UV photons are heavily affected by dust attenuation, making a galaxy's spectrum appear redder than it may actually be. This is the age-dust degeneracy, a stellar population could be young, star-forming, and dusty or old, quiescent, and red. To break the age-dust degeneracy one can obtain information like the infrared luminosity due to the UV luminosity being re-radiated, or the strength of the Balmer and 4000 Å-break.

An important spectral feature for broad-band photometric study of galaxies is the 4000 Å-break. This feature occurs due to increased opacity of stellar populations as stellar temperature decreases, causing increasing metal absorption when transitioning to older, redder, and more metal-rich stellar populations. Therefore, the flux ratio above and below this break can be used as a proxy for the galaxy's age, and is key when determining the photometric redshift of a given source. The Balmer break is a similar discontinuity which occurs at $\sim$ 3600Å due to the complete ionization of electrons from the second energy level of hydrogen atoms at wavelengths below the

break. This effect is the strongest in A type stars, and as such its presence can also be used as an age indicator.

However, it is clear from observations that a galaxy's morphology and color, and therefore its physical properties, vary depending on position within a galaxy. The bulges of spiral galaxies in the local universe generally appear redder in colour and have older stellar populations, while recent star formation is occurring in the disk. This highlights an important fact that stellar populations vary within a galaxy, and high resolution spectra, especially at high redshift, are needed to resolve these different populations.

As the integration time for obtaining spectral information, especially for a large sample, is quite costly, an alternative is using a well-sampled spectral energy distribution (SED). The basis of SED fitting is to fit the data to model spectra to extract physical properties about the galaxy in question. The following section describes the importance of SED fitting on a spatially resolved scale.

1.3 Spatially Resolved SED Fitting: Importance and History

Since galaxies were first observed, it has been known that they are spatially extended objects with properties varying with radial distance from the galactic center. Thus, classifying a galaxy by a single integrated spectral energy distribution severely limits our understanding of the undergoing processes in the evolution of galaxies. Questions that cannot be entirely answered with a single SED include: 1) the variation of properties of the interstellar medium (ISM); 2) the stellar populations within the galaxy; and 3) kinematic properties within the galaxy (see review by Sánchez 2020). As such, the rise of spatially resolved studies with integral field spectroscopy (IFS) and high spatial resolution imaging are furthering our collective knowledge of galaxy evolution. Here, I provide an overview of previous spatially resolved galaxy studies in both the local and high redshift universe.

Constructing spatially resolved star formation histories has already been done for the Small and Large Magellanic Clouds (Harris & Zaritsky, 2004, 2009) and the Local Group (Lazzarini et al., 2022; Lewis et al., 2015). As mentioned, UV emission remains a popular method for directly measuring the star formation rate. For a tracer of instantaneous star formation ($\sim$ 10 Myr), Hα emission from gas ionized by young O-stars is used as an indirect measure of SFR.

A more direct measure for the current SFR is being able to actually count the population of young, massive stars and use the distribution to infer the SFR. Obviously this method (known as color-magnitude diagram fitting due to the fact that the distribution of stars on the CMD is a product of the galaxy's SFH) requires high resolution observations; however, it can provide the highest time and spatial resolution SFHs and has been done for an area as large as 1/3 of M31 (Lewis et al., 2015).

Lewis et al. (2015) was able to deduce that the star formation in M31 is largely confined to three ring features at roughly 5, 10, and 15 kpc, with the highest fraction coming from the middle ring. The SFH for both the Small and Large Magellanic Clouds (SMC and LMC) are similar to each other, but not to their larger local neighbors. The SMC and LMC both experienced an early epoch where approximately half of their stellar mass was built up. Then they both experienced a long quiescent epoch ending approximately 5 Gyr ago in the LMC and 3 Gyr ago in the SMC, and both are experiencing rejuvenated star formation currently with bursts starting 400 Myr ago. Spatial analysis reveals that the stars that formed when star formation rejuvenated in the LMC are now centrally concentrated, and in the SMC the rejuvenated star formation has settled into a ring-like structure similar to M31. Spatial analysis also shows that the star formation in the LMC is not symmetric, with the recent star formation peaking in the southeast arm 600 Myr ago and the star formation in the north west arm continuing to climb steadily (Harris & Zaritsky, 2004, 2009). These spatial variations allow us to infer the formation histories of these galaxies, and hypothesize what physical processes are driving or suppressing star formation.

Spatially resolved (pixel-by-pixel) SED fitting was first done by Abraham et al. (1999), using galaxies at $z \sim 1$ in the Hubble Deep Field to study the evolutionary histories of the stellar populations within these galaxies. With the advent of instruments such as the Wide Field Camera 3 (WFC3) on board the Hubble Space Telescope (*HST*), we were able to place spatially resolved constraints on large samples of galaxies. New generation optical to near IR spectroscopy instruments such as SINFONI on the Very Large Telescope (VLT) have also increased the viability of spatially resolved mapping of galaxies at $z \geq 1$; however, high resolution spectroscopy requires high integration time making it difficult to apply these instruments to large data samples. Wuyts et al. (2012) analyzed the resolved photometry of high mass star-forming galaxies ($> 10^{10}\mathrm{M}_{\odot}$) between $0.5 < z < 2.5$ using *HST* imaging, the largest and only mass-complete sample at the time. They deduced that the average star-forming galaxy has a red core due to extinction and stellar

ages, and a disk with young and blue star-forming regions, supporting an "inside-out" growth scenario. Wuyts et al. (2013) expanded on their previous work by combining spatially-resolved stellar population modeling of broadband photometry with resolved Hα information, comparing two independent diagnostics of SFR. Nelson et al. (2016b) used WFC3 grism capabilities to create Hα maps at $\sim$ 1 kpc spatial resolution for over 2500 galaxies at z $\sim$ 1. They found the Hα emission was more extended than the stellar continuum emission, further supporting inside-out assembly. Additionally, they found the radially averaged surface profiles for SFR and mass, and stacked galaxies based on their position within the main sequence. Importantly, they found that star formation is enhanced at all radii for galaxies above the main sequence, and is suppressed at all radii for galaxies below the main sequence. This result shows that the enhanced star formation we observe for galaxies above the main sequence is not due to a misinterpreted active galactic nuclei (AGN), and since Hα SFR is independent of UV and IR SFR, the scatter we observe around the SFMS is real and due to variations of star formation rate at a fixed stellar mass, not due to measurement errors.

There have been numerous studies that have additionally provided support for inside-out quenching, using both observational (Abdurro'uf & Akiyama, 2018; Nelson et al., 2016b; Tacchella et al., 2015, 2018) and cosmological (Nelson et al., 2021; Tacchella et al., 2016) data. Tacchella et al. (2015) measured the mass and SFRs for 22 star-forming galaxies at z $\sim$ 2 on scales of 1 kpc. They found that the the cores of massive ($\sim 10^{11}$ $M_\odot$) galaxies quench within $\lesssim$ 200 Myr, and the outskirts still form stars for 1-3 Gyr. Tacchella et al. (2016) utilized zoom-in cosmological simulations for massive galaxies in the redshift range z = 6-1 and specifically looked at how star-forming galaxies evolved along the main sequence. While not explicitly doing a spatially-resolved study, Tacchella et al. (2016) do concur that gas depletion starts from the center of the galaxy and that galaxies quench rapidly between $1 < z < 3$.

Finally, Genzel et al. (2014) utilized SINFONI spectroscopic data to look at the Hα surface brightness profile at 2 kpc resolution for 19 z $\sim$ 2 star-forming galaxies. They found more than half of their sample (more towards the high mass end) exhibited Hα rings, similar to those found in massive galaxies in the local universe, suggesting that the physical mechanism that formed these rings is present at cosmic noon. Additionally, they found that 10-25$\%$ of the integrated Hα emission came from a handful of bright clumps. Star-forming clumps are prominent substructures characterized by having a factor of several times higher specific star formation rate (sSFR, the star

formation rate divided by an object's total mass) compared to its host galaxy. They are considered to be common structures in star-forming galaxies between $1 \leq z \leq 2$ and generally contribute $\sim 10\%$ of the total SFR; however, in the local universe they are considered rarer (Guo et al., 2012, 2015). The UV luminosity of clumps is also shown to correlate with the host's star formation rate density, absolute magnitude, and size (Martin et al., 2023). This indicates that the formation and growth of substructure within a galaxy directly impacts the evolution of the entire galaxy, meriting the study of spatially resolved properties of galaxies.

Another important finding from these spatially resolved studies is that scaling relations observed over multiple galaxies originates within galaxies themselves (Sánchez, 2020). An example of this is the spatially resolved SFMS (Abdurro'uf & Akiyama, 2017, 2018; Abdurro'uf et al., 2023; Ellison et al., 2018; Wuyts et al., 2013). On scales of ~ 1 kpc, there is a nearly linear relationship between the surface mass density and surface SFR density, and this has been found for galaxies in the local universe (Abdurro'uf & Akiyama, 2017) to $z \sim 1$ (Abdurro'uf & Akiyama, 2018). The spatially resolved SFMS shows a larger decline in the high surface mass density regions from $z \sim 1$ to $z \sim 0$ when compared to the low surface mass density regions. This suggests that the SFR in central regions of galaxies is being suppressed, providing additional support for inside-out quenching. This trend is a clear analogue to the global SFMS and encourages the continued study of specially resolved properties to further understand the origin of these fundamental relationships.

1.4 Motivation and Goals of this Thesis

The goal of this project is to explore on a spatially-resolved scale how galaxies are evolving in relation to the main sequence. We will use high resolution NIRCam imaging data from the James Webb Space Telescope taken as part of the Canadian NIRISS Unbiased Cluster Survey. This data is unique as access to the infrared allows observations of high redshift sources, and its high resolution allows for the probing of inner regions of a galaxy. This study focuses on objects between $0.7 < z < 3$ to target the epoch of the highest star formation rate in cosmic history. We will perform pixel-by-pixel SED fitting on these galaxies using the SED fitting software `Dense Basis` to compare various radial profiles for galaxies below, on, or above the main sequence to explore where the galaxy star formation, or the lack thereof, is occurring. We also look at the

spatial variation in the star formation in the disk of the galaxies.

This thesis is structured as follows. In Chapter 2, we discuss the data, the data reduction pipeline, and the sample selection. In Chapter 3 we describe the methodology behind SED fitting and extracting the radial profiles, and present the pixel-by-pixel 2D property maps for various galaxies. Chapter 4 we show the radial profiles of various properties extracted from the 2D property maps for galaxies on, above, and below the main sequence. In Chapter 5 we compare our results to those obtained with a different binning technique. In Chapter 6 we interpret the radial profiles and provide preliminary results on how the star formation is changing within galaxies, and in Chapter 7 we present our conclusions and possible avenues for future work. All magnitudes are given in the AB photometric system, and all logarithms are computed in base 10 unless otherwise explicitly stated. We assume a ΛCDM cosmology with $\Omega_{\rm M} = 0.3$, $\Omega_{\Lambda} = 0.7$, and $\rm H_0 = 70$ km s^{-1} Mpc^{-1}.

Chapter 2

Data

2.1 The James Webb Space Telescope

This project uses observations taken by the James Webb Space Telescope (*JWST*). A review of the history and science objectives of *JWST* can be found in Gardner et al. (2023) and is summarized here.

JWST launched on December 25, 2021 with four science instruments on board. This project predominately utilizes data from one of those instruments, NIRCam, which is an infrared imager that covers the edge of the visible to the near-infrared wavelength range (0.6μm to 5μm). This thesis will also briefly discuss data from NIRISS, a slitless spectrograph, and the Hubble Space Telescope (*HST*). *JWST* orbits at the Sun-Earth L2 point, due to Earth's atmosphere absorbing large regions of infrared wavelengths. The infrared wavelength allows for observations of galaxies at Cosmic Noon, and allows us the ability to spatially resolve their stellar populations.

The data was taken as part of a *JWST* guaranteed time observation program, The Canadian NIRISS Unbiased Cluster Survey (CANUCS, Willott et al., 2022), which consists of 200 hours of observing time between NIRCam, NIRSpec, and NIRISS. CANUCS targets five strongly lensed galaxy fields, a summary of the five clusters and their properties are provided in Table 2.1. The main science goal of CANUCS is to understand the evolution of low-mass galaxies ($< 10^9 M_\odot$) across cosmic time. Lensing clusters were targeted due to their advantages in seeing smaller and fainter galaxies, and these clusters specifically were all chosen due to existing available multi-wavelength data and because of their lensing geometries which ensure that most of the magnified image plane is located within a single NIRISS field.

Table 2.1. CANUCS Target Clusters

Cluster	RA	DEC	Redshift	Obs. Date
MACS J0417.5-1154	04:17:35.1	-11:54:38	0.443	October 12th-17th 2022
Abell 370	02:39:54.1	-01:34:34	0.375	December 17th-31st 2022
MACS J0416.1-2403	04:16:09.4	-24:04:21	0.395	January 4th-11th 2023
MACS J1423.8+2404	14:23:47.8	+24:04:40	0.545	February 25th-28th 2023
MACS J1149.6+2223	11:49:36.7	+22:23:53	0.543	May 10th-12th 2023

The NIRCam and NIRISS observations are performed in parallel, so each target has a central field and two flanking fields, one observed with NIRCam and one observed with NIRISS (an example of the field layout for the CANUCS observations is shown in Figure 2.1). Hereafter, the term 'flanking field' or the acronym NCF will be used to refer to the flanking field observed with NIRCam. The acronym CLU will refer to the cluster field observation. The cluster fields are imaged in the NIRCam filters F090W, F115W, F150W, F200W, F277W, F356W, F410M and F444W with exposure times of 6.4 ks each, reaching S/N between 5 and 10 for a AB=29 point source. The filters for the flanking fields are dependent on the field, generally including more filters than the cluster fields, especially medium bands. An example of the filter transmission curves for both the cluster and flanking fields of MACS J1149.6+2223 are shown in Figure 2.2. Three of the clusters (A370, MACS J0416.1-2403, MACS J1149.6+2223) have Hubble optical and IR imaging from the Hubble Frontier Fields Project (Lotz et al., 2017) and the other two (MACS J0417.5-1154, MACS J1423.8+2404) have existing HST WFC3/UVIS imaging. For both the cluster fields and the flanking fields, we include the Hubble Space Telescope Advanced Camera for Surveys (ACS) photometric filters F435W, F606W, and F814W and the Hubble Space Telescope Wide Field Camera 3 (WFC3/UVIS) filters F438W and F606W in the SED fitting, depending on their availability, due to these filters being able to trace recent star formation at the redshifts this project is interested in. This project uses 7 out of 10 fields of the CANUCS sample, listed in Table 2.2, for which galaxy morphology measurements are available.

2.2 Data Reduction Pipeline

The data were processed by the CANUCS collaboration team using a data reduction pipeline similar to those described in Noirot et al. (2023) and Mowla et al. (2022) for the SMACS 0723 field. Detailed below are the steps for reducing the photometric products.

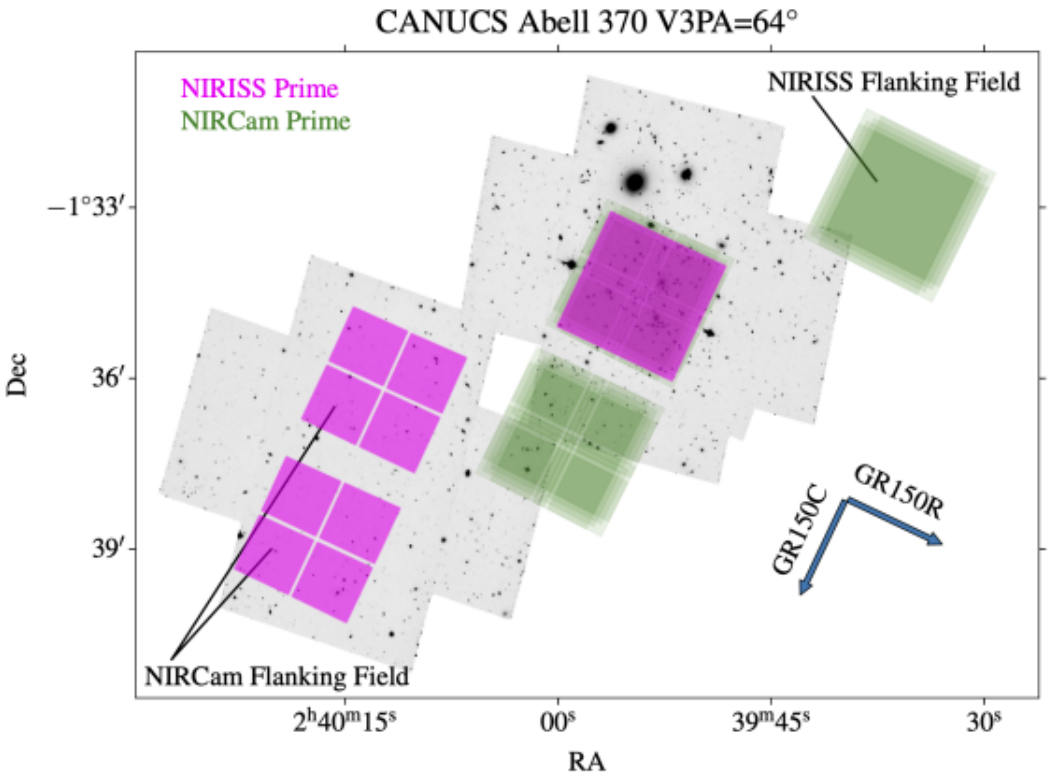

Figure 2.1: Figure 9 from Willott et al. (2022). Field layout for the observations of Abell A370. The background greyscale images are from the archival HST data in F814W. The green squares indicate NIRCam Prime pointings and the purple squares indicate NIRISS Prime pointings. NIRISS and NIRCam module B are centered on the cluster core, the other pointings indicate the parallel observations and show that the NIRCam flanking field overlaps with the pre-existing HST data.

First, the JWST Science Calibration Pipeline, the official STScI pipeline, is used for all instruments and all modes and includes calibrating instrumental signatures, combining relevant exposures, and performing basic spectral and imaging source extraction. The first stage of the pipeline, `calwebb_detector1`, processes the images from raw ramps (the number of photon counts in a given time interval) to uncalibrated slope images by performing a linear fit to the ramp data in each pixel. First, noisy and saturated pixels are flagged and a pixel correction using the non-light sensitive pixels at the edge of the detector is applied. This includes the flagging of artifacts known as "snowballs", large cosmic ray impacts, as well as general cosmic ray rejection. Persistence correction is needed because of leftover charge in a detector after a previous observation of bright objects. Dark current is corrected as well. The final step in `calwebb_detector1` is to fit a slope to the reads of each pixel. NIRCam's detectors are 10 light-sensitive HgCdTe photodiode arrays, which accumulate charge during integration and are

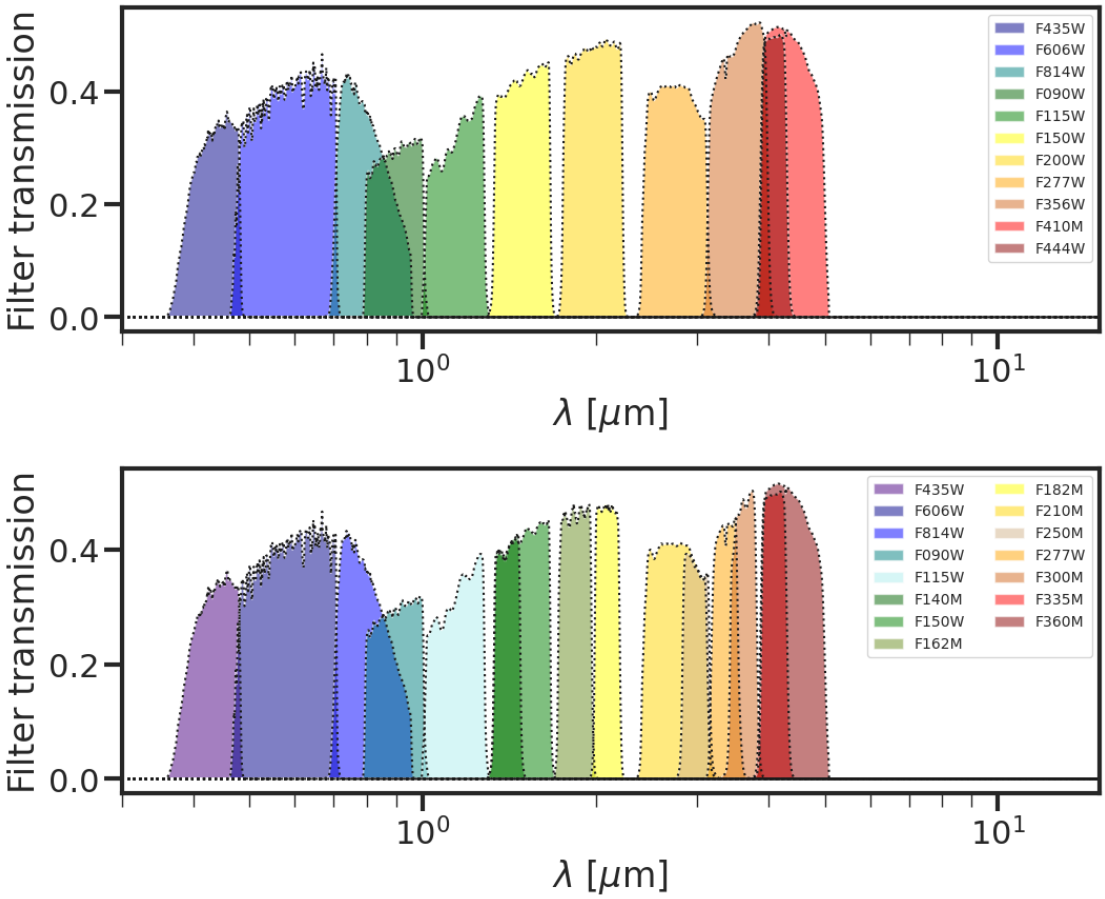

Figure 2.2: Filter transmission curves for both the CANUCS NIRCam cluster field (top) and flanking field (bottom) for the cluster MACS J1149.6+2223. Each of these photometric filters used in SED fitting.

read out "non-destructively" - leaving charge unaffected in each pixel. After each integration the pixels are read out a final time and reset. To determine the number of average counts/second of each pixel, a slope is fit to the readouts. Additionally, if there are multiple integrations, those integrations are averaged.

To perform the final steps in data reduction, `Grizli` (Brammer & Matharu, 2021) is used to align the different exposures to the auxiliary HST data, subtract the sky background from the exposures, and drizzle all images to a common pixel grid with a scale of 0.04 arcsec/pixel. The intracluster light and light from the brightest galaxies in the lensing cluster fields are also modeled using a custom code and removed as described in Martis et al. (2024).

Finally, to enable the measurement of accurate colors, the PSFs in all filters were degraded to the lowest resolution image (F444W) by collaborator Ghassan Sarrouh, as described in Sarrouh et al. (2024). This is completed using bright stars in the field of each filter and determining their empirical PSFs. From there, the images are convolved with a kernel to degrade the PSF in all images to the PSF in F444W.

Object detection and photometry are run and photometric redshifts are derived by collaborator Yoshihisa Asada as described in Asada et al. (2024) and briefly recapped here. Object detection was run on the $\chi_{\rm mean}$ detection image (this combines all available images into one stack) using the `photutils` package (Bradley et al., 2023), which uses a similar strategy as `SExtractor` and is described in greater detail in Section 3.1. The photometry is extracted in multiple circular apertures of different diameters, and photometry errors were measured from the 1σ width of the Gaussian distribution from measuring 2000 empty-aperture fluxes multiplied by the noise level at the position of a source.

Photometric redshifts are derived using `EAZY` (Brammer et al., 2008). A systematic error of 5% of the flux is added in quadrature to the error, and a magnitude prior is applied to reduce the probability of unphysical solutions. After the pipeline `EAZY` is also used to rederive zero-point offsets consistent with the photometric redshift fitting of the full catalogue. The photometric redshifts are used in this work to fix the redshift of the galaxy when doing spatially-resolved SED fitting.

Integrated SED fitting is performed by CANUCS collaborator Kartheik Iyer using `Dense Basis` (the methodology behind SED fitting is discussed in Section 3.3). From this, we obtain integrated stellar masses and star formation rates for all sources that are used in this work. These

are used to divide the sample relative to the star-forming main sequence.

2.3 Sample Selection

The types of galaxies necessary for this analysis need to have high signal to noise to discern features in the SED. Initially, we apply a magnitude cut of < 25 in any of the wide band JWST filters that are available in a given field. In addition, galaxies that are near the edge of the NIRCam field of view are removed, due to dithering pattern edge artifacts. Furthermore, galaxies located behind the galaxy clusters may be highly magnified; thus, we only include galaxies in the cluster fields with a magnification factor $\mu < 2$, estimated using a gravitational lens model by Desprez et al. (in prep.) for MACS 1423, Gledhill et al. (2024) for Abell 370, Rihtaršič et al. (2024) for MACS 0416, and Rihtaršič et al. (in prep.) for MACS 1149. This is done to ignore any magnification corrections that may need to be made. During this work we also want to target the epoch in cosmic history where the star formation rate density was the highest, so we target galaxies in the redshift range of $0.7 < \mathrm{z} < 3$.

This work will also be focusing on the evolution of disk-dominated galaxies. As such, we apply a cut on the Sérsic index of the galaxy of less than 2. To apply this restriction, morphology fitting for each galaxy was performed with `GALFIT` (Peng et al., 2002) by a collaborator as described in George et al. (2024). Morphology fitting was done in the F444W filter to derive the effective radius, position angle, and axis ratio. The red filter was chosen because the light in the F444W image is dominated by emission from long-lived low-mass stars that contain most of a galaxy's stellar mass. A galaxy's shape at these wavelengths is more stable due to these long-lived stars compared to the shorter wavelengths which are dominated by emission from young stars.

Disk-dominated galaxies have round disks, and due to random orientation in 3D they are projected on the sky as ellipses, this induces an inclination affect when determining distances within galaxies. Accurate distances are needed in this project due to the goal of learning how star formation varies as a function of galactocentric radius. We can correct for this observational bias by using the equation

$$\cos(\mathrm{i}) = b/a, \tag{2.1}$$

where a is the semi-major axis of a galaxy and b is the semi-minor axis of a galaxy. The semi-

Table 2.2. Each of the CANUCS fields used in this analysis with the number of galaxies in the final sample and the number of photometric bands used in SED fitting with `Dense Basis`.

Field	# of Galaxies	# of Photometric Bands
MACS 0416 NCF	15	25
MACS 0416 CLU	29	11
MACS 1149 CLU	19	11
Abell 370 NCF	22	25
Abell 370 CLU	10	11
MACS 1423 NCF	42	16
MACS 1423 CLU	29	11

major and semi-minor axis are the observed quantities for a circular symmetric (round) galactic disk. By using Equation 2.1, we obtain the inclination of the galaxy, and we impose an inclination cut of $< 60°$ to omit edge-on galaxies from the sample.

After the initial redshift, magnitude, and morphology cuts, across the seven fields there were 413 galaxies remaining. Each of these galaxies was fit using the methods described in Chapter 3 and was then visually inspected to remove galaxies that were not sufficiently isolated or did not have enough spatial extent to provide meaningful information, leaving 186 galaxies.

2.3.1 The Star-Forming Main Sequence

To contextualize the sample, Figure 2.3 shows the star-forming main sequence with stellar masses and star formation rates obtained with integrated SED fitting with `Dense Basis`. The star-forming main sequence shown is described as

$$\log(\mathrm{SFR_{MS}}) = \alpha + \beta \log(\mathrm{M_\star}) \tag{2.2}$$

and is computed by doing linear fits to the cluster galaxies in the larger CANUCS sample in four redshift bins between $0.5 < \mathrm{z} < 2.5$, as shown by the dashed lines in Figure 2.3. The values for the main sequence fits are

$$0.5 < z < 1 : \alpha = -7.300, \beta = 0.741$$

$$1 < z < 1.5 : \alpha = -6.796, \beta = 0.722$$

$$1.5 < z < 2 : \alpha = -6.150, \beta = 0.679$$

$$2 < z < 2.5 : \alpha = -5.332, \beta = 0.614.$$

Linear interpolation between the fits in each of the four redshift bins is then used to determine the main sequence at a given redshift between $0.7 < z < 3$. Each of the lines is shown with a shaded region representing the intrinsic scatter of 0.3 dex of the main sequence.

The second panel in Figure 2.3 shows the offset from the main sequence as a function of stellar mass. The offset from the main sequence is defined as

$$\Delta\mathrm{MS} = \log(\mathrm{SFR}) - \log(\mathrm{SFR}_{\mathrm{MS}}). \tag{2.3}$$

Here, the SFR of the galaxy is the SFR averaged over the last 100 Myr of the galaxy's lifetime, and SFR_{MS} is the star formation rate calculated using Equation 2.2. Galaxies that were > 1.5 dex below the main sequence were removed from the sample, to ensure no contamination from a potentially quiescent population. This resulted in a final sample of 166 galaxies. Table 2.2 contains a list of each field and the number of galaxies in each field as well as the number of photometric bands used in the SED fitting.

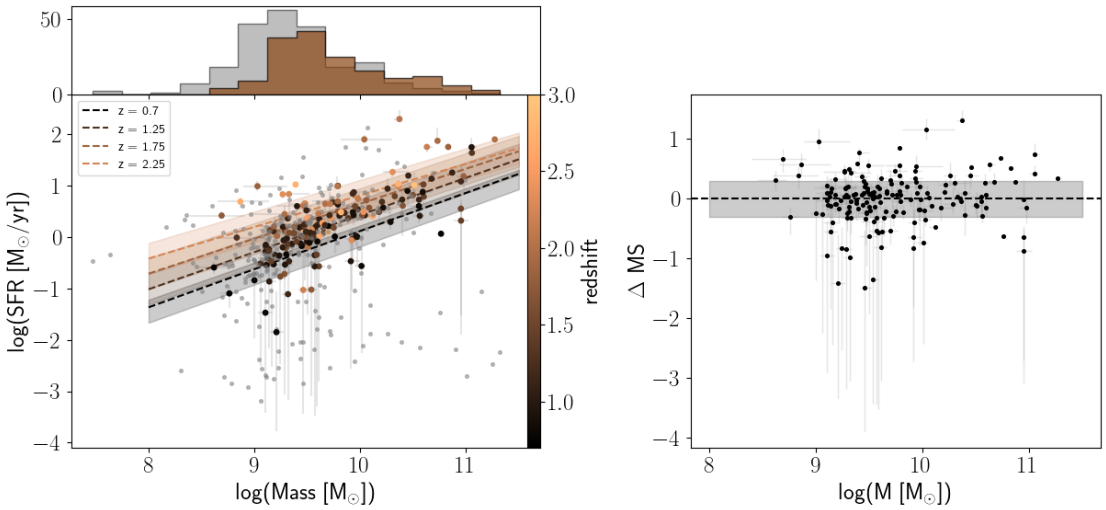

Figure 2.3: *Left:* The star-forming main sequence for this sample of galaxies using median stellar mass and star formation rates obtained from integrated SED fits using `Dense Basis`. The lines show the fits to the main sequence performed on the larger CANUCS data at a given redshift, with a scatter of 0.3 dex. The grey points are galaxies that met the initial inclination and Sérsic index cuts, while the coloured points show the final sample of galaxies after additional visual and ΔMS cuts. The mass histograms show the sample of galaxies excluded (grey) and included (coloured) for this analysis. *Right:* The offset of the galaxies from the main sequence, with the shaded region indicating the intrinsic scatter of the main sequence of 0.3 dex.

Chapter 3

Methods

Here, we provide an overview of the methods involved in this work.

1. Source detection is run on each field by a CANUCS collaborator and each object is segmented as described in Asada et al. (2024).

2. Pixel-by-pixel SED fitting is performed using the non-parametric SFH SED fitting code `Dense Basis`.

3. Using the results from `Dense Basis`, 2D spatially-resolved property maps of each source are made using pixels in each galaxy that meet a certain S/N criteria.

4. Finally, the deprojected galactocentric radius to each pixel is found to see how different physical properties in a galaxy vary with radius.

In the rest of this chapter, we give more detail on the general methods when performing spatially-resolved SED fitting and why from the methods available we adopted the choices that we did.

Abdurro'uf & Akiyama (2017) describe "pixel-to-pixel" SED fitting with three main steps; (1) point spread function (PSF) matching, segmentation, and pixel binning to obtain photometric flux in each pixel of the galaxy; (2) constructing model photometric SEDs; and (3) fitting the observed SED to the models.

The PSF describes the spreading of light from a point source object when viewed through an imager. The extent of the spreading depends on the instrument as well as the wavelength of light. As such, to ensure that the resolution is the same in all photometric bands, it is common practice

to degrade all the photometry to the lowest resolution image (largest full width at half maximum (FWHM)) by convolution with the PSF in that band (Abdurro'uf & Akiyama, 2017; Abdurro'uf et al., 2023). This process is described for the data at the end of Section 2.2.

3.1 Segmentation

Segmentation is the method of determining which pixels belong to a specific galaxy. A popular method to produce a segmentation map (used by Abdurro'uf & Akiyama (2017), Abdurro'uf & Akiyama (2018)) is to use the software SExtractor (Bertin & Arnouts, 1996). To begin, the flux value in each pixel is a combination of light from objects we are interested in and background flux. SExtractor makes two passes through the data, the first pass is to create a model of the sky background. During the second pass the pixels are background-subtracted and segmented. The detections are then deblended for merged objects and poor detections are filtered out. Finally, properties such as magnitudes are measured and outputted into a catalogue. This procedure is typically done in each photometric band, and the final segmentation map is constructed by merging all the maps. Other segmentation codes include SEP (Barbary, 2016) (used by Abdurro'uf et al. (2023)) which uses the same algorithm as SExtractor but presents them as a library of functions and classes rather than an executable.

Another method for segmentation is known as the watershed algorithm (Soille & Ansoult, 1990) (used by Sorba & Sawicki (2018)). SExtractor as stated before needs multiple passes through the data to properly deblend objects; however, when the location of objects is already known, then the watershed algorithm may be more straightforward (Sorba & Sawicki, 2018). The watershed algorithm begins by defining markers, such as the pixel location of known galaxies in the image. These markers are used to create 'basins' with the walls of the basin determined by a signal-to-noise (S/N) threshold, when one basin overflows into another one, there marks the delineation between two objects.

This project uses data segmented by the `photutils` package which uses a similar methodology as SExtractor.

3.2 Binning Techniques

Pixel binning is the technique of combining multiple pixels' fluxes and their uncertainties to increase the S/N ratio to fit meaningful data and not return the priors. This method allows for features within the SEDs to become more apparent; however, when doing a spatially resolved analysis it is important not to wash out features with over-binning. One of Wuyts et al. (2012) main conclusions was that the masses derived from the integrated multi-wavelength photometry are consistent with those obtained from resolved SED modelling at ~ 0.7 kpc resolution. However, Sorba & Sawicki (2015) observed a bias where the unresolved mass estimate systematically underestimated the resolved mass estimate when studying 67 nearby galaxies and Sorba & Sawicki (2018) found an offset in mass from $1.2 < z < 2.5$. Sorba & Sawicki (2018) deduced that it was a difference in binning methods between the two studies that resulted in Wuyts et al. (2012) obscuring the effects due to outshining. Thus, which binning method is chosen directly impacts the results.

A common binning method is using the the Voronoi two-dimensional binning technique by Cappellari & Copin (2003) in order to achieve a minimum S/N value (Belfiore et al., 2019; Wuyts et al., 2012). This method is briefly described here: it starts with taking the pixel with the highest S/N of the image, and the unbinned pixel closest to that pixel. The unbinned pixel is then added to the current bin if the following conditions are satisfied: 1) the pixel is adjacent to the bin, 2) If the S/N of the bin is higher than the threshold, then adding the pixel to the bin will not deviate the S/N from the threshold, and 3) by adding a new pixel the 'roundness' of the bin remains below a certain threshold. If these criteria are successful, the pixel is binned. Figure 5.1 shows an example of Voronoi binning and it is discussed more in comparison to pixel-by-pixel SED fitting in Section 5.1. Abdurro'uf & Akiyama (2017) introduce a binning method which considered the conditions of increasing the (S/N) as well as the similarity of SED shapes and the closeness of the pixels. If the shape of the SED is not taken into account, then certain pixels in the same bin will have drastically different SEDs. The method they develop first takes the brightest pixel (b) from a r-band image of a galaxy. The pixels within a radius of r =2 are examined to compare how similar the SEDs are. The pixels are compared using a χ^2 statistic

$$\chi^2 = \sum_i \frac{(f_{m,i} - s_{mb} f_{b,i})^2}{\sigma_{m,i}^2 + \sigma_{b,i}^2}, \tag{3.1}$$

where i represents an image band, and $f_{m,i}$ and $f_{b,i}$ refer to the i-th band flux of pixels m and b. s_{mb} accounts for scaling differences between m and b. How these differences are derived is explained in detail in Abdurro'uf & Akiyama (2017). If the χ^2 value is less than a certain threshold, then m is binned with b. After all pixels in the radius are binned, the total S/N is checked, if the S/N$\geq$10 in all bands, the binning is completed, and starts again with the next brightest pixel in the r-band. If the threshold is not met, the the radius is increased by 2 pixels and continues until the threshold is met. It is possible that pixels, especially at the outskirts, cannot be binned if their SEDs are not similar, in which case all remaining pixels are binned into one bin.

Abdurro'uf et al. (2023) expand on Abdurro'uf & Akiyama (2017) by using the software piXedfit (Abdurro'uf et al., 2021) to perform pixel binning. PiXedfit adds an additional consideration when binning which is the smallest diameter of a bin in pixels. This is to prevent a single bright pixel from being an entire bin. The smallest diameter bin can be thought of as the FWHM of the PSF, although the user can define this diameter to be anything.

Sorba & Sawicki (2015), Sorba & Sawicki (2018), and Giménez-Arteaga et al. (2023) did not bin their pixels and purely performed pixel-by-pixel SED fitting. Giménez-Arteaga et al. (2023) state as part of their caveats that there may not be enough S/N per pixel to infer robust physical parameters. As such they also apply a Voronoi tesselation binning to achieve a constant and higher S/N across the entire image. With this method they find the same gradients and trends as pure pixel-by-pixel binning and thus are confident that their results are trustworthy. This research follows these previous studies and does not bin the pixels, and enforces a S/N threshold of 1 in all the *JWST* wide filters in a given field, and a S/N $>$ 5 in both the F200W and F277W bands, or in the case of MACS 1423 NCF where F200W is not available, a S/N $>$ 5 in both the F277W and F444W bands. Pixels that do not satisfy the S/N criterion are not shown in the following property maps, or used in the analysis. Additionally, a comparison to the results of this analysis using purely pixel-by-pixel SED fitting and Voronoi tesselation binning is done in Section 5.1.

3.3 Constructing and Fitting Observed SEDs to Models

3.3.1 Stellar Population Synthesis

The integrated light from a region within a galaxy contains vast information about the physical processes that formed that region. The principal goal of stellar population synthesis (SPS) is to

extract these physical processes from the region's SED (review by Conroy (2013)) by fitting the SED to synthetic spectra. The large number of variables in the model has led to the popularity of techniques to explore the posterior space such as Markov Chain Monte Carlo (MCMC) and nested sampling.

The basis of modelling a region's spectrum is to assume several model parameters. An overview of the building blocks required to model a SED is shown in Figure 3.1. The first step is to model a simple stellar population (SSP) which describes how a single population of stars with the same metallicity evolves over time. This involves three ingredients; first, specifying an initial mass function (IMF). The IMF describes how many stars of a given mass are formed in the SSP. For SPS, the IMF affects the shape of the model SED and determines the normalization for the stellar mass-to-light ratio. The IMF has been studied for decades, with the canonical Salpeter IMF taking the functional form of a power law

$$N(m)dm = \xi_0 \left(\frac{m}{M_\odot}\right)^{-2.35} \left(\frac{\Delta m}{M_\odot}\right). \tag{3.2}$$

This work, utilizes a Chabrier IMF (Chabrier, 2003), which is a lognormal distribution.

Secondly, the process assumes a series of stellar isochrones, which traces a path on the Hertzsprung-Russell diagram for stars of the same age but different masses. Finally, an empirical library of stellar spectra is needed to convert to outputs of stellar evolution calculations to observable SEDs. These empirical libraries are drawn from stars in the solar neighborhood. This work utilizes the Basel stellar tracks and the Padova isochrones.

Once a simple stellar population is assumed, the spectra are then manipulated under the effects of a presumed dust law and star formation history. This work adopts the Calzetti attenuation law for the dust attenuation (Calzetti, 2001). The SFH is a fossilized record of all the physical processes that formed the galaxy including mergers, AGN and supernovae feedback, and gas inflows and outflows that impact the rate of star formation. From the SFH, properties such as the stellar mass of the region (the star formation rate integrated over the lifetime of the region), as well as the sSFR and the mass-weighted age can be determined.

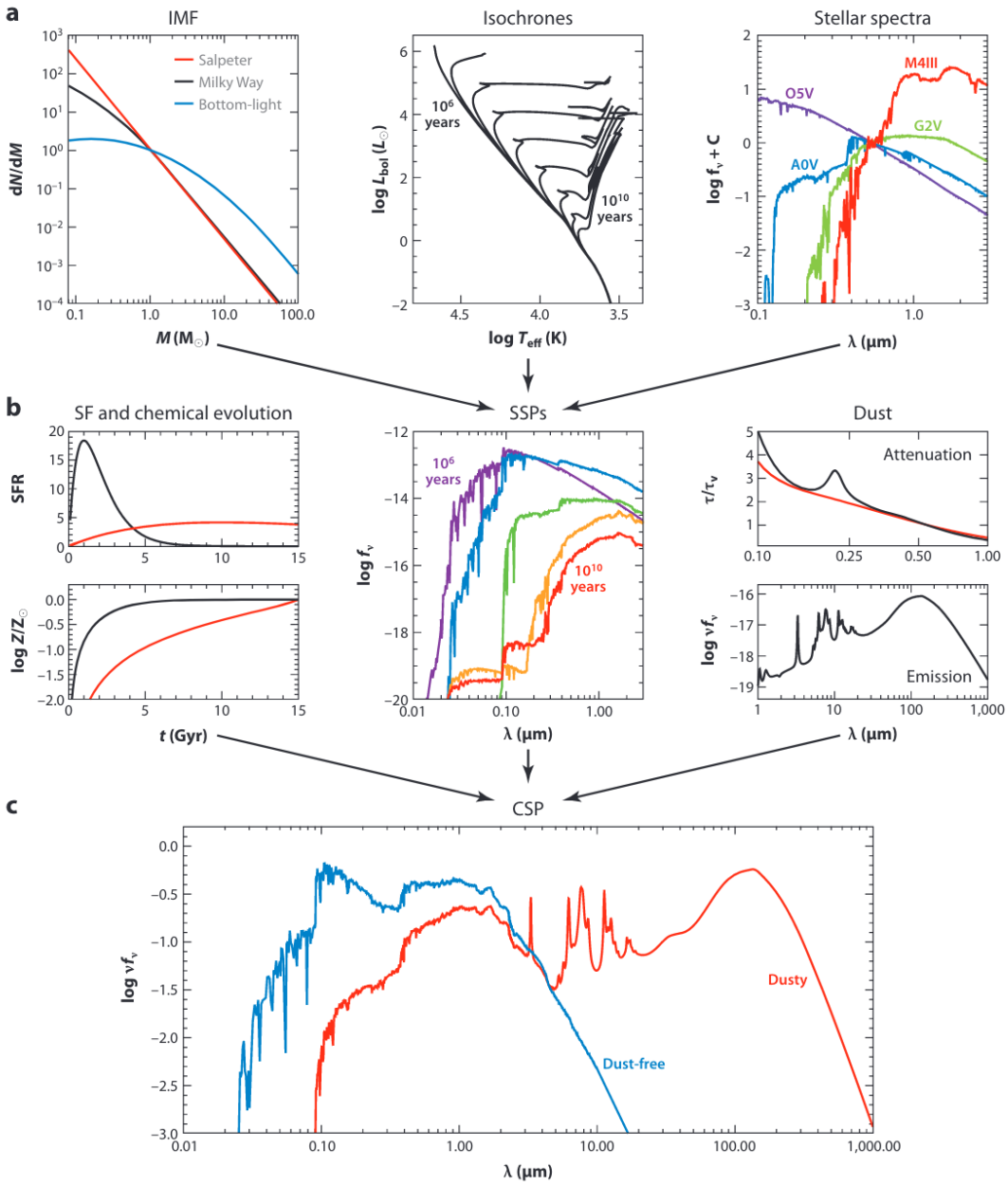

Figure 3.1: Figure 1 from Conroy (2013). An overview of the process of creating composite stellar populations. The ingredients needed for creating a simple stellar population given in the first row are an initial mass function, isochrones of different ages and metallicities, and either observed or empirical stellar spectra. The simple stellar population is then combined with models for the star formation history and dust attenuation to make a composite stellar population.

3.3.2 Parametric vs. Nonparametric Star Formation Histories

The models generated to fit the SED normally include a presumed SFH. Since many properties are derived from the SFH, many properties are dependent upon what priors are assumed for the SFH. The SFH presumed could be arbitrarily complex; however, a minimum number of

parameters is generally preferred as the amount of information that can be robustly extracted is limited. Parametric models approximate the SFH using simple functional forms, the most commonly applied SFH is the exponentially-declining or τ-model

$$\mathrm{SFR(t)} \propto \begin{cases} \exp\left(-\frac{\mathrm{t}-\mathrm{T}_0}{\tau}\right), & t > T_0 \\ 0, & t < T_0. \end{cases} \tag{3.3}$$

This assumes that the star formation jumps to a peak value at T_0 after which it declines exponentially with timescale τ. However, it has been shown that assuming an exponentially-declining SFH can underestimate the SFR on average by a factor of 5-10 since the models are unable to reproduce rising SFHs (Reddy et al., 2012; Simha et al., 2014). Other popular parametric SFH models are delayed exponentially declining, lognormal, and double power law (Carnall et al., 2019).

Due to their lack of flexibility, parametric SFHs impose strong priors on the SFR(t). This results in tight posteriors leading to unrealistically precise answers on low S/N data, and biasing the deduced physical quantities (Iyer & Gawiser, 2017; Leja et al., 2019). Additionally, comparison to simulations shows that SFHs with complex behaviour such as multiple bursts of star formation or rejuvenation cannot be recovered from parametric models (Leja et al., 2019; Simha et al., 2014). A solution to this problem is to assume a "nonparametric" SFH. A bit of a misnomer, Ivezić et al. (2014) describes "nonparametric" as not meaning there are no parameters, but rather exploring distribution-free models. Ideally, the shape of the SFH will be flexible and determined based off of the data. The simplest nonparametric methods to recover the SFH fit for the mass formed in a series of time bins; however, this method leads to trade-off between the computational time and the amount of information recovered from the SED due to the number of bins/parameters, as well as leading to unnatural discontinuities in the SFH. (Leja et al., 2017).

This work utilizes the software `Dense Basis` to perform SED fitting (Iyer et al., 2019). There are multiple SED fitting codes that take advantage of new Bayesian statistical techniques such as `Bagpipes` (Carnall et al., 2018), `Prospector` (Johnson et al., 2021), and `Beagle` (Chevallard & Charlot, 2016). The difference between these codes and `Dense Basis` is that the `Dense Basis` method uses nonparametric SFHs constructed using Gaussian Process Regression (GPR). An advantage of which is that it can make smooth SFHs with a minimal number of parameters. The following sections outline the GPR and `Dense Basis` method as

described in Iyer et al. (2019).

3.3.3 `Dense Basis`

`Dense Basis` defines a SFH by a tuple: $(M_*, SFR, \{t_X\})$, where M_* and SFR is the stellar mass and the star formation rate at the time of observation, and the set t_X contains N number of "shape" parameters that describe the SFH. The shape parameters are N lookback times at which the galaxy formed equally spaced quantiles of mass (ie. t_{50} is the time at which 50% of the mass in a region in a galaxy formed). The user defines how many N lookback times to define the shape of their SFH, and these N lookback times correspond to the number of shape parameters as

$$
\begin{aligned}
N = 1 \quad & P = \{t_{50}\} \\
N = 2 \quad & P = \{t_{33}\, t_{67}\} \\
N = 3 \quad & P = \{t_{25}\, t_{50}\, t_{75}\} \\
N = 4 \quad & P = \{t_{20}\, t_{40}\, t_{60}\, t_{80}\} \\
& \ldots
\end{aligned}
$$

Naturally, the shape of the SFH is better captured as N increases, however; Iyer & Gawiser (2017) state that it is possible to recover multiple episodes of star formation with as few as three $\{t_X\}$ parameters. This tuple describes the constraints on the shape and normalization of the SFH. To reconstruct the SFH from the tuple, the constraints are quantified as points on a fractional mass ($M_{*,tot}(t)$)-cosmic time (t) plane, and a smooth curve is drawn through the points. Differentiating the curve would result in the SFH, the star formation rate as a function of lookback time. The simplest solution, connecting the points with a piecewise linear function, would result in a SFR with jump discontinuities when taking the derivative. `Dense Basis` uses GPR implemented with the `george` python package (Ambikasaran et al., 2015) to reconstruct a smooth SFH with uncertainties.

To properly reconstruct the SFH from a SED, several factors must be considered such as the chemical enrichment, initial mass function, and dust attenuation. The SFH can then be written as

Table 3.1. SED fitting priors for all fields used to solve the Bayesian inference equation in Equation 3.4.

Parameter	Symbol/Unit	Range	Prior
Stellar Mass	M_*/log(M/$M_\odot$)	(4, 11)	Flat
Redshift	z	($z_{\rm phot}$ - 0.02, $z_{\rm phot}$ + 0.02)	Flat
Dust	A_V/mag	(0, 4)	Exponential
Metallicity	log(Z/$Z_\odot$)	(-1.5, 0.25)	Flat
Star Formation Rate	SFR/log(SFR/$M_\odot yr^{-1}$)	(-14, -7)	Flat (in sSFR)

a Bayesian inference problem:

$$P(SFH, A_V, Z, z...|F^{obs}_{\nu,j}) = \frac{P(F^{obs}_{\nu,j}|SFH, A_V, Z, z...)P(SFH, A_V, Z, z...)}{P(F^{obs}_{\nu,j})} \tag{3.4}$$

Here, $F^{obs}_{\nu,j}$ is the observed photometry being fit in the jth photometric filter. SFH is the SFH tuple defined in Section 3.3.3 $(M_*, SFR, \{t_X\})$, A_V is the dust model, Z is the metallicity, and z is the redshift. Overall, there are N+5 $(\{t_X\}, M_*, SFR, A_V, Z, z)$ free parameters that the method fits for.

The posterior computation is completed by a "brute-force" Bayesian approach. A large number of model SEDs are constructed via random draws of the prior distribution corresponding to each free parameter. The user must ensure that the number of pregrid samples computed is sufficient such that the model SEDs effectively explore the parameter space given the problem they are trying to solve. Iyer et al. (2019) performed fits to a sample of 1000 galaxies while varying the size of the pregrid, and deduced that the optimal size of the pregrid is $\sim$ 900,000 SEDs.

The uncertainties in the SFH are calculated after the fit is completed by performing 100 self-consistent draws from the posterior for each parameter in the tuple $(M_*, SFR, \{t_X\})$. The corresponding realization of the SFH with those set of parameters is calculated using GPR. The 68$\%$ confidence intervals are then calculated at each point in lookback time by using the 16th and 84th percentiles of the combined SFR distribution using all draws.

A summary of the priors for the free parameters is described in Table 3.1, and shown in Figure 3.2. For this work, we assumed the set $\{t_X\}$ has three parameters to describe the SFH, and these three parameters represent t_{25}, t_{50}, and t_{75}, making a total of 8 free parameters.

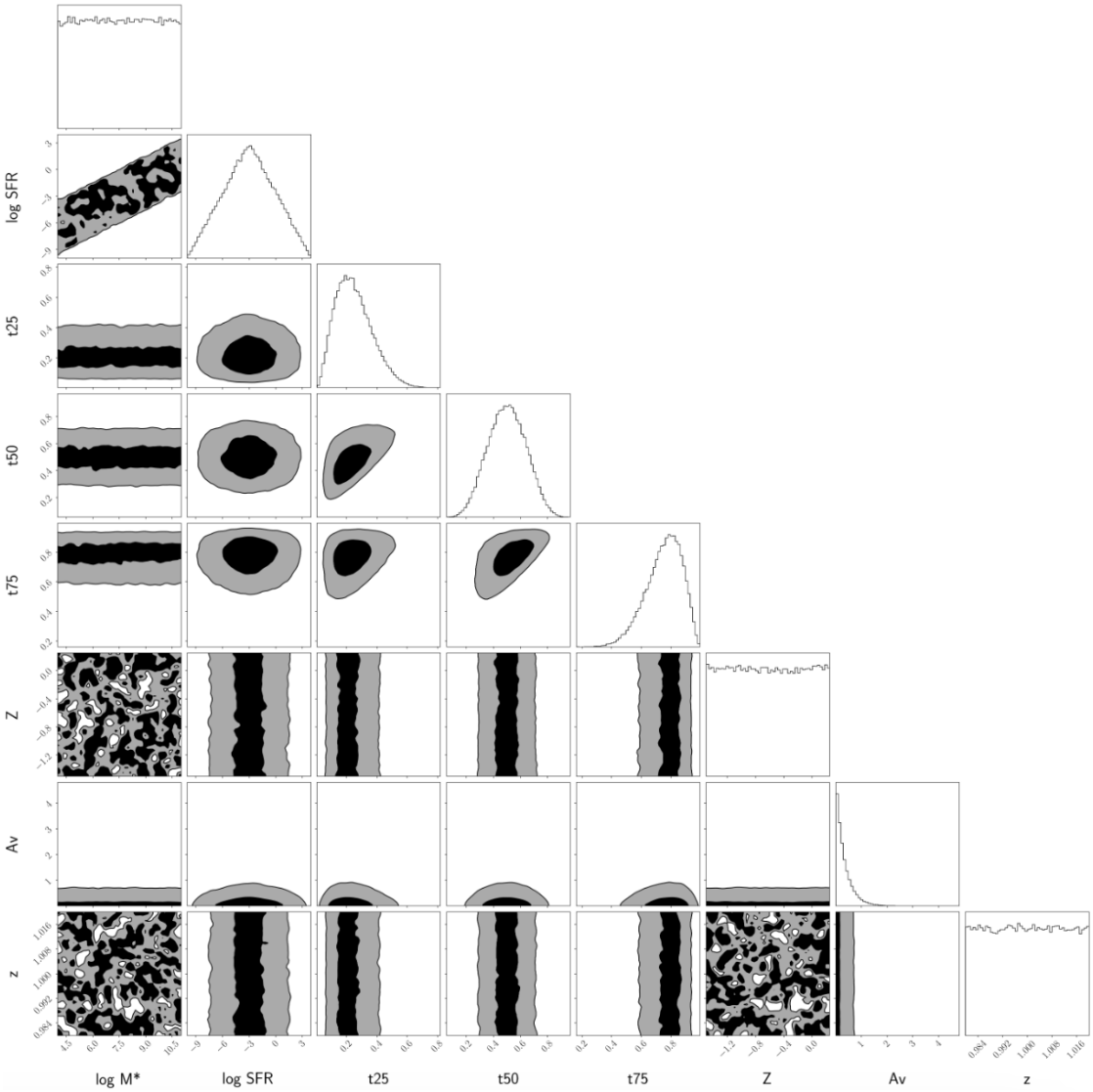

Figure 3.2: The prior distribution of parameters as given in Table 3.1. The redshift prior changes to be centered on the photometric redshift of a given galaxy.

To quantify the goodness-of-fit, we use χ^2 given by

$$\chi^2 = \sum_{j=1}^{N_{\rm filters}} \left(\frac{F_{\nu,j}^{\rm obs} - F_{\nu,j}^{\rm model}({\rm SFH}, A_V, Z, z)}{\sigma_j} \right)^2 . \tag{3.5}$$

To ensure a good fit, we look at the reduced χ^2 (χ^2_ν) given by

$$\chi^2_\nu = \frac{\chi^2}{\nu}, \tag{3.6}$$

where ν is the number of degrees of freedom. The number of degrees of freedom is calculated by subtracting the number of observations minus the number of fitted parameters. In the case

of the cluster field, where there are 11 photometric filters used and 8 free parameters, the total number of degrees of freedom is 3. If $\chi^2_\nu \gg 1$, then the residuals of the fit (shown in Equation 3.5 as $F^{\rm obs}_{\nu,j} - F^{\rm model}_{\nu,j}$) are larger than the errors, meaning a poor model fit. If the $\chi^2_\nu \ll 1$, the model is overfitting the data, either the errors are overestimated or the model is fitting noise. Ideally, the size of the residuals would be the same size as the error, giving a $\chi^2_\nu \sim 1$ (Bailer-Jones, 2017).

3.4 Spatially Resolved Property Maps

Using `Dense Basis` as described above, spatially resolved SED fitting is used to create different spatially resolved property maps such as mass, SFR, and dust. This is done by running `Dense Basis` on each pixel in a galaxy (which pixels are included are deduced using the S/N criterion discussed in Section 3.2) and the maps are assembled by placing these values at a pixel's location. Each pixel has a size of 0.04 arcsec which corresponds to 0.320 kpc/pixel at z $= 1$ and 0.308 kpc/pixel at z $= 3$. To account for systematic uncertainties within the photometry, the errors are increased by adding in quadrature 3% of the flux to the flux errors before running SED fitting.

Using the offset from the main sequence shown in Figure 2.3, galaxies were divided into bins below, on, and above the main sequence according to log(ΔMS) = [-1.5, -0.4], [-0.4, 0.4], and [0.4, 1.5], respectively. This binning was decided using the intrinsic scatter of the main sequence ($\approx$ 0.3 dex) and such that we are not looking too far below the main sequence that we are looking at a passive sample. This binning scheme results in 22 galaxies above the MS, 122 galaxies on the MS, and 22 galaxies below the MS. In addition, galaxies were separated into 2 mass bins according to log(M/M$_\odot$) = [8.5-9.9], and [9.9-11.3]; this binning ensures there are at least 10 galaxies in each mass bin above the main sequence, and 5 galaxies in each mass bin below the main sequence.

Figures 3.3, 3.4, and 3.5 show examples of the physical property maps inferred with `Dense Basis` for galaxies that lie on, above, and below the main sequence in the highest mass bin. All physical property values that are shown are the median values evaluated from the Bayesian posterior distribution function, with uncertainties for each pixel extracted from the 16th and 84th percentiles of the posterior distribution. The property maps are smooth and lack any discontinuities that would indicate areas of parameter space that are not being sufficiently explored when constructing the atlas within `Dense Basis`. The size of the FWHM of the

F444W PSF is shown in each figure (0.145" or $\sim$ 2.302 pixels). With that knowledge we are able to resolve individual star-forming regions within all three galaxies. The star formation rate density plotted is the instantaneous star formation rate, which is the star formation averaged over the last 1% of mass formed; thus, this timescale is longer for quenched galaxies, and smaller for star-bursting galaxies. An additional property that is plotted is the t_{50} of the region, the time at which the region has formed half its mass over its lifetime, and is used as a proxy for the age of a region.

Figures 3.3 and 3.5 illustrate galaxies with old, quiescent populations in their bulges with multiple star-forming clumps that trace the spiral structure that is observed in the RGB image, features that would be washed out if using a single integrated SED. We see that star-forming regions are associated with lower t_{50} values, indicating these regions are home to younger stellar populations. Figure 3.4 shows a galaxy with multiple star-forming clumps and a star-forming bulge, with a high amount of dust in the center.

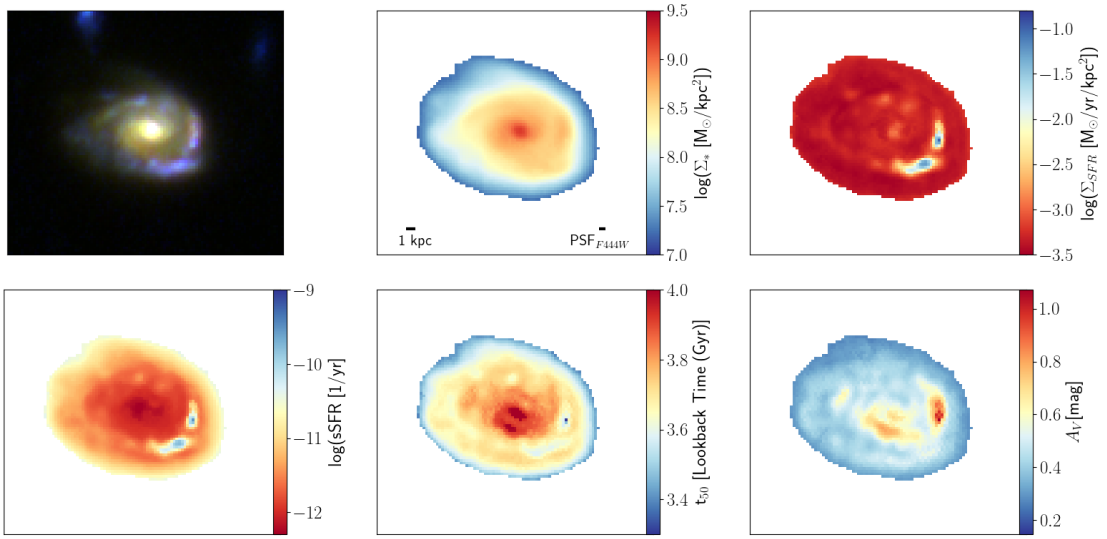

Figure 3.3: Property maps for galaxy CANUCS-2201596, z_{phot} = 0.73, and integrated $\log(M_\star/M_\odot) = 10.76$, an example of a galaxy that is below the main sequence. The RGB image is made from combining the filters F606W (blue), F150W (green), and F444W (red). The rest of the maps are physical properties inferred with `Dense Basis`. The top row, from left to right, shows the maps for the logarithm of the stellar mass surface density, and the logarithm of the star formation rate surface density. The bottom row shows the logarithm of the specific star formation rate, t_{50}, and the visual extinction A_V.

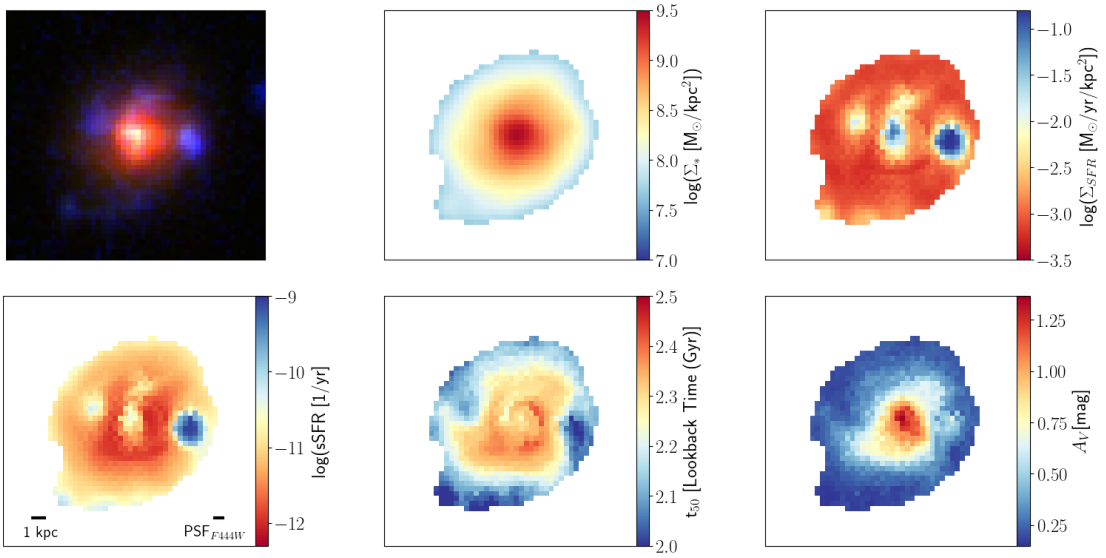

Figure 3.4: Property maps inferred with `Dense Basis` for galaxy CANUCS-5109174, z_{phot} = 1.44 and $\log(M_\star/M_\odot) = 10.60$, an example of a galaxy that is on the main sequence. Additional details can be found in Figure 3.3.

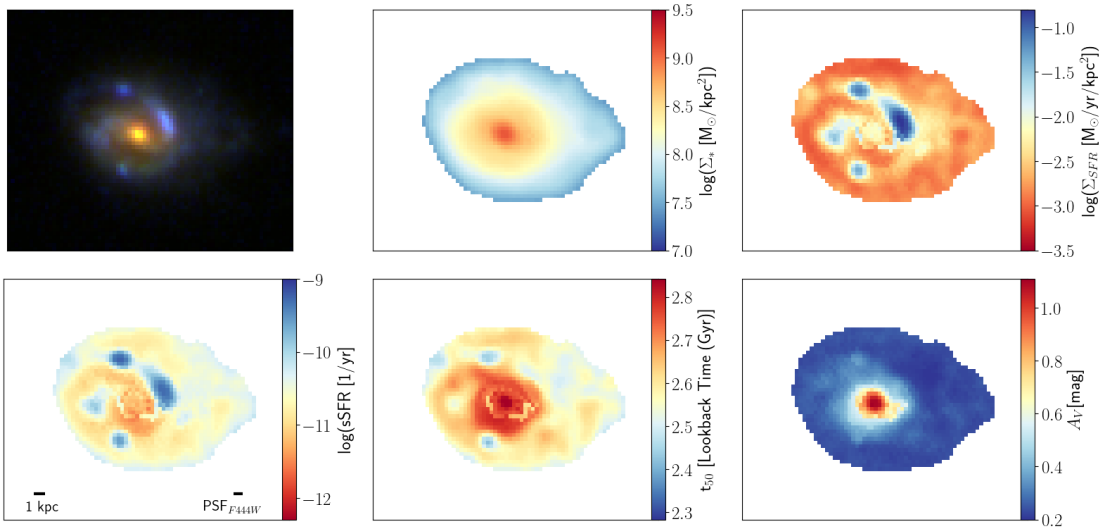

Figure 3.5: Property maps inferred with `Dense Basis` for galaxy CANUCS-2200493, z_{phot} = 1.10, and $\log(M_\star/M_\odot) = 10.46$, an example of a galaxy that is above the main sequence. Additional details can be found in Figure 3.3.

3.5 Making Radial Profiles

To accurately make radial profiles of different properties, we need to find the deprojected galactocentric radius to each pixel in a given galaxy. To do this we can construct a 2D rotation matrix R that rotates points in the observed xy plane counterclockwise about the origin. It can then be multiplied by a column vector with coordinates $\mathbf{v} = (x, y)$ to arrive at the rotated

coordinates (x', y'):

$$R\mathbf{v} = \begin{bmatrix} \cos\theta & -\sin\theta \\ \sin\theta & \cos\theta \end{bmatrix} \begin{bmatrix} x \\ y \end{bmatrix} = \begin{bmatrix} \mathrm{x}\cos\theta - \mathrm{y}\sin\theta \\ \mathrm{x}\sin\theta + \mathrm{y}\cos\theta \end{bmatrix} = \begin{bmatrix} x' \\ y' \end{bmatrix}. \tag{3.7}$$

With this assumption, and knowing the ellipticity of the galaxy, we may deproject the galaxy along its minor axis according to

$$y' \longmapsto y'/(\mathrm{b/a}), \tag{3.8}$$

where b/a is the axis ratio of the galaxy. As previously mentioned, the axis ratio and position angle of the galaxy is determined using `GALFIT`.

Once the ellipticity is known, the image of the galaxy is rotated, such that its semi-major axis aligns with the x-axis. Then the y-coordinate (along the semi-minor axis) of each pixel is stretched according to Equation 3.8.

Once the y-coordinate has been deprojected for each pixel, the distance to that pixel is measured from the center of mass of the galaxy. The center of mass is determined from fitting the spatially resolved mass maps acquired from pixel-by-pixel SED fitting with a `Sersic2D` model provided by `astropy.modelling`. Notably, only the center coordinates of the galaxy are used from this fitting procedure and not other properties that are derived such as the Sérsic index. This is due to the SED fitting procedure being performed on PSF convolved images, resulting in the galaxy appearing more extended then it is. To account for this the `Sersic2D` fitting would have to be performed with the PSF information. Figure 3.6 shows an example of this procedure and shows the common trend that the center of mass is very close to the pixel with the maximum mass from SED fitting. Finally, since a galaxy's offset from the main sequence is determined by its integrated stellar mass and star formation rate, the extracted profiles in both stellar mass and star formation rate are normalized to the mean integrated values from `Dense Basis`, as was done in Nelson et al. (2021).

After all of this, we have maps of the stellar mass, star formation rate, and other physical quantities outputted by `Dense Basis` for all 166 galaxies in our sample from Chapter 2 as well as the galactocentric radius of each pixel in the galaxy. Using these maps we are able to deduce average trends in where star formation is relative to a galaxy's placement to the star-forming main sequence.

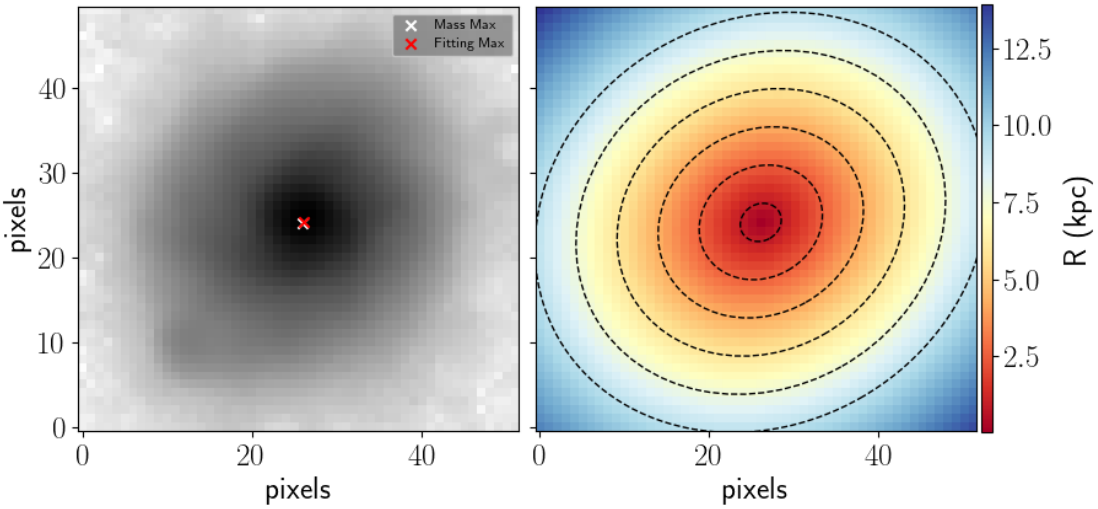

Figure 3.6: *Left:* The two-dimensional mass map for a galaxy in the sample obtained from pixel-by-pixel SED fitting. The white cross indicates the pixel with the maximum mass, and the red cross indicates the coordinates for the center of mass using a `Sersic2D` model on the mass map. *Right:* The deprojected physical radii at different pixels in the galaxy using Equations 3.7 and 3.8. The contours indicate the centers of the elliptical annuli radial bins [0.25R_e, 0.75R_e, 1.25R_e, 1.75R_e, 2.25R_e, 2.75R_e] used to calculate the radial profiles described in Section 4.2

.

Chapter 4

Results

This chapter introduces the results of the spatially resolved SED fitting and the extraction of the radial profiles for different properties.

4.1 Where Star Formation is Occurring within a Galaxy

Here we present the results from the pixel-by-pixel SED fitting that was described in Chapter 3. First, to give an overview of the sample, Figures 4.1 and 4.7 show the RGB image for a random subsample of galaxies in the high mass bin ($10^{9.9}M_{\odot}$-$10^{11.3}M_{\odot}$) and low mass bin ($10^{8.5}M_{\odot}$-$10^{9.9}M_{\odot}$) respectively, with galaxies separated depending on whether they are above, on, or below the main sequence. The images are constructed such that there are two filters, F277W (green) and F444W (red) that lie above the Balmer break at the redshifts of all the galaxies. The blue filter is dynamic and is either F606W, F090W, or F115W, depending on the redshift of the galaxy such that the filter lies below the Balmer break. This is done to probe the physical differences in the SED of a galaxy above and below the Balmer break based on the age of the galaxy. These images highlight the morphological differences between the different galaxies, where even galaxies that are below the main sequence exhibit bluish regions in their disk that may be areas of active star formation. Further details can be discerned by looking at the different property maps. These same subsamples of galaxies are shown in the following figures to show their different properties. The rest of the sample of galaxies can be found in the Appendix.

Figures 4.2 and 4.8 show the stellar mass surface density maps. All of the galaxies in these figures show similar trends: the center of the galaxy has the highest concentration of mass, and

the stellar mass decreases smoothly towards the outskirts of the galaxy. There are no regions in any of the galaxies where there is more mass than at the center. Any structure that is observed in the RGB images of the galaxy, such as in the blue regions of galaxy I in Figure 4.1, are greatly smoothed out. The general smoothness in the stellar mass surface density of galaxies has been observed in nearby galaxies (Zibetti et al., 2009), and is a stark contrast to what is observed in other properties.

Figures 4.3 and 4.9 show the star formation rate surface density maps and Figures 4.4 and 4.10 show the specific star formation rate maps, It is immediately clear from these figures that the star formation rate is not as spatially smooth or uniform as the mass in a galaxy is. It is also clear that there are similarities in the morphology and the star formation rate of the galaxies, with enhanced star-forming regions like those observed in Galaxies L and O in Figure 4.3 corresponding to bluish regions in Figure 4.1. The inhomogeneities in these maps are further discussed in Section 4.3.

Note that in the maps, neither the stellar mass surface density values nor the star formation rate surface density values have been inclination corrected. This correction accounts for the increased area in a given pixel due to the projection of the galaxy on the sky. In the sample criteria, we omit heavily inclined galaxies from the sample, as such the consequences from this increased area that is observed is minimal. Additionally, we note that applying an inclination correction here does not seem necessary: Bluck et al. (2020) applied an inclination correction to their sample and found none of their results depended on this correction. Furthermore, any inclination and magnification corrections would cancel out in the sSFR radial profiles.

Figures 4.5 and 4.11 show the dust maps. For low mass galaxies we can see concentrations of dust that trace star formation (for example, Galaxies h, n, p, and q) and for the high mass galaxies we see eight out of the ten galaxies above the main sequence have high dust attenuation in their centers, with a smaller number of galaxies on and below the main sequence having dust concentrated in their centers.

Finally, Figures 4.6 and 4.12 show t_{50} maps. Here, t_{50} is presented as a fraction of the age of the universe, where 0 is the Big Bang and 1 is the epoch of observation of the galaxy. Similar to dust, we see younger stellar populations where there are enhanced areas of star formation (for example, Galaxies L, V, O, and n).

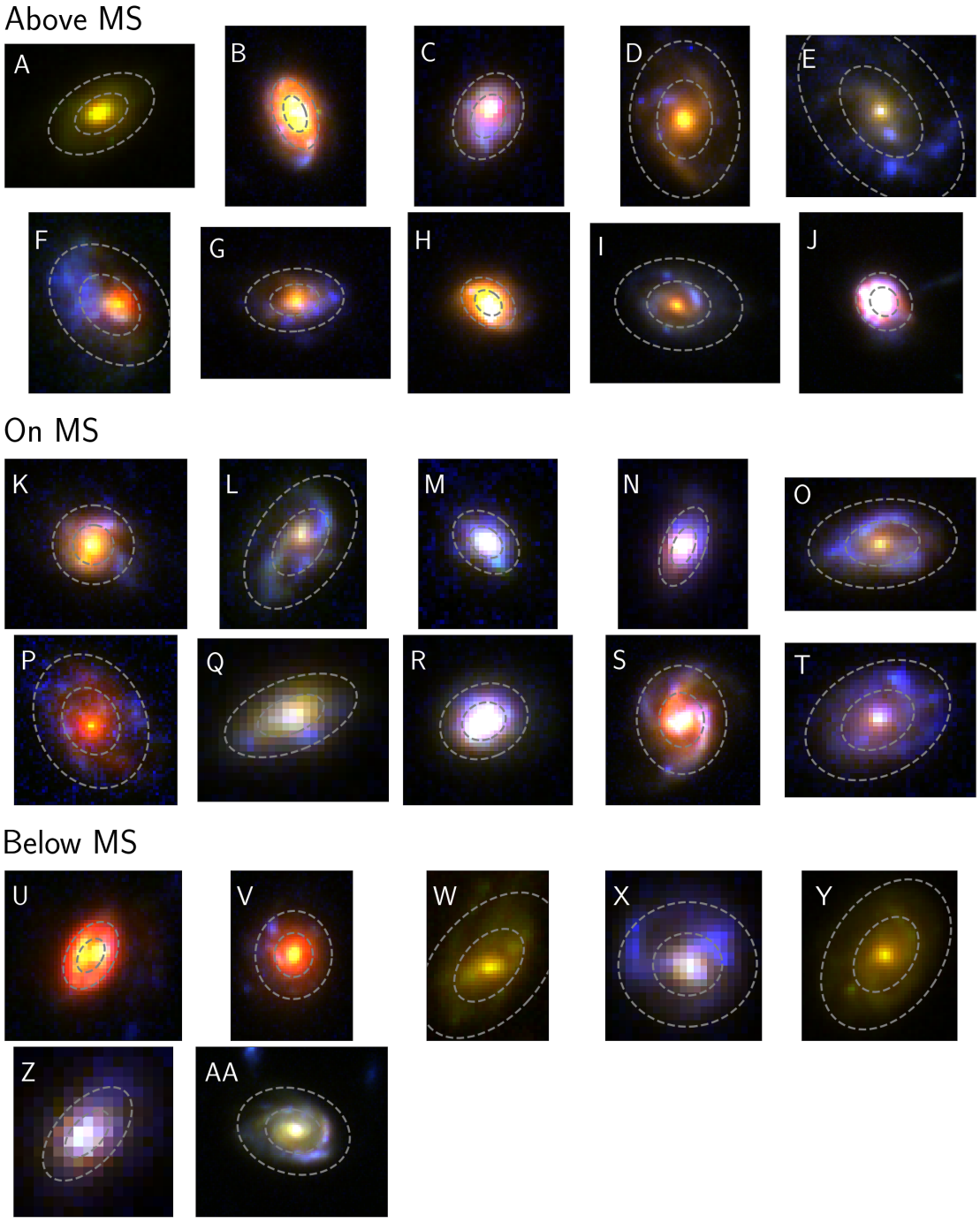

Figure 4.1: RGB images for a randomly selected subsample of galaxies in the high mass bin ($10^{9.9}M_{\odot}$-$10^{11.3}M_{\odot}$) separated by their placement relative to the main sequence. The RGB images are made from combining F277W (green) and F444W (red), and either F606W, F090W, or F115W (blue) depending on the redshift of the galaxy. The grey ellipses show $1R_e$ and $2R_e$ as determined by `GALFIT` on the F444W images.

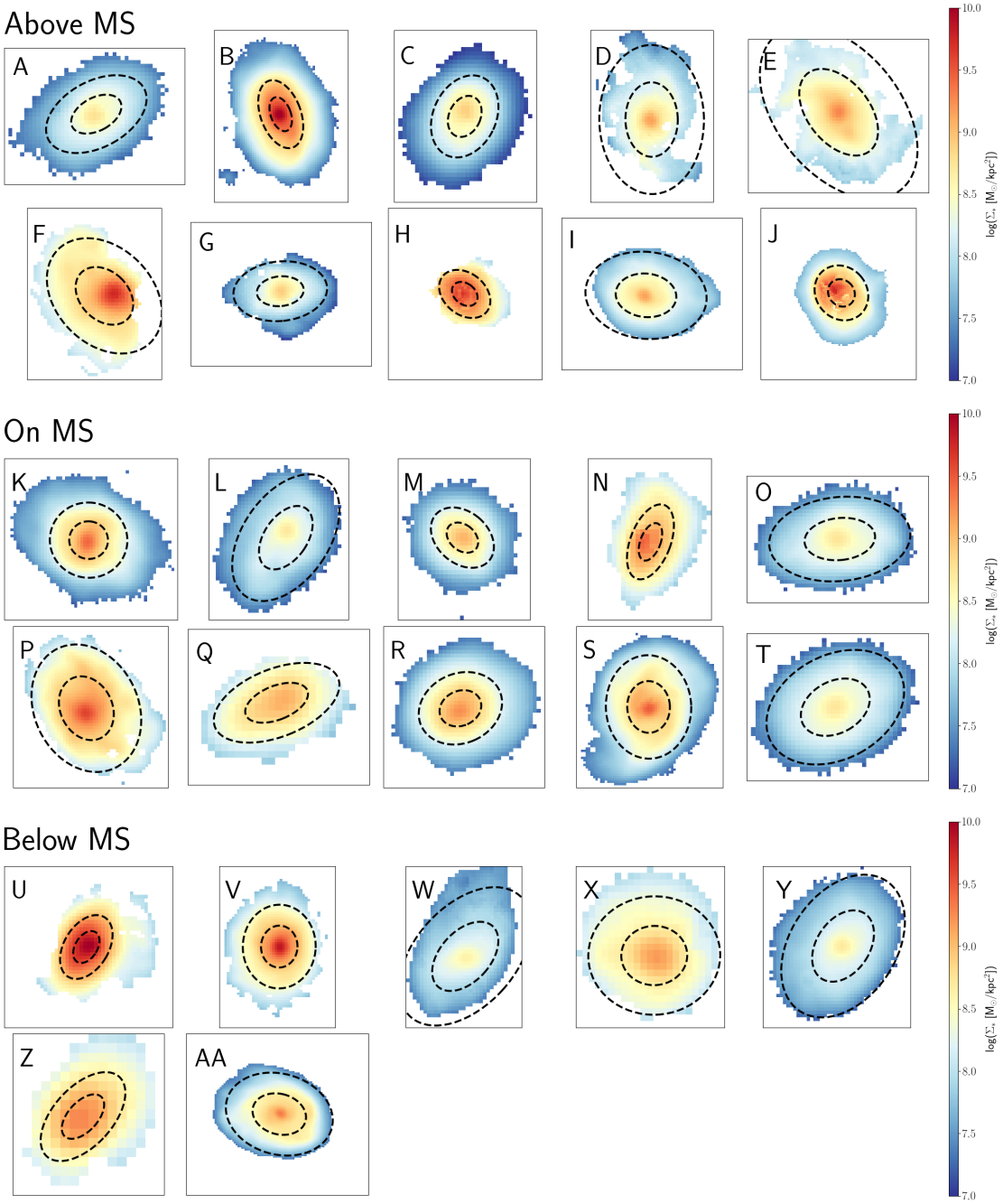

Figure 4.2: Stellar mass maps for a randomly selected subsample of galaxies in the high mass bin ($10^{9.9}$M$_\odot$-$10^{11.3}$M$_\odot$), as determined with `Dense Basis`. Galaxies are separated by their placement relative to the main sequence. The grey ellipses show 1R$_e$ and 2R$_e$ as determined by `GALFIT`.

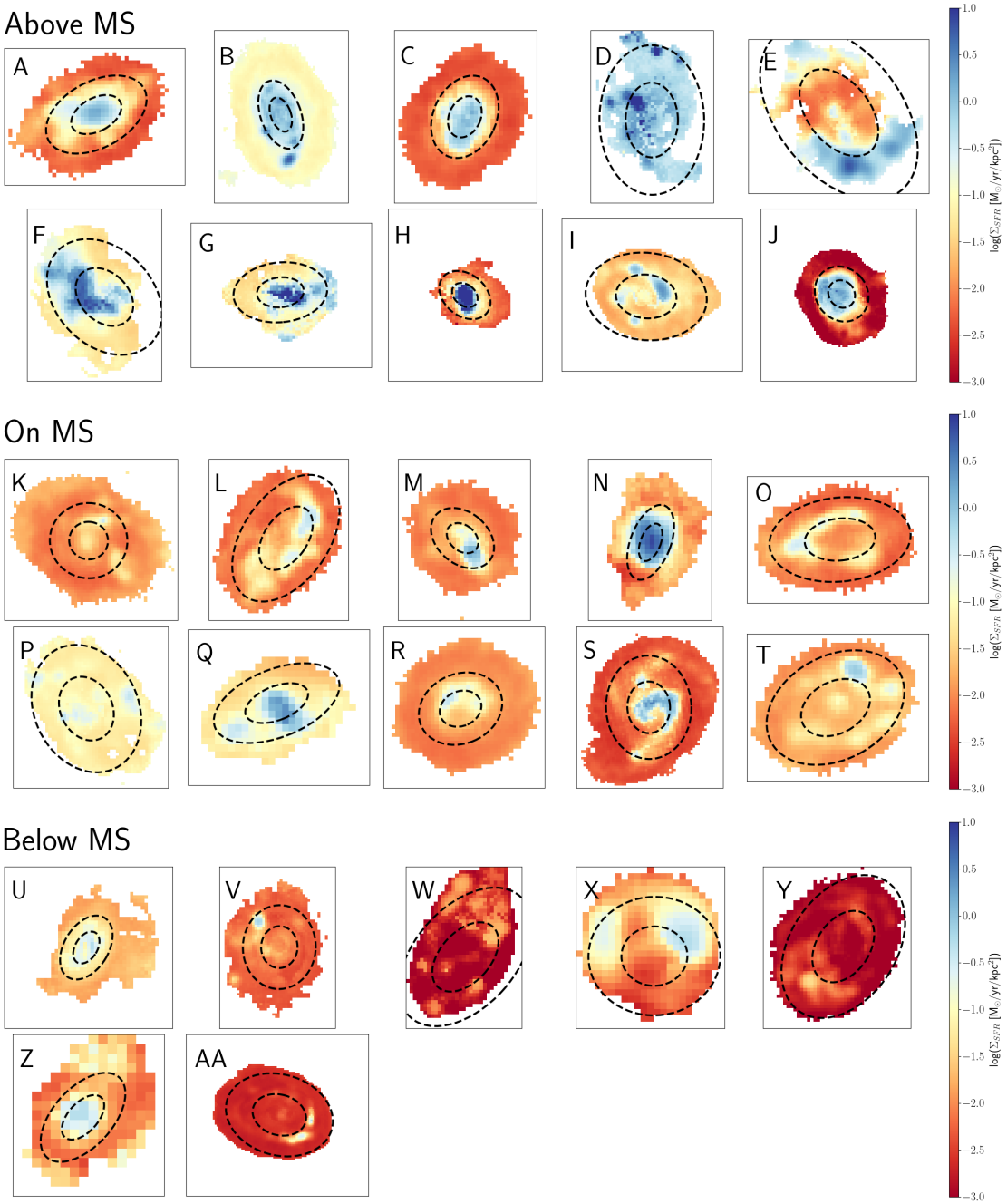

Figure 4.3: Star formation rate maps. Additional details can be found in Figure 4.2.

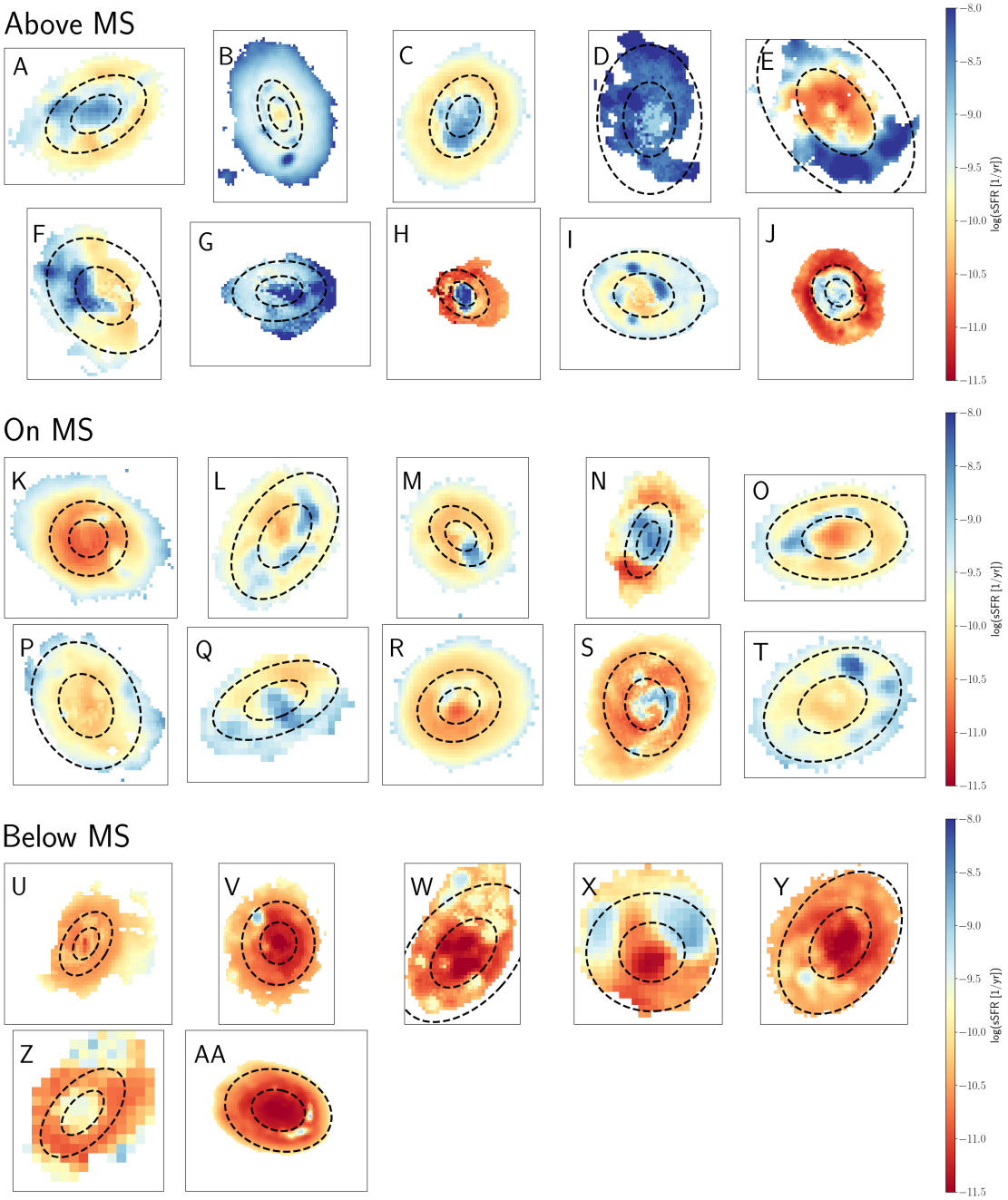

Figure 4.4: Specific star formation rate maps. Additional details can be found in Figure 4.2.

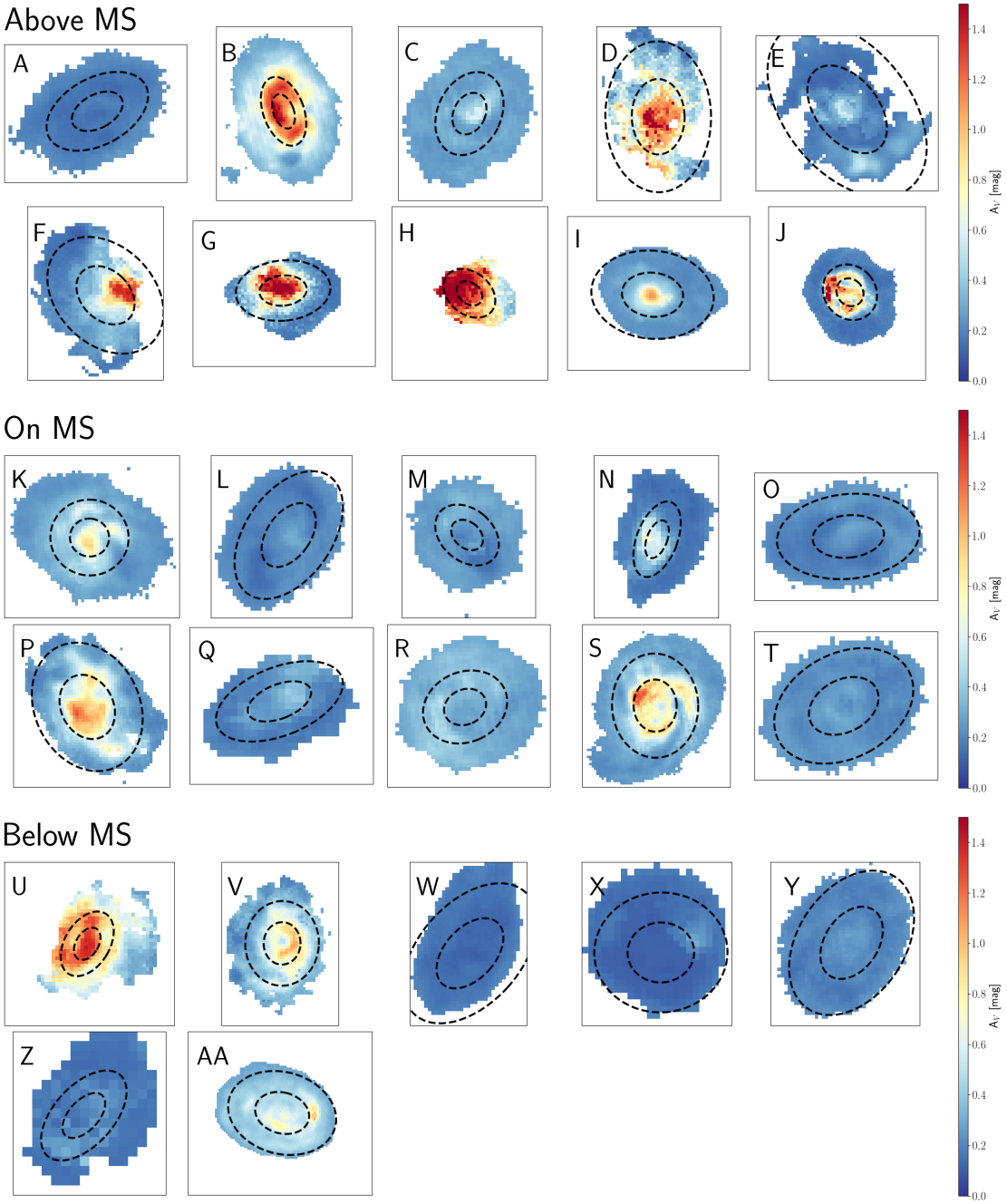

Figure 4.5: Dust maps. Additional details can be found in Figure 4.2.

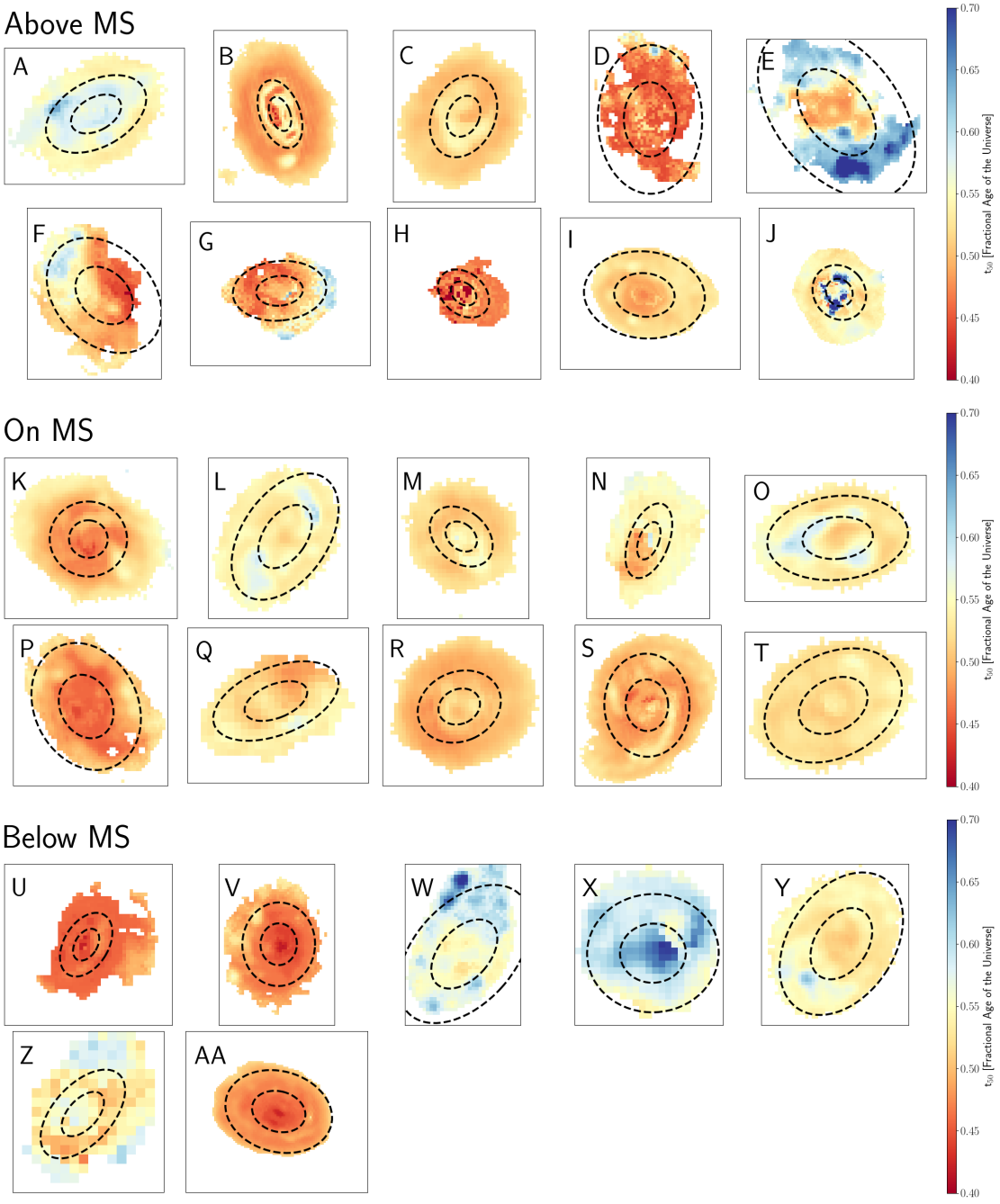

Figure 4.6: t_{50} maps, given as a fraction of the age of the universe at a given redshift, with 0 being the Big Bang and 1 being the epoch of observation. Additional details can be found in Figure 4.2.

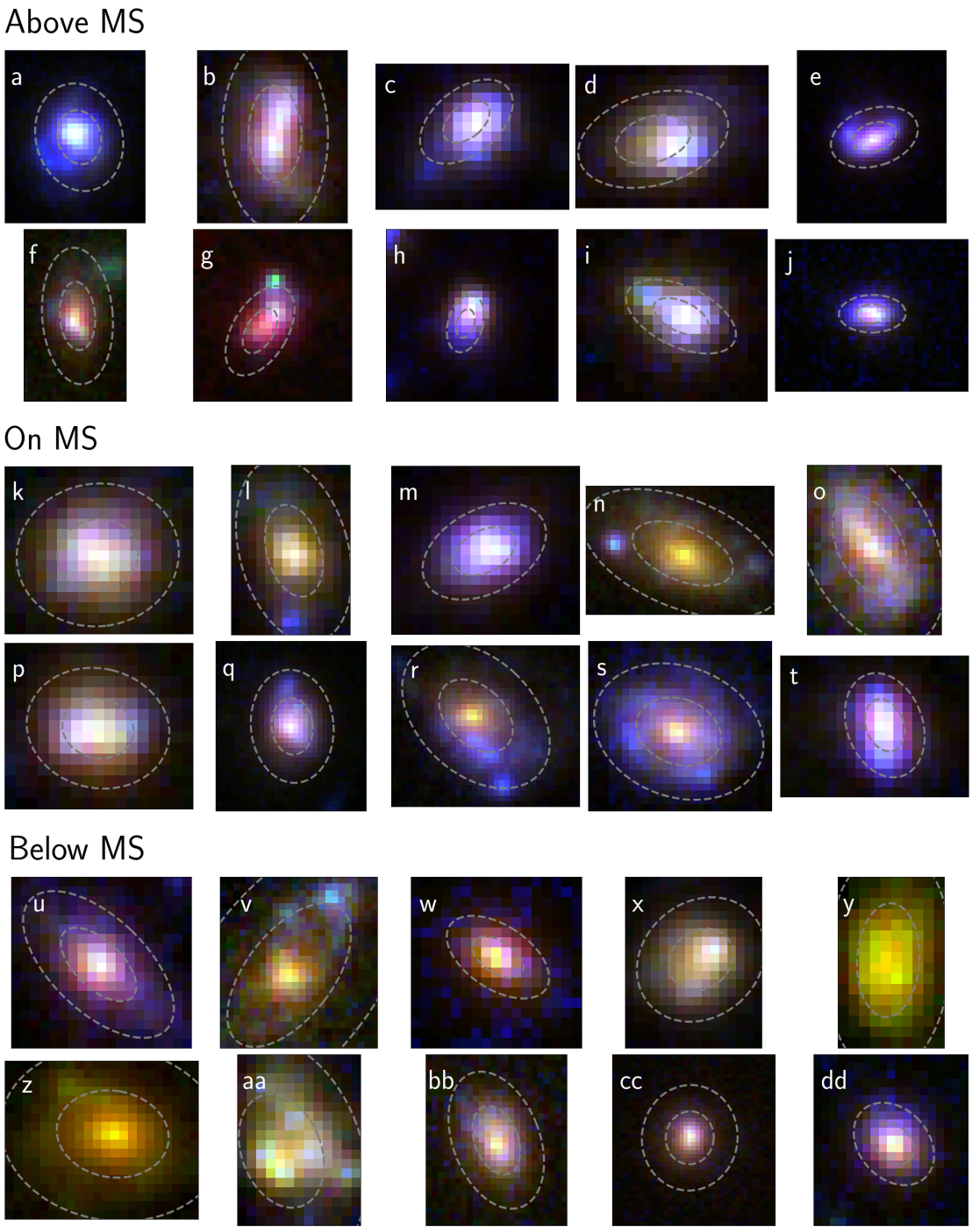

Figure 4.7: RGB images for a randomly selected subsample of galaxies in the low mass bin ($10^{8.5}M_{\odot}$-$10^{9.9}M_{\odot}$) separated by their placement relative to the main sequence. The RGB images are made from combining F277W (green) and F444W (red), and either F606W, F090W, or F115W (blue) depending on the redshift of the galaxy. The grey ellipses show $1R_e$ and $2R_e$ as determined by GALFIT in F444W.

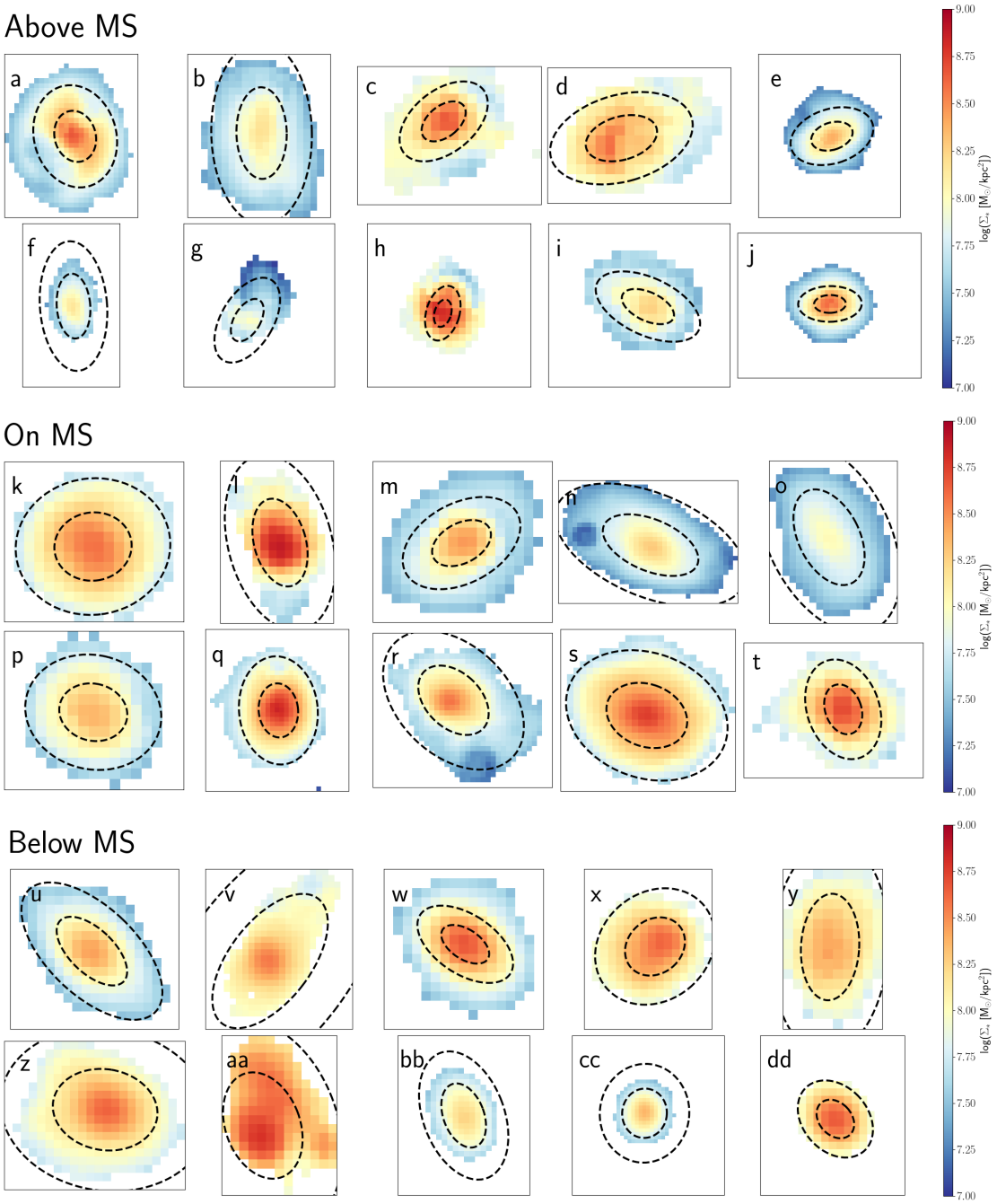

Figure 4.8: Stellar mass maps for a randomly selected subsample of galaxies in the high mass bin ($10^{8.5}$M$_\odot$-$10^{9.9}$M$_\odot$), as determined with `Dense Basis`. Galaxies are separated by their placement relative to the main sequence. The black ellipses show 1R$_e$ and 2R$_e$ as determined by `GALFIT`.

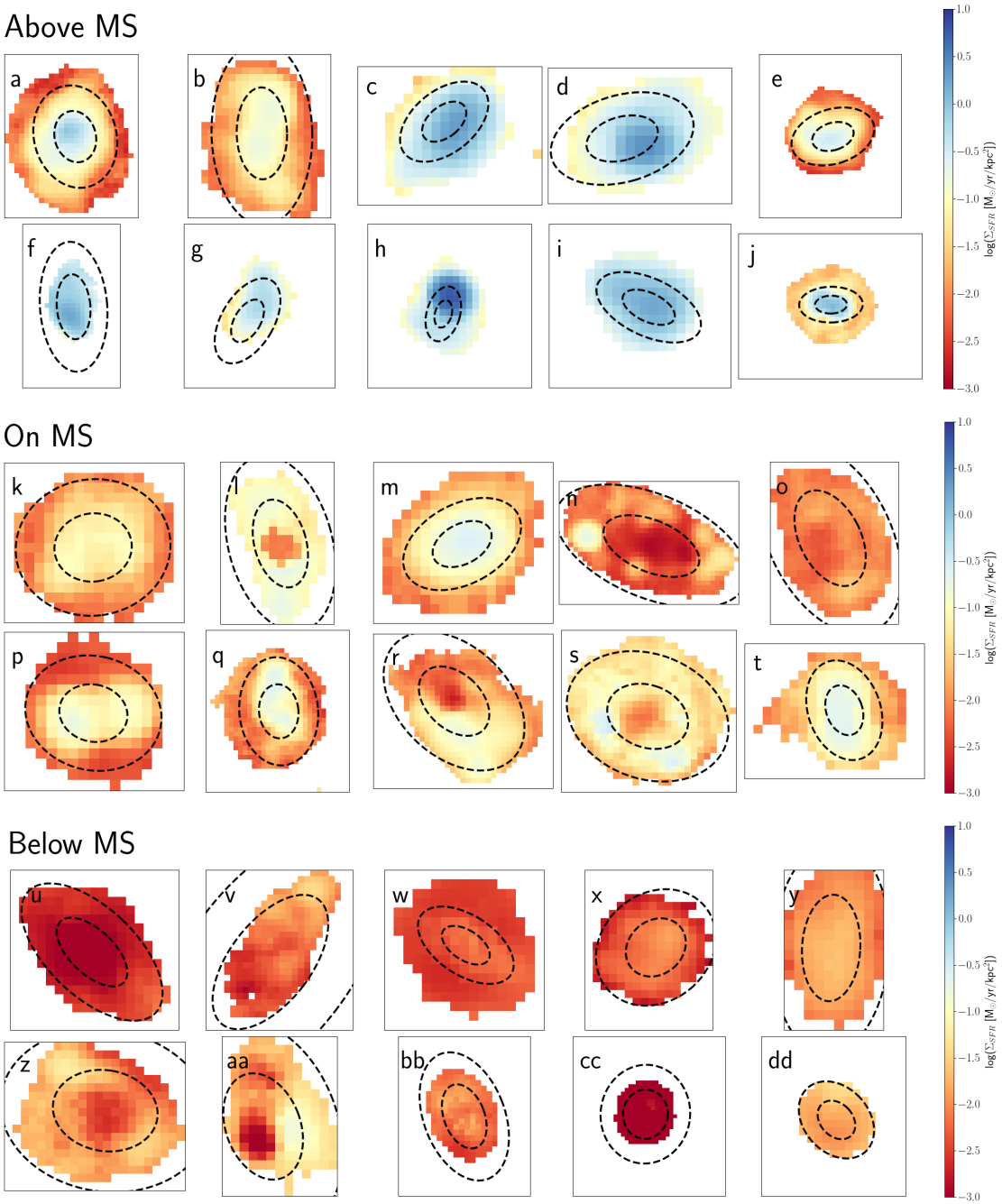

Figure 4.9: Star formation rate maps. Additional details can be found in Figure 4.8.

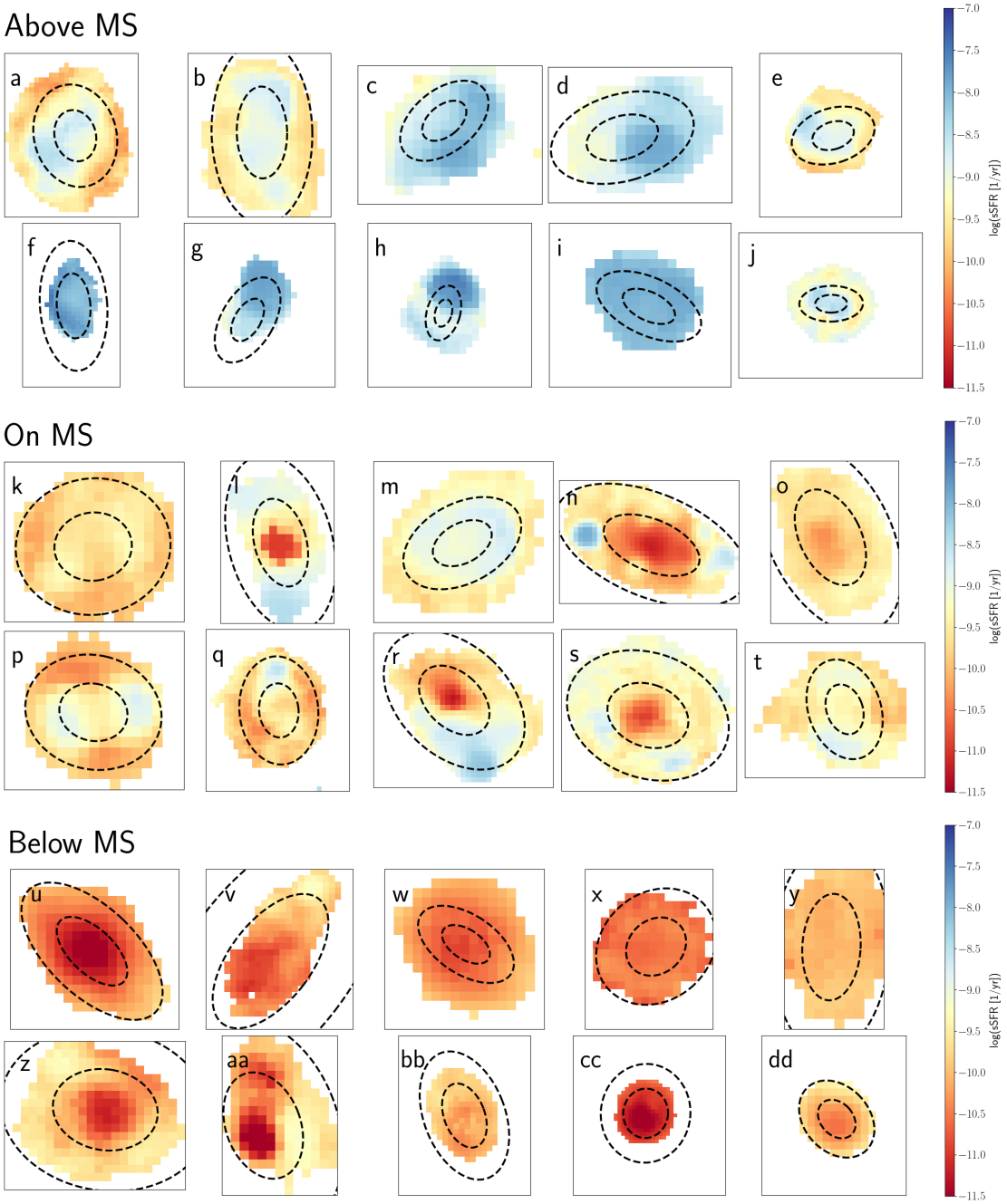

Figure 4.10: Specific star formation rate maps. Additional details can be found in Figure 4.8.

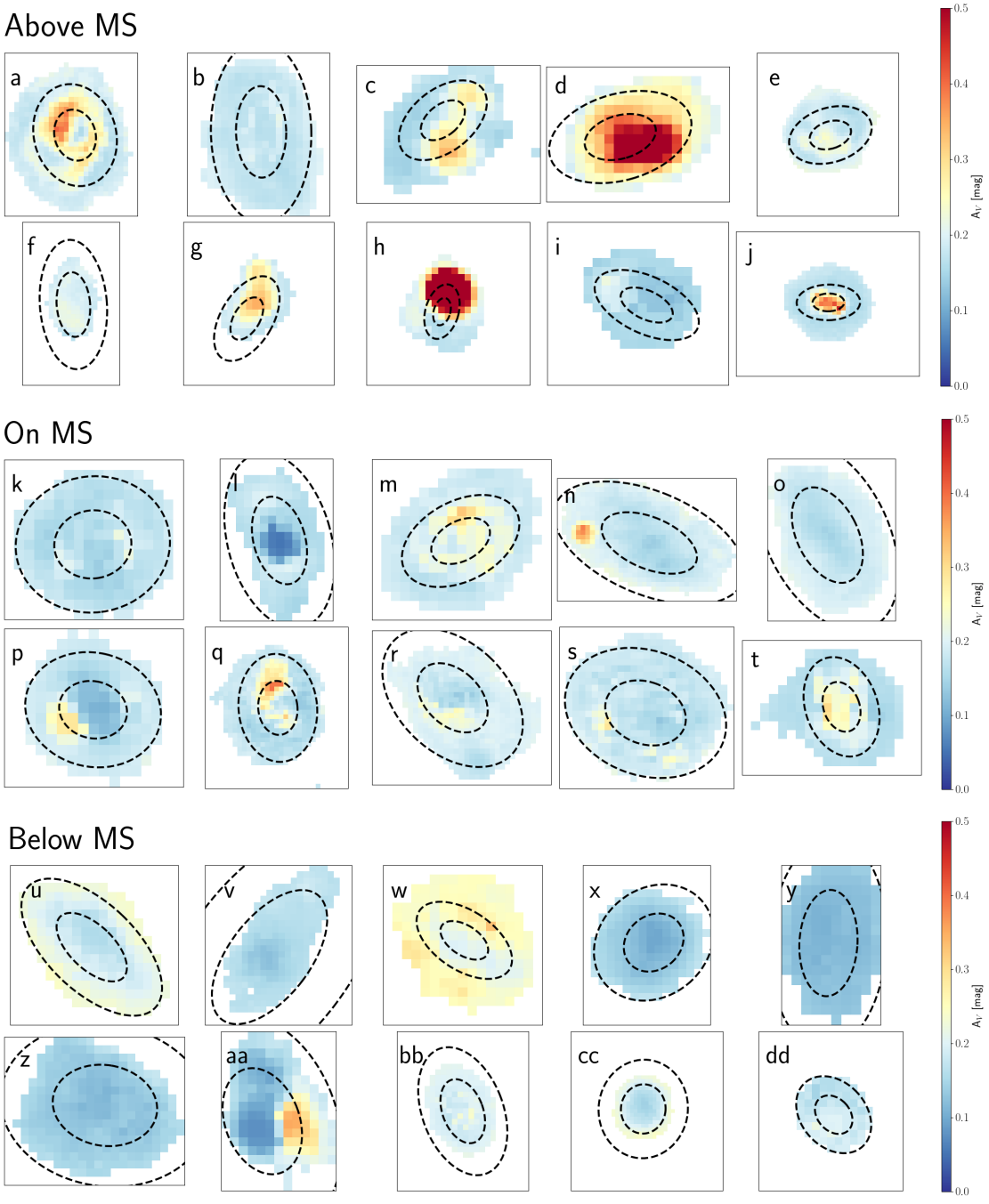

Figure 4.11: Dust maps. Additional details can be found in Figure 4.8.

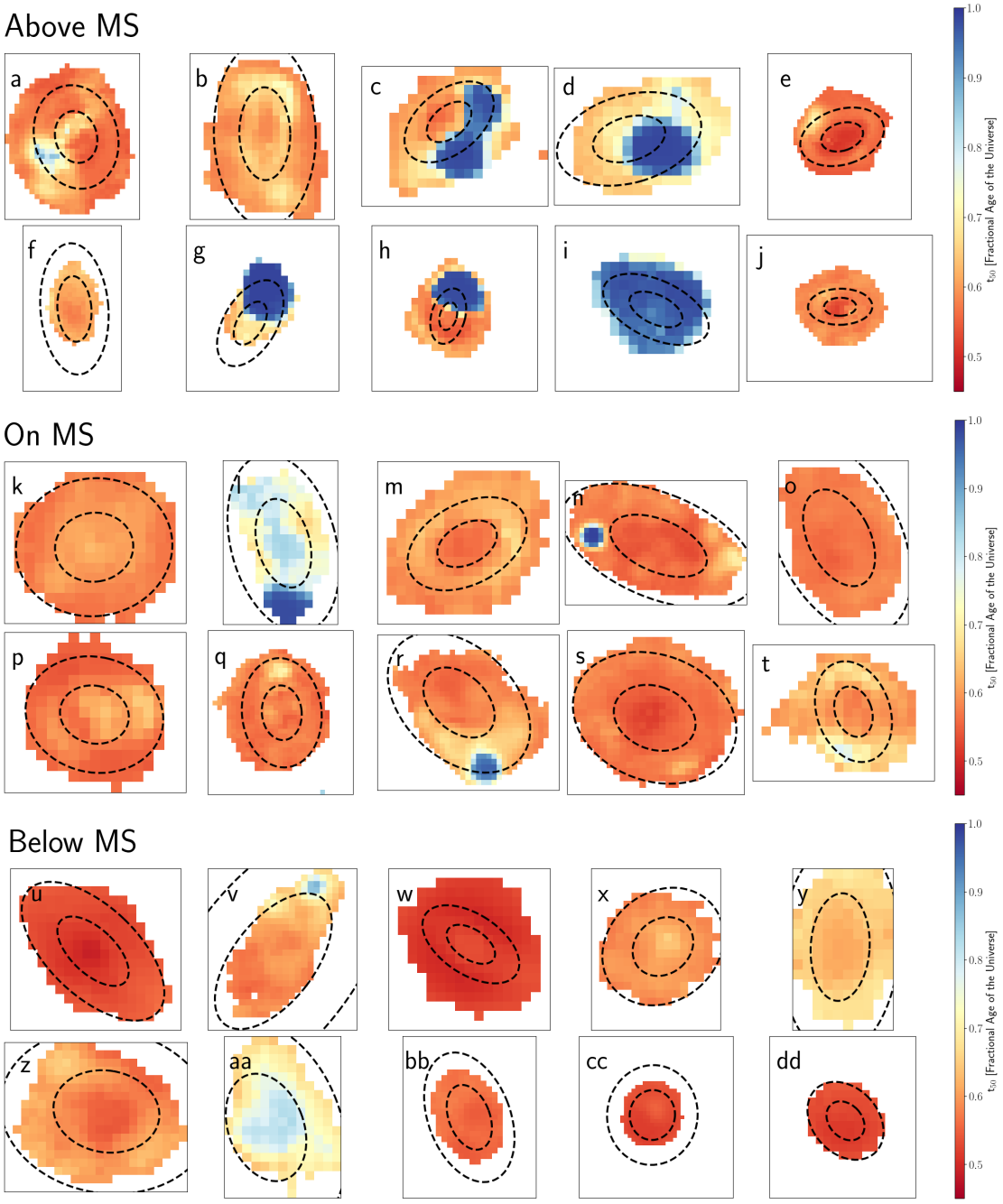

Figure 4.12: t_{50} maps, given as a fraction of the age of the universe at a given redshift, with 0 being the Big Bang and 1 being the epoch of observation. Additional details can be found in Figure 4.8.

4.2 Radial Distribution of Physical Properties

Using the 2D property maps that were extracted from SED fitting with `Dense Basis` shown in Section 4.1, we look at how various properties vary as a function of galactocentric radius to understand where galaxies on average build up their mass and start to quench.

The method for extracting the radial profile for a given galaxy is similar to the method found in Mun et al. (2024). The radial profiles are calculated in six discrete bins of width 0.5 R_e from 0 to 3.0 R_e. The results do not change significantly for different bin widths, and for an idea of the scale of each elliptical annulus, $1R_e$ and $2R_e$ are plotted on each of the RGB and property maps from Section 4.1. For each galaxy, the radial profile is calculated by taking the median of all the pixels in a given radial bin, and a radial bin value is only calculated for that galaxy if there were more than 10 pixels in that bin. The global radial profiles are then calculated by taking the average of all the individual galaxy radial profiles, ensuring that at least 5 galaxies contribute to each radial bin. For each radial profile plot, the individual radial profile of a given galaxy is shown in light grey. The errors in the average for all radial profiles are calculated using the standard error of the mean.

Figure 4.13 shows the SFR, $M_\star$, and sSFR radial profiles for galaxies that are on, above, and below the star-forming main sequence. Here, the radial profiles have been inclination corrected, to account for the increased area visible in a given pixel. However, we find a minimal difference between the inclination corrected radial profiles and the not inclination corrected profiles. The radial trends in $M_\star$ are similar at all masses and distances from the main sequence. We see that the stellar mass surface density increases towards the galactic center, in complete agreement with Figure 4.2 and our expectations given the extensive previous research of light profiles of galaxies increasing towards their centers (Wuyts et al., 2012; Zibetti et al., 2009). We see that in both mass bins and at all radii, galaxies above the main sequence have enhanced star formation and galaxies below the main sequence have depressed star formation relative to those on the main sequence. As a reminder, in this work, the star formation rate is the star formation rate averaged over the last 1% of the mass formed; thus, it shows where star formation is currently occurring within a galaxy. In both mass bins, the SFR is centrally concentrated and decreases towards the outskirts, this trend is more prominent for galaxies in the high mass bin.

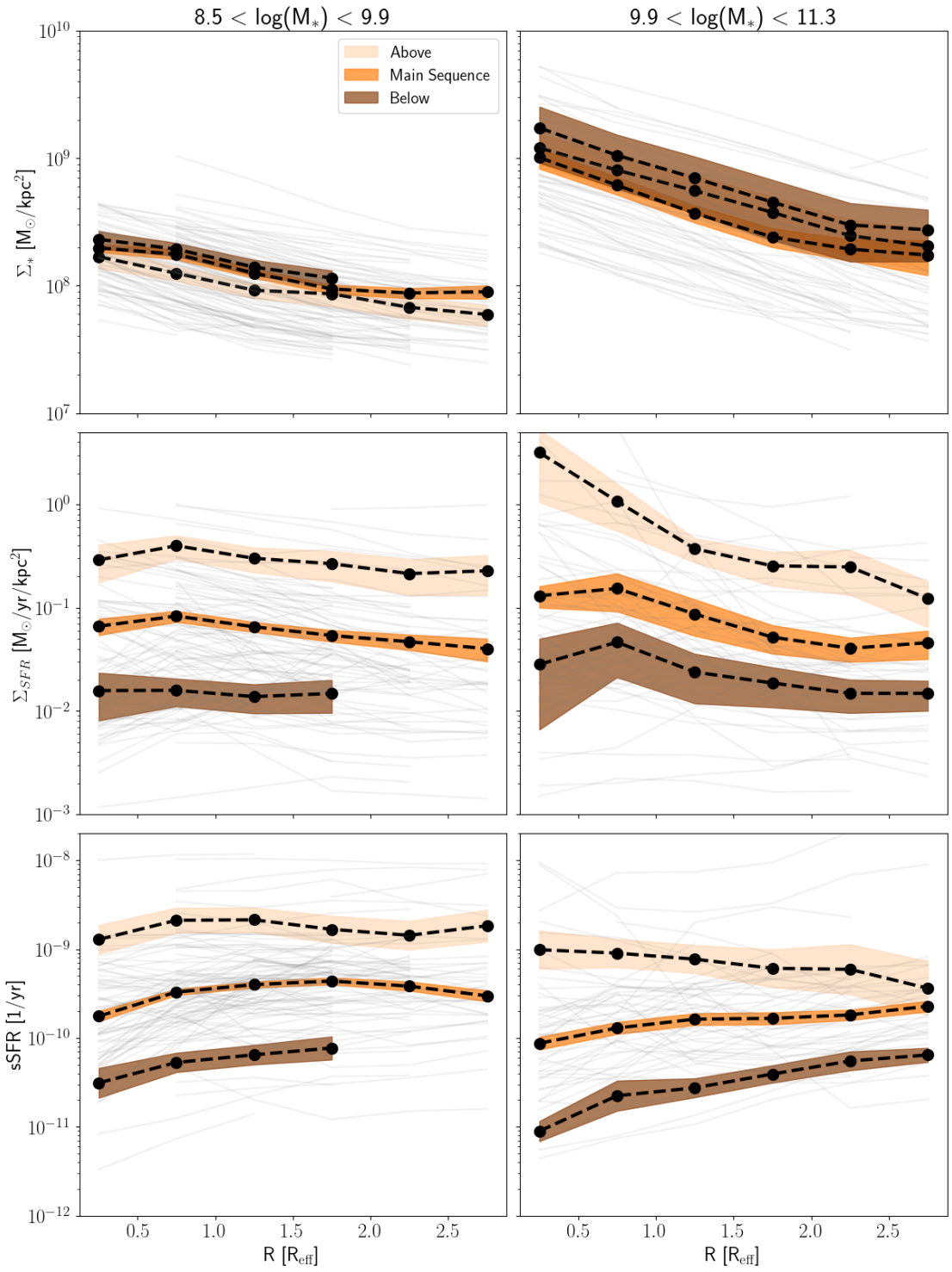

Figure 4.13: Average SFR, $M_\star$, and sSFR radial profiles for galaxies that are above, on, and below the star-forming main sequence. Individual profiles for a given galaxy in that mass bin are shown in light grey. For $M_\star$, the radial profiles are similar regardless of where a galaxy is relative to the MS. For SFR, at all radii in galaxies above the MS the SFR is enhanced, and depressed at all radii in galaxies below the MS. In sSFR, for galaxies above the main sequence the radial profile is relatively constant regardless of mass. For galaxies on the main sequence, the profile is fairly flat with a slight central depression in the highest mass bin. For galaxies below the MS at all masses the sSFR rises radially. The errors for the average radial profiles are calculated by standard error of the mean.

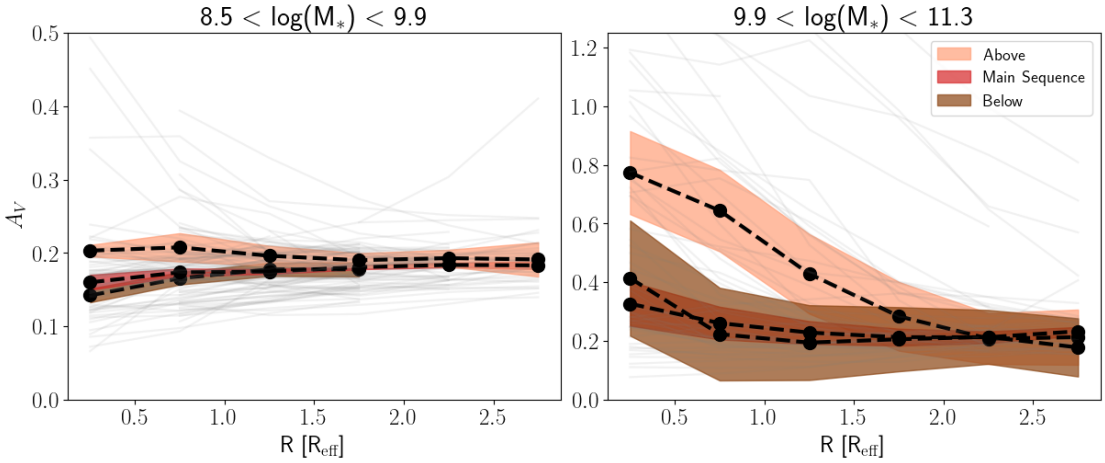

Figure 4.14: Average dust radial profiles for galaxies that are above, on, and below the star-forming main sequence in a given mass bin. Regardless of a galaxy's place respective to the main sequence, in the lower mass bin the dust profile is relatively flat. In the highest mass bin ($> 10^{9.9}M_{\odot}$), the average dust profile is more elevated throughout galaxy and is centrally concentrated, especially for galaxies above the main sequence.

For the sSFR profiles for galaxies on the main sequence the profile is relatively flat, with a slight central depression in both mass bins. For galaxies above the main sequence the profiles are again relatively flat; however, for galaxies in the high mass bin, the sSFR is enhanced in the cores of galaxies. Finally, for galaxies below the main sequence, the sSFR profile is more centrally depressed in both mass bins compared to those on the main sequence, and steadily rises towards the outskirts. This trend of centrally depleted sSFR profiles in massive galaxies has been observed in both observations and simulations (Abdurro'uf & Akiyama, 2018; Ellison et al., 2018; Nelson et al., 2016b, 2021; Tacchella et al., 2018), and can be interpreted as 'inside-out' quenching, where galaxies quench their star formation in their central regions first and then in their outer regions.

Figure 4.14 shows the dust attenuation profiles for galaxies on, above, or below the MS. At lower masses, regardless of a galaxy's place relative to the main sequence, the average dust attenuation profile is constant across the galaxy. This trend continues for galaxies below and on the main sequence at high masses; however, for galaxies above the main sequence the profile increases towards the center, with on average the profile rising to $A_V \sim 0.8$ mag. We can see the direct parallel for high dust attenuation in the centers of these galaxies with the increased star formation in the center in Figure 4.13. However, similar to what is observed in star formation rate, even though the dust profiles appear relatively smooth, the dust can also be concentrated

in specific regions in a galaxy. Figures 4.5 and 4.11 show the dust maps for a subsample of the galaxies, and particularly Galaxies g, n, and p have compact dust regions that trace enhanced star formation.

Figure 4.15 shows the t_{50} radial profiles. The t_{50} is presented as a fractional age of the Universe at the redshift of the galaxy, with 0 representing the start of the Universe and 1 representing the time of observation. We can see that regardless of a galaxy being above, on, or below the main sequence, on average stellar populations are younger for lower mass galaxies than for higher mass galaxies. In Figure 4.12, we see that the younger stellar populations correspond to regions of galaxies that are actively experiencing star formation (see Galaxies c, g, h, l, etc.) and that it appears there are more of these younger stellar populations above the main sequence than on or below it. For massive galaxies, we can see that galaxies below the main sequence have older stellar populations in their centers compared to the outskirts. This shows the inside-out growth of these galaxies where the mass in the bulge forms first and then the outskirts. Additionally, this shows why despite the instantaneous star formation rate increasing towards the center for these galaxies in Figure 4.13, it is not reflected in the sSFR radial plots, due to the substantial amount of mass that has already formed in the center. For the galaxies on and above the main sequence, the averaged profiles are flatter, but do exhibit inside-out growth. This point is emphasized when looking at the t_{50} maps in Figures 4.6, where we see that all galaxies except Galaxy X have older stellar populations in their centers or cores compared to their disks.

A caveat for the radial profiles is the effects of the PSF in the centers of these galaxies, especially the low-mass galaxies. At z $\sim$ 1 the PSF of the F444W filter is $\sim$ 0.75 kpc. The median effective radius for the low-mass galaxies is 1.85 kpc and for the high mass galaxies it is 2.80 kpc. This means that on average the PSF is 0.26R_e for high-mass galaxies and 0.40R_e for low-mass galaxies. This makes our choice of bin width larger than the PSF; however, the centers of the low-mass galaxies especially may be affected by observational smearing. This observational smearing will act to dilute trends in the cores of galaxies, and for this reason we focus our analysis on the high-mass sub-sample where the effects of the smearing are smaller.

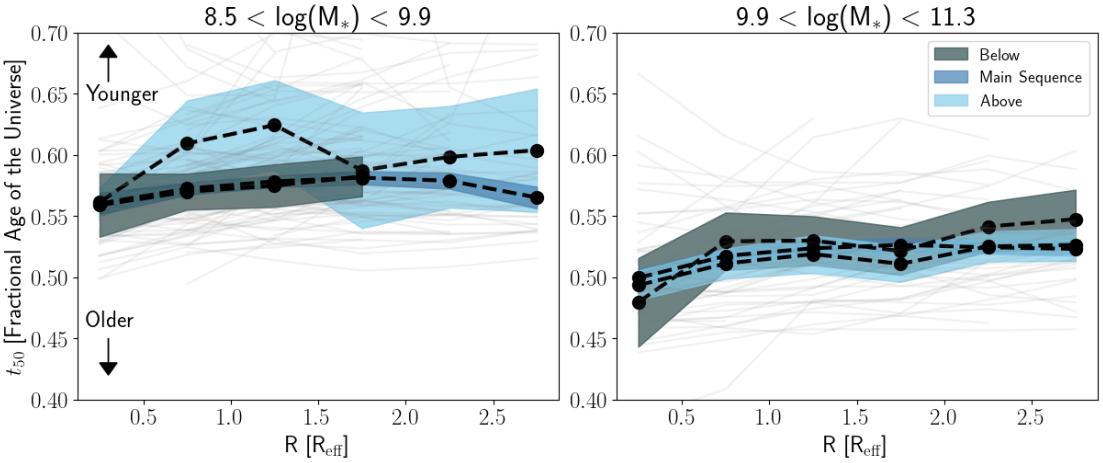

Figure 4.15: Average t_{50} radial profiles for galaxies above, on, and below the star-forming main sequence. t_{50} is plotted as a fraction of the age of the universe at the redshift of a given galaxy, with 0 being the time of the Big Bang and 1 being the time of observation. Lower mass galaxies have younger stellar populations on average compared to their more massive counterparts.

4.3 Inhomogeneities in the Average Star Formation Rate

The average radial profiles are a powerful tool in understanding where on average star formation may be occurring in a given galaxy. However, by taking the average star formation in a given elliptical annulus, we average out any inhomogeneities in the star formation in that annulus. As a consequence of this the averaged radial profile may appear smoother than it actually is in a given galaxy. Here, we compare the results from the radial profiles to what we observe in the 2D spatially resolved maps, to see if the enhanced star formation that we observe throughout galaxies above the main sequence is due to a uniform increase in the star formation throughout the disk, or due to multiple star-forming clumps within the disk.

First, evidence for the claim that the star formation on average is enhanced at all radii for galaxies above the main sequence and depressed at all radii below the main sequence is seen in the star formation rate surface density maps presented in Figures 4.3 and 4.9. All color bars are normalized to be the same for each galaxy, and we can see a clear gradient in SFR going from above the main sequence to below the main sequence. In addition, we see that 8 out of 10 massive galaxies above the main sequence have star-forming cores.

The most notable difference between the individual star formation rate and specific star formation rate maps and the average radial profiles is that while the radial profile is on average smooth from the center of the galaxy to the outskirts, the maps do not exhibit this smoothness,

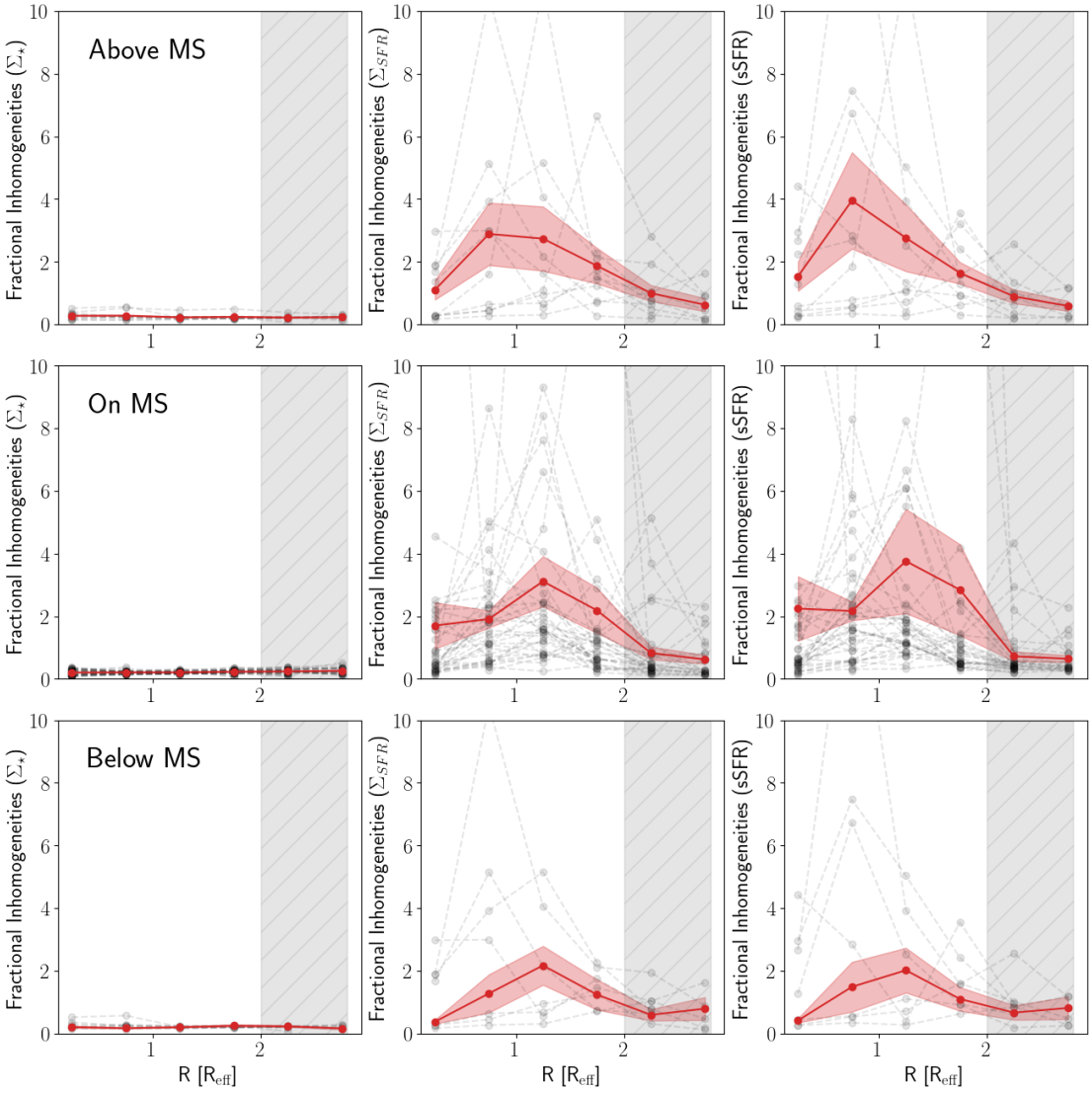

Figure 4.16: The fractional fluctuation for high mass galaxies ($> 10^{9.9}M_\odot$) calculated using Equation 4.1. The grey lines indicate individual galaxies in a given bin, with the red line indicating the mean fluctuation of all the galaxies in a given radial bin. Due to a lack of pixels above $2R_e$, the regions beyond that radii are greyed out. We see that for all galaxies the fractional variation in the stellar mass is very minimal, in contrast to the high variation observed in both star formation and specific star formation rate. The inhomogeneities appears to peak at all distances from the main sequence between 0.5-1.5R_e. The errors in the mean inhomogeneities is once again calculated using the standard error of the mean.

and instead show regions of enhanced and depressed star formation. Even if a galaxy is positioned below the main sequence, such as Galaxy AA or V in Figure 4.4, there are star-forming regions with the same SFR surface density as those on or above the main sequence. These star-forming clumps are more apparent for high-mass galaxies, whereas for low-mass galaxies the SFR and sSFR are more smooth (although is this not true for all galaxies, see Galaxy v in Figure 4.3). For

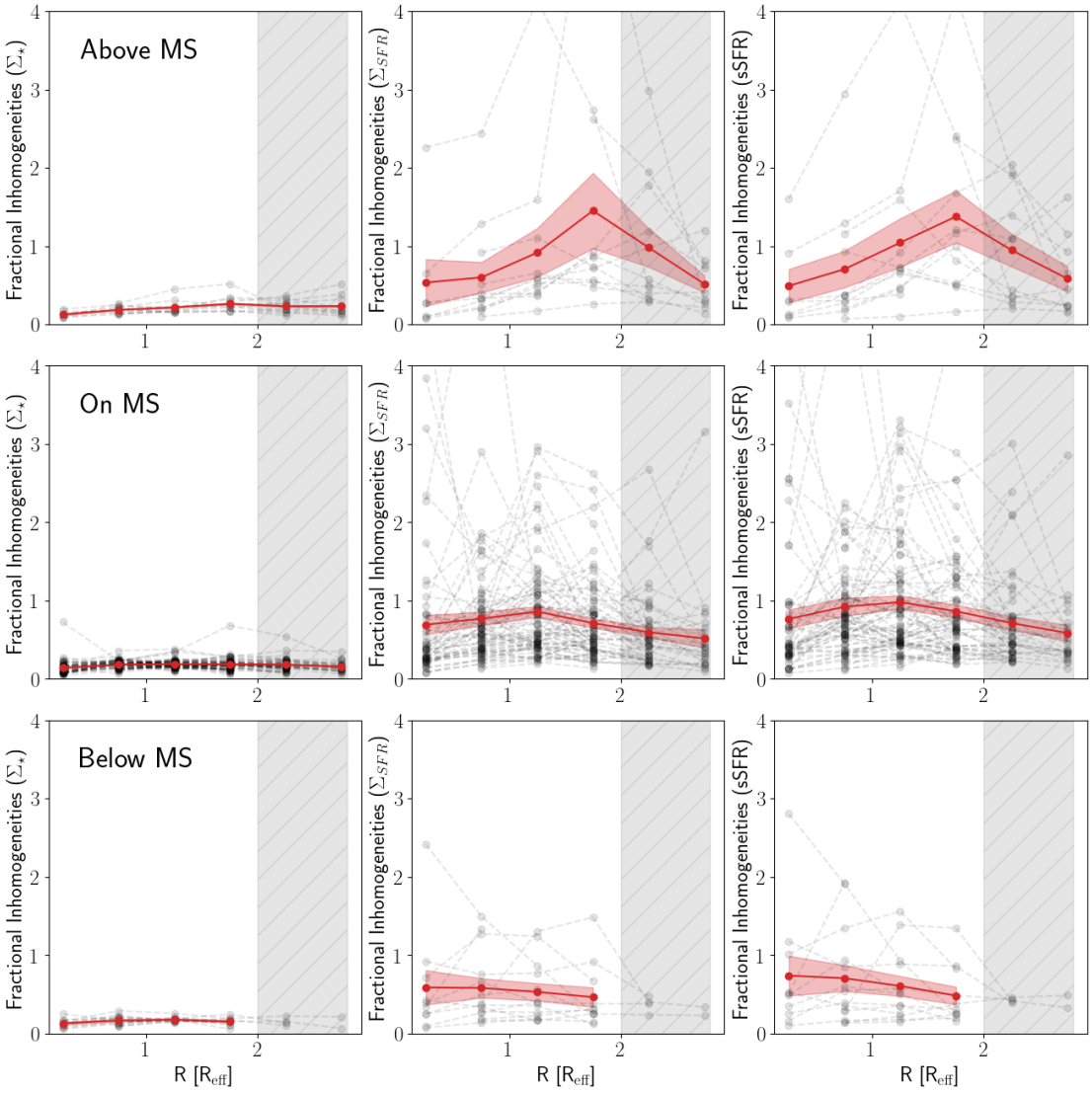

Figure 4.17: The fractional fluctuation for low mass galaxies ($10^{8.5}$M$_\odot$-$10^{9.9}$M$_\odot$). More information can be found in Figure 4.16.

Galaxies I, S, and D in 4.3, these regions appear to be similar to spiral-arm structure; however, for the rest of the galaxies in the high-mass sample these star-forming regions are not symmetric and appear as asymmetric star-forming clumps. The spiral structure is also not found in any of our sample at low masses.

To try and quantify the inhomogeneities that we observe in the SFR and sSFR maps, we use the following equation on each pixel in each galaxy

$$X_H = \frac{|X_R - \bar{X}_R|}{\bar{X}_R}, \tag{4.1}$$

where X_R is the property value (either stellar mass, star formation rate, or sSFR) of a pixel in

a given radial bin in a galaxy, $\bar{X}_R$ is the median value of that property in the same radial bin and X_H is the resulting inhomogeneity of a given pixel. The median inhomogeneities are then determined by taking the median of all the pixels in a radial bin, using the same restrictions as was done for the radial profiles in Section 4.2.

Figures 4.16 and 4.17 show the results of Equation 4.1. The first column in each of the figures shows the inhomogeneities in the stellar mass surface density. Unsurprisingly, given the uniform smoothness that is observed in the stellar mass surface density maps and in the average radial profile, the average inhomogeneity in a radial bin is very flat for all galaxies at all masses. This is in sharp contrast to the second and third columns, which show the star formation rate surface density and specific star formation rate respectively. Before discussing results from these figures, a major caveat for both the high and low mass galaxies is the number of pixels in each radial bin. As we see in each of the property map figures, where $1R_e$ and $2R_e$ are traced out on each plot, for many of the galaxies there are minimal pixels above $2R_e$. While it is possible to trace the average star formation in this regime, the inhomogeneities in the star formation are less robust, especially if a galaxy is asymmetric. Thus, in both figures, radii beyond $2R_e$ are greyed out. Figure 4.16 shows that for all high-mass galaxies the fractional inhomogeneity is much larger for SFR and sSFR than for stellar mass, and that there appears to be a preferred radius where that fluctuation is the largest. This radius is between 0.5-1.5R_e with the inhomogeneities appearing to be larger for those above the main sequence compared to on the main sequence, although there is a large amount of scatter in the data. It is important to emphasize the notable difference between the stellar mass surface density and star formation rate surface density inhomogenities where the data is more robust ($< 2R_e$) and how the decline in the inhomogenities occurs before $2R_e$, indicating this result to be real.

Figure 4.17 shows that for low mass galaxies the inhomogeneities are still substantial for those above and on the main sequence; however, once a galaxy is below the main sequence, there is on average less inhomogeneity. This can be observed qualitatively in the bottom panel of Figure 4.9, where the differences in the SFR are not as dramatic as those below the main sequence in Figure 4.3.

Overall, we can see from the various property maps presented in Section 4.1 the star formation rate surface density within galaxies is diverse. On average, galaxies, especially high mass galaxies that lie above the main sequence, have star formation that is enhanced in their centers and

decreases towards the outskirts. This increase in the instantaneous star formation that is observed, but is not observed in the specific star formation rate, may indicate galaxies have already a large amount of mass built up in the centers, indicating an inside-out growth scenario. However, even galaxies below the main sequence exhibit enhanced star formation clumps with the same amount of star formation surface density as those above the main sequence, with the largest variation in the average star formation in a given radius occurring between 0.5-1.5R_e of a galaxy.

Chapter 5

Additional Testing

After presenting the results of our analysis in Chapter 4, here we present additional work done to prove the robustness of our results before moving on to interpretations.

5.1 Comparison to Binning

Besides establishing a S/N threshold on certain filters, it is valid to question whether there is enough signal in a given pixel to extract robust physical parameters. To test the validity of our results, we implement a Voronoi tessellation binning method using the software package `vorbin` on our sample of galaxies in the two different mass bins. As a reminder, the methodology behind Voronoi tessellation binning is described in Section 3.2 and in Cappellari & Copin (2003).

Figure 5.1 shows an example of the Voronoi binning being done on CANUCS-5109174. Binning is only applied to pixels that already satisfy the S/N cut for the galaxy, as binning pixels without signal will still not provide meaningful physical values. For this test, binning was done in the F090W filter, due to it being the noisiest wide-band filter, and bins were chosen to have a S/N of 10 as was done in Wuyts et al. (2012) and Giménez-Arteaga et al. (2023). We see in Figure 5.1 how the binning is prominent in the outskirts of the galaxy, with numerous bins in the center of the galaxy being comprised of only a single pixel because of the high S/N in the center.

Figure 5.2 shows the 2D property maps of the galaxy using the Voronoi tessellation binning method as done in Figure 5.1. We can compare these maps to those obtained with the pixel-by-pixel SED fitting method as shown in Figure 3.4. We see qualitatively that many of the features that emerge in the pixel-by-pixel maps, also emerge when binning the pixels, such as the

star-forming clumps offset from the center, and the high dust concentration that is observed in the center of the galaxy. This validates the pixel-by-pixel method.

Finally, we look at Figure 5.3 which shows the sSFR radial profile for all galaxies using the Voronoi tessellation binning method and extracted in the same way as discussed in Section 4.2. We also compare these results to the sSFR radial profiles obtained by the pixel-by-pixel method as shown in Figure 4.13. The two profiles agree exceedingly well, once again giving validity to the pixel-by-pixel method.

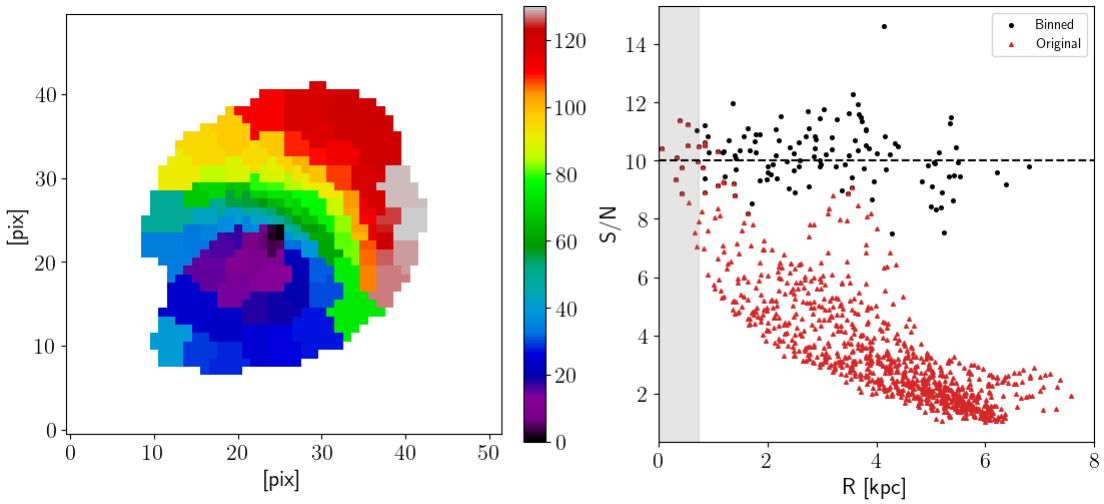

Figure 5.1: *Left:* The binning of the galaxy CANUCS-5109174 according to the Voronoi tessellation binning method with the different colours indicating a different bin index. *Right:* The signal-to-noise radius profile of the galaxy before binning (red triangles) and after binning (black circles) in F090W. The grey shaded region indicates the scale of the F444W PSF. The target S/N threshold is given by the dashed line. The fractional scatter of the S/N is 8%.

5.2 Star-Forming Centers of Galaxies

As previously mentioned, the age-dust metallicity relationship can obscure whether a stellar population is young, star-forming, and dusty or old, quiescent, and red. Here, we look at data from NIRCam as well as NIRISS to show that the massive galaxies above the main sequence in our sample are experiencing dusty star formation in their centers.

Figure 5.4 shows the RGB image of two galaxies with dusty cores in the sample, CANUCS-5109174 and CANUCS-4200419. Figure 5.5 shows the cutouts of each galaxy in their native resolution for all of the available NIRCam bands for CANUCS-5109174, and a sample of the bands for CANUCS-4200419. Even with the presence of dust, if these galaxies are star-forming

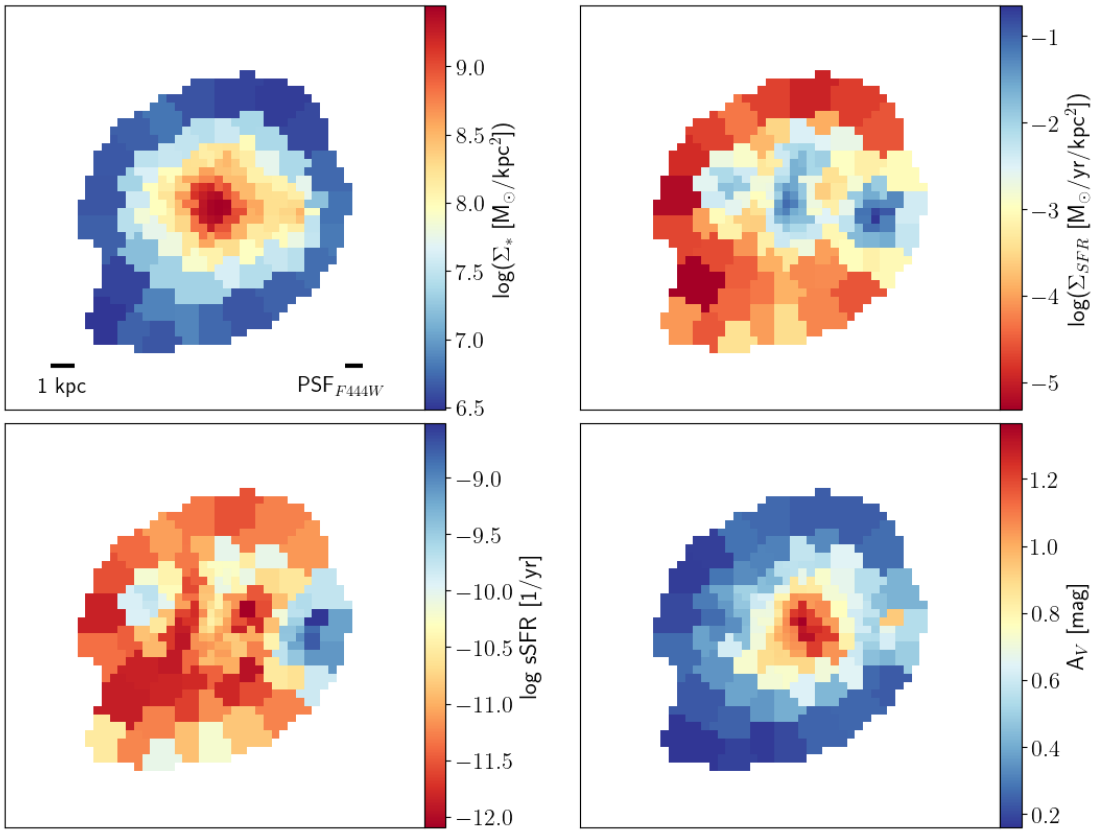

Figure 5.2: 2D property maps of the galaxy CANUCS-5109174 (the pixel-by-pixel SED fitting version is shown in Figure 3.4) at z=1.44 with binned data as according to Figure 5.1, computed with `Dense Basis`. We see that many of the features that are observed in the pixel-by-pixel version, such as the star-forming clump offset from the center, and the high concentration of dust in the center, are replicated in the binned SED version.

in their centers, one may expect to find some rest-frame UV flux originating from younger stellar populations. CANUCS-4200419 is located at z = 1.10, placing a potential Balmer Break at the observed wavelength of 7655 Å, or between the F606W and F090W photometric filter. In the four photometric bands below the Balmer Break where we have observations (F435W and F606W), there is clear rest-UV emission coming from the center of the galaxy, indicating star formation. CANUCS-5109174 is located at z = 1.44, with the two filters below the Balmer Break (F435W and F606W) containing emission at the bulge of the galaxy, once again indicating star formation.

Additionally, CANUCS-5109174 lies in the field MACS J1149.6+2223, where there are additional observations with JWST/NIRISS. NIRISS is a wide field slitless spectroscopy instrument that disperses all the light in a given field with a grism, allowing for spectra to be obtained for every object in a given field. Figure 5.6 shows the grism spectra for CANUCS-5109174. NIRISS has two orthogonal grisms, due to the fact that it is common that grism spectra of different objects

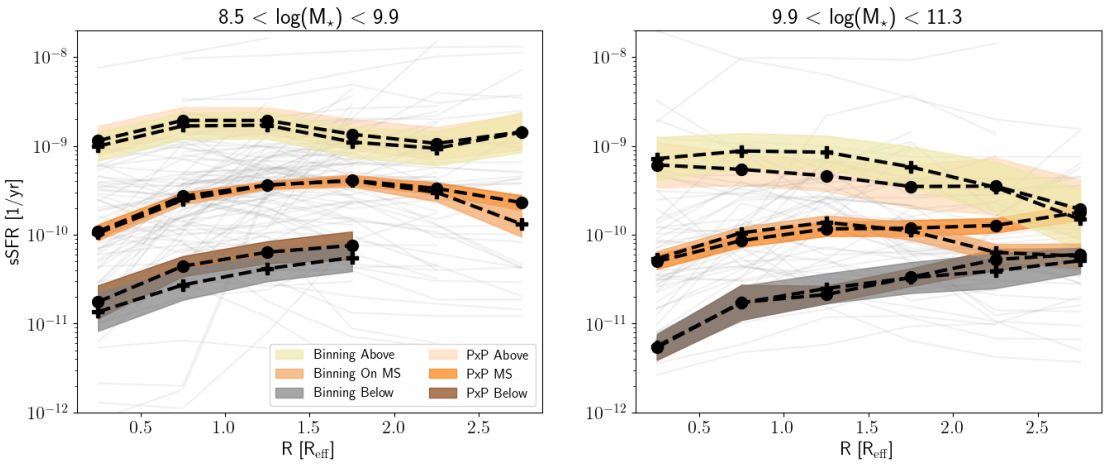

Figure 5.3: The sSFR radial profiles for galaxies using the Voronoi tessellation binning method discussed in Section 5.1 ("+" markers). The grey lines indicate the individual galaxy profiles, and the dashed lines indicate the average profile for galaxies either above, on, or below the main sequence. These profiles are compared to the sSFR radial profiles obtained for galaxies using the pixel-by-pixel SED method shown in Figure 4.13 ("·" markers). As we can see, the two methods overall give very comparable results, giving validity to the pixel-by-pixel method.

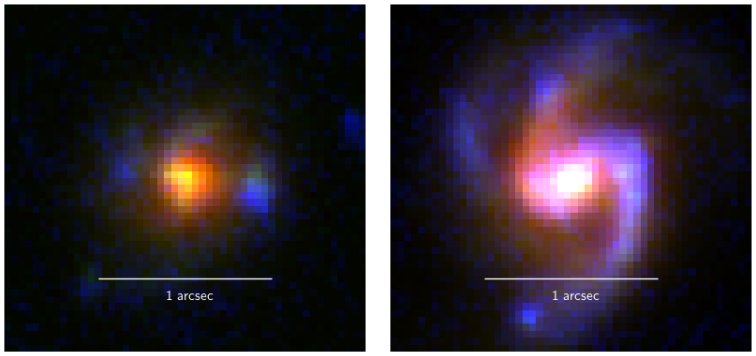

Figure 5.4: RGB images for CANUCS-5109174 (left) and CANUCS-4200419 (right), both of which constructed from the F606W (blue), F277W (red), and F444W (red) NIRCam photometric bands.

overlap, by dispersing the light at different angles one can still obtain spectral information from the galaxy if one orientation is contaminated. The first two rows in Figure 5.6 show the two orthogonal grism spectra taken in three filters, which match the wavelength ranges of the similarly named photometric filters. The last row shows the grism spectra stacked, with the continuum modelled and subtracted off. This should highlight any emission features within the galaxy. In the F150W spectrum, we see a bright emission feature at ~ 1.6 μm which corresponds to Hα at the redshift of this galaxy. Specifically, one can see the emission originates from the center of

the galaxy, and not entirely in the clump that is offset from the center. This indicates that there is Hα present at the center of this galaxy, and as discussed previously, Hα is emitted from the HII regions around young stars, and is an indicator for star formation. Thus, observing Hα in the core indicates that there is star formation in the center of this galaxy.

Overall, by examining NIRCam and NIRISS data, we have shown UV and Hα originating in the centers of these galaxies, showing their cores can be star-forming.

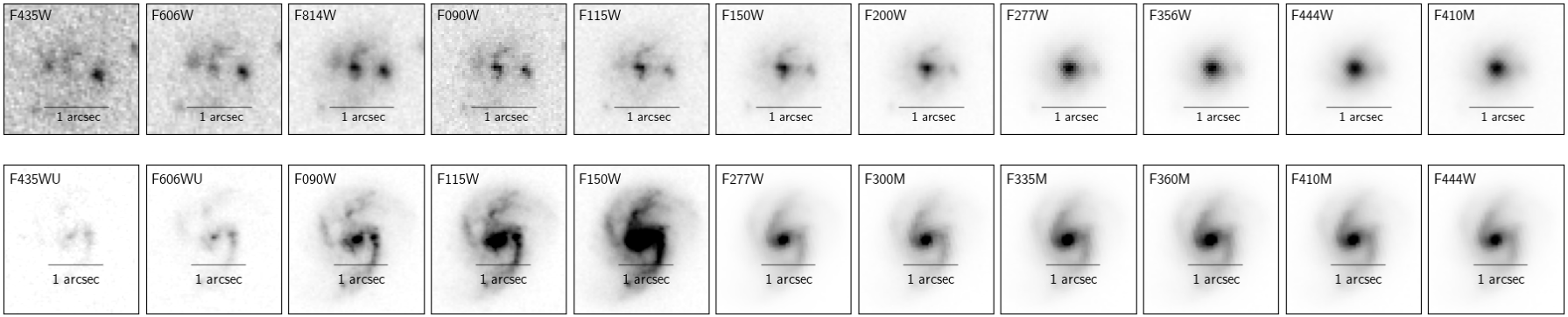

Figure 5.5: Cutouts of galaxies CANUCS-5109174 (top) in all available NIRCam bands and CANUCS-4200419 (bottom) in a sample of the available NIRCam bands, all in their native resolution. The filters up to F150W are normalized to the same scale, and the filters above F150W are normalized to the same scale for the two galaxies. We see that for both galaxies, there is flux in the center of the galaxy at wavelengths below where the Balmer break would be positioned at the redshifts of these galaxies, indicating star formation in these cores.

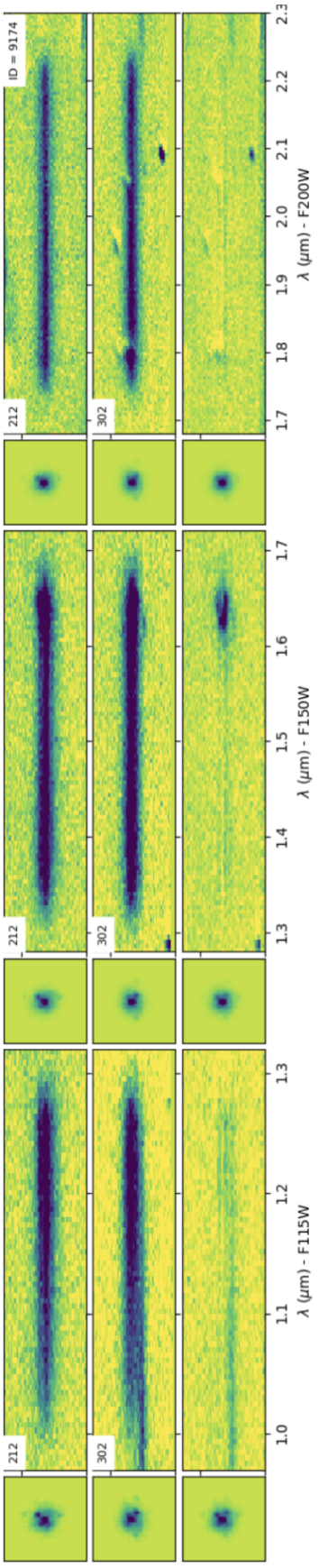

Figure 5.6: The JWST/NIRISS spectrum for CANUCS-5109174 at z = 1.44, the top two rows show the two orthogonal grism spectra, and the bottom row shows the combined spectrum with the continuum modelled and subtracted off. We see in the absence of the continuum, a strong emission feature located at ~ 1.6 μm which corresponds to Hα at this redshift. Importantly we can see this emission originating from the center of the galaxy as well as the clumps that are offset from the center as seen in Figure 5.5.

Chapter 6

Discussion

6.1 Comparison to Previous Literature

Now that the robustness of our results has been validated, we move onto the interpretation of our results.

In Chapter 4, we noted the following trends:

1. Star formation in galaxies above the main sequence is enhanced at all radii, and star formation in galaxies below the main sequence is depressed at all radii.

2. High-mass galaxies above the main sequence are experiencing increased star formation in their centers, paralleled by high dust attenuation in their cores. Conversely, galaxies below the main sequence have their star formation suppressed in their cores.

3. Star formation is enhanced in the disk as well; however, this enhancement is not happening uniformly, but rather in localized clumps of star formation.

In this section, we provide a comparison between these results to what has been discussed in the literature.

6.1.1 Dust

First, we discuss the increase in dust attenuation for galaxies above the main sequence. The increase of dust attenuation towards the centers of massive galaxies has been studied extensively before (Matharu et al., 2023; Nelson et al., 2016a; Tacchella et al., 2018; Wuyts et al., 2012). Nelson et al. (2016a) found that the dust attenuation on average was small ($A_{H_\alpha} < 0.5$ mag) at all

radii for galaxies with M $< 10^{10}$ M$_\odot$, and that galaxies with greater masses had dust attenuation as high as A_{H_α} =3 mag towards their centers, a similar trend that is observed in Figure 4.14; however, they did not divide their sample relative to the main sequence and they came to this conclusion by looking at spatially resolved Balmer decrements. Tacchella et al. (2018) derived dust attenuation from (FUV-NUV) color and found similarly that for galaxies with $> 10^{10}$ M$_\odot$ the dust attenuation decreases from the $\sim$ 1.8 mag in the centers of galaxies to $\sim$ 0.6 mag at 3 half-mass radii. Interestingly Matharu et al. (2023) looked at the dust attenuation as traced by the Balmer decrement for galaxies behind the CANUCS cluster MACS J0417-1154 and found the higher-mass galaxies to have flat dust attenuation profiles; however, they describe that the differences between their work and Nelson et al. (2016a) and Tacchella et al. (2018) could be due to their small sample size and challenges in the data processing. Overall, the centrally peaked dust attenuation in the centers of massive galaxies has been observed before. However, none of the previous studies investigated whether there are differences in dust content relative to the main sequence. Here, we are able to add for the first time that it is galaxies above the main sequence that have the higher dust attenuation in their cores compared to their counterparts on and below the main sequence.

6.1.2 Star Formation

Next, the trend that star formation is enhanced at all radii above the main sequence and depressed at all radii below the main sequence has been discussed before. Nelson et al. (2016b) recovered this trend as discussed in Chapter 1 using Hα as the tracer for star formation. To do so they stacked 2500 galaxies to derive their average radial profile, and thus did not have access to individual star formation surface density maps for each galaxy. In contrast, by utilizing high signal-to-noise data, we have access to the individual maps and are able to recover their trends and expand upon their results.

In addition to examining the dust attenuation profile, Tacchella et al. (2018) additionally split their sample into galaxies on, above, or below the main sequence, and overall found galaxies above the main sequence to have higher sSFR in the center than in the outskirts, a trend that reverses for galaxies below the main sequence. However, a caveat for their analysis is that they calculated sSFRs for 9/10 galaxies in their sample, such that they only had 4 galaxies above the main sequence, 4 galaxies on the main sequence, and 1 below the main sequence.

Figure 6.1 shows the sSFR ratio of the center 1 R_e of galaxies to the outskirts between 1 R_e-3 R_e as a function of distance from the main sequence for all galaxies in our highest mass bin ($10^{9.9}$ - $10^{11.3}$ $M_\odot$), a similar plot to what is shown in Tacchella et al. (2018) and is used here to better illustrate the differences in the radial profiles. On average, for galaxies above the main sequence the sSFR is higher or at the least comparable to that in the outskirts, and this correlates with these galaxies having a higher dust attenuation value. For galaxies below the main sequence, the sSFR is on average $\sim$ 3 times greater in the outskirts than in the center. This agrees with what was found in Tacchella et al. (2018) and Nelson et al. (2016b), and additionally we find that it is not just massive galaxies with high dust attenuation and SFR values, but massive galaxies above the main sequence that are experiencing this dusty starburst.

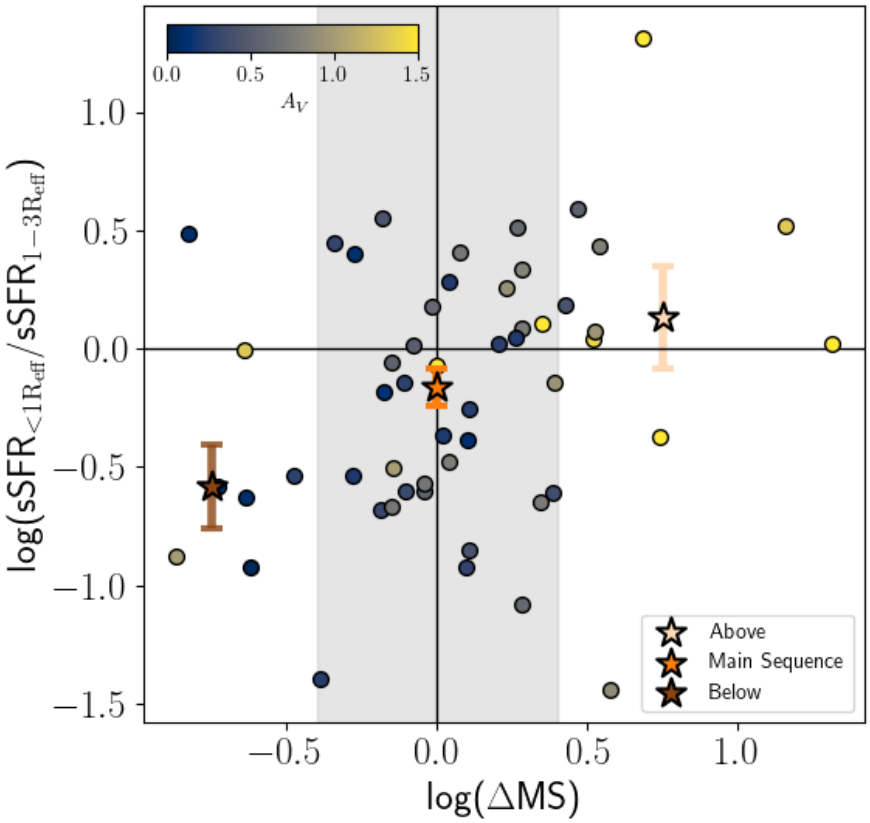

Figure 6.1: Ratio of the sSFR in the inner regions of a galaxy to the outskirts against the distance of the galaxy from the main sequence for all galaxies in the highest mass bin ($10^{9.9}$ - $10^{11.3}$ $M_\odot$). The galaxies are coloured by their integrated dust attenuation values and galaxies above the main sequence appear to have higher dust values. The grey shaded region indicates the definition of on the main sequence used in this work. The stars indicate the average value in a given bin, with the errors calculated using the standard error of the mean.

Abdurro'uf et al. (2023) perform spatially resolved SED fitting on 444 galaxies between

$0.3 < z < 6$ observed with *JWST*. A caveat is that they split their sample differently than this study, electing to analyze galaxies that are star-forming, quiescent or transitioning between the two in a phase known as the green valley. They also did not perform pixel-by-pixel SED fitting but chose to bin their pixels. However, they do find that star-forming galaxies between $0.8 < z < 2.5$ have flat or centrally-peaked sSFR radial profiles, whereas the quiescent population have centrally suppressed sSFR radial profiles. Here they concluded that these galaxies were experiencing a ongoing nuclear starburst. These trends again mimic what we observe for galaxies relative to the main sequence shown in Figure 6.1, where our galaxies above the main sequence have centrally-peaked sSFR radial profiles, and those below have centrally suppressed profiles. However, due to the difference in how they split their sample, it is important to note that we observed different sub-populations that do not map directly onto each other.

Now we turn to where stars are forming in the outskirts of galaxies, as for galaxies above the main sequence, star formation is also enhanced in the disk. Interestingly, while some galaxies exhibit spiral arm structure seen at low-redshift, others contain massive asymmetric clumps within a galaxy. The clumpiness of high redshift galaxies has been apparent with *HST* (Elmegreen et al., 2007), in the era of *JWST* near-IR detections has only increased the number of clumps visible at these redshifts. Kalita et al. (2024) found using a mass complete sample of 418 galaxies between $1 < z < 2$ that 40% of their galaxies have clumps visible in the near-IR, with an average clump mass of $\sim 10^{8.5}$ $M_{\odot}$. With the high S/N data available to us, we are able to add that the enhancement in star formation that is observed in the radial profiles in their disk is not distributed smoothly, but localized in these star-forming clumps.

6.2 Inside-out growth scenario of galaxy assembly

Finally, we discuss the physical scenario for the trends that have been observed in this research as well as in previous literature.

Nelson et al. (2016b), Tacchella et al. (2016), Tacchella et al. (2018) and Abdurro'uf et al. (2023) describe that galaxies build their structure inside-out. First, mass forms in the center and then the galaxy builds its disk, this agrees with the trend of older stellar population in the center of the galaxy compared to its outskirts shown in Figure 4.15. There are two possible scenarios in which gas may be funneled to the centers of galaxies, triggering star formation. First,

galaxy-galaxy gas-rich mergers/interactions, this could also explain the number of star-bursting clumps we observe in our sample. It has been shown that starbursting galaxies have more clumps than main sequence galaxies, and that mergers may be responsible for the formation of these clumps (Calabrò et al., 2019). However, interacting galaxies were removed from the sample when doing visual inspection. Second, counter-rotating streams from violent disc instabilities (VDI) (Abdurro'uf et al., 2023; Tacchella et al., 2016). Kalita et al. (2024) also mention that the clumps at these redshifts have high enough masses that they could drive inflows of gas to the core of these galaxies through tidal torques at higher rates than spiral arms (Bournaud et al., 2014; Kalita et al., 2024). However, as seen in the stellar mass surface density maps, the clumps in our sample do not contain significant amount of mass. These high inflows of gas are also characterized with short depletion timescales (Tacchella et al., 2018), leading to the onset of inside-out quenching, where star formation first ceases in the center of the galaxy. This quenching also moves the galaxy below the star-forming main sequence. The reason why a galaxy may inside-out quench is still debated, but it may be due to AGN feedback or the cut-off of gas to the central region of these galaxies. This pattern of galaxy growth and quenching has been observed over this epoch and mass range (Daikuhara et al., 2024; Nelson et al., 2016b, 2021; Shen et al., 2024; Tacchella et al., 2016). As mentioned in Chapter 1, this cycle of compaction and quenching may occur multiple times over a galaxy's lifetime, causing it to oscillate between the upper and lower envelopes of the main sequence (Tacchella et al., 2016).

Overall, enhancement in sSFR in the cores of massive galaxies above the main sequence and the depression of sSFR in the cores of galaxies below the main sequence observed in the radial profiles agree with the inside-out galaxy growth scenario that has been found in various works. We add that the nuclear starburst of star-forming galaxies that was observed in Abdurro'uf et al. (2023) seems to preferentially occur in galaxies above the main sequence. Additionally, the enhancement of star formation in the disks of galaxies is not spatially uniform but occurs in asymmetric star-forming clumps.

6.3 Caveats

Due to the necessity of high S/N data for this research, we have a small sample size, especially for galaxies that are above and below the main sequence as shown in the histogram in Figure 2.3.

As such, our sample does not probe the entire stellar mass space, especially for galaxies below 10^9 $M_\odot$. Additionally, all the radial profiles are averages, and do not properly convey areas of localized star formation (ie. star formation occurring in individual clumps) that may be occurring in an individual galaxy.

The other explanation for increased SFR in the centers of the galaxies could be due to X-ray luminous AGN. Florez et al. (2020) showed that the stellar mass and SFR of a galaxy can be overestimated by a factor of 10 if AGN emission templates are not included when doing SED fitting for galaxies at cosmic noon. Notably, these results hold for galaxies with an X-ray luminosity $L_X > 10^{44.03}$ erg s^{-1} at our redshift of interest for this sample. Possible future work would include looking for archival data for the clusters used in this work and applying an X-ray luminosity cut as prescribed by Florez et al. (2020) and done in Nelson et al. (2016b), to ensure no AGN contamination in the sample.

Chapter 7

Conclusion

We performed spatially resolved pixel-by-pixel SED fitting on 166 galaxies at or around cosmic noon ($0.7 < z < 3$) using the SED fitting software `Dense Basis` to determine where star formation or quenching is occurring within these galaxies. We selected a sample of galaxies using a criteria of (1) a Sérsic index of < 2 to select disk-dominated galaxies, (2) an inclination cut of $< 60°$ so that we are not targeting galaxies that are heavily inclined, and (3) an offset from the star-forming main sequence of $>$ -1.5 dex, to focus on galaxies that are not fully quenched. We split the sample into galaxies on, above, and below the star-forming main sequence as well as by mass to understand how the star formation rate within these different subgroups varied. We deprojected the distance from the pixels to the galaxy center using available morphological information to obtain a physical radius from the center-of-mass for each pixel in a galaxy. Using the physical quantities outputted by `Dense Basis` for each pixel, we constructed 2D property maps for each galaxy, then for each galaxy we radially averaged various properties and combined multiple galaxies to build an average radial profile. Using these radial profiles and the property maps, we came to the following results:

1. The star formation rate radial profile is enhanced at all radii for galaxies above the main sequence, and depressed at all radii below the main sequence, in both mass bins.

2. For high-mass galaxies, the star formation rate profile is centrally peaked; however, the sSFR radial profile is either constant (for galaxies above the main sequence) or depressed (for galaxies on or below the main sequence). The t_{50} radial profile highlights that these galaxies have older stellar populations in their centers compared to the outskirts, indicating

they have built up their mass from the inside-out.

3. The dust radial profile is consistent and small (A_V<0.3 mag) on average for galaxies below $10^{9.9}$ $M_\odot$, regardless of a galaxy's placement relative to the main sequence. For galaxies above $10^{9.9}$ $M_\odot$, their average dust profile is elevated and centrally concentrated, with galaxies above the main sequence having an average $A_V \sim 0.8$ mag. This directly parallels the instantaneous star formation rate profiles that are also centrally concentrated.

4. Low-mass galaxies ($<10^{9.9}$ $M_\odot$) have younger stellar populations on average compared to their high mass counterparts.

5. Despite the radial profiles being fairly smooth, visual inspection of the 2D star formation rate maps for each galaxy shows that there are regions of clumpy star formation for all galaxies above, on, and below the main sequence. While some galaxies exhibit spiral structure, most of the star formation inhomogeneities are asymmetric. By measuring the average inhomogeneity in each radial bin, we found these inhomogeneities to peak at 0.5-1.5R_e in a given galaxy and begin to decline beyond this radius; however, results at $>2R_e$ may be biased because of less pixels at these radii.

We compared the results we get by pure pixel-by-pixel SED fitting to those obtained by using Voronoi tessellation binning to ensure a constant S/N of 10 across the galaxy, and found similar trends in the radial profiles.

Overall, all these results support an inside-out growth scenario of galaxies at these redshifts. The high sensitivity and spatial resolution of our *JWST* data have helped us refine this picture further in two ways: by showing that (1) the growth of disks via star formation is not spatially uniform but rather consists of either symmetric spiral arm-like structure or clumpy, spatially asymmetric regions of star formation; while the growth of central regions (likely to be bulges) is enhanced via dusty, centrally-located starbursts that preferentially occur in galaxies above the star formation main sequence.

7.1 Future Directions

In the immediate future, expanding the analysis to the rest of the CANUCS fields would add to the sample size and improve the statistics.

7.1.1 Burstiness of Galaxies

As mentioned in the Introduction, the star formation in a galaxy can fluctuate on different timescales. Strong emission lines like Hα originate from recombination in HII regions surrounding O-type stars, while UV photons are emitted from O-type stars as well as longer lived B- and A- type stars. These different star formation rate indicators act on timescales of $\sim$ 10 Myr for Hα and 100 Myr for the UV. Therefore, if the star formation rate varies on timescales less than 100 Myr, the Hα-to-UV ratio can be used to quantify the star formation rate fluctuations, or the "burstiness" of the star formation on these short timescales (Asada et al., 2024; Emami et al., 2019; Estrada-Carpenter et al., 2024).

Figure 7.1 shows the sample of galaxies as a function of their offset from the main sequence and their SFR_{10}/SFR_{100} ratio. SFR_{10} is the star formation rate averaged over 10 Myr, and SFR_{100} is the star formation rate averaged over 100 Myr, each of which is calculated by averaging over the star formation history of the galaxy obtained from integrated SED fitting with `Dense Basis` as described in Section 2.2. The SFR_{10}/SFR_{100} ratio was calculated on a pixel-by-pixel basis for each galaxy; however, the strength of the emission line in a given pixel would need to be quite strong to make a notable difference in the broad-band photometry, and overall it appeared the data did not contain enough S/N to discern if the star formation rate changed meaningfully on these timescales. Therefore, we used the integrated SFR_{10}/SFR_{100} to separate galaxies.

In Figure 7.1 we see that a large majority of the galaxies lie within 0.1 dex of having a constant star formation, showing that even integrated photometry with multiple medium bands may not be sufficient in distinguishing changes in the star formation at this timescale. SFR_{10} from broad and medium band photometry has been recovered before in Cole et al. (2023), with a similar dataset to the one used in this study, which shows that this method of obtaining the SFR_{10} from the star formation histories may be possible; however, differences in the methodology such as different SED fitting codes and priors may lead to the differences in the results, and further work into the differences in the two methodologies is required.

In the upper panel of Figure 7.1 we plot the histogram of $\log(SFR_{10}/SFR_{100})$ values and calculate the standard deviation of the distribution. This region is indicated on the plot in shaded grey, and defines the sample of galaxies that has constant (ratio $\sim$ 1) SFR_{10}/SFR_{100}. Galaxies that lie above this shaded region are considered "bursting", and galaxies that lie below this

region considered "quenching". Thus, in addition to a galaxy's placement on the main sequence, additional work can be done to separate them based on the change in their star formation rate.

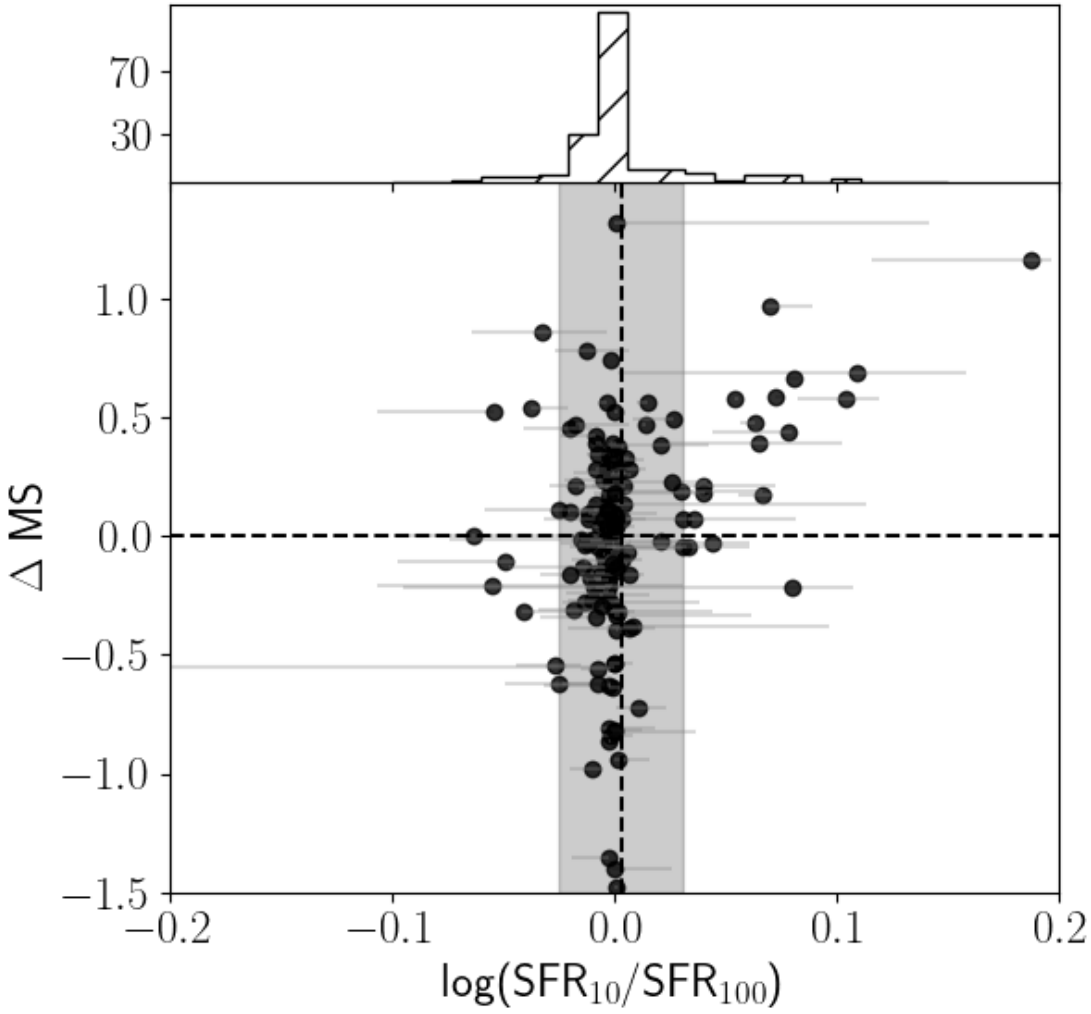

Figure 7.1: A comparison of a galaxy's offset from the main sequence and their burstiness (SFR_{10}/SFR_{100}) ratio. The grey shaded region is the standard deviation of the distribution of galaxies according to their burstiness. We see that a majority of galaxies have a constant SFR_{10}/SFR_{100}, with galaxies that deviate from that norm lying mainly on and above the main sequence.

Another area of future work is the study of clumpy galaxies. High resolution data from both *HST* and *JWST* has unveiled that galaxies at high redshift are more 'clumpy' than their low redshift counterparts, and that as the bulge of a galaxy becomes more prominent, the clumpiness decreases (Kalita et al., 2024). With the 2D property maps, it would be possible to identify clumps within the galaxies, and whether the number of clumps in a galaxy correlates with a galaxy's placement on the main sequence, and how the number of clumps impacts the conclusion of bulge growth of massive galaxies above the main sequence at these redshifts. Additionally, once a

method for determining a clump is tested, one could test how much star formation is occurring within the clumps versus the rest of the disk to see how much star formation comes from clumps.

Bibliography

Abdurro'uf Akiyama M., 2017, MNRAS, 469, 2806

Abdurro'uf Akiyama M., 2018, MNRAS, 479, 5083

Abdurro'uf Lin Y.-T., Wu P.-F., Akiyama M., 2021, ApJS, 254, 15

Abdurro'uf et al., 2023, ApJ, 945, 117

Abraham R. G., Ellis R. S., Fabian A. C., Tanvir N. R., Glazebrook K., 1999, MNRAS, 303, 641

Ambikasaran S., Foreman-Mackey D., Greengard L., Hogg D. W., O'Neil M., 2015, IEEE Transactions on Pattern Analysis and Machine Intelligence, 38, 252

Asada Y., et al., 2024, MNRAS, 527, 11372

Bailer-Jones C. A. L., 2017, Practical Bayesian Inference: A Primer for Physical Scientists. Cambridge University Press

Barbary K., 2016, Journal of Open Source Software, 1, 58

Belfiore F., et al., 2019, AJ, 158, 160

Bertin E., Arnouts S., 1996, , 117, 393

Bluck A. F. L., et al., 2020, MNRAS, 499, 230

Bournaud F., et al., 2014, ApJ, 780, 57

Bradley L., et al., 2023, astropy/photutils: 1.8.0, doi:10.5281/zenodo.7946442, `https://doi.org/10.5281/zenodo.7946442`

Brammer G., Matharu J., 2021, gbrammer/grizli: Release 2021, doi:10.5281/zenodo.5012699, `https://doi.org/10.5281/zenodo.5012699`

Brammer G. B., van Dokkum P. G., Coppi P., 2008, ApJ, 686, 1503

Calabrò A., et al., 2019, A&A, 632, A98

Calzetti D., 2001, PASP, 113, 1449

Cappellari M., Copin Y., 2003, MNRAS, 342, 345

Carnall A. C., McLure R. J., Dunlop J. S., Davé R., 2018, MNRAS, 480, 4379

Carnall A. C., Leja J., Johnson B. D., McLure R. J., Dunlop J. S., Conroy C., 2019, ApJ, 873, 44

Carnall A. C., et al., 2023, Nature, 619, 716

Chabrier G., 2003, PASP, 115, 763

Chevallard J., Charlot S., 2016, MNRAS, 462, 1415

Cole J. W., et al., 2023, arXiv e-prints, p. arXiv:2312.10152

Conroy C., 2013, Annual Review of Astronomy and Astrophysics , 51, 393

Daikuhara K., Kodama T., Pérez-Martínez J. M., Shimakawa R., Suzuki T. L., Tadaki K.-i., Koyama Y., Tanaka I., 2024, MNRAS, 531, 2335

Dome T., Tacchella S., Fialkov A., Ceverino D., Dekel A., Ginzburg O., Lapiner S., Looser T. J., 2024, MNRAS, 527, 2139

Ellison S. L., Sánchez S. F., Ibarra-Medel H., Antonio B., Mendel J. T., Barrera-Ballesteros J., 2018, MNRAS, 474, 2039

Elmegreen D. M., Elmegreen B. G., Ravindranath S., Coe D. A., 2007, ApJ, 658, 763

Emami N., Siana B., Weisz D. R., Johnson B. D., Ma X., El-Badry K., 2019, ApJ, 881, 71

Estrada-Carpenter V., et al., 2024, MNRAS, 532, 577

Florez J., et al., 2020, MNRAS, 497, 3273

Gardner J. P., et al., 2023, PASP, 135, 068001

Genzel R., et al., 2014, ApJ, 785, 75

George A., et al., 2024, MNRAS, 528, 4797

Giménez-Arteaga C., et al., 2023, ApJ, 948, 126

Gledhill R., et al., 2024, arXiv e-prints, p. arXiv:2403.07062

Guo Y., Giavalisco M., Ferguson H. C., Cassata P., Koekemoer A. M., 2012, ApJ, 757, 120

Guo Y., et al., 2015, ApJ, 800, 39

Harris J., Zaritsky D., 2004, AJ, 127, 1531

Harris J., Zaritsky D., 2009, AJ, 138, 1243

Hubble E. P., 1926, ApJ, 64, 321

Hubble E. P., 1936, Realm of the Nebulae

Ivezić Ž., Connolly A. J., VanderPlas J. T., Gray A., 2014, Statistics, Data Mining, and Machine Learning in Astronomy: A Practical Python Guide for the Analysis of Survey Data, doi:10.1515/9781400848911.

Iyer K., Gawiser E., 2017, ApJ, 838, 127

Iyer K. G., Gawiser E., Faber S. M., Ferguson H. C., Kartaltepe J., Koekemoer A. M., Pacifici C., Somerville R. S., 2019, ApJ, 879, 116

Johnson B. D., Leja J., Conroy C., Speagle J. S., 2021, ApJS, 254, 22

Kalita B. S., Silverman J. D., Daddi E., Bottrell C., Ho L. C., Ding X., Yang L., 2024, ApJ, 960, 25

Kennicutt Robert C. J., 1992, ApJ, 388, 310

Kormendy J., Bender R., 1996, ApJL, 464, L119

Lazzarini M., et al., 2022, ApJ, 934, 76

Leja J., Johnson B. D., Conroy C., van Dokkum P. G., Byler N., 2017, ApJ, 837, 170

Leja J., Carnall A. C., Johnson B. D., Conroy C., Speagle J. S., 2019, ApJ, 876, 3

Lewis A. R., et al., 2015, ApJ, 805, 183

Lilly S. J., Le Fevre O., Hammer F., Crampton D., 1996, ApJL, 460, L1

Looser T. J., et al., 2023, arXiv e-prints, p. arXiv:2306.02470

Looser T. J., et al., 2024, Nature, 629, 53

Lotz J. M., et al., 2017, ApJ, 837, 97

Madau P., Dickinson M., 2014, Annual Review of Astronomy and Astrophysics , 52, 415

Man A., Belli S., 2018, Nature Astronomy, 2, 695

Martin A., et al., 2023, ApJ, 955, 106

Martis N. S., et al., 2024, arXiv e-prints, p. arXiv:2401.01945

Matharu J., et al., 2023, ApJL, 949, L11

Mowla L., et al., 2022, ApJL, 937, L35

Mun M., et al., 2024, MNRAS, 530, 5072

Nelson E. J., et al., 2016a, ApJL, 817, L9

Nelson E. J., et al., 2016b, ApJ, 828, 27

Nelson E. J., et al., 2021, MNRAS, 508, 219

Noirot G., et al., 2023, MNRAS,

Peng C. Y., Ho L. C., Impey C. D., Rix H.-W., 2002, AJ, 124, 266

Peng Y.-j., et al., 2010, ApJ, 721, 193

Reddy N. A., Pettini M., Steidel C. C., Shapley A. E., Erb D. K., Law D. R., 2012, ApJ, 754, 25

Rihtaršič G., et al., 2024, arXiv e-prints, p. arXiv:2406.10332

Sánchez S. F., 2020, Annual Review of Astronomy and Astrophysics , 58, 99

Sarrouh G. T. E., et al., 2024, ApJL, 967, L17

Sawicki M. J., Lin H., Yee H. K. C., 1997, The Astronomical Journal, 113, 1

Schneider P., 2006, Extragalactic Astronomy and Cosmology

Schreiber C., et al., 2015, A&A, 575, A74

Sersic J. L., 1968, Atlas de Galaxias Australes

Shen L., et al., 2024, ApJL, 963, L49

Simha V., Weinberg D. H., Conroy C., Dave R., Fardal M., Katz N., Oppenheimer B. D., 2014, arXiv e-prints, p. arXiv:1404.0402

Soille P. J., Ansoult M. M., 1990, Signal Processing, 20, 171

Sorba R., Sawicki M., 2015, MNRAS, 452, 235

Sorba R., Sawicki M., 2018, MNRAS, 476, 1532

Speagle J. S., Steinhardt C. L., Capak P. L., Silverman J. D., 2014, ApJS, 214, 15

Strait V., et al., 2023, ApJL, 949, L23

Tacchella S., et al., 2015, Science, 348, 314

Tacchella S., Dekel A., Carollo C. M., Ceverino D., DeGraf C., Lapiner S., Mandelker N., Primack Joel R., 2016, MNRAS, 457, 2790

Tacchella S., et al., 2018, ApJ, 859, 56

Willott C. J., et al., 2022, PASP, 134, 025002

Wuyts S., et al., 2012, ApJ, 753, 114

Wuyts S., et al., 2013, ApJ, 779, 135

Zibetti S., Charlot S., Rix H.-W., 2009, MNRAS, 400, 1181

Zolotov A., et al., 2015, MNRAS, 450, 2327

de Vaucouleurs G., 1959, Handbuch der Physik, 53, 275

Appendices

Appendix A

Property Maps for all Galaxies

The following pages show all the property maps for each galaxy used in this study. The panels include an RGB image, stellar mass surface density, star formation rate surface density, specific star formation rate, t_{50}, and dust. Each galaxy is presented with various global properties including the galaxy's ID in the CANUCS catalogue, redshift, mass, SFR, sSFR, offset from the main sequence, t_{50} in lookback time, and SFR_{10}/SFR_{100}. All parameters that are obtained from SED fitting are given as the 50th percentile of the posterior distribution, and the errors represent the 16th and 84th percentiles.

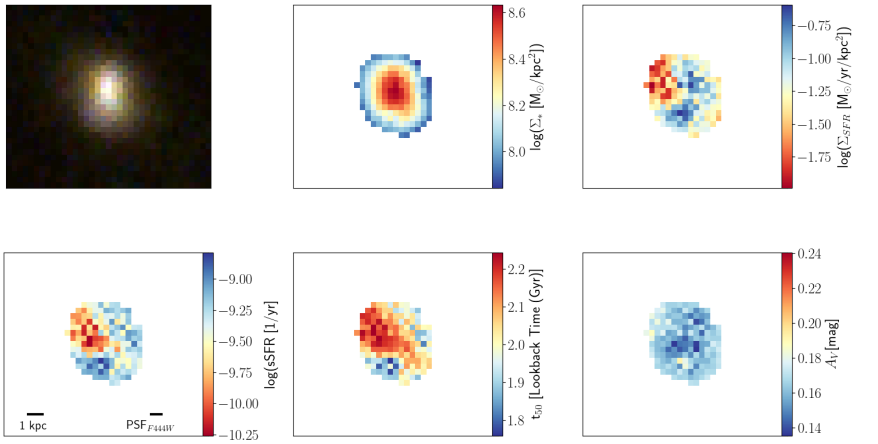

CANUCS - 2100063
$z = 1.13^{+0.43}_{-0.02}$
$\log(M_*/M_\odot) = 9.49^{+0.06}_{-0.09}$
$SFR_{100} = 1.27^{+0.45}_{-0.45}\ M_\odot/yr$
$\log(sSFR/yr) = -9.38^{+0.07}_{-0.10}$
$\Delta\ MS = 0.13^{+0.14}_{-0.20}$ dex
$t_{50} = 2.68^{+0.66}_{-1.04}$ Gyr
$SFR_{10}/SFR_{100} = 0.992^{+0.00}_{-0.00}$

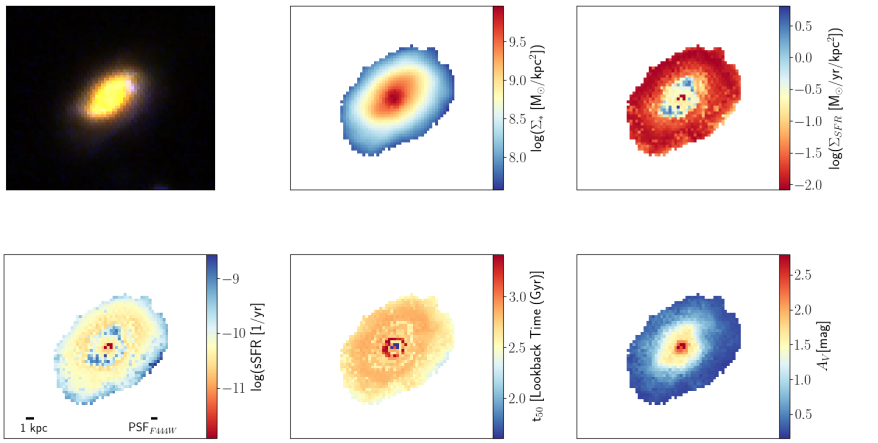

CANUCS - 2100076
$z = 1.19^{+0.14}_{-0.10}$
$\log(M_*/M_\odot) = 10.95^{+0.00}_{-0.00}$
$SFR_{100} = 11.99^{+12.40}_{-0.00}\ M_\odot/yr$
$\log(sSFR/yr) = -9.87^{+0.31}_{-0.00}$
$\Delta\ MS = -0.00^{+0.31}_{-0.00}$ dex
$t_{50} = 2.29^{+0.00}_{-0.01}$ Gyr
$SFR_{10}/SFR_{100} = 0.999^{+0.00}_{-0.00}$

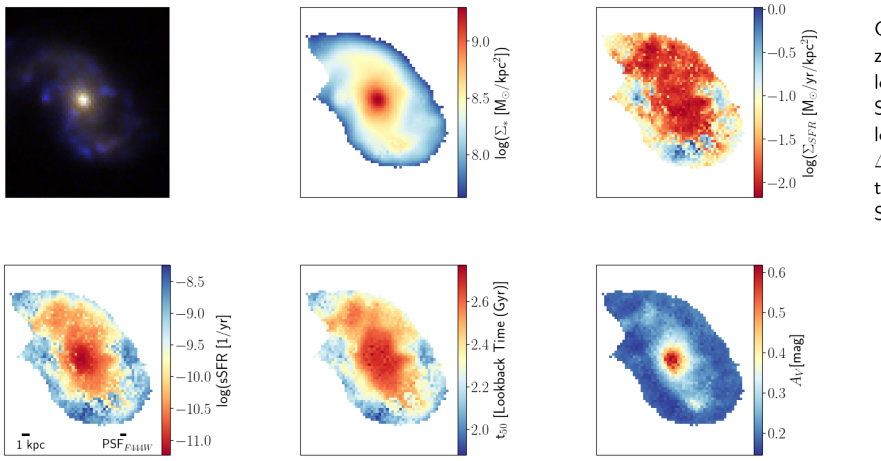

CANUCS - 2100085
$z = 1.15^{+0.17}_{-0.09}$
$\log(M_*/M_\odot) = 10.68^{+0.00}_{-0.08}$
$SFR_{100} = 13.59^{+5.87}_{-0.15}\ M_\odot/yr$
$\log(sSFR/yr) = -9.54^{+0.15}_{-0.08}$
$\Delta\ MS = 0.28^{+0.16}_{-0.06}$ dex
$t_{50} = 3.45^{+0.01}_{-1.05}$ Gyr
$SFR_{10}/SFR_{100} = 0.991^{+0.00}_{-0.00}$

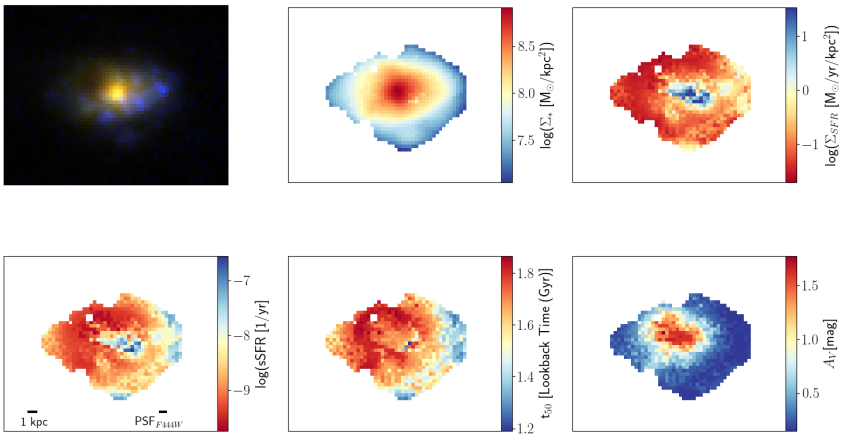

CANUCS - 2100144
$z = 1.96^{+0.09}_{-0.30}$
$\log(M_*/M_\odot) = 10.04^{+0.26}_{-0.23}$
$SFR_{100} = 78.98^{+15.53}_{-13.23}$ $M_\odot$/yr
$\log(sSFR/yr) = -8.14^{+0.19}_{-0.15}$
Δ MS $= 1.16^{+0.19}_{-0.17}$ dex
$t_{50} = 0.16^{+0.79}_{-0.11}$ Gyr
$SFR_{10}/SFR_{100} = 1.537^{+0.01}_{-0.07}$

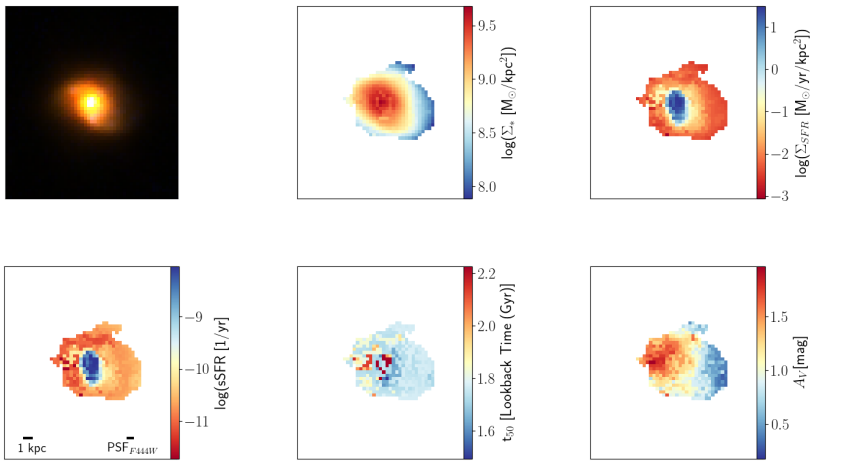

CANUCS - 2100159
$z = 1.94^{+0.23}_{-0.22}$
$\log(M_*/M_\odot) = 10.73^{+0.00}_{-nan}$
$SFR_{100} = 73.87^{+59.13}_{-0.00}$ $M_\odot$/yr
$\log(sSFR/yr) = -8.86^{+0.26}_{-nan}$
Δ MS $= 0.68^{+0.26}_{---}$ dex
$t_{50} = 1.26^{+0.05}_{-0.00}$ Gyr
$SFR_{10}/SFR_{100} = 1.284^{+0.05}_{-0.11}$

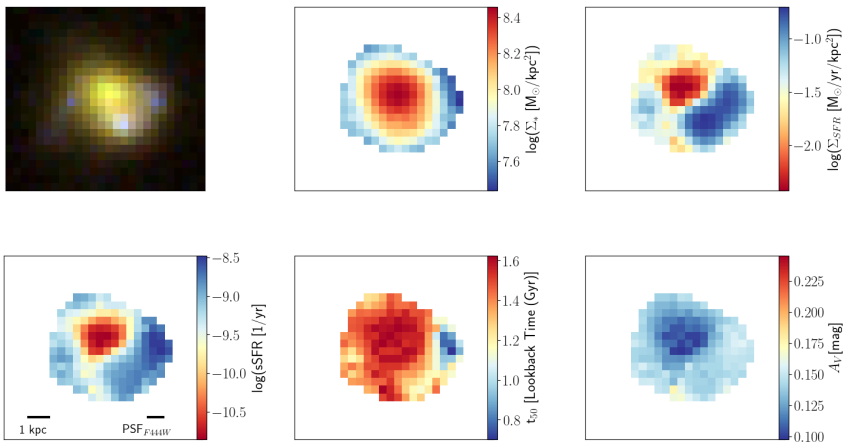

CANUCS - 2100195
$z = 1.59^{+0.07}_{-0.27}$
$\log(M_*/M_\odot) = 9.33^{+0.07}_{-0.05}$
$SFR_{100} = 1.20^{+0.54}_{-0.47}$ $M_\odot$/yr
$\log(sSFR/yr) = -9.25^{+0.09}_{-0.16}$
Δ MS $= -0.03^{+0.17}_{-0.22}$ dex
$t_{50} = 2.03^{+0.49}_{-1.01}$ Gyr
$SFR_{10}/SFR_{100} = 1.107^{+0.02}_{-0.05}$

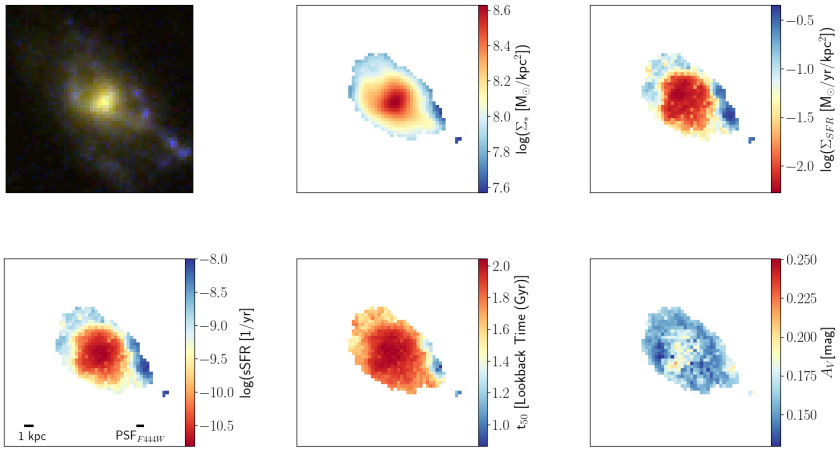

CANUCS - 2100275
$z = 1.50^{+0.32}_{-0.25}$
$\log(M_*/M_\odot) = 9.95^{+0.02}_{-0.00}$
$SFR_{100} = 3.96^{+0.02}_{-1.86}$ $M_\odot$/yr
$\log(sSFR/yr) = -9.35^{+0.02}_{-0.27}$
Δ MS $= 0.09^{+0.01}_{-0.28}$ dex
$t_{50} = 1.61^{+0.67}_{-0.17}$ Gyr
$SFR_{10}/SFR_{100} = 0.973^{+0.01}_{-0.00}$

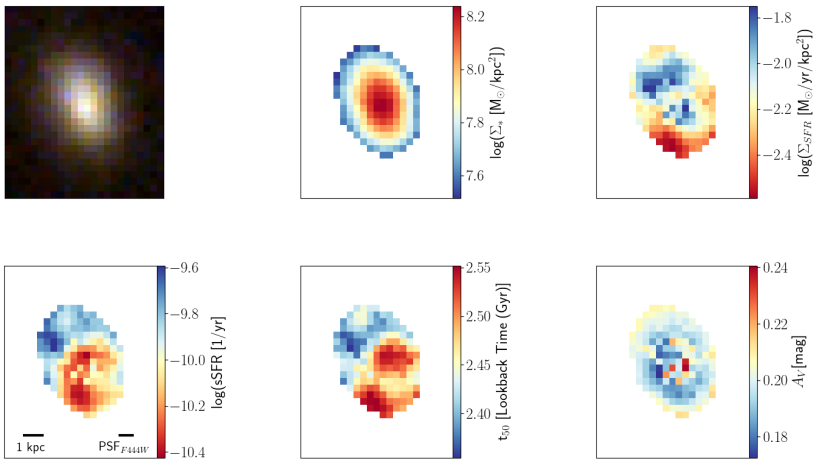

CANUCS - 2101004
$z = 1.05^{+0.03}_{-0.08}$
$\log(M_*/M_\odot) = 9.14^{+0.07}_{-0.06}$
$SFR_{100} = 0.14^{+0.12}_{-0.13}$ $M_\odot$/yr
$\log(sSFR/yr) = -10.01^{+0.20}_{-1.24}$
Δ MS $= -0.54^{+0.27}_{-1.31}$ dex
$t_{50} = 2.54^{+1.02}_{-1.20}$ Gyr
$SFR_{10}/SFR_{100} = 0.939^{+0.01}_{-0.02}$

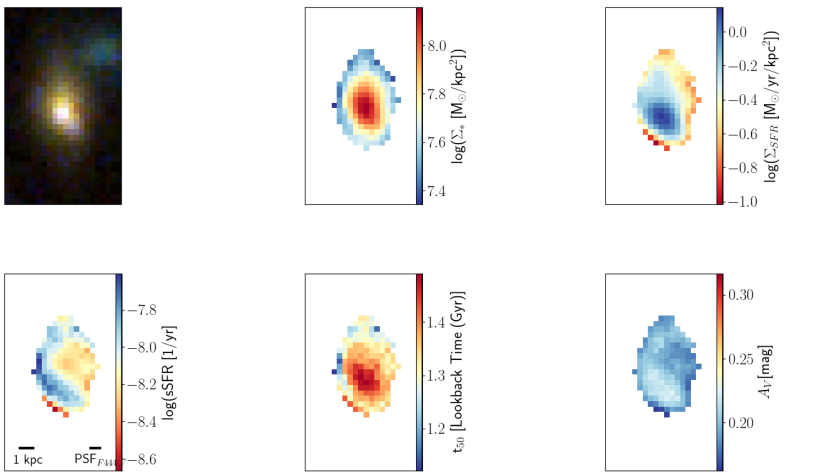

CANUCS - 2101253
$z = 1.83^{+0.09}_{-0.13}$
$\log(M_*/M_\odot) = 9.03^{+0.29}_{-0.14}$
$SFR_{100} = 9.70^{+2.78}_{-1.87}$ $M_\odot$/yr
$\log(sSFR/yr) = -8.04^{+0.18}_{-0.04}$
Δ MS $= 0.96^{+0.22}_{-0.13}$ dex
$t_{50} = 0.08^{+0.18}_{-0.04}$ Gyr
$SFR_{10}/SFR_{100} = 1.174^{+0.02}_{-0.00}$

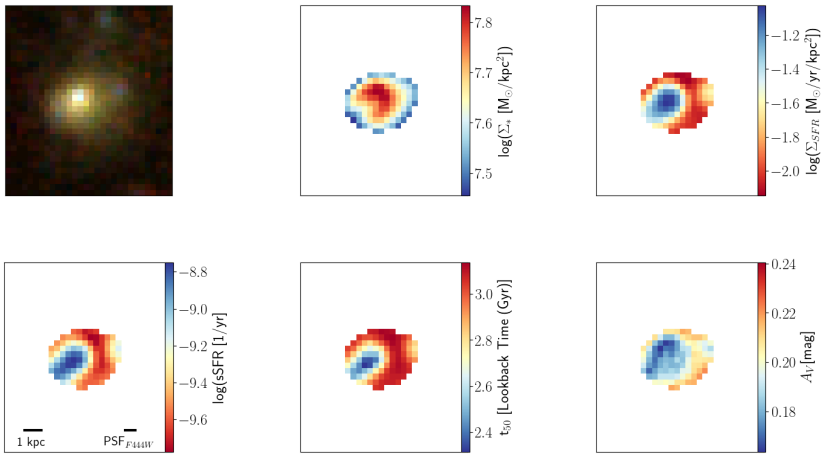

CANUCS - 2200240
$z = 0.72^{+0.01}_{-0.01}$
$\log(M_*/M_\odot) = 8.62^{+0.11}_{-0.16}$
$SFR_{100} = 0.26^{+0.09}_{-0.07}$ $M_\odot$/yr
$\log(sSFR/yr) = -9.21^{+0.01}_{-0.03}$
Δ MS $= 0.32^{+0.15}_{-0.18}$ dex
$t_{50} = 3.47^{+1.14}_{-1.18}$ Gyr
$SFR_{10}/SFR_{100} = 0.996^{+0.01}_{-0.00}$

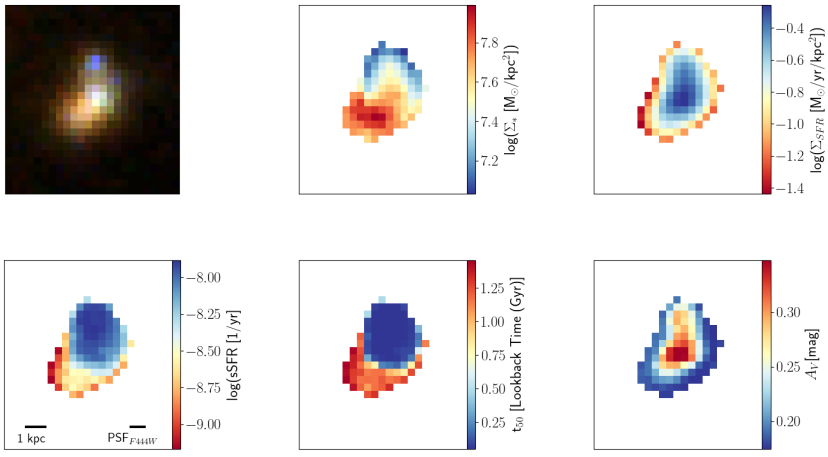

CANUCS - 2200321
$z = 1.74^{+0.00}_{-0.01}$
$\log(M_*/M_\odot) = 8.69^{+0.21}_{-0.30}$
$SFR_{100} = 2.61^{+0.55}_{-0.36}$ $M_\odot$/yr
$\log(sSFR/yr) = -8.27^{+0.13}_{-0.23}$
Δ MS $= 0.66^{+0.17}_{-0.21}$ dex
$t_{50} = 0.20^{+1.67}_{-0.15}$ Gyr
$SFR_{10}/SFR_{100} = 1.203^{+0.00}_{-0.00}$

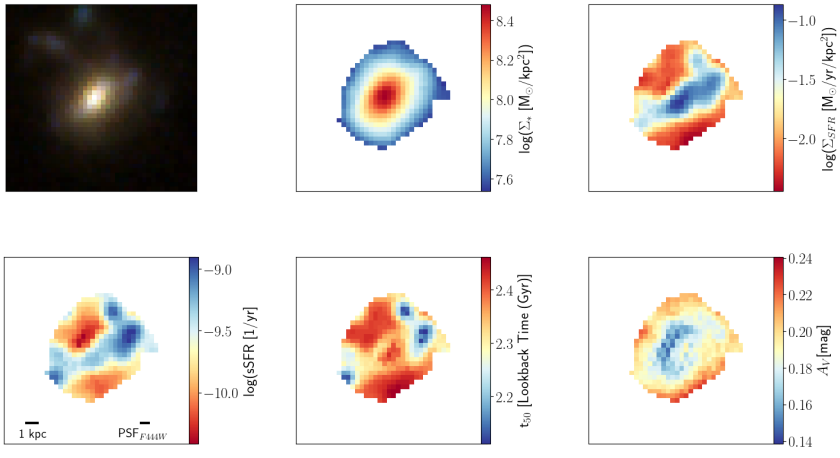

CANUCS - 2200385
$z = 1.11^{+0.04}_{-0.03}$
$\log(M_*/M_\odot) = 9.56^{+0.08}_{-0.13}$
$SFR_{100} = 1.15^{+0.33}_{-0.17}$ $M_\odot$/yr
$\log(sSFR/yr) = -9.50^{+0.03}_{-0.06}$
Δ MS $= 0.04^{+0.12}_{-0.12}$ dex
$t_{50} = 2.58^{+1.53}_{-1.59}$ Gyr
$SFR_{10}/SFR_{100} = 0.991^{+0.00}_{-0.00}$

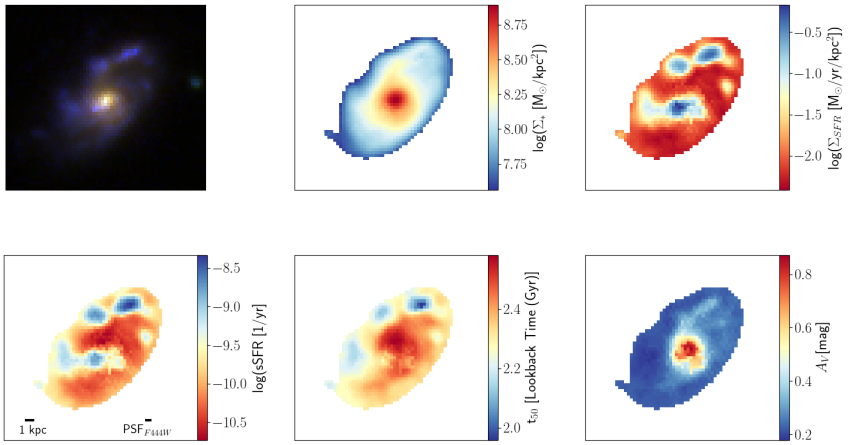

CANUCS - 2200403
$z = 1.25^{+0.04}_{-0.01}$
$\log(M_*/M_\odot) = 10.21^{+0.00}_{-0.03}$
$SFR_{100} = 4.82^{+1.60}_{-0.03}\ M_\odot/yr$
$\log(sSFR/yr) = -9.52^{+0.12}_{-0.03}$
$\Delta\ MS = 0.11^{+0.12}_{-0.03}$ dex
$t_{50} = 1.80^{+0.78}_{-0.00}$ Gyr
$SFR_{10}/SFR_{100} = 0.994^{+0.00}_{-0.00}$

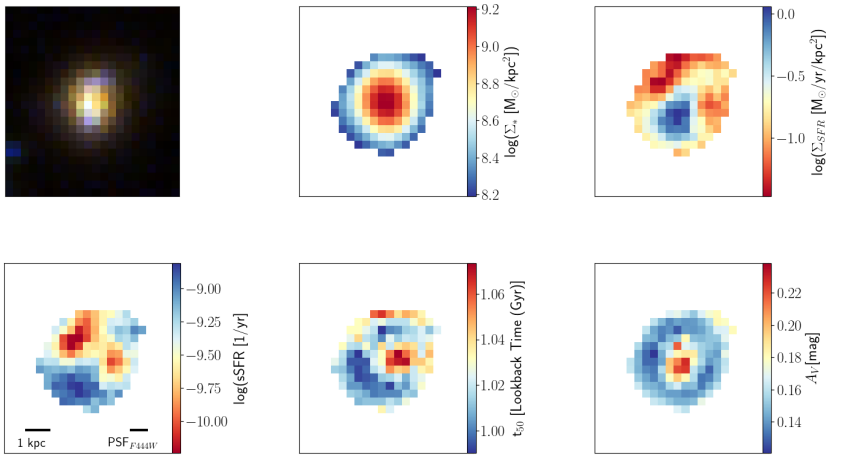

CANUCS - 2200457
$z = 2.77^{+0.03}_{-0.01}$
$\log(M_*/M_\odot) = 9.82^{+0.04}_{-0.07}$
$SFR_{100} = 3.02^{+0.87}_{-0.61}\ M_\odot/yr$
$\log(sSFR/yr) = -9.34^{+0.07}_{-0.02}$
$\Delta\ MS = -0.22^{+0.11}_{-0.11}$ dex
$t_{50} = 1.03^{+0.11}_{-0.40}$ Gyr
$SFR_{10}/SFR_{100} = 1.202^{+0.03}_{-0.18}$

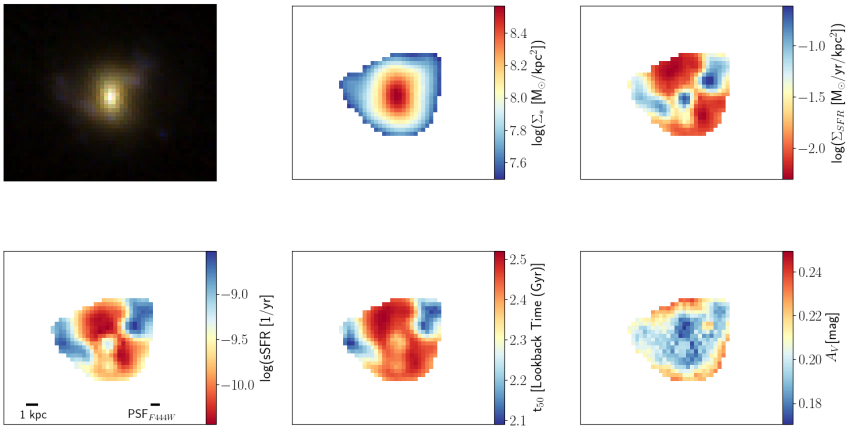

CANUCS - 2200460
$z = 1.15^{+0.04}_{-0.02}$
$\log(M_*/M_\odot) = 9.67^{+0.07}_{-0.06}$
$SFR_{100} = 1.70^{+0.47}_{-0.35}\ M_\odot/yr$
$\log(sSFR/yr) = -9.44^{+0.03}_{-0.04}$
$\Delta\ MS = 0.11^{+0.12}_{-0.11}$ dex
$t_{50} = 2.78^{+1.03}_{-0.71}$ Gyr
$SFR_{10}/SFR_{100} = 0.991^{+0.00}_{-0.01}$

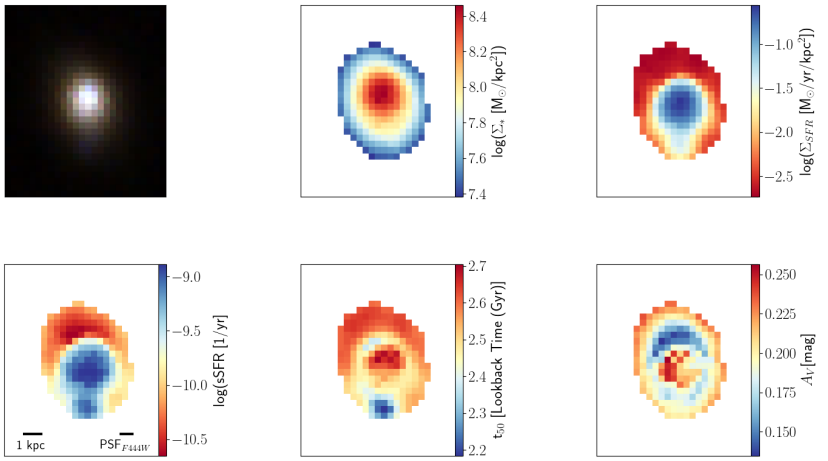

CANUCS - 2200471
$z = 1.01^{+0.02}_{-0.04}$
$\log(M_*/M_\odot) = 9.28^{+0.08}_{-0.04}$
$SFR_{100} = 0.86^{+0.38}_{-0.17}\ M_\odot/yr$
$\log(sSFR/yr) = -9.34^{+0.08}_{-0.05}$
Δ MS $= 0.18^{+0.17}_{-0.10}$ dex
$t_{50} = 2.89^{+0.81}_{-0.71}$ Gyr
$SFR_{10}/SFR_{100} = 0.999^{+0.01}_{-0.00}$

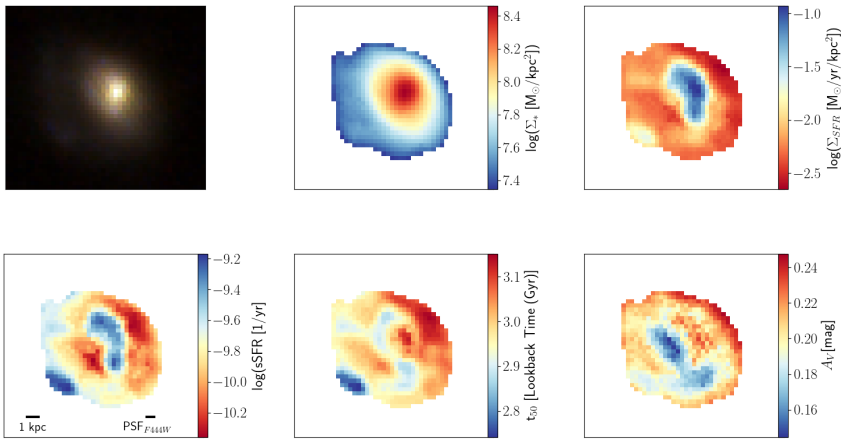

CANUCS - 2200478
$z = 0.81^{+0.01}_{-0.02}$
$\log(M_*/M_\odot) = 9.60^{+0.05}_{-0.06}$
$SFR_{100} = 0.82^{+0.20}_{-0.13}\ M_\odot/yr$
$\log(sSFR/yr) = -9.68^{+0.05}_{-0.01}$
Δ MS $= 0.06^{+0.10}_{-0.09}$ dex
$t_{50} = 3.06^{+1.03}_{-0.96}$ Gyr
$SFR_{10}/SFR_{100} = 1.000^{+0.00}_{-0.01}$

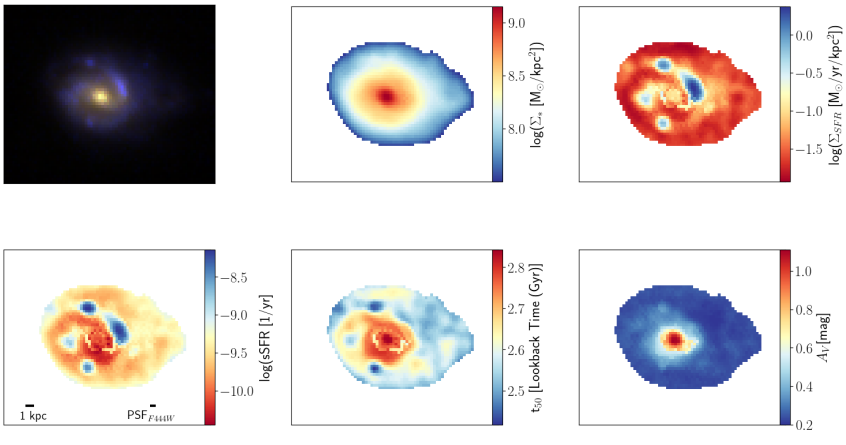

CANUCS - 2200493
$z = 1.10^{+0.04}_{-0.03}$
$\log(M_*/M_\odot) = 10.46^{+0.00}_{-0.00}$
$SFR_{100} = 15.55^{+0.17}_{-0.00}\ M_\odot/yr$
$\log(sSFR/yr) = -9.26^{+0.00}_{-0.00}$
Δ MS $= 0.52^{+0.00}_{-0.00}$ dex
$t_{50} = 4.60^{+0.01}_{-0.00}$ Gyr
$SFR_{10}/SFR_{100} = 0.881^{+0.00}_{-0.05}$

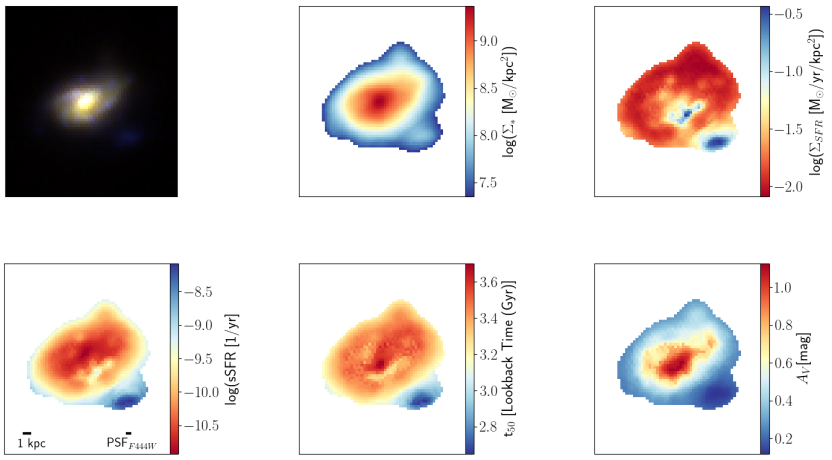

CANUCS - 2200538
$z = 0.80^{+0.02}_{-0.03}$
$\log(M_*/M_\odot) = 10.56^{+0.00}_{-0.12}$
$SFR_{100} = 3.99^{+0.40}_{-2.11}$ $M_\odot$/yr
$\log(sSFR/yr) = -9.95^{+0.04}_{-0.21}$
Δ MS $= 0.04^{+0.04}_{-0.34}$ dex
$t_{50} = 5.12^{+0.21}_{-2.42}$ Gyr
$SFR_{10}/SFR_{100} = 0.998^{+0.01}_{-0.00}$

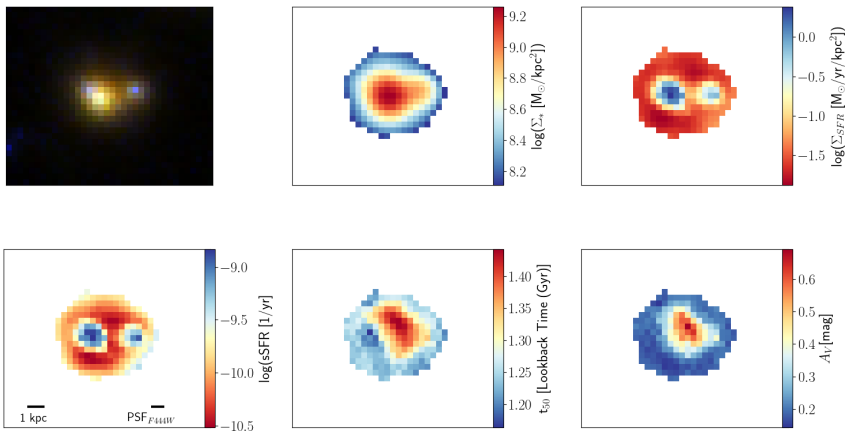

CANUCS - 2200566
$z = 2.42^{+0.02}_{-0.04}$
$\log(M_*/M_\odot) = 10.03^{+0.05}_{-0.07}$
$SFR_{100} = 3.07^{+0.83}_{-0.64}$ $M_\odot$/yr
$\log(sSFR/yr) = -9.54^{+0.05}_{-0.03}$
Δ MS $= -0.34^{+0.11}_{-0.11}$ dex
$t_{50} = 1.07^{+0.58}_{-0.52}$ Gyr
$SFR_{10}/SFR_{100} = 0.981^{+0.00}_{-0.02}$

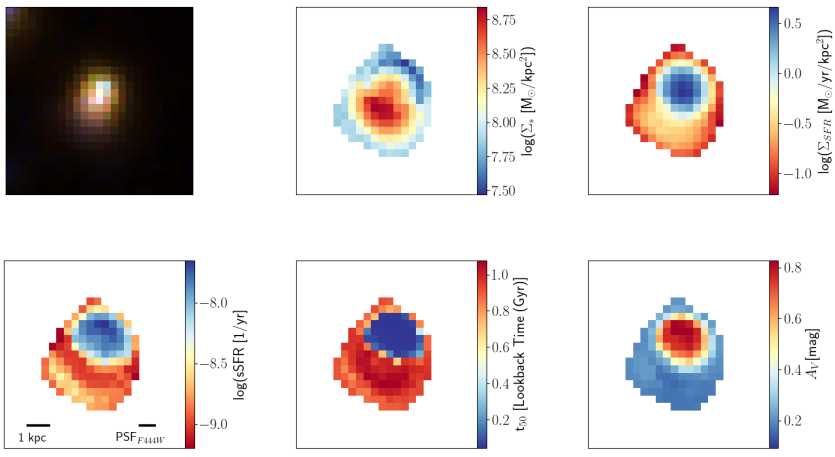

CANUCS - 2200594
$z = 2.75^{+0.00}_{-0.01}$
$\log(M_*/M_\odot) = 9.39^{+0.00}_{-0.00}$
$SFR_{100} = 10.45^{+0.07}_{-0.00}$ $M_\odot$/yr
$\log(sSFR/yr) = -8.37^{+0.00}_{-0.00}$
Δ MS $= 0.59^{+0.00}_{-0.00}$ dex
$t_{50} = 0.78^{+0.00}_{-0.00}$ Gyr
$SFR_{10}/SFR_{100} = 1.180^{+0.00}_{-0.00}$

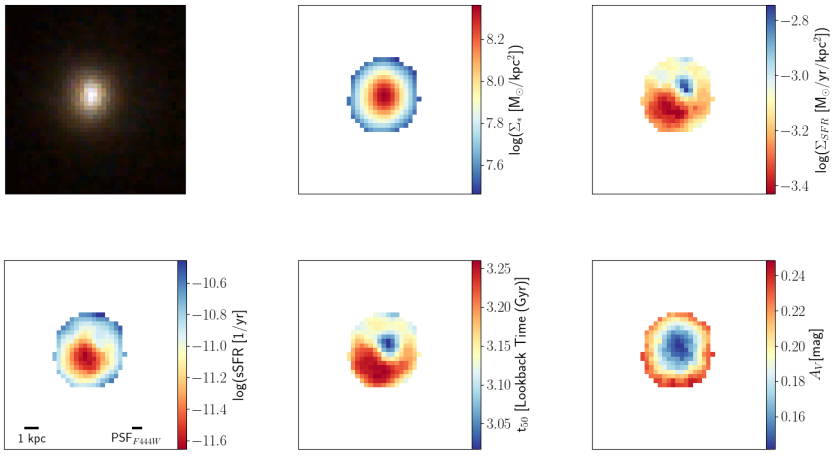

CANUCS - 2200973
$z = 0.79^{+0.06}_{-0.02}$
$\log(M_*/M_\odot) = 9.21^{+0.07}_{-0.06}$
$SFR_{100} = 0.01^{+0.08}_{-0.01}$ $M_\odot$/yr
$\log(sSFR/yr) = -11.06^{+0.74}_{-1.87}$
Δ MS = $-1.40^{+0.80}_{-1.93}$ dex
$t_{50} = 2.98^{+1.24}_{-1.21}$ Gyr
$SFR_{10}/SFR_{100} = 0.999^{+0.03}_{-0.00}$

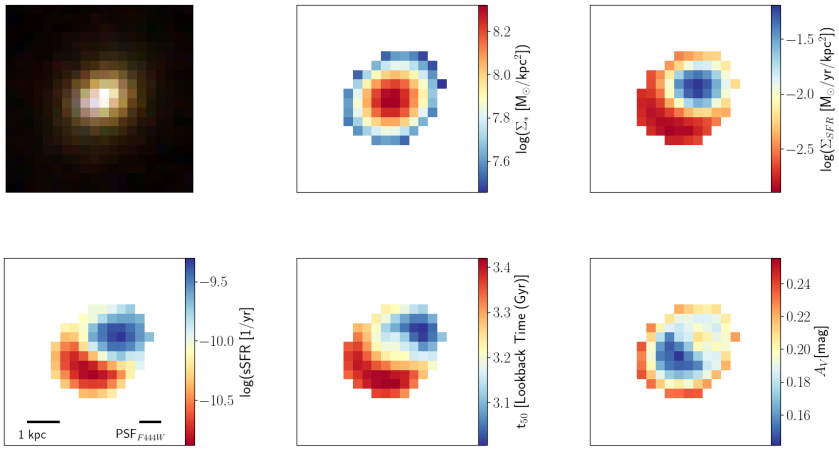

CANUCS - 2201088
$z = 0.72^{+0.01}_{-0.03}$
$\log(M_*/M_\odot) = 8.76^{+0.07}_{-0.08}$
$SFR_{100} = 0.08^{+0.03}_{-0.04}$ $M_\odot$/yr
$\log(sSFR/yr) = -9.86^{+0.06}_{-0.21}$
Δ MS = $-0.30^{+0.14}_{-0.29}$ dex
$t_{50} = 3.54^{+1.22}_{-1.33}$ Gyr
$SFR_{10}/SFR_{100} = 0.986^{+0.00}_{-0.00}$

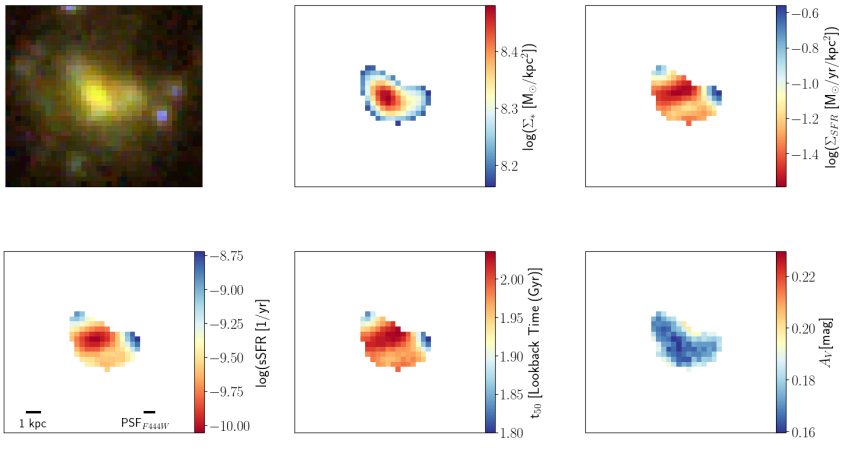

CANUCS - 2201206
$z = 1.41^{+0.04}_{-0.03}$
$\log(M_*/M_\odot) = 9.40^{+0.06}_{-0.09}$
$SFR_{100} = 0.81^{+0.23}_{-0.20}$ $M_\odot$/yr
$\log(sSFR/yr) = -9.49^{+0.05}_{-0.04}$
Δ MS = $-0.16^{+0.12}_{-0.14}$ dex
$t_{50} = 2.18^{+0.77}_{-0.70}$ Gyr
$SFR_{10}/SFR_{100} = 0.955^{+0.02}_{-0.01}$

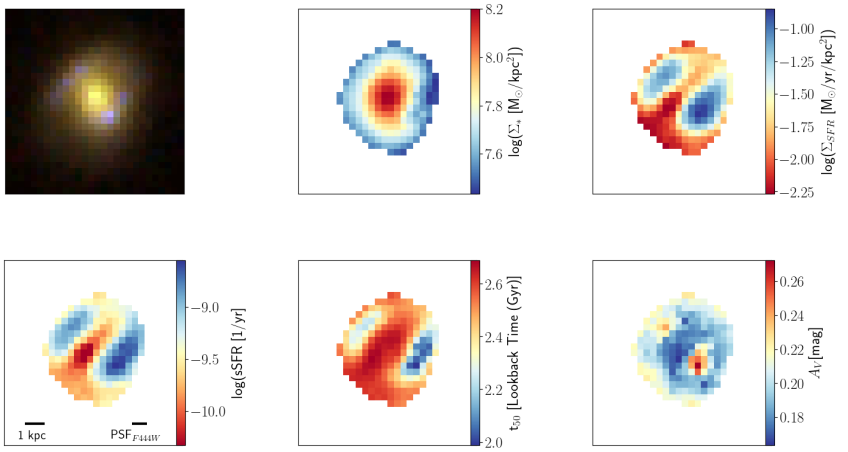

CANUCS - 2201207
$z = 1.00^{+0.01}_{-0.01}$
$\log(M_*/M_\odot) = 9.11^{+0.11}_{-0.06}$
$SFR_{100} = 0.70^{+0.27}_{-0.22}\ M_\odot/yr$
$\log(sSFR/yr) = -9.26^{+0.04}_{-0.10}$
$\Delta\ MS = 0.23^{+0.16}_{-0.17}$ dex
$t_{50} = 3.21^{+0.50}_{-1.08}$ Gyr
$SFR_{10}/SFR_{100} = 1.060^{+0.02}_{-0.03}$

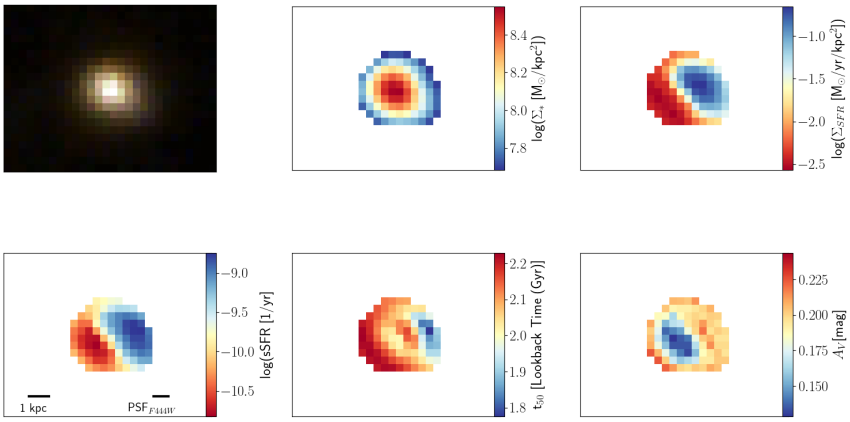

CANUCS - 2201218
$z = 1.33^{+0.01}_{-0.03}$
$\log(M_*/M_\odot) = 9.14^{+0.06}_{-0.06}$
$SFR_{100} = 0.53^{+0.18}_{-0.11}\ M_\odot/yr$
$\log(sSFR/yr) = -9.41^{+0.06}_{-0.04}$
$\Delta\ MS = -0.12^{+0.14}_{-0.11}$ dex
$t_{50} = 2.37^{+1.11}_{-0.68}$ Gyr
$SFR_{10}/SFR_{100} = 0.998^{+0.01}_{-0.00}$

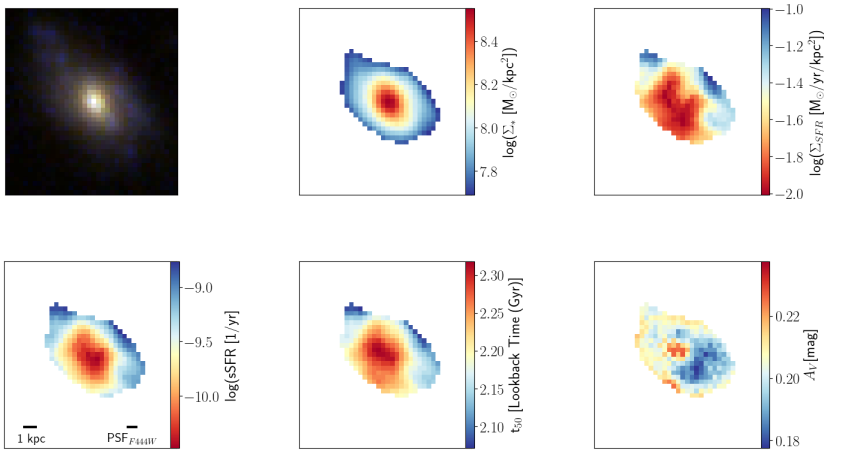

CANUCS - 2201230
$z = 1.30^{+0.04}_{-0.06}$
$\log(M_*/M_\odot) = 9.56^{+0.06}_{-0.05}$
$SFR_{100} = 0.99^{+0.30}_{-0.15}\ M_\odot/yr$
$\log(sSFR/yr) = -9.56^{+0.06}_{-0.02}$
$\Delta\ MS = -0.13^{+0.12}_{-0.08}$ dex
$t_{50} = 2.35^{+0.78}_{-0.74}$ Gyr
$SFR_{10}/SFR_{100} = 1.002^{+0.00}_{-0.02}$

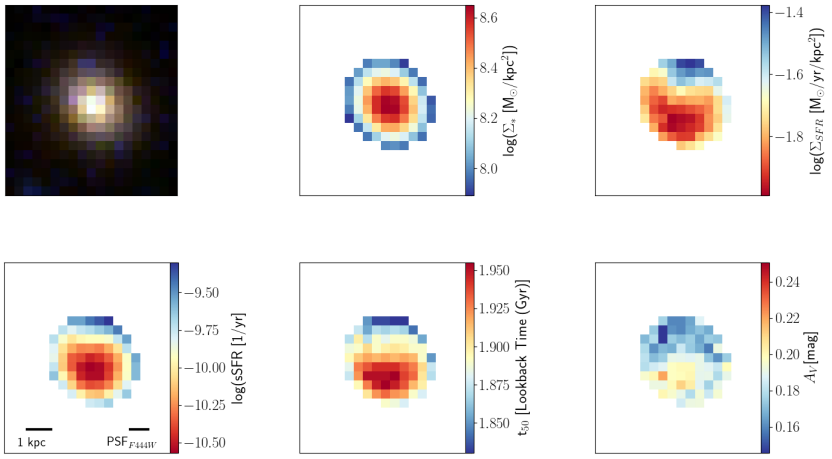

CANUCS - 2201278
$z = 1.58^{+0.05}_{-0.04}$
$\log(M_*/M_\odot) = 9.25^{+0.05}_{-0.06}$
$SFR_{100} = 0.17^{+0.21}_{-0.17}$ $M_\odot$/yr
$\log(sSFR/yr) = -10.02^{+0.30}_{-1.65}$
Δ MS = $-0.82^{+0.35}_{-1.71}$ dex
$t_{50} = 1.67^{+0.94}_{-0.88}$ Gyr
$SFR_{10}/SFR_{100} = 0.999^{+0.01}_{-0.00}$

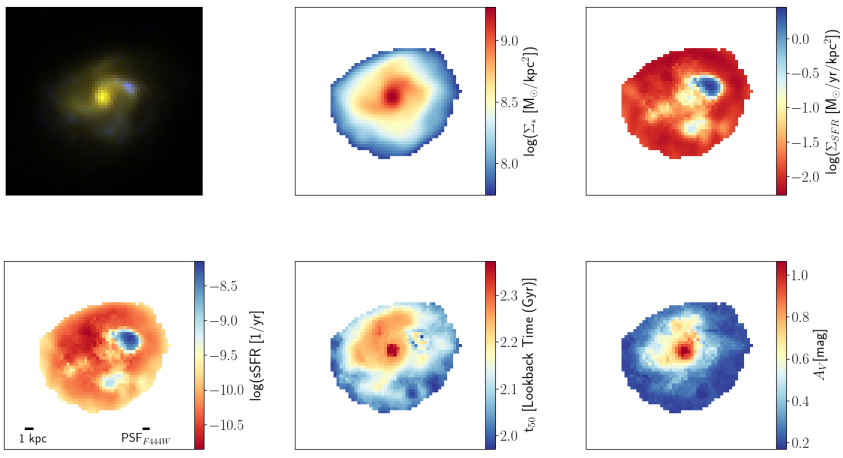

CANUCS - 2201306
$z = 1.47^{+0.01}_{-0.04}$
$\log(M_*/M_\odot) = 10.60^{+0.00}_{-0.00}$
$SFR_{100} = 10.49^{+0.15}_{-1.33}$ $M_\odot$/yr
$\log(sSFR/yr) = -9.58^{+0.01}_{-0.05}$
Δ MS = $0.07^{+0.01}_{-0.06}$ dex
$t_{50} = 2.27^{+0.00}_{-0.63}$ Gyr
$SFR_{10}/SFR_{100} = 1.000^{+0.01}_{-0.00}$

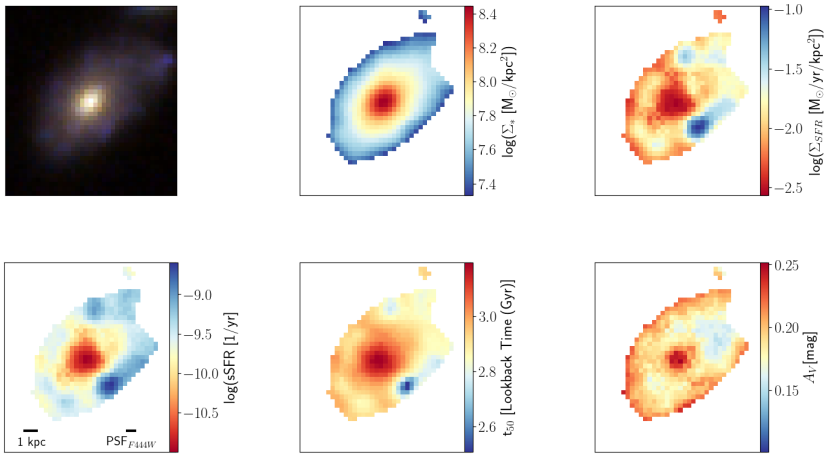

CANUCS - 2201592
$z = 0.84^{+0.03}_{-0.02}$
$\log(M_*/M_\odot) = 9.52^{+0.05}_{-0.06}$
$SFR_{100} = 0.77^{+0.33}_{-0.15}$ $M_\odot$/yr
$\log(sSFR/yr) = -9.63^{+0.10}_{-0.03}$
Δ MS = $0.07^{+0.16}_{-0.10}$ dex
$t_{50} = 2.97^{+1.34}_{-0.91}$ Gyr
$SFR_{10}/SFR_{100} = 0.989^{+0.00}_{-0.00}$

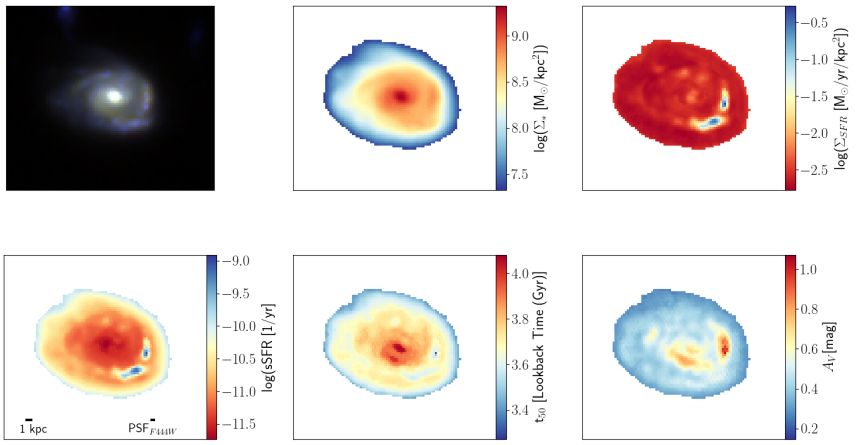

CANUCS - 2201596
$z = 0.73^{+0.02}_{-0.04}$
$\log(M_*/M_\odot) = 10.76^{+0.00}_{-0.01}$
$SFR_{100} = 1.15^{+0.08}_{-0.01}\ M_\odot/yr$
$\log(sSFR/yr) = -10.70^{+0.03}_{-0.01}$
Δ MS = $-0.62^{+0.03}_{-0.01}$ dex
$t_{50} = 4.21^{+0.32}_{-0.01}$ Gyr
$SFR_{10}/SFR_{100} = 0.983^{+0.00}_{-0.02}$

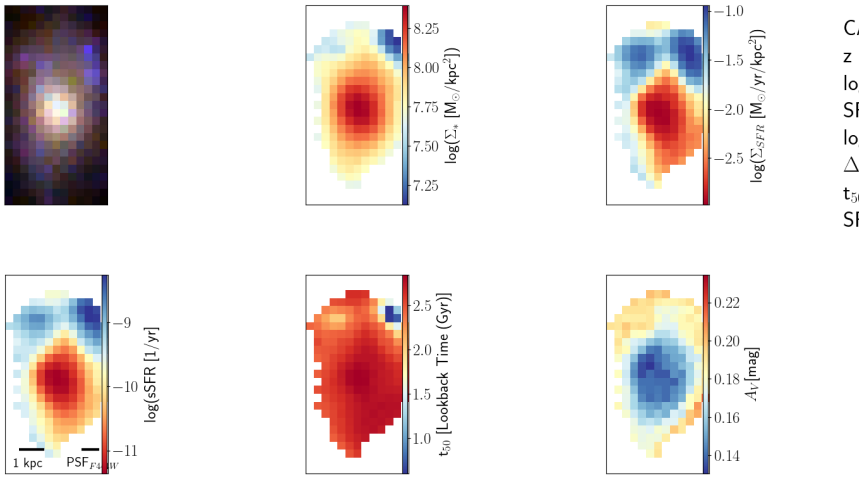

CANUCS - 3100033
$z = 0.93^{+0.06}_{-0.13}$
$\log(M_*/M_\odot) = 9.23^{+0.05}_{-0.07}$
$SFR_{100} = 0.43^{+0.22}_{-0.12}\ M_\odot/yr$
$\log(sSFR/yr) = -9.60^{+0.12}_{-0.07}$
Δ MS = $-0.03^{+0.18}_{-0.15}$ dex
$t_{50} = 3.14^{+0.82}_{-1.26}$ Gyr
$SFR_{10}/SFR_{100} = 0.972^{+0.01}_{-0.01}$

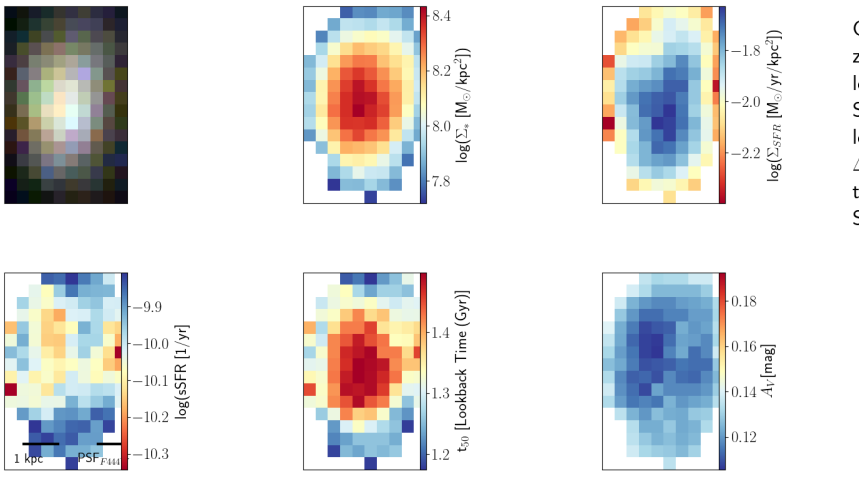

CANUCS - 3100041
$z = 1.66^{+0.06}_{-0.27}$
$\log(M_*/M_\odot) = 9.28^{+0.05}_{-0.04}$
$SFR_{100} = 0.19^{+1.00}_{-0.19}\ M_\odot/yr$
$\log(sSFR/yr) = -10.01^{+0.74}_{-2.30}$
Δ MS = $-0.84^{+0.80}_{-2.34}$ dex
$t_{50} = 0.70^{+1.15}_{-0.25}$ Gyr
$SFR_{10}/SFR_{100} = 0.995^{+0.01}_{-0.00}$

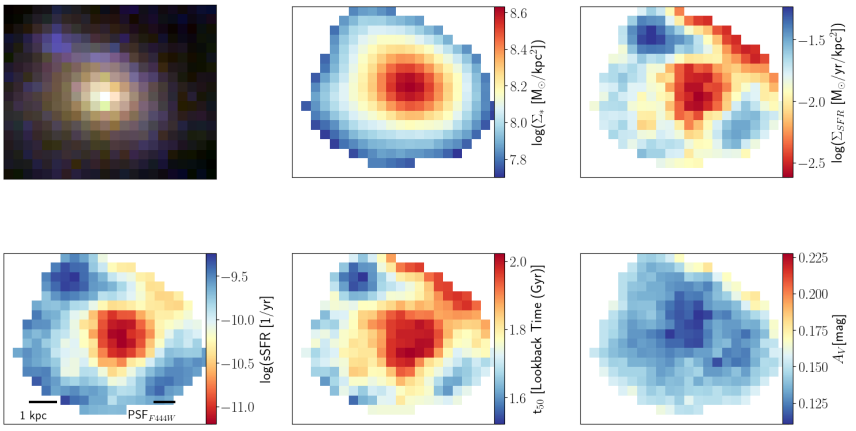

CANUCS - 3100055
$z = 1.43^{+0.38}_{-0.14}$
$\log(M_*/M_\odot) = 9.59^{+0.05}_{-0.06}$
$SFR_{100} = 0.45^{+0.45}_{-0.45}$ $M_\odot$/yr
$\log(sSFR/yr) = -9.93^{+0.25}_{-2.90}$
Δ MS = $-0.56^{+0.30}_{-2.96}$ dex
$t_{50} = 1.77^{+0.69}_{-0.75}$ Gyr
$SFR_{10}/SFR_{100} = 0.982^{+0.01}_{-0.01}$

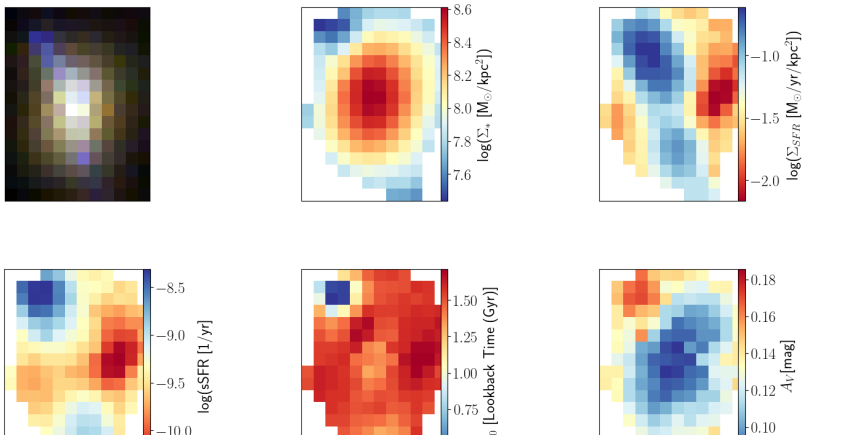

CANUCS - 3100069
$z = 1.57^{+0.07}_{-0.10}$
$\log(M_*/M_\odot) = 9.38^{+0.09}_{-0.14}$
$SFR_{100} = 1.16^{+0.38}_{-0.56}$ $M_\odot$/yr
$\log(sSFR/yr) = -9.31^{+0.03}_{-0.15}$
Δ MS = $-0.07^{+0.14}_{-0.30}$ dex
$t_{50} = 1.64^{+1.10}_{-0.97}$ Gyr
$SFR_{10}/SFR_{100} = 1.012^{+0.00}_{-0.01}$

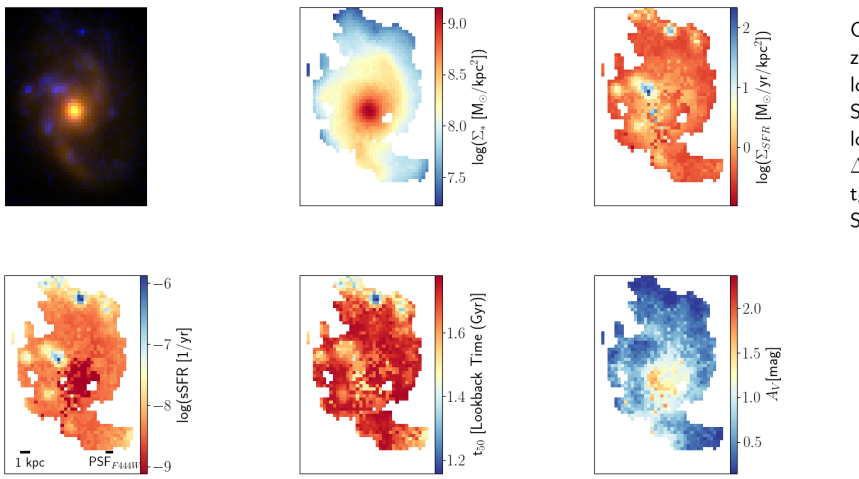

CANUCS - 3100085
$z = 2.05^{+0.06}_{-0.30}$
$\log(M_*/M_\odot) = 10.37^{+0.00}_{-0.05}$
$SFR_{100} = 196.38^{+93.52}_{-0.00}$ $M_\odot$/yr
$\log(sSFR/yr) = -8.08^{+0.17}_{-0.05}$
Δ MS = $1.31^{+0.17}_{-0.03}$ dex
$t_{50} = 0.08^{+0.00}_{-0.03}$ Gyr
$SFR_{10}/SFR_{100} = 1.000^{+0.14}_{-0.00}$

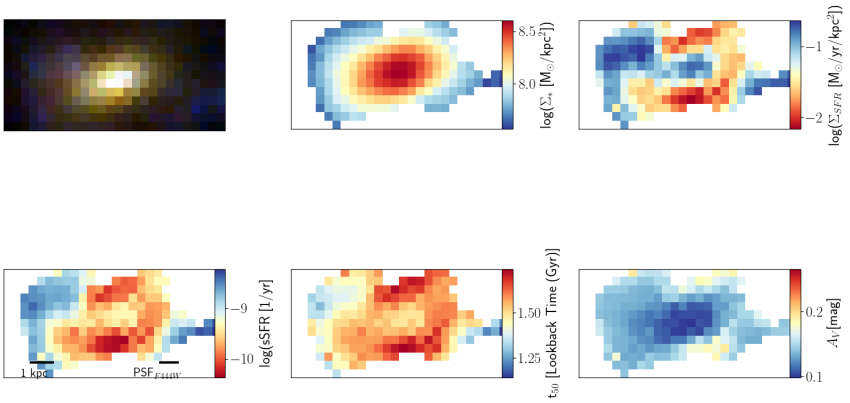

CANUCS - 3100102
$z = 1.71^{+0.17}_{-0.10}$
$\log(M_*/M_\odot) = 9.48^{+0.08}_{-0.05}$
$SFR_{100} = 1.66^{+0.84}_{-1.51}$ $M_\odot$/yr
$\log(sSFR/yr) = -9.26^{+0.09}_{-1.02}$
Δ MS = $-0.05^{+0.19}_{-1.06}$ dex
$t_{50} = 1.61^{+1.06}_{-0.95}$ Gyr
$SFR_{10}/SFR_{100} = 1.000^{+0.03}_{-0.00}$

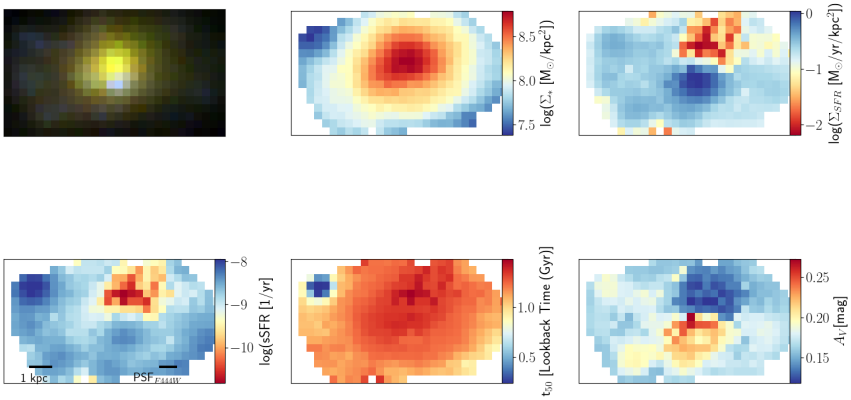

CANUCS - 3100106
$z = 2.04^{+0.13}_{-0.25}$
$\log(M_*/M_\odot) = 9.79^{+0.03}_{-0.11}$
$SFR_{100} = 9.72^{+5.42}_{-0.04}$ $M_\odot$/yr
$\log(sSFR/yr) = -8.80^{+0.17}_{-0.10}$
Δ MS = $0.39^{+0.19}_{-0.07}$ dex
$t_{50} = 1.59^{+0.44}_{-0.90}$ Gyr
$SFR_{10}/SFR_{100} = 1.161^{+0.04}_{-0.04}$

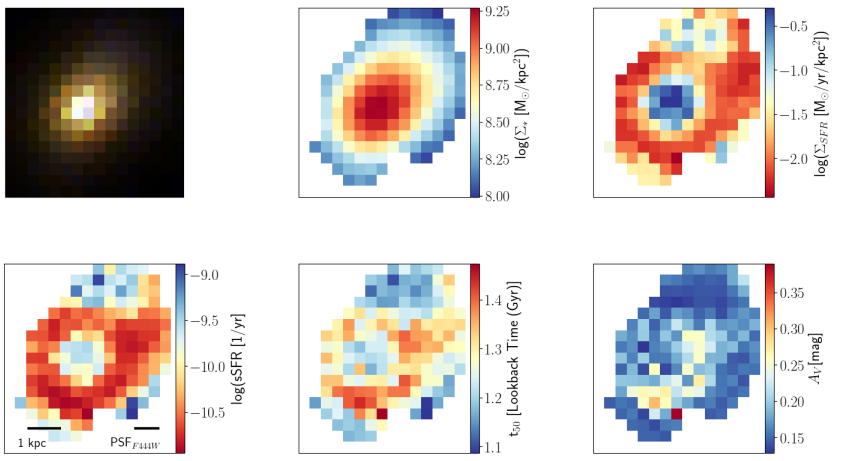

CANUCS - 3100182
$z = 2.32^{+0.09}_{-0.14}$
$\log(M_*/M_\odot) = 9.92^{+0.02}_{-0.02}$
$SFR_{100} = 0.86^{+0.18}_{-0.77}$ $M_\odot$/yr
$\log(sSFR/yr) = -9.98^{+0.06}_{-0.96}$
Δ MS = $-0.82^{+0.08}_{-0.98}$ dex
$t_{50} = 0.50^{+0.09}_{-0.21}$ Gyr
$SFR_{10}/SFR_{100} = 0.999^{+0.04}_{-0.00}$

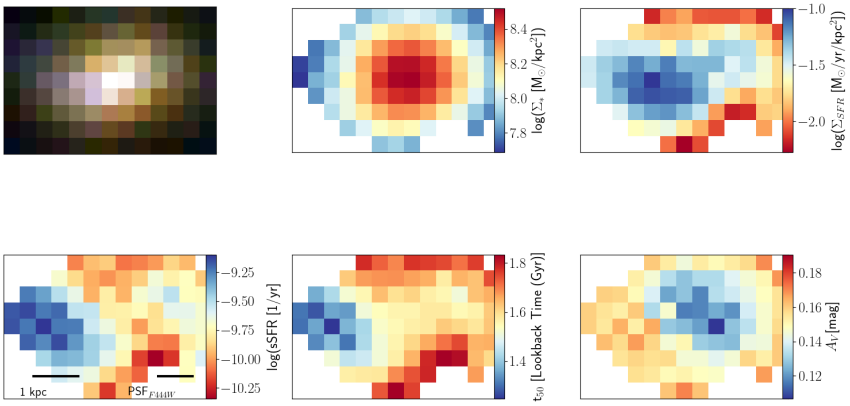

CANUCS - 3100189
$z = 1.45^{+0.11}_{-0.12}$
$\log(M_*/M_\odot) = 9.16^{+0.06}_{-0.09}$
$SFR_{100} = 0.34^{+0.27}_{-0.33}\ M_\odot/yr$
$\log(sSFR/yr) = -9.63^{+0.19}_{-1.96}$
Δ MS = $-0.40^{+0.26}_{-2.05}$ dex
$t_{50} = 1.64^{+0.94}_{-0.95}$ Gyr
$SFR_{10}/SFR_{100} = 1.000^{+0.00}_{-0.00}$

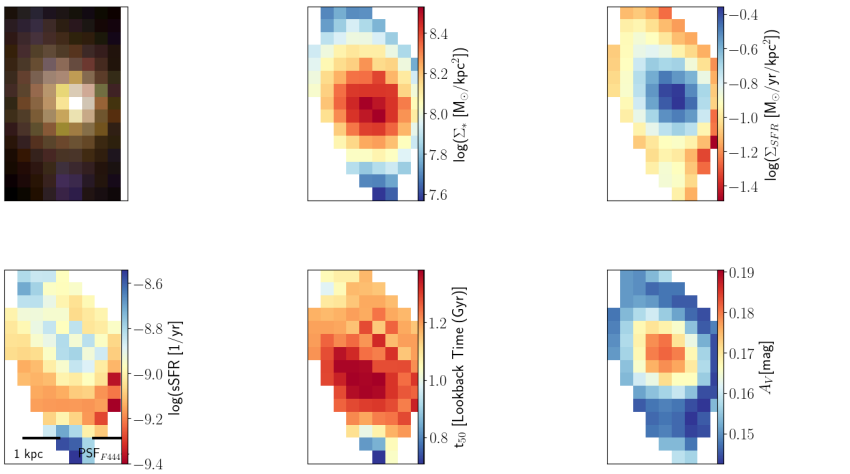

CANUCS - 3100190
$z = 1.84^{+0.23}_{-0.08}$
$\log(M_*/M_\odot) = 9.19^{+0.08}_{-0.13}$
$SFR_{100} = 1.60^{+0.85}_{-0.46}\ M_\odot/yr$
$\log(sSFR/yr) = -8.98^{+0.10}_{-0.02}$
Δ MS = $0.07^{+0.19}_{-0.17}$ dex
$t_{50} = 1.75^{+0.64}_{-0.61}$ Gyr
$SFR_{10}/SFR_{100} = 1.072^{+0.05}_{-0.03}$

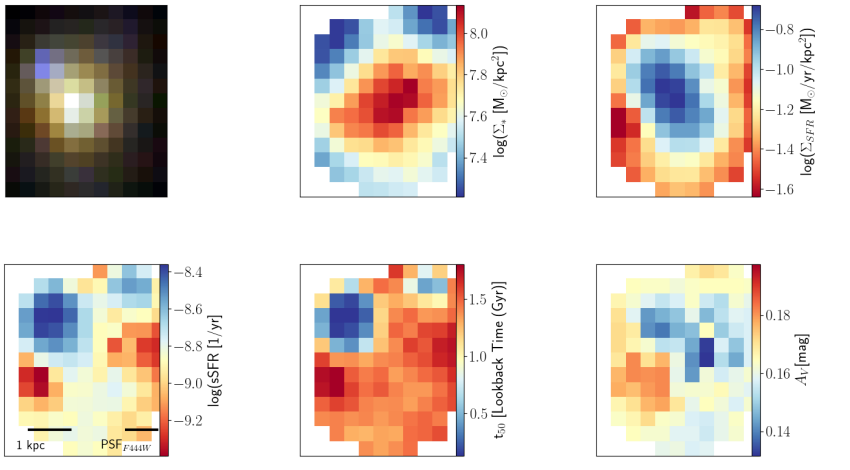

CANUCS - 3100226
$z = 1.28^{+0.05}_{-0.11}$
$\log(M_*/M_\odot) = 8.83^{+0.19}_{-0.24}$
$SFR_{100} = 0.97^{+0.23}_{-0.22}\ M_\odot/yr$
$\log(sSFR/yr) = -8.85^{+0.09}_{-0.13}$
Δ MS = $0.39^{+0.16}_{-0.20}$ dex
$t_{50} = 2.11^{+0.72}_{-0.98}$ Gyr
$SFR_{10}/SFR_{100} = 1.048^{+0.02}_{-0.02}$

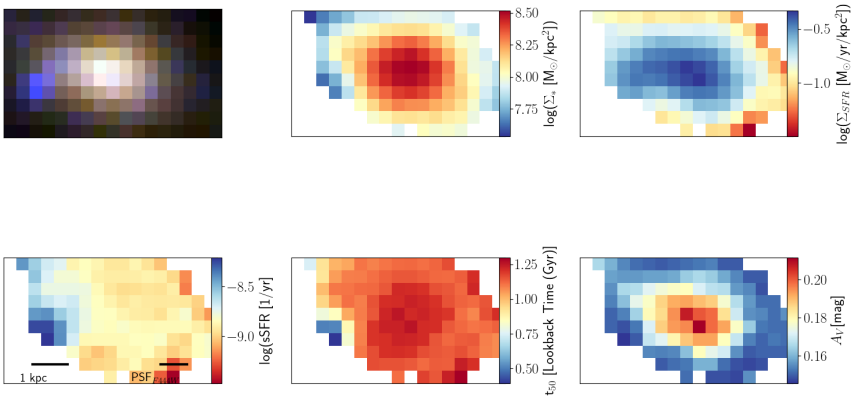

CANUCS - 3100239
z = $1.98^{+0.09}_{-0.21}$
log (M$_*$/M$_\odot$) = $9.29^{+0.09}_{-0.30}$
SFR$_{100}$ = $2.78^{+1.44}_{-1.18}$ M$_\odot$/yr
log(sSFR/yr) = $-8.84^{+0.09}_{-0.06}$
Δ MS = $0.19^{+0.19}_{-0.31}$ dex
t$_{50}$ = $1.48^{+0.49}_{-0.96}$ Gyr
SFR$_{10}$/SFR$_{100}$ = $1.071^{+0.04}_{-0.03}$

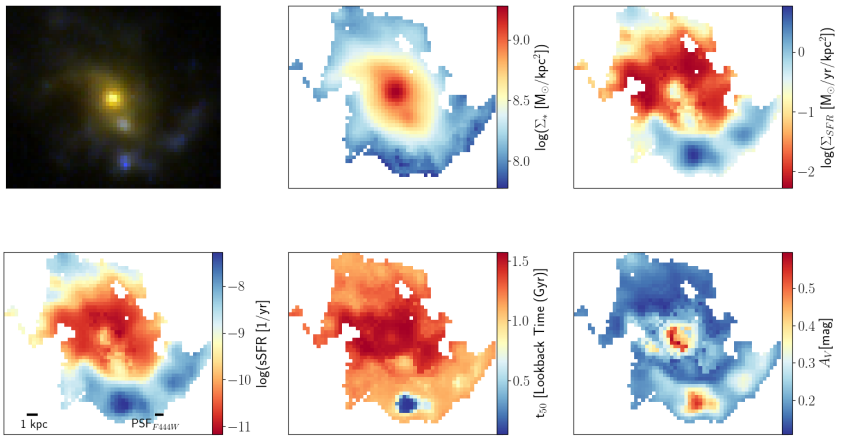

CANUCS - 3100550
z = $2.16^{+0.04}_{-0.14}$
log (M$_*$/M$_\odot$) = $10.63^{+0.06}_{-0.00}$
SFR$_{100}$ = $56.26^{+0.65}_{-12.53}$ M$_\odot$/yr
log(sSFR/yr) = $-8.88^{+0.05}_{-0.11}$
Δ MS = $0.58^{+0.04}_{-0.11}$ dex
t$_{50}$ = $1.21^{+0.80}_{-0.00}$ Gyr
SFR$_{10}$/SFR$_{100}$ = $1.131^{+0.00}_{-0.00}$

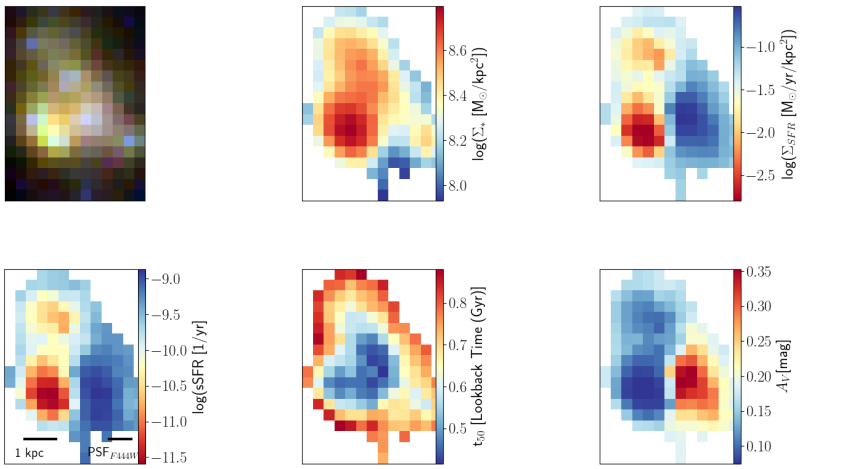

CANUCS - 3100582
z = $2.62^{+0.02}_{-0.34}$
log (M$_*$/M$_\odot$) = $9.62^{+0.05}_{-0.00}$
SFR$_{100}$ = $1.05^{+1.13}_{-0.54}$ M$_\odot$/yr
log(sSFR/yr) = $-9.60^{+0.27}_{-0.31}$
Δ MS = $-0.55^{+0.32}_{-0.31}$ dex
t$_{50}$ = $0.27^{+0.25}_{-0.01}$ Gyr
SFR$_{10}$/SFR$_{100}$ = $0.438^{+0.36}_{-0.00}$

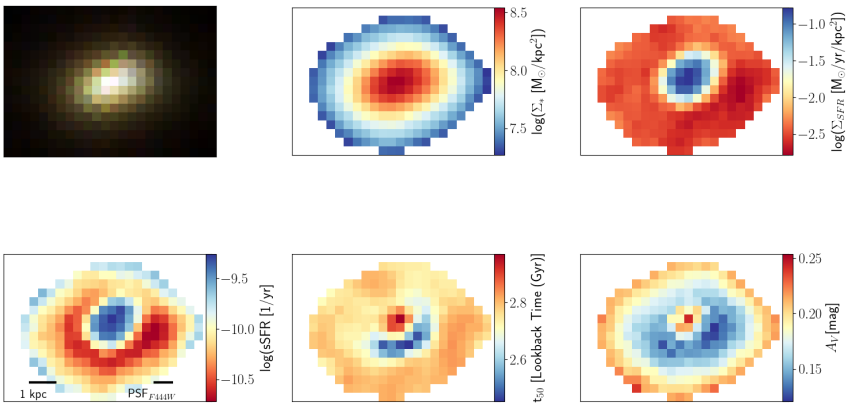

CANUCS - 3100585
$z = 0.93^{+0.02}_{-0.09}$
$\log(M_*/M_\odot) = 9.29^{+0.07}_{-0.04}$
$SFR_{100} = 0.29^{+0.11}_{-0.14}$ $M_\odot$/yr
$\log(sSFR/yr) = -9.83^{+0.07}_{-0.24}$
Δ MS = $-0.24^{+0.15}_{-0.29}$ dex
$t_{50} = 2.54^{+1.00}_{-0.96}$ Gyr
$SFR_{10}/SFR_{100} = 0.983^{+0.01}_{-0.01}$

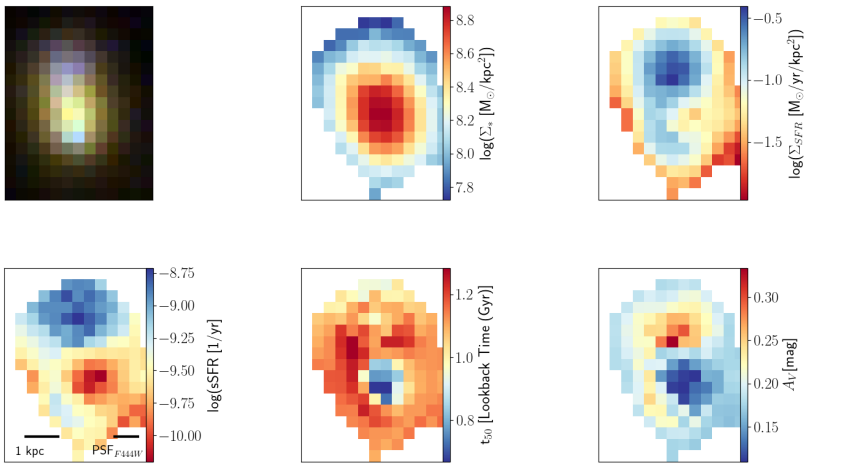

CANUCS - 3100689
$z = 2.30^{+0.10}_{-0.05}$
$\log(M_*/M_\odot) = 9.54^{+0.10}_{-0.12}$
$SFR_{100} = 1.40^{+0.86}_{-0.05}$ $M_\odot$/yr
$\log(sSFR/yr) = -9.40^{+0.11}_{-0.10}$
Δ MS = $-0.38^{+0.22}_{-0.07}$ dex
$t_{50} = 0.76^{+0.64}_{-0.35}$ Gyr
$SFR_{10}/SFR_{100} = 1.018^{+0.09}_{-0.01}$

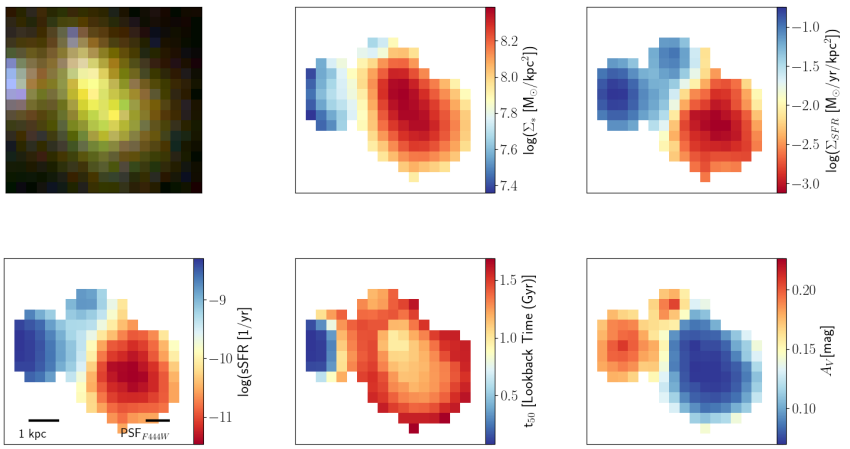

CANUCS - 3100730
$z = 1.60^{+0.03}_{-0.01}$
$\log(M_*/M_\odot) = 9.30^{+0.05}_{-0.05}$
$SFR_{100} = 0.61^{+0.28}_{-0.09}$ $M_\odot$/yr
$\log(sSFR/yr) = -9.51^{+0.12}_{-0.02}$
Δ MS = $-0.31^{+0.17}_{-0.08}$ dex
$t_{50} = 1.07^{+0.90}_{-0.41}$ Gyr
$SFR_{10}/SFR_{100} = 0.999^{+0.01}_{-0.00}$

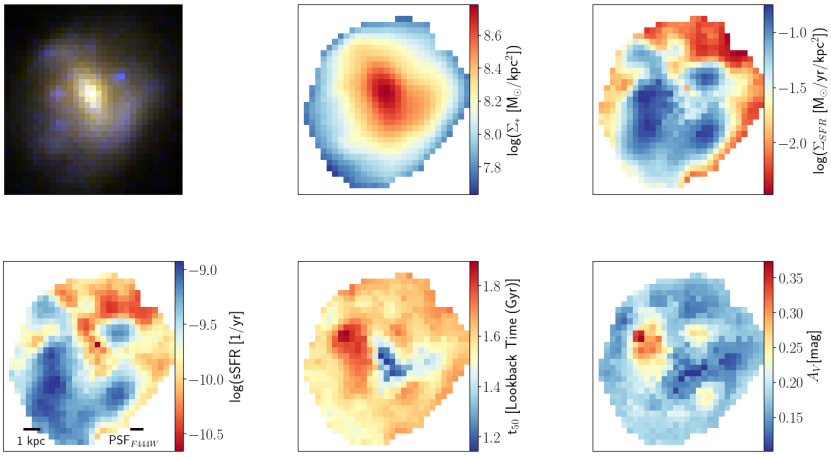

CANUCS - 3100813
$z = 1.68^{+0.02}_{-0.12}$
$\log(M_*/M_\odot) = 10.09^{+0.01}_{-0.05}$
$SFR_{100} = 3.68^{+0.48}_{-0.14}$ $M_\odot$/yr
$\log(sSFR/yr) = -9.52^{+0.05}_{-0.04}$
Δ MS = $-0.11^{+0.05}_{-0.04}$ dex
$t_{50} = 2.00^{+0.46}_{-0.46}$ Gyr
$SFR_{10}/SFR_{100} = 0.892^{+0.00}_{-0.05}$

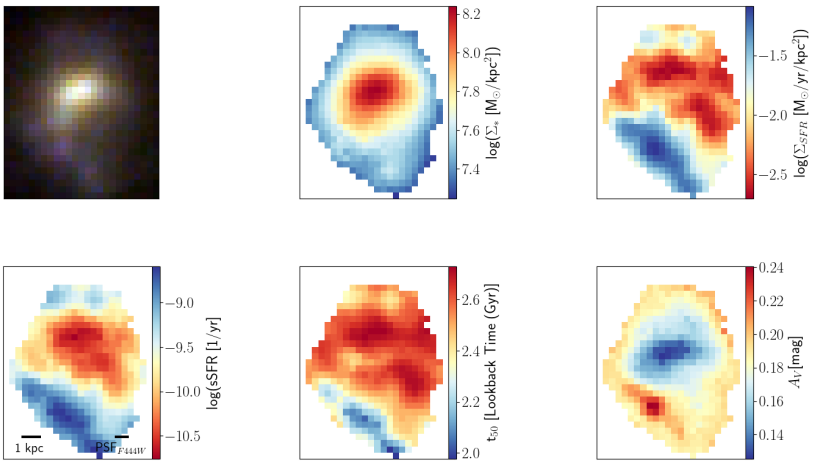

CANUCS - 3100921
$z = 1.00^{+0.05}_{-0.06}$
$\log(M_*/M_\odot) = 9.35^{+0.06}_{-0.04}$
$SFR_{100} = 0.73^{+0.27}_{-0.17}$ $M_\odot$/yr
$\log(sSFR/yr) = -9.49^{+0.08}_{-0.07}$
Δ MS = $0.07^{+0.14}_{-0.12}$ dex
$t_{50} = 2.52^{+1.20}_{-0.49}$ Gyr
$SFR_{10}/SFR_{100} = 0.972^{+0.01}_{-0.02}$

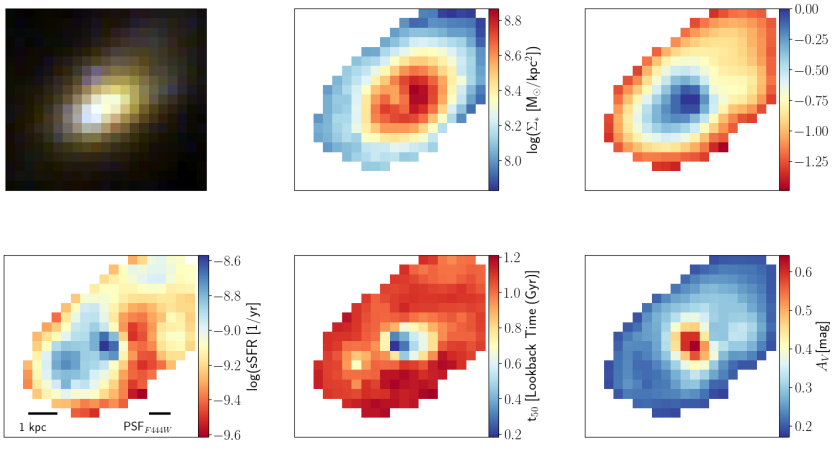

CANUCS - 3100975
$z = 2.09^{+0.07}_{-0.09}$
$\log(M_*/M_\odot) = 9.72^{+0.05}_{-0.06}$
$SFR_{100} = 4.41^{+2.95}_{-1.81}$ $M_\odot$/yr
$\log(sSFR/yr) = -9.07^{+0.17}_{-0.17}$
Δ MS = $0.07^{+0.22}_{-0.23}$ dex
$t_{50} = 1.70^{+0.33}_{-0.62}$ Gyr
$SFR_{10}/SFR_{100} = 1.085^{+0.00}_{-0.00}$

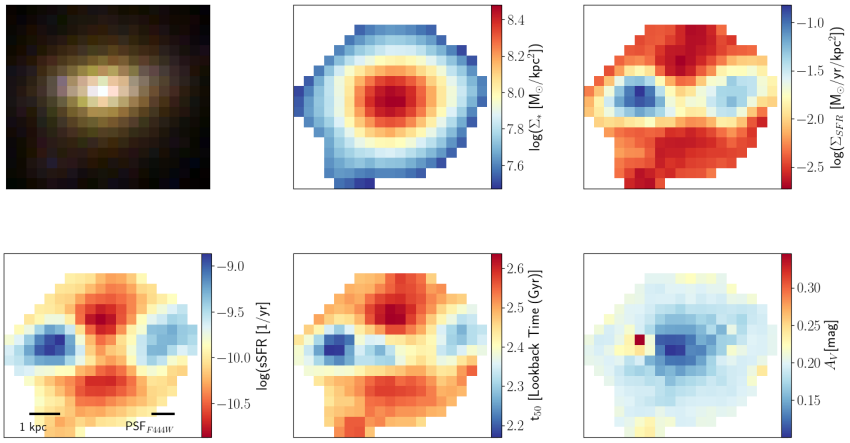

CANUCS - 3101071
$z = 1.09^{+0.05}_{-0.04}$
$\log(M_*/M_\odot) = 9.33^{+0.05}_{-0.07}$
$SFR_{100} = 0.34^{+0.13}_{-0.15}$ $M_\odot$/yr
$\log(sSFR/yr) = -9.80^{+0.10}_{-0.20}$
Δ MS $= -0.31^{+0.15}_{-0.27}$ dex
$t_{50} = 2.63^{+0.77}_{-1.09}$ Gyr
$SFR_{10}/SFR_{100} = 0.958^{+0.01}_{-0.02}$

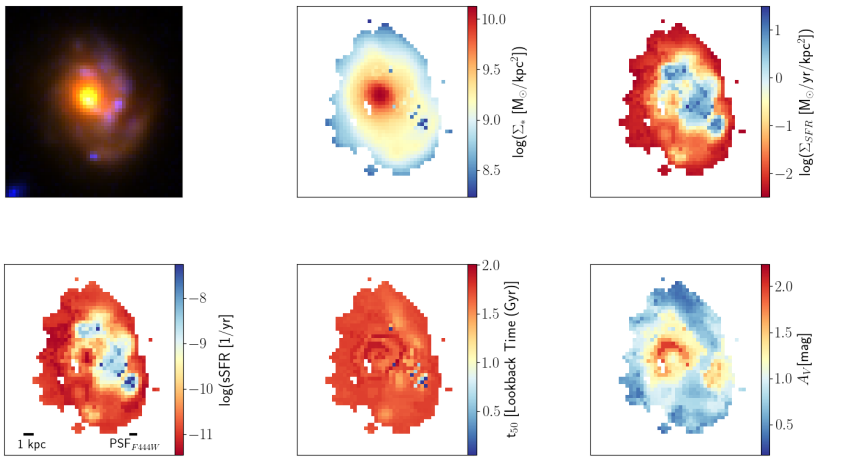

CANUCS - 3101095
$z = 2.00^{+0.05}_{-0.07}$
$\log(M_*/M_\odot) = 11.27^{+0.00}_{-0.00}$
$SFR_{100} = 78.85^{+0.30}_{-0.00}$ $M_\odot$/yr
$\log(sSFR/yr) = -9.38^{+0.00}_{-0.00}$
Δ MS $= 0.35^{+0.00}_{-0.00}$ dex
$t_{50} = 1.63^{+0.00}_{-0.00}$ Gyr
$SFR_{10}/SFR_{100} = 0.993^{+0.00}_{-0.00}$

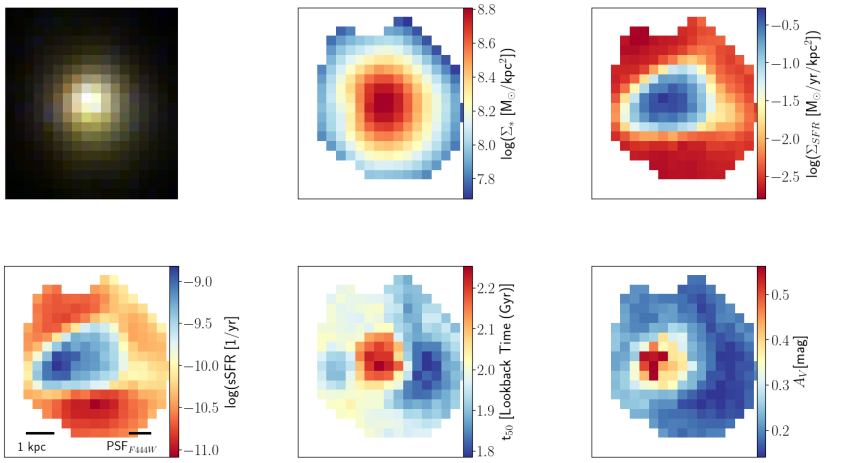

CANUCS - 3101102
$z = 1.52^{+0.02}_{-0.07}$
$\log(M_*/M_\odot) = 9.66^{+0.04}_{-0.03}$
$SFR_{100} = 1.24^{+0.32}_{-0.28}$ $M_\odot$/yr
$\log(sSFR/yr) = -9.57^{+0.06}_{-0.08}$
Δ MS $= -0.21^{+0.10}_{-0.12}$ dex
$t_{50} = 2.14^{+0.51}_{-0.44}$ Gyr
$SFR_{10}/SFR_{100} = 0.977^{+0.01}_{-0.00}$

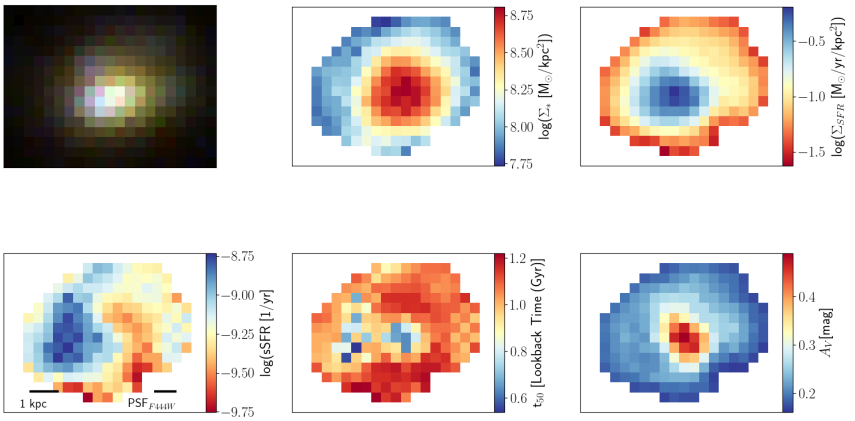

CANUCS - 3101169
z = $2.08^{+0.05}_{-0.10}$
log ($M_*/M_\odot$) = $9.61^{+0.05}_{-0.06}$
SFR_{100} = $2.84^{+1.32}_{-0.69}$ $M_\odot$/yr
log(sSFR/yr) = $-9.15^{+0.12}_{-0.07}$
Δ MS = $-0.05^{+0.17}_{-0.13}$ dex
t_{50} = $1.64^{+0.41}_{-0.47}$ Gyr
SFR_{10}/SFR_{100} = $1.072^{+0.00}_{-0.05}$

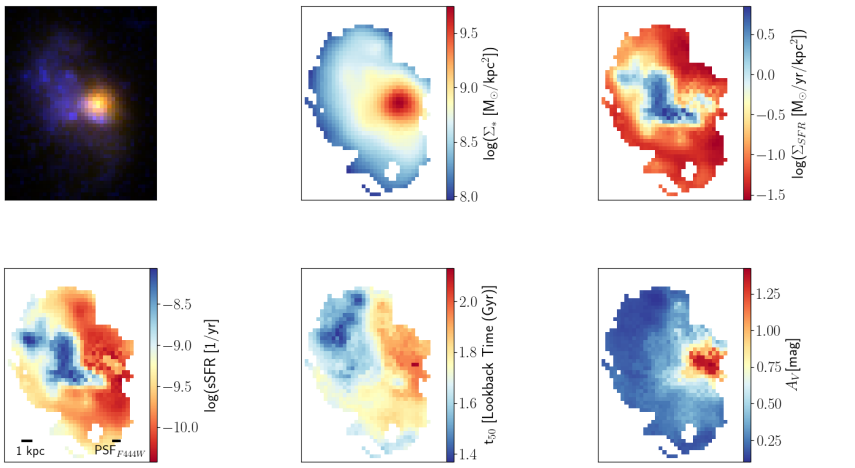

CANUCS - 3101186
z = $1.84^{+0.08}_{-0.02}$
log ($M_*/M_\odot$) = $10.83^{+0.00}_{-0.00}$
SFR_{100} = $56.30^{+4.47}_{-6.48}$ $M_\odot$/yr
log(sSFR/yr) = $-9.08^{+0.03}_{-0.05}$
Δ MS = $0.52^{+0.03}_{-0.05}$ dex
t_{50} = $2.06^{+0.00}_{-0.00}$ Gyr
SFR_{10}/SFR_{100} = $0.998^{+0.00}_{-0.00}$

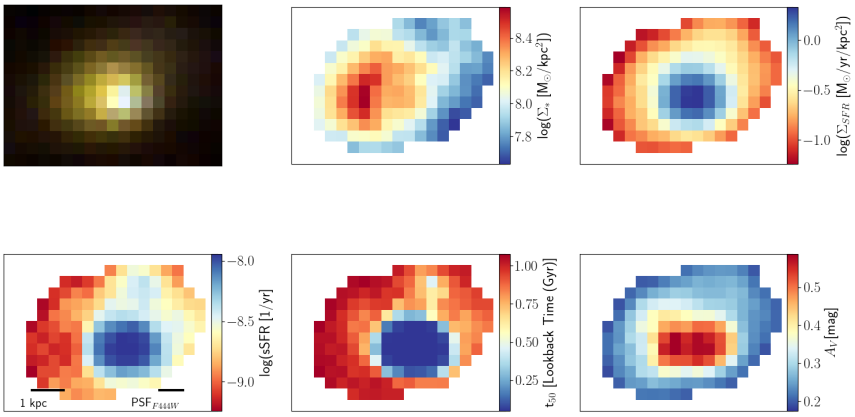

CANUCS - 3101273
z = $2.27^{+0.02}_{-0.04}$
log ($M_*/M_\odot$) = $9.33^{+0.19}_{-0.00}$
SFR_{100} = $6.81^{+0.05}_{-4.25}$ $M_\odot$/yr
log(sSFR/yr) = $-8.49^{+0.19}_{-0.42}$
Δ MS = $0.44^{+0.12}_{-0.42}$ dex
t_{50} = $1.32^{+0.00}_{-0.24}$ Gyr
SFR_{10}/SFR_{100} = $1.197^{+0.00}_{-0.03}$

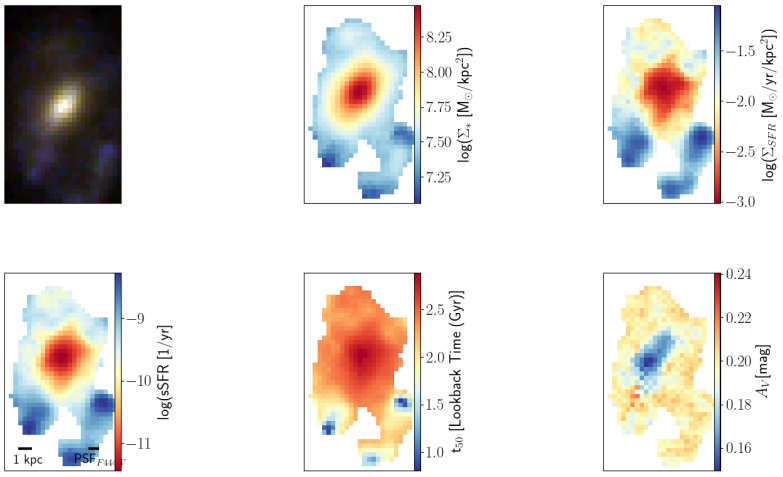

CANUCS - 3101292
$z = 1.09^{+0.05}_{-0.04}$
$\log(M_*/M_\odot) = 9.53^{+0.15}_{-0.04}$
$SFR_{100} = 1.21^{+0.08}_{-0.27}\ M_\odot/yr$
$\log(sSFR/yr) = -9.45^{+0.12}_{-0.07}$
Δ MS $= 0.10^{+0.11}_{-0.11}$ dex
$t_{50} = 3.45^{+0.15}_{-1.14}$ Gyr
$SFR_{10}/SFR_{100} = 0.993^{+0.00}_{-0.00}$

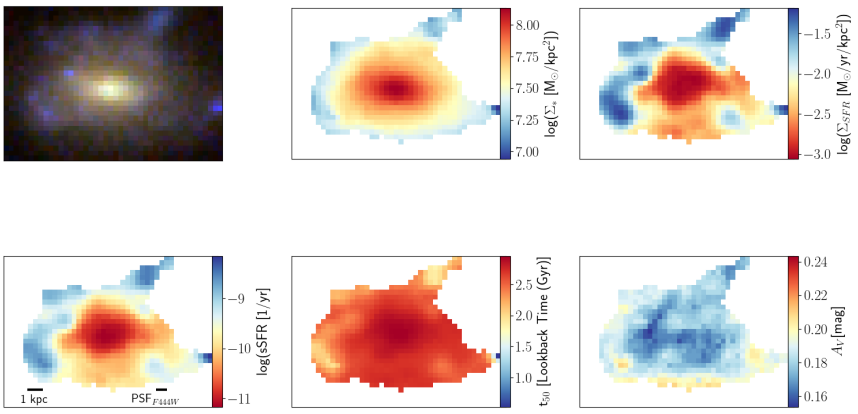

CANUCS - 3101338
$z = 0.92^{+0.04}_{-0.04}$
$\log(M_*/M_\odot) = 9.44^{+0.07}_{-0.04}$
$SFR_{100} = 0.75^{+0.23}_{-0.10}\ M_\odot/yr$
$\log(sSFR/yr) = -9.56^{+0.05}_{-0.03}$
Δ MS $= 0.07^{+0.13}_{-0.07}$ dex
$t_{50} = 2.84^{+1.52}_{-0.95}$ Gyr
$SFR_{10}/SFR_{100} = 0.994^{+0.00}_{-0.00}$

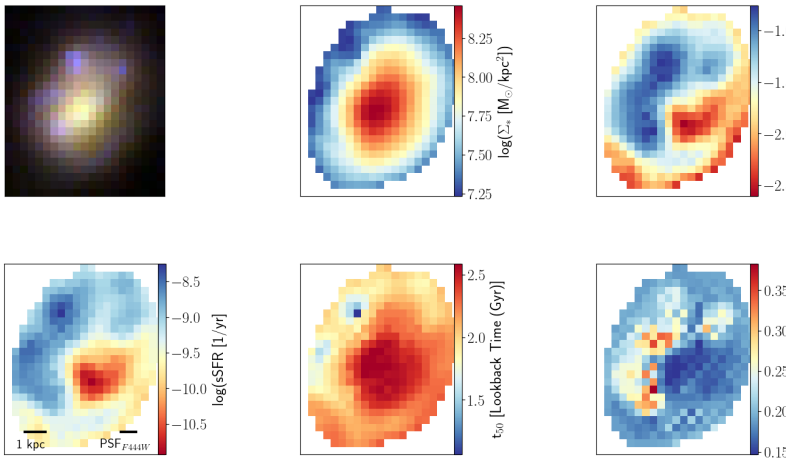

CANUCS - 3101351
$z = 1.16^{+0.03}_{-0.01}$
$\log(M_*/M_\odot) = 9.47^{+0.06}_{-0.02}$
$SFR_{100} = 1.75^{+0.54}_{-0.29}\ M_\odot/yr$
$\log(sSFR/yr) = -9.23^{+0.06}_{-0.06}$
Δ MS $= 0.26^{+0.12}_{-0.08}$ dex
$t_{50} = 2.65^{+0.73}_{-0.63}$ Gyr
$SFR_{10}/SFR_{100} = 0.998^{+0.01}_{-0.00}$

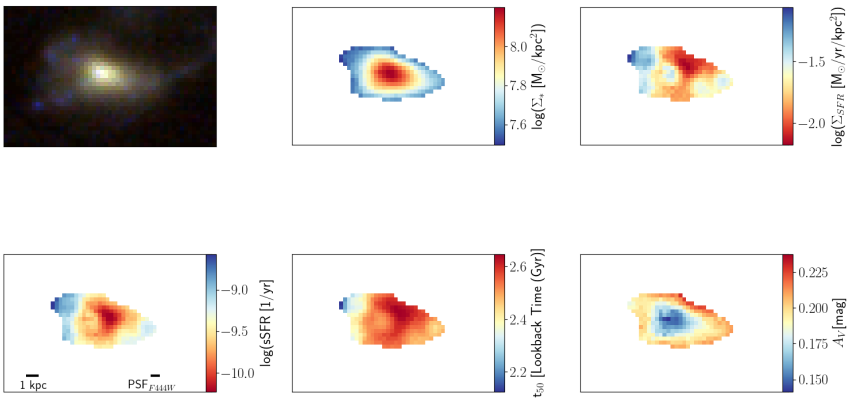

CANUCS - 3200125
$z = 1.03^{+0.03}_{-0.05}$
$\log(M_*/M_\odot) = 9.27^{+0.08}_{-0.08}$
$SFR_{100} = 0.63^{+0.23}_{-0.12}\ M_\odot/yr$
$\log(sSFR/yr) = -9.47^{+0.06}_{-0.01}$
$\Delta\ MS = 0.04^{+0.15}_{-0.11}$ dex
$t_{50} = 2.72^{+1.23}_{-1.05}$ Gyr
$SFR_{10}/SFR_{100} = 0.995^{+0.01}_{-0.00}$

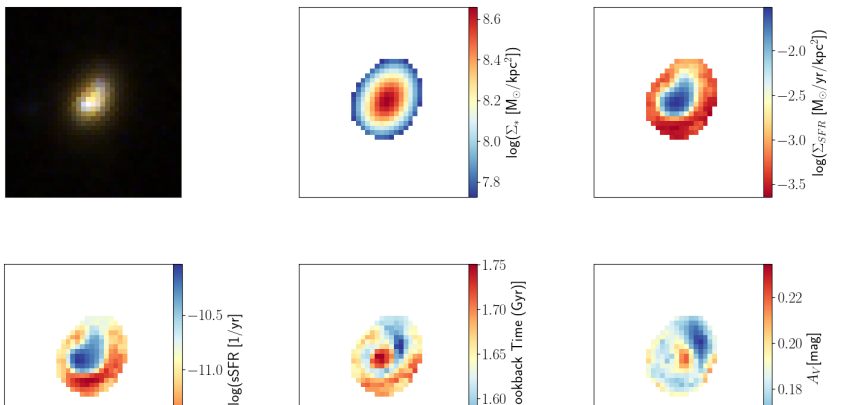

CANUCS - 3200343
$z = 1.74^{+0.06}_{-0.03}$
$\log(M_*/M_\odot) = 9.54^{+0.05}_{-0.03}$
$SFR_{100} = 0.09^{+0.83}_{-0.09}\ M_\odot/yr$
$\log(sSFR/yr) = -10.56^{+0.94}_{-2.04}$
$\Delta\ MS = -1.35^{+0.99}_{-2.08}$ dex
$t_{50} = 1.04^{+0.65}_{-0.70}$ Gyr
$SFR_{10}/SFR_{100} = 0.994^{+0.00}_{-0.02}$

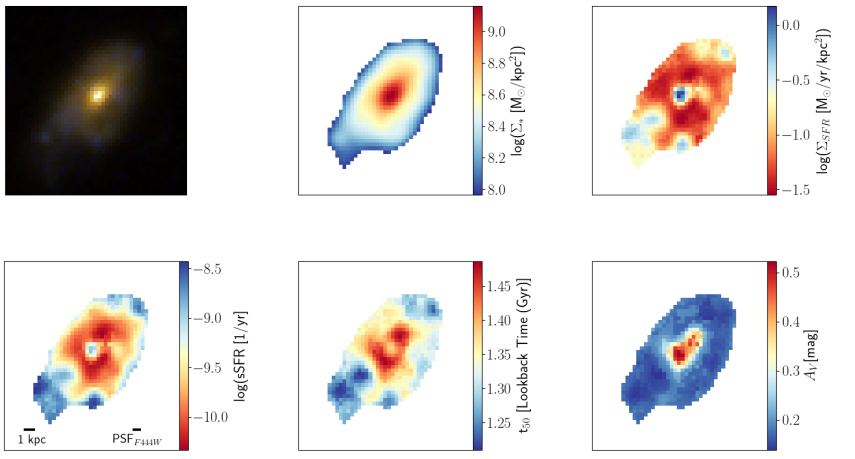

CANUCS - 3200407
$z = 2.24^{+0.01}_{-0.12}$
$\log(M_*/M_\odot) = 10.36^{+0.03}_{-0.04}$
$SFR_{100} = 9.65^{+3.09}_{-1.75}\ M_\odot/yr$
$\log(sSFR/yr) = -9.38^{+0.09}_{-0.05}$
$\Delta\ MS = -0.04^{+0.12}_{-0.09}$ dex
$t_{50} = 1.32^{+0.13}_{-0.44}$ Gyr
$SFR_{10}/SFR_{100} = 0.981^{+0.01}_{-0.00}$

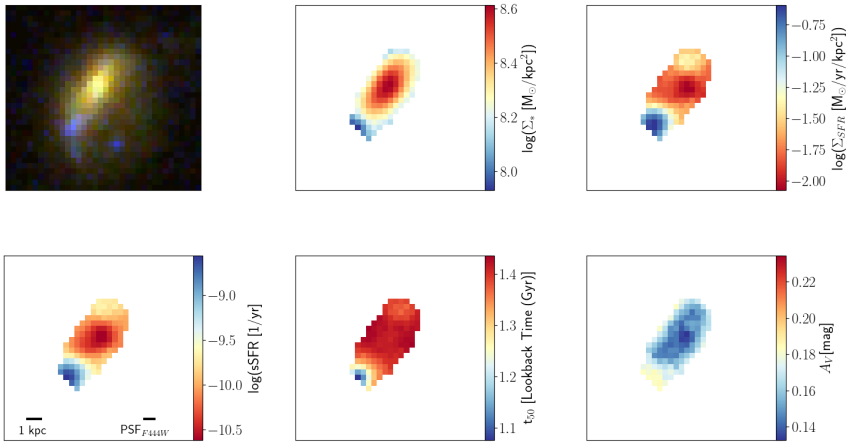

CANUCS - 3200466
$z = 2.04^{+0.05}_{-0.08}$
$\log(M_*/M_\odot) = 9.50^{+0.06}_{-0.09}$
$SFR_{100} = 0.63^{+0.49}_{-0.60}$ $M_\odot$/yr
$\log(sSFR/yr) = -9.70^{+0.18}_{-1.21}$
Δ MS = $-0.62^{+0.25}_{-1.30}$ dex
$t_{50} = 1.02^{+0.68}_{-0.54}$ Gyr
$SFR_{10}/SFR_{100} = 0.944^{+0.02}_{-0.02}$

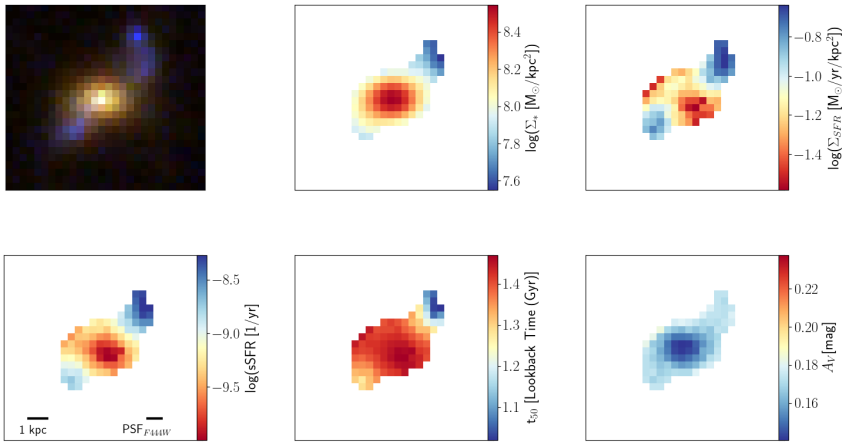

CANUCS - 3200476
$z = 1.92^{+0.02}_{-0.03}$
$\log(M_*/M_\odot) = 9.21^{+0.09}_{-0.12}$
$SFR_{100} = 1.05^{+0.46}_{-0.38}$ $M_\odot$/yr
$\log(sSFR/yr) = -9.19^{+0.07}_{-0.07}$
Δ MS = $-0.17^{+0.17}_{-0.21}$ dex
$t_{50} = 1.69^{+0.61}_{-0.60}$ Gyr
$SFR_{10}/SFR_{100} = 1.014^{+0.01}_{-0.01}$

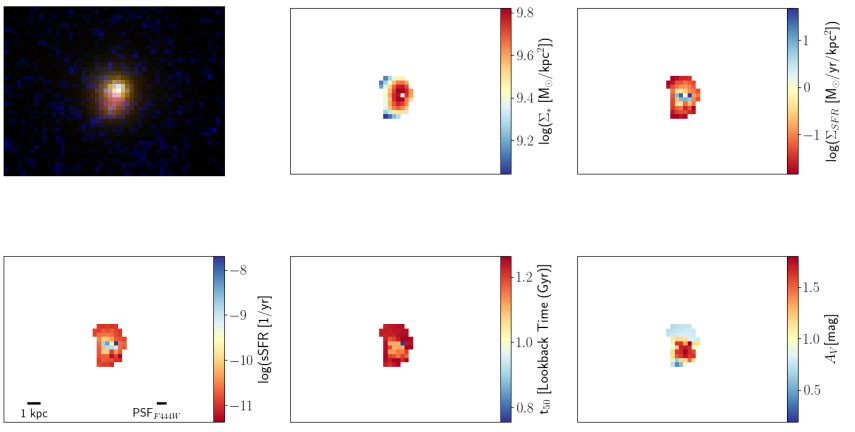

CANUCS - 3200592
$z = 2.78^{+0.01}_{-0.01}$
$\log(M_*/M_\odot) = 10.36^{+0.00}_{-0.00}$
$SFR_{100} = 10.68^{+0.24}_{-0.00}$ $M_\odot$/yr
$\log(sSFR/yr) = -9.33^{+0.01}_{-0.00}$
Δ MS = $0.00^{+0.01}_{-0.00}$ dex
$t_{50} = 1.45^{+0.00}_{-0.00}$ Gyr
$SFR_{10}/SFR_{100} = 0.864^{+0.08}_{-0.03}$

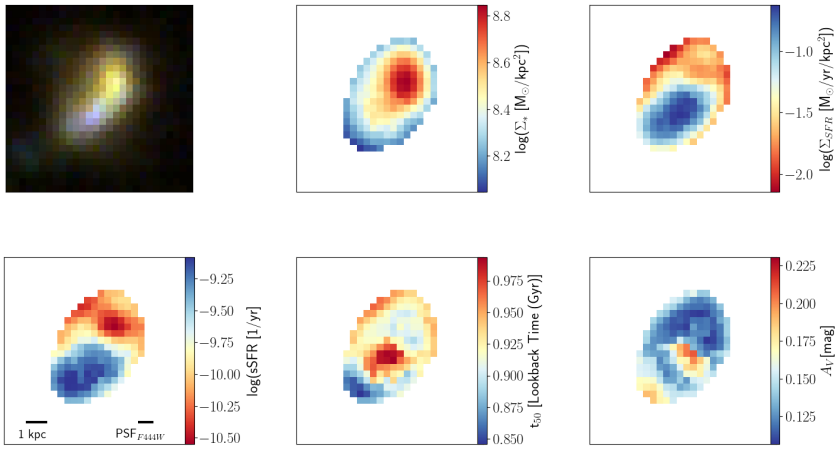

CANUCS - 3200594
$z = 2.92^{+0.02}_{-0.01}$
$\log(M_*/M_\odot) = 9.70^{+0.07}_{-0.14}$
$SFR_{100} = 1.23^{+1.22}_{-0.48}$ $M_\odot$/yr
$\log(sSFR/yr) = -9.61^{+0.23}_{-0.07}$
Δ MS $= -0.53^{+0.30}_{-0.23}$ dex
$t_{50} = 0.37^{+0.19}_{-0.14}$ Gyr
$SFR_{10}/SFR_{100} = 0.999^{+0.00}_{-nan}$

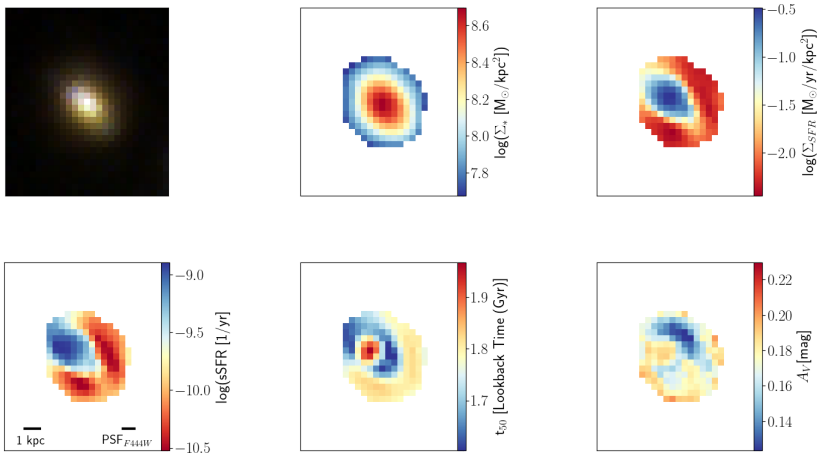

CANUCS - 3200620
$z = 1.59^{+0.02}_{-0.02}$
$\log(M_*/M_\odot) = 9.47^{+0.05}_{-0.07}$
$SFR_{100} = 0.99^{+0.26}_{-0.22}$ $M_\odot$/yr
$\log(sSFR/yr) = -9.48^{+0.06}_{-0.04}$
Δ MS $= -0.22^{+0.11}_{-0.12}$ dex
$t_{50} = 1.62^{+0.96}_{-0.57}$ Gyr
$SFR_{10}/SFR_{100} = 0.988^{+0.00}_{-0.00}$

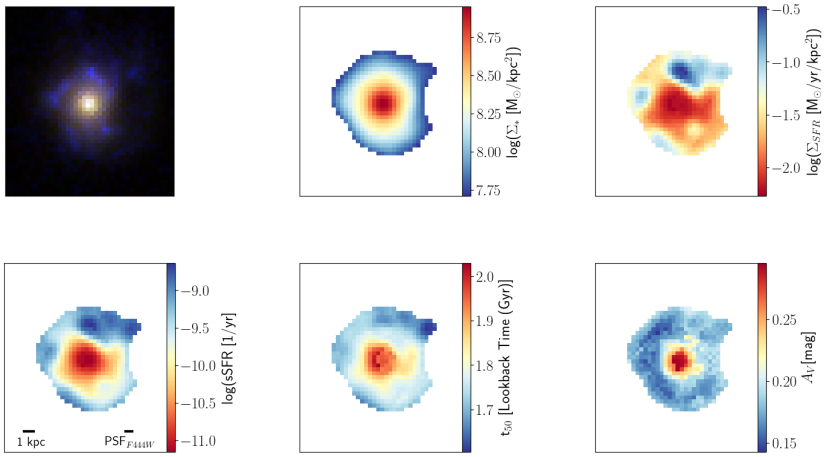

CANUCS - 3200639
$z = 1.64^{+0.05}_{-0.03}$
$\log(M_*/M_\odot) = 10.02^{+0.08}_{-0.06}$
$SFR_{100} = 2.65^{+0.24}_{-0.37}$ $M_\odot$/yr
$\log(sSFR/yr) = -9.60^{+0.04}_{-0.00}$
Δ MS $= -0.19^{+0.06}_{-0.08}$ dex
$t_{50} = 2.06^{+0.54}_{-0.19}$ Gyr
$SFR_{10}/SFR_{100} = 0.985^{+0.00}_{-0.00}$

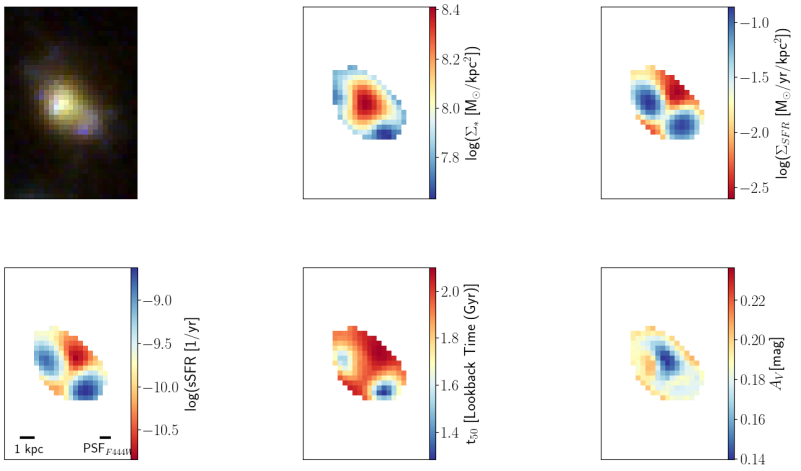

CANUCS - 3200689
$z = 1.37^{+0.03}_{-0.01}$
$\log(M_*/M_\odot) = 9.31^{+0.04}_{-0.08}$
$SFR_{100} = 0.72^{+0.20}_{-0.16}$ $M_\odot$/yr
$\log(sSFR/yr) = -9.46^{+0.06}_{-0.03}$
Δ MS = $-0.13^{+0.11}_{-0.12}$ dex
$t_{50} = 2.23^{+0.46}_{-0.92}$ Gyr
$SFR_{10}/SFR_{100} = 0.995^{+0.00}_{-0.00}$

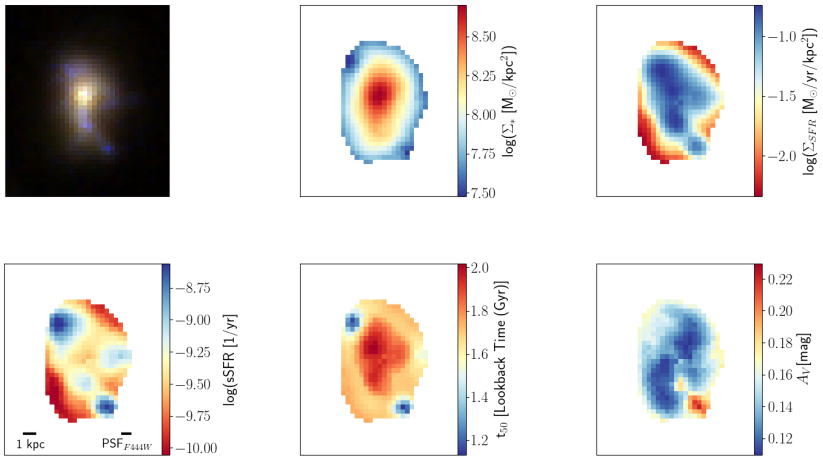

CANUCS - 3200754
$z = 1.59^{+0.01}_{-0.02}$
$\log(M_*/M_\odot) = 9.79^{+0.06}_{-0.16}$
$SFR_{100} = 3.12^{+0.58}_{-0.18}$ $M_\odot$/yr
$\log(sSFR/yr) = -9.30^{+0.02}_{-0.14}$
Δ MS = $0.06^{+0.08}_{-0.12}$ dex
$t_{50} = 2.45^{+0.16}_{-1.13}$ Gyr
$SFR_{10}/SFR_{100} = 1.000^{+0.00}_{-0.00}$

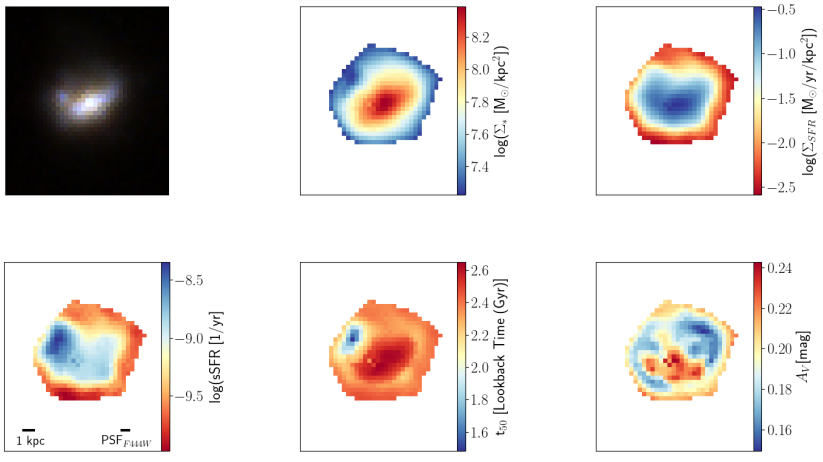

CANUCS - 3200938
$z = 1.09^{+0.00}_{-0.04}$
$\log(M_*/M_\odot) = 9.49^{+0.15}_{-0.00}$
$SFR_{100} = 3.30^{+0.01}_{-0.76}$ $M_\odot$/yr
$\log(sSFR/yr) = -8.97^{+0.15}_{-0.11}$
Δ MS = $0.56^{+0.11}_{-0.11}$ dex
$t_{50} = 2.50^{+0.73}_{-1.32}$ Gyr
$SFR_{10}/SFR_{100} = 0.991^{+0.00}_{-0.00}$

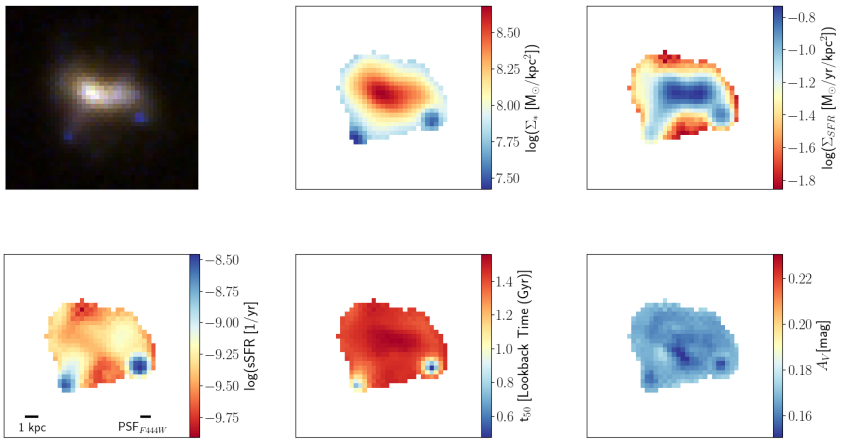

CANUCS - 3200958
$z = 1.79^{+0.10}_{-0.05}$
$\log(M_*/M_\odot) = 9.80^{+0.07}_{-0.09}$
$SFR_{100} = 3.03^{+0.81}_{-0.64}\ M_\odot/yr$
$\log(sSFR/yr) = -9.32^{+0.03}_{-0.01}$
$\Delta\ MS = -0.04^{+0.11}_{-0.12}$ dex
$t_{50} = 1.76^{+0.89}_{-0.52}$ Gyr
$SFR_{10}/SFR_{100} = 1.080^{+0.03}_{-0.04}$

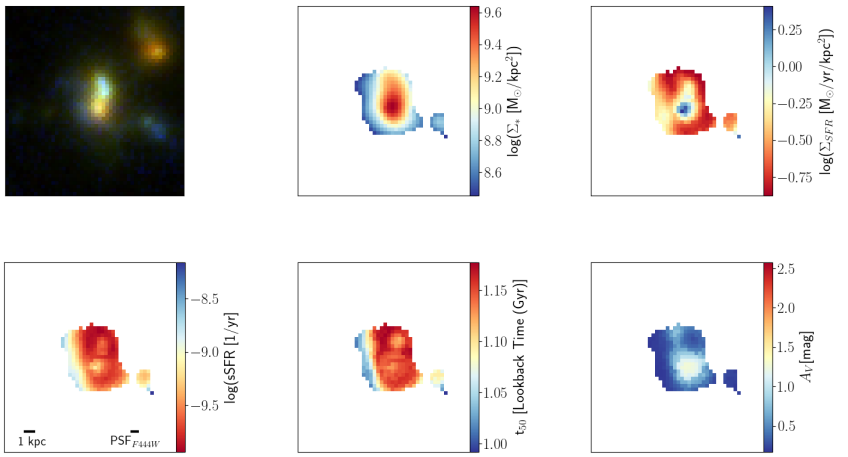

CANUCS - 3201552
$z = 2.93^{+0.02}_{-0.02}$
$\log(M_*/M_\odot) = 10.51^{+0.04}_{-0.06}$
$SFR_{100} = 10.23^{+7.16}_{-3.65}\ M_\odot/yr$
$\log(sSFR/yr) = -9.50^{+0.19}_{-0.13}$
$\Delta\ MS = -0.11^{+0.23}_{-0.20}$ dex
$t_{50} = 1.14^{+0.45}_{-0.45}$ Gyr
$SFR_{10}/SFR_{100} = 0.990^{+0.00}_{-0.01}$

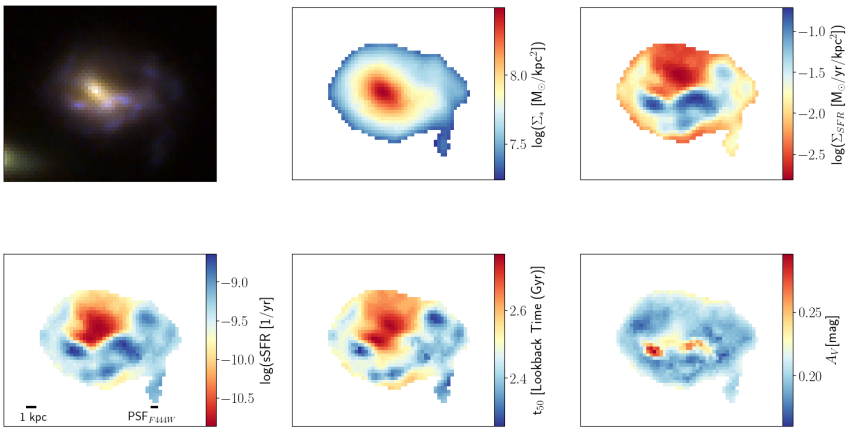

CANUCS - 3201587
$z = 1.03^{+0.01}_{-0.04}$
$\log(M_*/M_\odot) = 9.80^{+0.08}_{-0.02}$
$SFR_{100} = 2.58^{+0.68}_{-0.23}\ M_\odot/yr$
$\log(sSFR/yr) = -9.39^{+0.02}_{-0.02}$
$\Delta\ MS = 0.27^{+0.12}_{-0.04}$ dex
$t_{50} = 3.32^{+1.19}_{-0.92}$ Gyr
$SFR_{10}/SFR_{100} = 0.998^{+0.01}_{-0.02}$

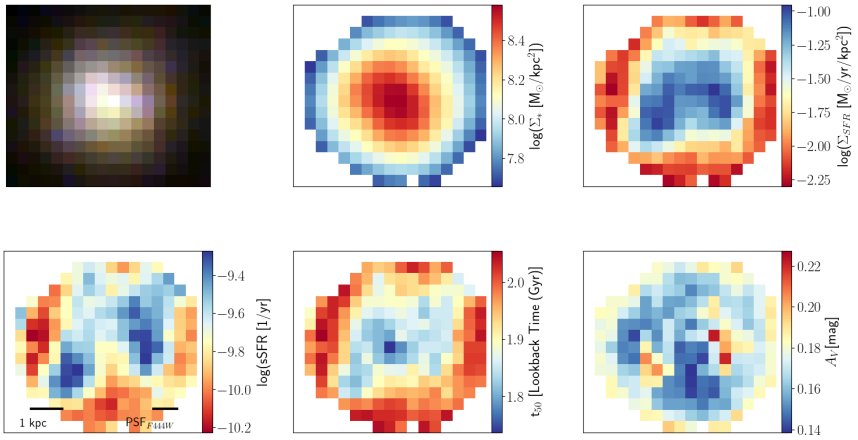

CANUCS - 4100061
$z = 1.31^{+0.03}_{-0.09}$
$\log(M_*/M_\odot) = 9.48^{+0.06}_{-0.08}$
$SFR_{100} = 0.70^{+0.32}_{-0.27}$ $M_\odot$/yr
$\log(sSFR/yr) = -9.63^{+0.10}_{-0.13}$
Δ MS = $-0.24^{+0.17}_{-0.22}$ dex
$t_{50} = 2.16^{+1.02}_{-0.95}$ Gyr
$SFR_{10}/SFR_{100} = 0.992^{+0.00}_{-0.00}$

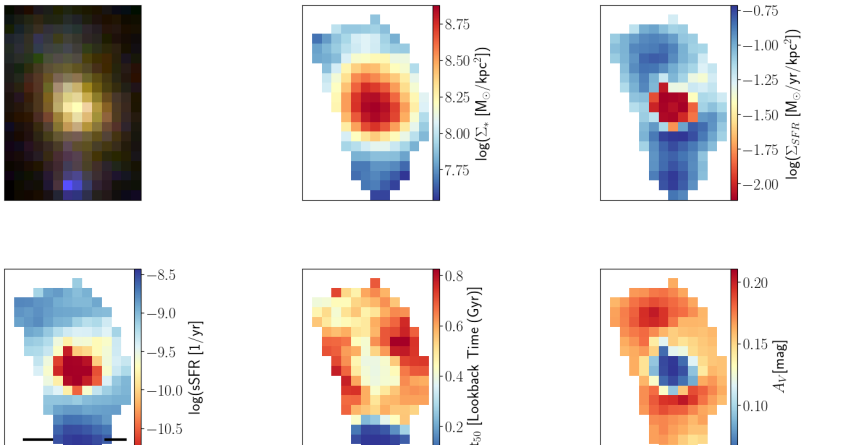

CANUCS - 4100185
$z = 2.67^{+0.07}_{-0.06}$
$\log(M_*/M_\odot) = 9.47^{+0.05}_{-0.11}$
$SFR_{100} = 1.41^{+0.25}_{-0.90}$ $M_\odot$/yr
$\log(sSFR/yr) = -9.32^{+0.02}_{-0.33}$
Δ MS = $-0.33^{+0.07}_{-0.44}$ dex
$t_{50} = 0.27^{+0.03}_{-0.04}$ Gyr
$SFR_{10}/SFR_{100} = 1.000^{+0.06}_{-0.00}$

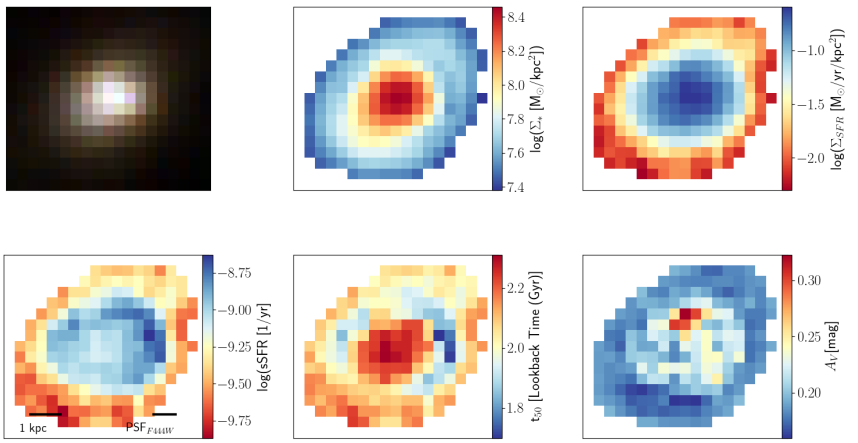

CANUCS - 4100213
$z = 1.16^{+0.03}_{-0.01}$
$\log(M_*/M_\odot) = 9.18^{+0.10}_{-0.07}$
$SFR_{100} = 1.28^{+0.26}_{-0.15}$ $M_\odot$/yr
$\log(sSFR/yr) = -9.07^{+0.02}_{-0.01}$
Δ MS = $0.33^{+0.11}_{-0.07}$ dex
$t_{50} = 2.48^{+0.78}_{-0.63}$ Gyr
$SFR_{10}/SFR_{100} = 1.011^{+0.00}_{-0.00}$

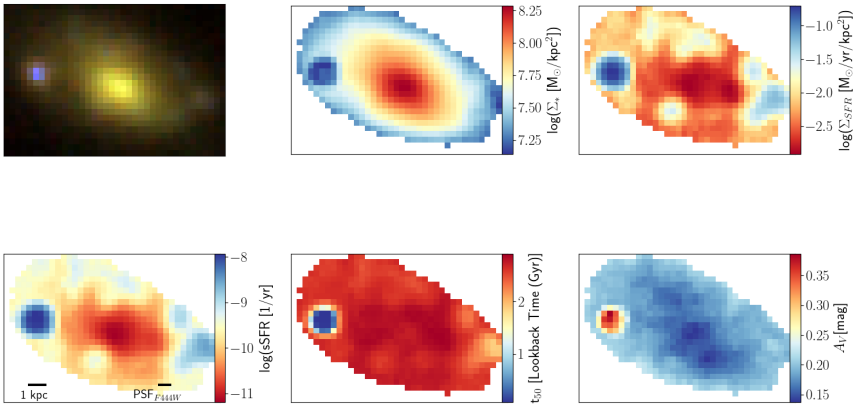

CANUCS - 4100234
$z = 0.90^{+0.03}_{-0.10}$
$\log(M_*/M_\odot) = 9.50^{+0.06}_{-0.06}$
$SFR_{100} = 0.84^{+0.26}_{-0.24}\ M_\odot/yr$
$\log(sSFR/yr) = -9.57^{+0.05}_{-0.08}$
Δ MS $= 0.09^{+0.13}_{-0.15}$ dex
$t_{50} = 2.99^{+1.31}_{-0.80}$ Gyr
$SFR_{10}/SFR_{100} = 0.992^{+0.00}_{-0.01}$

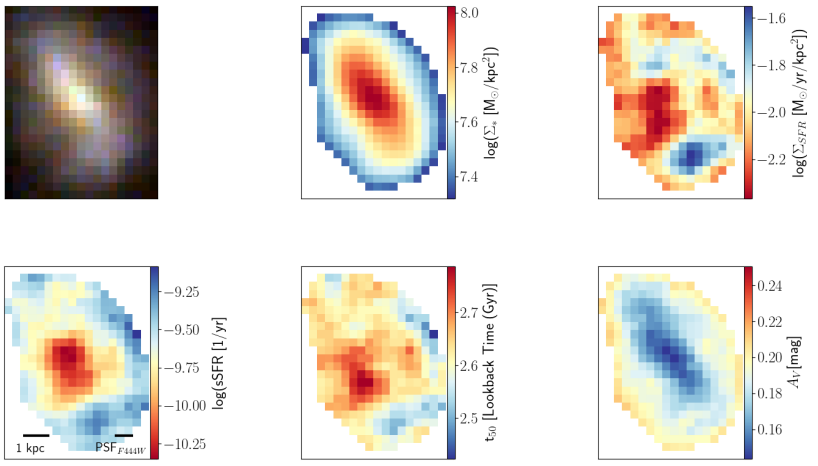

CANUCS - 4100257
$z = 0.89^{+0.03}_{-0.10}$
$\log(M_*/M_\odot) = 9.12^{+0.08}_{-0.06}$
$SFR_{100} = 0.29^{+0.15}_{-0.11}\ M_\odot/yr$
$\log(sSFR/yr) = -9.66^{+0.10}_{-0.14}$
Δ MS $= -0.09^{+0.19}_{-0.21}$ dex
$t_{50} = 2.82^{+1.32}_{-1.14}$ Gyr
$SFR_{10}/SFR_{100} = 0.995^{+0.00}_{-0.00}$

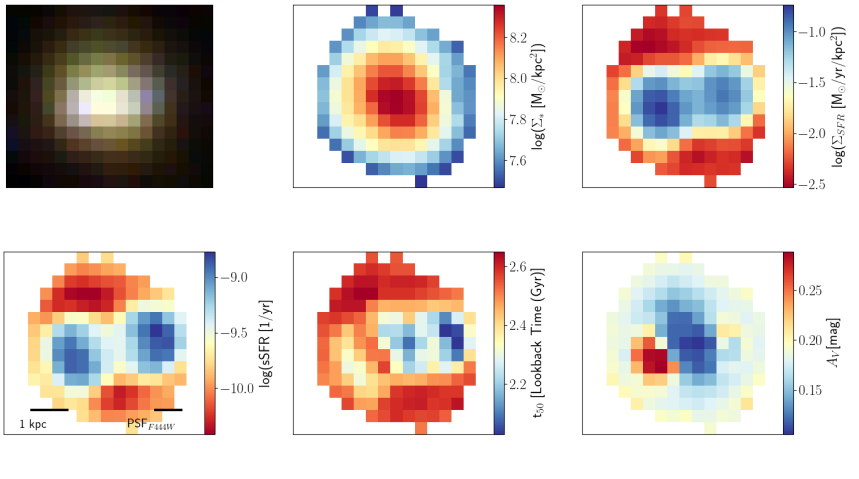

CANUCS - 4100331
$z = 0.99^{+0.03}_{-0.03}$
$\log(M_*/M_\odot) = 9.11^{+0.06}_{-0.10}$
$SFR_{100} = 0.52^{+0.23}_{-0.11}\ M_\odot/yr$
$\log(sSFR/yr) = -9.39^{+0.10}_{-0.00}$
Δ MS $= 0.10^{+0.16}_{-0.13}$ dex
$t_{50} = 3.23^{+0.64}_{-0.87}$ Gyr
$SFR_{10}/SFR_{100} = 0.996^{+0.00}_{-0.00}$

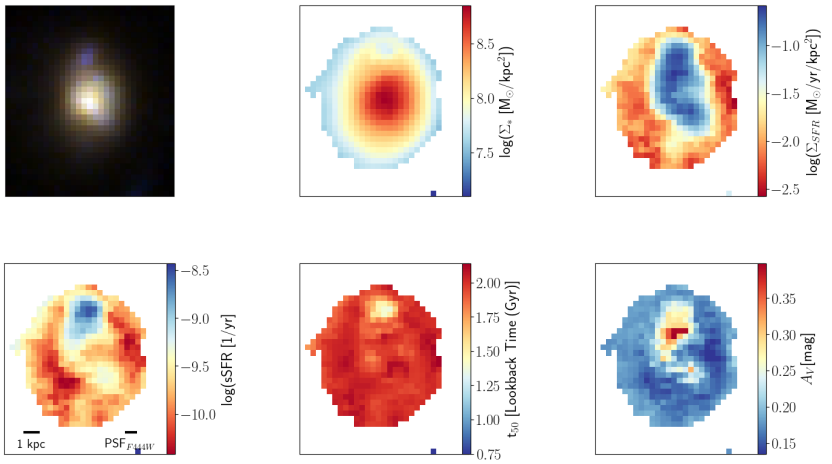

CANUCS - 4100334
$z = 1.32^{+0.13}_{-0.03}$
$\log(M_*/M_\odot) = 9.89^{+0.07}_{-0.06}$
$SFR_{100} = 2.31^{+0.86}_{-0.52}$ $M_\odot$/yr
$\log(sSFR/yr) = -9.52^{+0.07}_{-0.05}$
Δ MS = $-0.01^{+0.15}_{-0.12}$ dex
$t_{50} = 1.88^{+1.00}_{-0.22}$ Gyr
$SFR_{10}/SFR_{100} = 0.976^{+0.00}_{-0.00}$

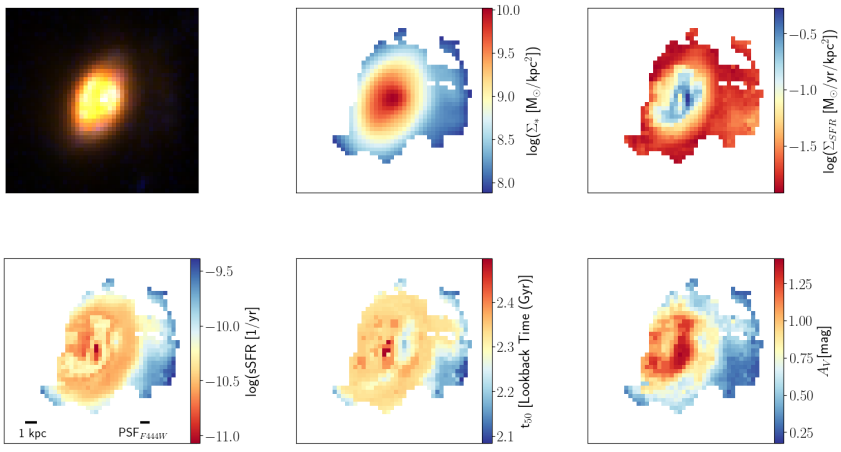

CANUCS - 4100363
$z = 1.46^{+0.06}_{-0.03}$
$\log(M_*/M_\odot) = 10.95^{+0.02}_{-0.04}$
$SFR_{100} = 3.54^{+1.91}_{-3.51}$ $M_\odot$/yr
$\log(sSFR/yr) = -10.40^{+0.17}_{-2.03}$
Δ MS = $-0.64^{+0.19}_{-2.07}$ dex
$t_{50} = 2.06^{+0.58}_{-0.47}$ Gyr
$SFR_{10}/SFR_{100} = 0.998^{+0.00}_{-0.00}$

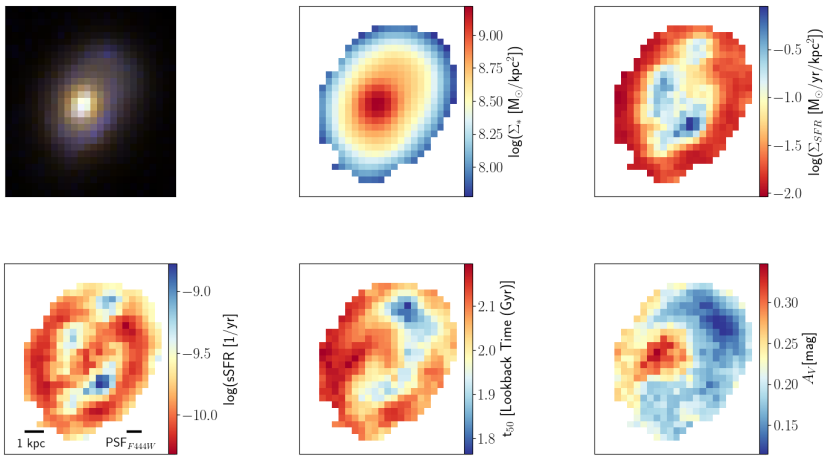

CANUCS - 4100374
$z = 1.44^{+0.02}_{-0.15}$
$\log(M_*/M_\odot) = 10.18^{+0.11}_{-0.05}$
$SFR_{100} = 3.06^{+1.29}_{-1.13}$ $M_\odot$/yr
$\log(sSFR/yr) = -9.69^{+0.04}_{-0.15}$
Δ MS = $-0.15^{+0.17}_{-0.20}$ dex
$t_{50} = 2.40^{+0.68}_{-0.57}$ Gyr
$SFR_{10}/SFR_{100} = 0.988^{+0.00}_{-0.00}$

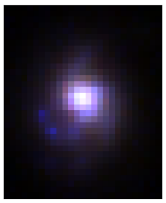

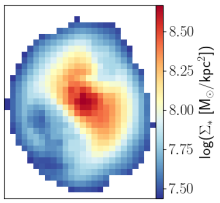

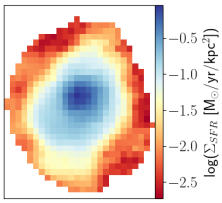

CANUCS - 4100403
$z = 1.21^{+0.08}_{-0.03}$
$\log(M_*/M_\odot) = 9.74^{+0.11}_{-0.08}$
$SFR_{100} = 4.78^{+1.12}_{-0.47}$ $M_\odot$/yr
$\log(sSFR/yr) = -9.06^{+0.02}_{-0.03}$
Δ MS $= 0.46^{+0.12}_{-0.07}$ dex
$t_{50} = 2.73^{+0.26}_{-1.23}$ Gyr
$SFR_{10}/SFR_{100} = 0.960^{+0.02}_{-0.00}$

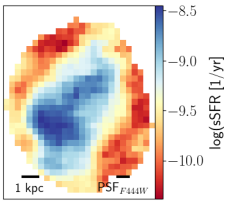

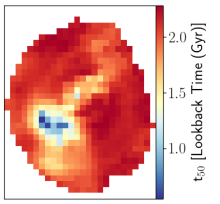

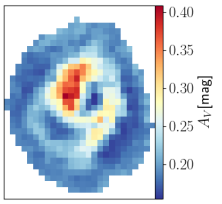

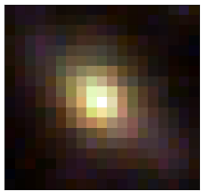

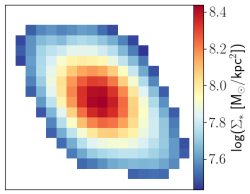

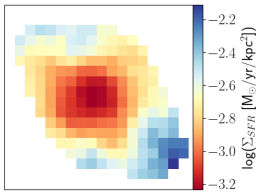

CANUCS - 4100429
$z = 0.78^{+0.04}_{-0.10}$
$\log(M_*/M_\odot) = 9.10^{+0.07}_{-0.07}$
$SFR_{100} = 0.03^{+0.09}_{-0.03}$ $M_\odot$/yr
$\log(sSFR/yr) = -10.58^{+0.50}_{-1.89}$
Δ MS $= -0.94^{+0.58}_{-1.95}$ dex
$t_{50} = 2.77^{+1.31}_{-1.43}$ Gyr
$SFR_{10}/SFR_{100} = 1.003^{+0.01}_{-0.00}$

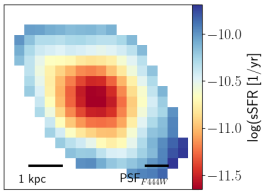

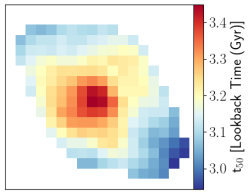

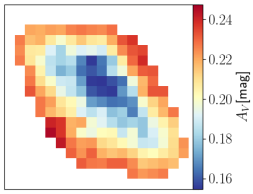

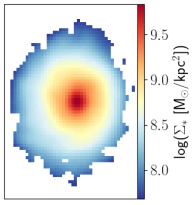

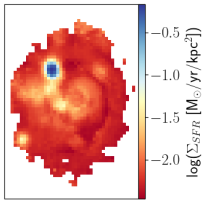

CANUCS - 4100524
$z = 1.43^{+0.03}_{-0.09}$
$\log(M_*/M_\odot) = 10.95^{+0.07}_{-0.07}$
$SFR_{100} = 2.07^{+2.50}_{-2.06}$ $M_\odot$/yr
$\log(sSFR/yr) = -10.64^{+0.27}_{-2.15}$
Δ MS $= -0.86^{+0.35}_{-2.22}$ dex
$t_{50} = 2.05^{+0.99}_{-0.62}$ Gyr
$SFR_{10}/SFR_{100} = 0.993^{+0.00}_{-0.00}$

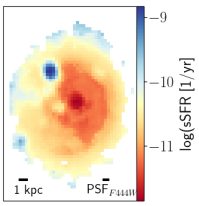

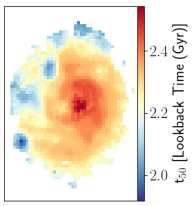

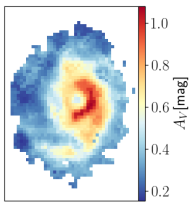

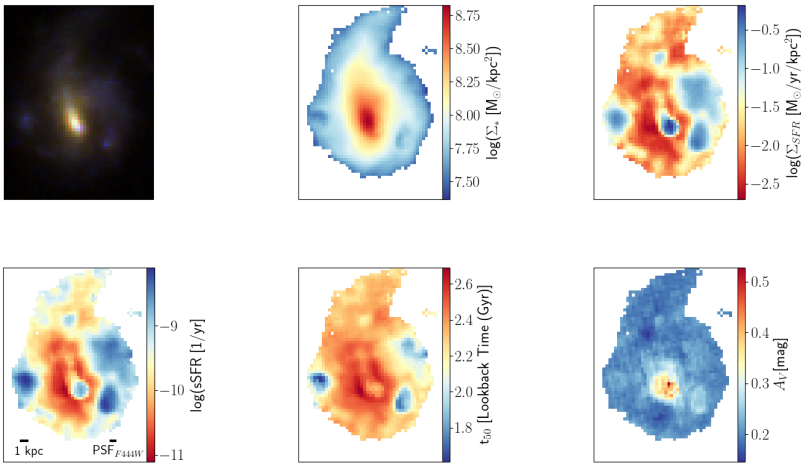

CANUCS - 4100557
z = $1.15^{+0.06}_{-0.01}$
log (M$_*$/M$_\odot$) = $10.26^{+0.07}_{-0.06}$
SFR$_{100}$ = $8.68^{+5.42}_{-2.31}$ M$_\odot$/yr
log(sSFR/yr) = $-9.32^{+0.15}_{-0.07}$
Δ MS = $0.39^{+0.22}_{-0.14}$ dex
t$_{50}$ = $2.65^{+0.59}_{-0.87}$ Gyr
SFR$_{10}$/SFR$_{100}$ = $0.997^{+0.00}_{-0.00}$

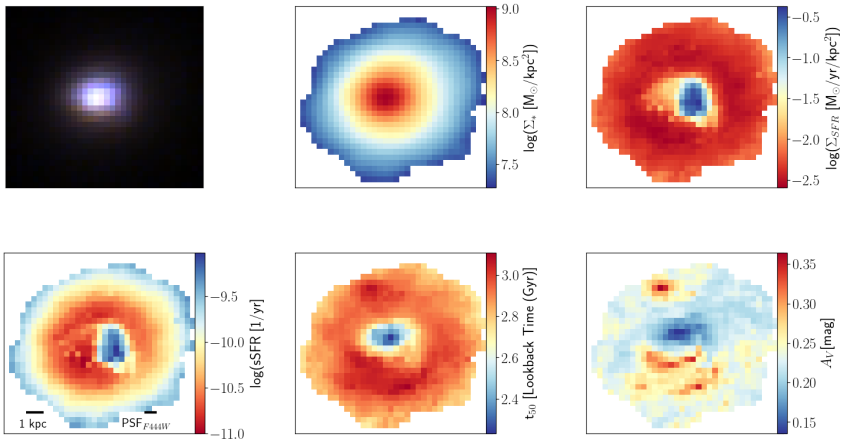

CANUCS - 4100598
z = $0.93^{+0.05}_{-0.09}$
log (M$_*$/M$_\odot$) = $9.96^{+0.07}_{-0.02}$
SFR$_{100}$ = $1.04^{+0.43}_{-0.37}$ M$_\odot$/yr
log(sSFR/yr) = $-9.95^{+0.08}_{-0.16}$
Δ MS = $-0.18^{+0.16}_{-0.19}$ dex
t$_{50}$ = $2.95^{+0.72}_{-0.73}$ Gyr
SFR$_{10}$/SFR$_{100}$ = $0.974^{+0.00}_{-0.00}$

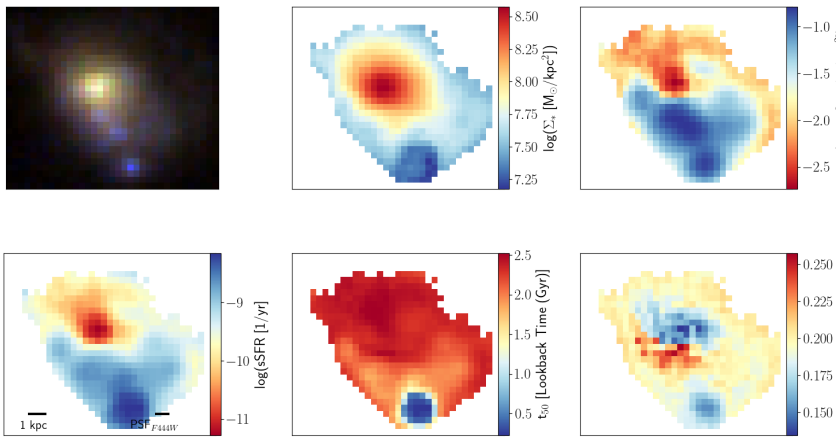

CANUCS - 4100697
z = $1.03^{+0.02}_{-0.09}$
log (M$_*$/M$_\odot$) = $9.61^{+0.06}_{-0.03}$
SFR$_{100}$ = $2.24^{+0.93}_{-0.47}$ M$_\odot$/yr
log(sSFR/yr) = $-9.26^{+0.09}_{-0.07}$
Δ MS = $0.34^{+0.16}_{-0.11}$ dex
t$_{50}$ = $3.19^{+0.23}_{-0.69}$ Gyr
SFR$_{10}$/SFR$_{100}$ = $0.998^{+0.00}_{-0.00}$

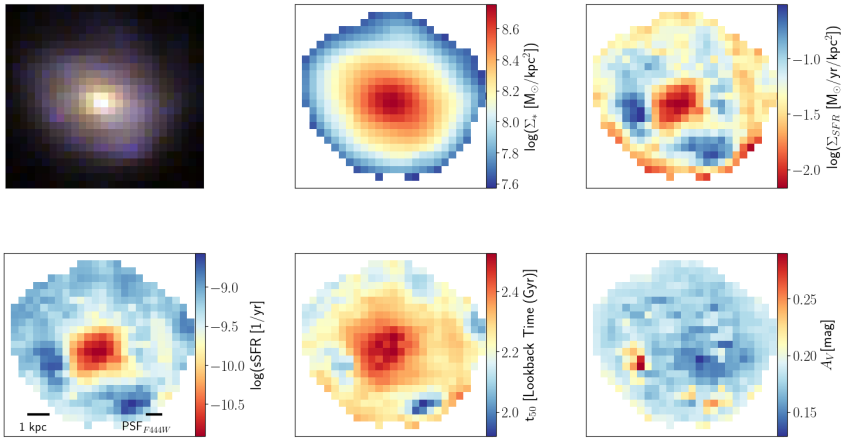

CANUCS - 4100784
$z = 1.15^{+0.07}_{-0.06}$
$\log(M_*/M_\odot) = 9.85^{+0.05}_{-0.05}$
$SFR_{100} = 2.93^{+0.22}_{-0.77}$ $M_\odot$/yr
$\log(sSFR/yr) = -9.39^{+0.02}_{-0.08}$
Δ MS $= 0.21^{+0.05}_{-0.14}$ dex
$t_{50} = 2.67^{+0.88}_{-0.63}$ Gyr
$SFR_{10}/SFR_{100} = 0.961^{+0.02}_{-0.01}$

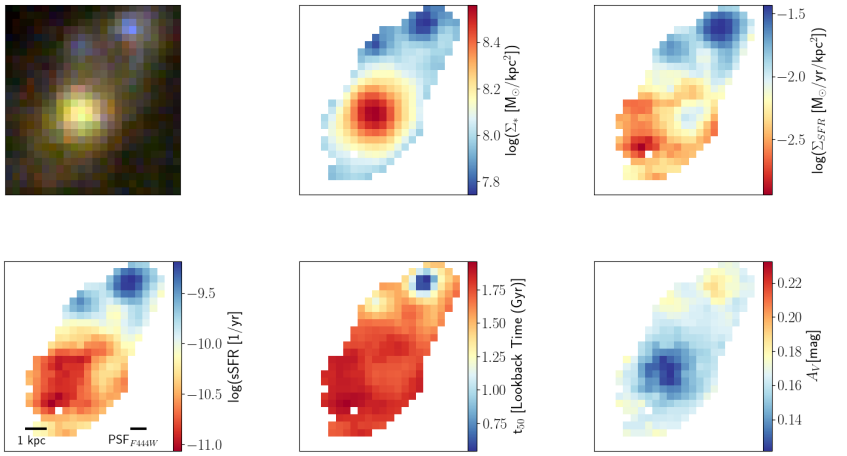

CANUCS - 4100788
$z = 1.44^{+0.05}_{-0.12}$
$\log(M_*/M_\odot) = 9.61^{+0.06}_{-0.06}$
$SFR_{100} = 0.27^{+0.36}_{-0.27}$ $M_\odot$/yr
$\log(sSFR/yr) = -10.18^{+0.31}_{-2.17}$
Δ MS $= -0.81^{+0.37}_{-2.24}$ dex
$t_{50} = 1.58^{+1.15}_{-0.83}$ Gyr
$SFR_{10}/SFR_{100} = 0.993^{+0.02}_{-0.00}$

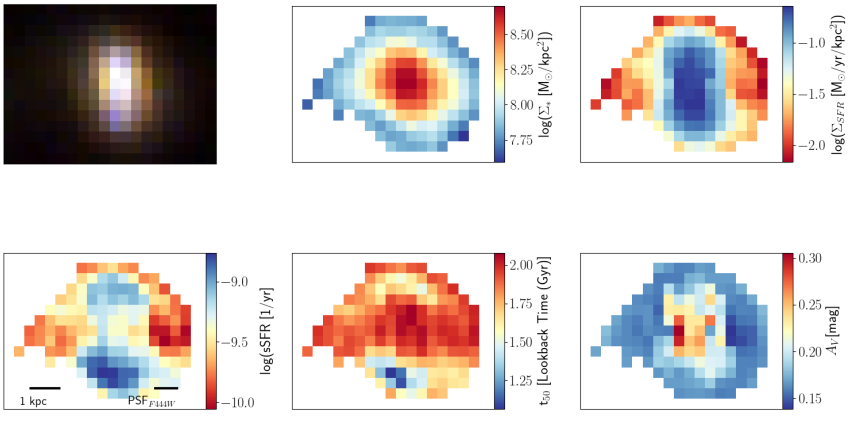

CANUCS - 4100819
$z = 1.27^{+0.06}_{-0.10}$
$\log(M_*/M_\odot) = 9.37^{+0.11}_{-0.09}$
$SFR_{100} = 1.18^{+0.47}_{-0.17}$ $M_\odot$/yr
$\log(sSFR/yr) = -9.30^{+0.04}_{-0.03}$
Δ MS $= 0.09^{+0.16}_{-0.09}$ dex
$t_{50} = 2.48^{+0.81}_{-0.99}$ Gyr
$SFR_{10}/SFR_{100} = 0.996^{+0.02}_{-0.00}$

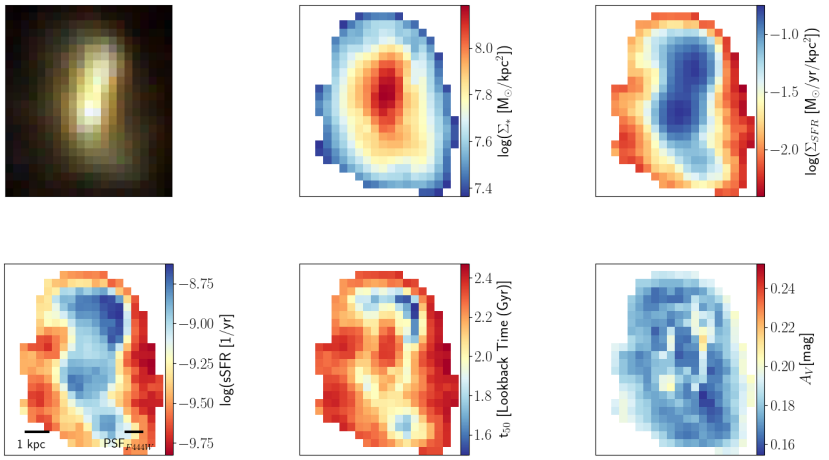

CANUCS - 4100833
$z = 1.02^{+0.06}_{-0.03}$
$\log(M_*/M_\odot) = 9.27^{+0.11}_{-0.20}$
$SFR_{100} = 1.58^{+0.42}_{-0.25}$ $M_\odot$/yr
$\log(sSFR/yr) = -9.07^{+0.01}_{-0.12}$
Δ MS $= 0.45^{+0.13}_{-0.16}$ dex
$t_{50} = 3.09^{+0.49}_{-2.19}$ Gyr
$SFR_{10}/SFR_{100} = 0.955^{+0.01}_{-0.02}$

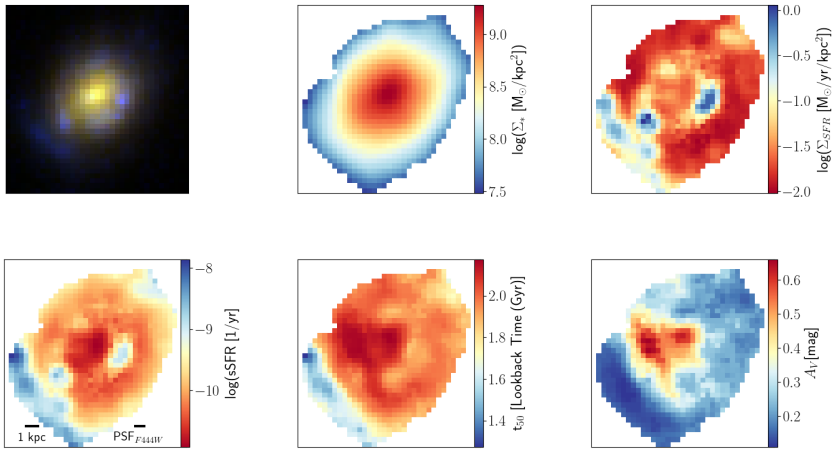

CANUCS - 4100840
$z = 1.59^{+0.04}_{-0.11}$
$\log(M_*/M_\odot) = 10.50^{+0.09}_{-0.03}$
$SFR_{100} = 6.51^{+1.49}_{-1.62}$ $M_\odot$/yr
$\log(sSFR/yr) = -9.68^{+0.00}_{-0.10}$
Δ MS $= -0.11^{+0.11}_{-0.13}$ dex
$t_{50} = 2.21^{+0.48}_{-0.45}$ Gyr
$SFR_{10}/SFR_{100} = 0.997^{+0.01}_{-0.01}$

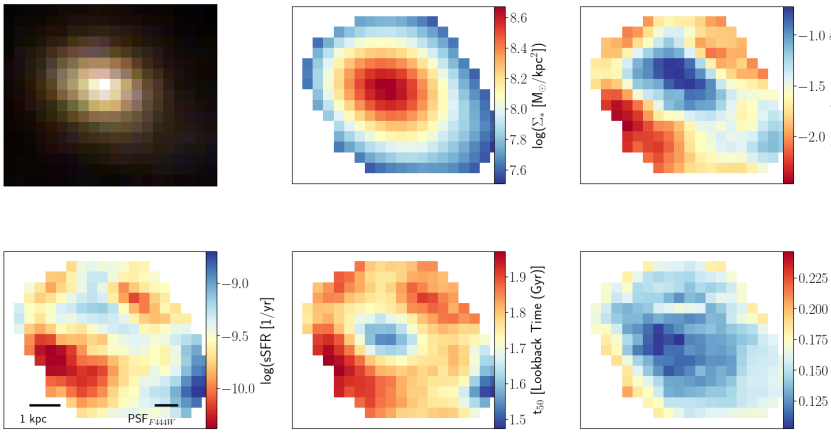

CANUCS - 4100916
$z = 1.48^{+0.06}_{-0.12}$
$\log(M_*/M_\odot) = 9.51^{+0.07}_{-0.08}$
$SFR_{100} = 0.99^{+0.28}_{-0.20}$ $M_\odot$/yr
$\log(sSFR/yr) = -9.51^{+0.03}_{-0.02}$
Δ MS $= -0.19^{+0.12}_{-0.11}$ dex
$t_{50} = 2.01^{+1.14}_{-0.78}$ Gyr
$SFR_{10}/SFR_{100} = 0.993^{+0.00}_{-0.01}$

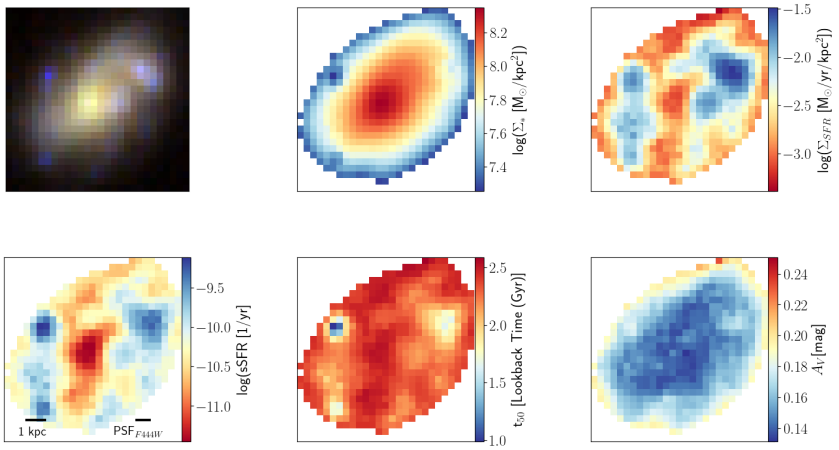

CANUCS - 4100958
$z = 1.01^{+0.04}_{-0.12}$
$\log(M_*/M_\odot) = 9.57^{+0.04}_{-0.07}$
$SFR_{100} = 0.27^{+1.05}_{-0.27}\ M_\odot/yr$
$\log(sSFR/yr) = -10.14^{+0.65}_{-2.84}$
$\Delta\ MS = -0.54^{+0.69}_{-2.90}$ dex
$t_{50} = 0.64^{+1.89}_{-0.07}$ Gyr
$SFR_{10}/SFR_{100} = 1.000^{+0.01}_{-0.00}$

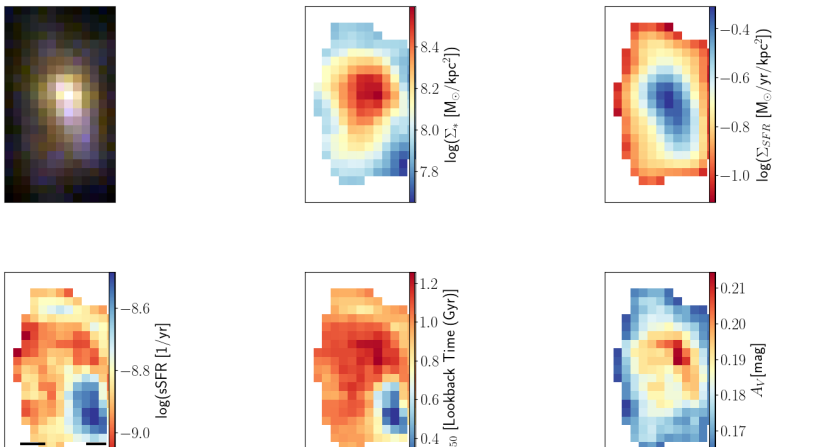

CANUCS - 4100959
$z = 2.04^{+0.10}_{-0.25}$
$\log(M_*/M_\odot) = 9.46^{+0.08}_{-0.26}$
$SFR_{100} = 4.04^{+1.26}_{-1.18}\ M_\odot/yr$
$\log(sSFR/yr) = -8.86^{+0.04}_{-0.11}$
$\Delta\ MS = 0.21^{+0.13}_{-0.22}$ dex
$t_{50} = 1.49^{+0.64}_{-0.59}$ Gyr
$SFR_{10}/SFR_{100} = 1.096^{+0.03}_{-0.02}$

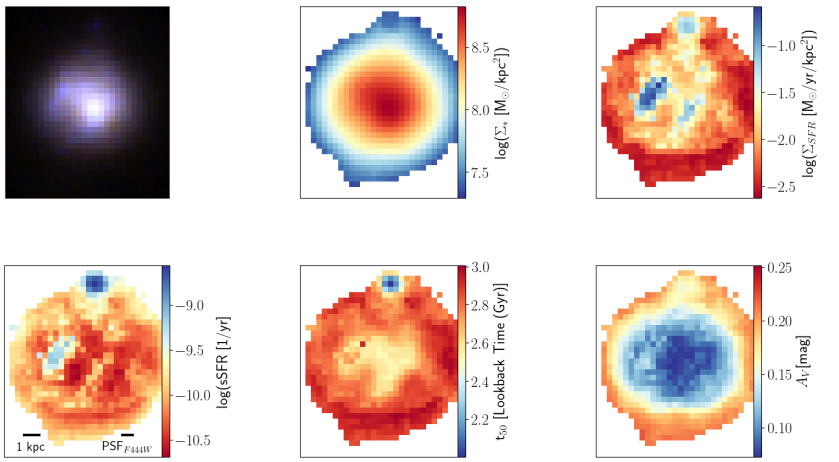

CANUCS - 4100976
$z = 0.89^{+0.05}_{-0.16}$
$\log(M_*/M_\odot) = 9.97^{+0.06}_{-0.04}$
$SFR_{100} = 1.01^{+0.50}_{-0.75}\ M_\odot/yr$
$\log(sSFR/yr) = -9.97^{+0.12}_{-0.56}$
$\Delta\ MS = -0.18^{+0.18}_{-0.60}$ dex
$t_{50} = 3.22^{+0.87}_{-0.45}$ Gyr
$SFR_{10}/SFR_{100} = 0.981^{+0.00}_{-0.00}$

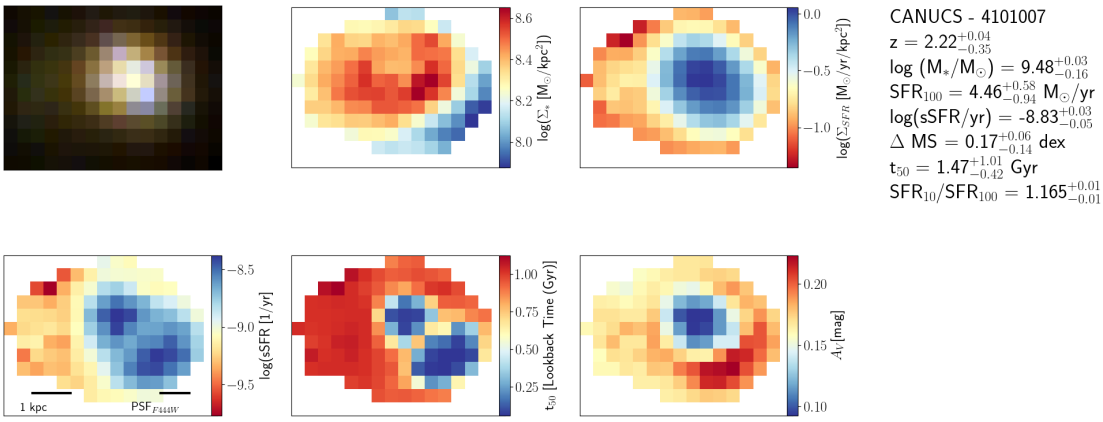

CANUCS - 4101007
$z = 2.22^{+0.04}_{-0.35}$
$\log(M_*/M_\odot) = 9.48^{+0.03}_{-0.16}$
$SFR_{100} = 4.46^{+0.58}_{-0.94}\ M_\odot/yr$
$\log(sSFR/yr) = -8.83^{+0.03}_{-0.05}$
$\Delta\ MS = 0.17^{+0.06}_{-0.14}$ dex
$t_{50} = 1.47^{+1.01}_{-0.42}$ Gyr
$SFR_{10}/SFR_{100} = 1.165^{+0.01}_{-0.01}$

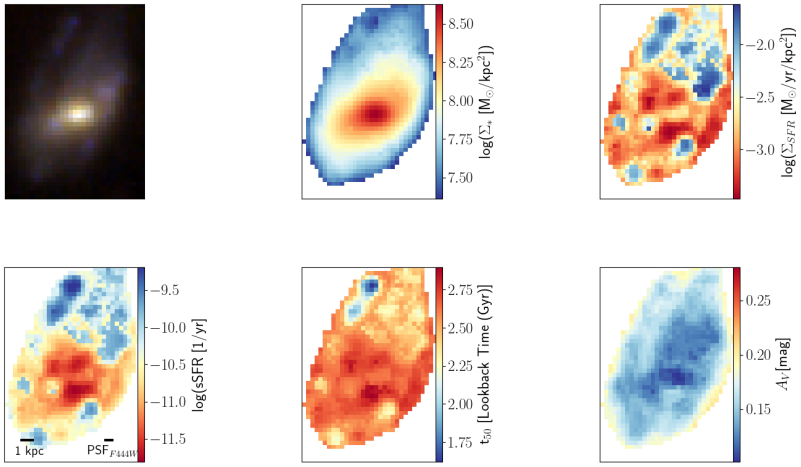

CANUCS - 4101041
$z = 0.93^{+0.06}_{-0.17}$
$\log(M_*/M_\odot) = 9.91^{+0.09}_{-0.06}$
$SFR_{100} = 0.34^{+1.04}_{-0.33}$ $M_\odot$/yr
$\log(sSFR/yr) = -10.38^{+0.53}_{-2.03}$
Δ MS = $-0.63^{+0.62}_{-2.09}$ dex
$t_{50} = 2.12^{+1.27}_{-1.13}$ Gyr
$SFR_{10}/SFR_{100} = 0.994^{+0.00}_{-0.03}$

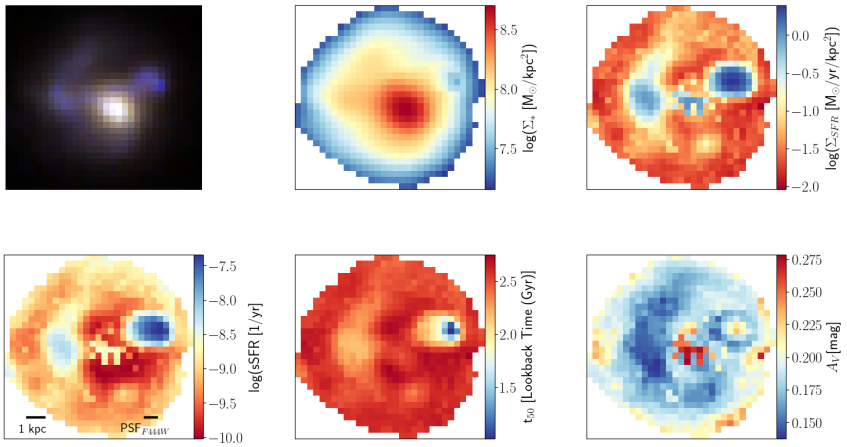

CANUCS - 4101071
$z = 1.03^{+0.07}_{-0.14}$
$\log(M_*/M_\odot) = 9.79^{+0.00}_{-0.01}$
$SFR_{100} = 9.83^{+0.08}_{-0.00}$ $M_\odot$/yr
$\log(sSFR/yr) = -8.80^{+0.00}_{-0.01}$
Δ MS = $0.86^{+0.00}_{-0.00}$ dex
$t_{50} = 1.32^{+0.00}_{-0.01}$ Gyr
$SFR_{10}/SFR_{100} = 0.927^{+0.03}_{-0.03}$

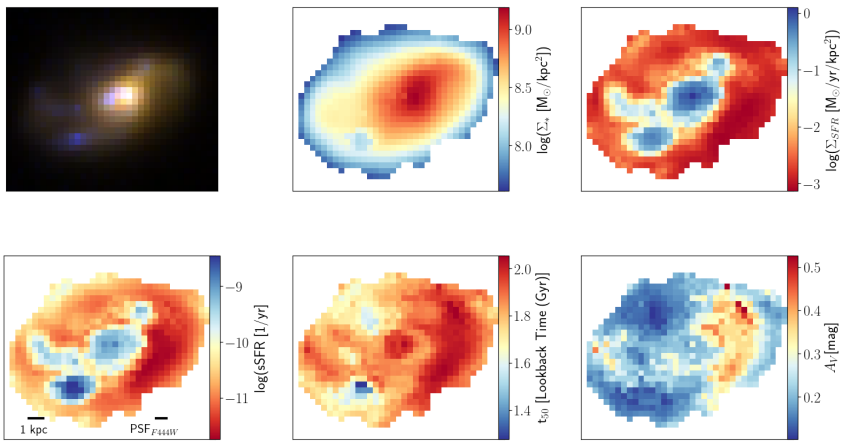

CANUCS - 4101086
$z = 1.66^{+0.16}_{-0.17}$
$\log(M_*/M_\odot) = 10.40^{+0.04}_{-0.01}$
$SFR_{100} = 4.05^{+1.98}_{-0.12}$ $M_\odot$/yr
$\log(sSFR/yr) = -9.79^{+0.13}_{-0.00}$
Δ MS = $-0.27^{+0.17}_{-0.01}$ dex
$t_{50} = 1.27^{+0.85}_{-0.22}$ Gyr
$SFR_{10}/SFR_{100} = 0.977^{+0.01}_{-0.01}$

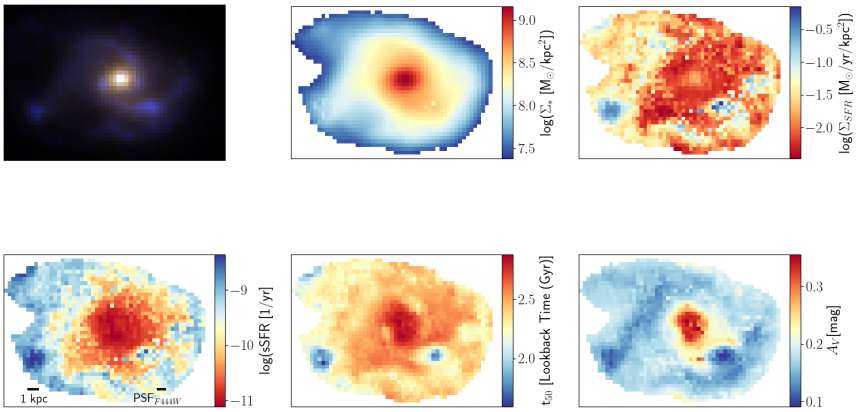

CANUCS - 4101185
z = $1.10^{+0.07}_{-0.15}$
log ($M_*/M_\odot$) = $10.40^{+0.05}_{-0.06}$
SFR_{100} = $5.31^{+3.12}_{-4.28}$ $M_\odot$/yr
log(sSFR/yr) = $-9.67^{+0.15}_{-0.65}$
Δ MS = $0.11^{+0.20}_{-0.71}$ dex
t_{50} = $2.47^{+0.81}_{-0.87}$ Gyr
SFR_{10}/SFR_{100} = $0.994^{+0.00}_{-0.01}$

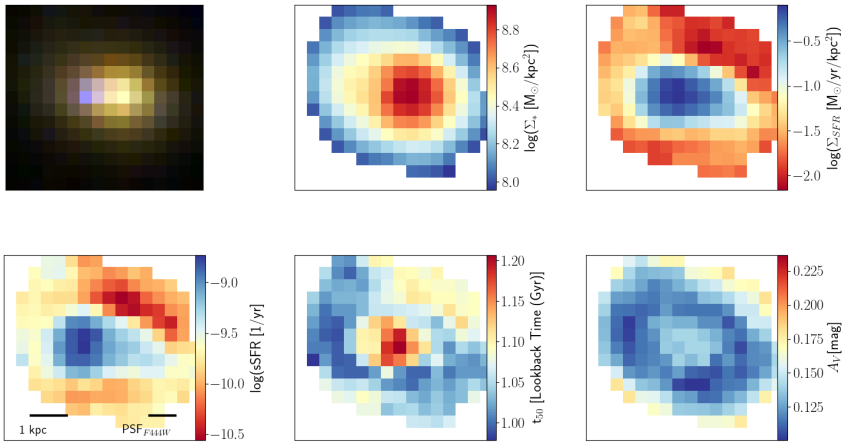

CANUCS - 4200021
z = $2.55^{+0.06}_{-0.06}$
log ($M_*/M_\odot$) = $9.64^{+0.02}_{-0.06}$
SFR_{100} = $1.87^{+1.01}_{-0.93}$ $M_\odot$/yr
log(sSFR/yr) = $-9.37^{+0.16}_{-0.24}$
Δ MS = $-0.32^{+0.19}_{-0.30}$ dex
t_{50} = $0.90^{+0.66}_{-0.33}$ Gyr
SFR_{10}/SFR_{100} = $0.910^{+0.08}_{-0.00}$

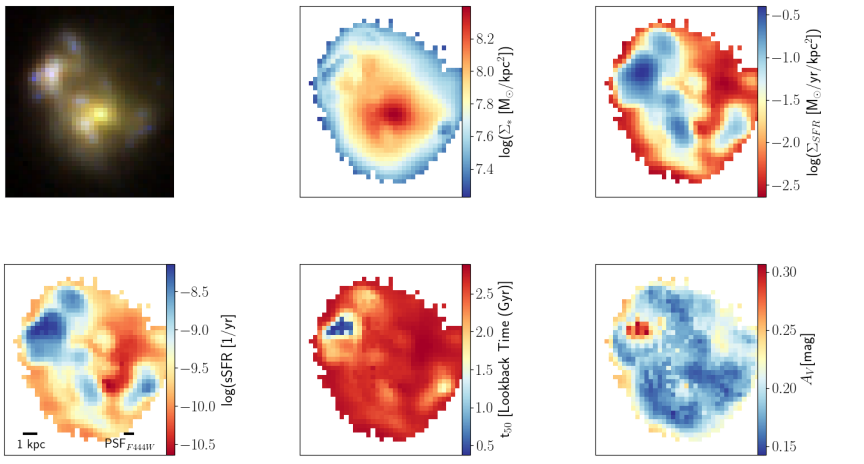

CANUCS - 4200059
z = $0.93^{+0.02}_{-0.06}$
log ($M_*/M_\odot$) = $9.79^{+0.00}_{-0.13}$
SFR_{100} = $4.28^{+0.68}_{-0.02}$ $M_\odot$/yr
log(sSFR/yr) = $-9.16^{+0.06}_{-0.13}$
Δ MS = $0.56^{+0.06}_{-0.10}$ dex
t_{50} = $3.34^{+0.11}_{-0.01}$ Gyr
SFR_{10}/SFR_{100} = $1.034^{+0.00}_{-0.00}$

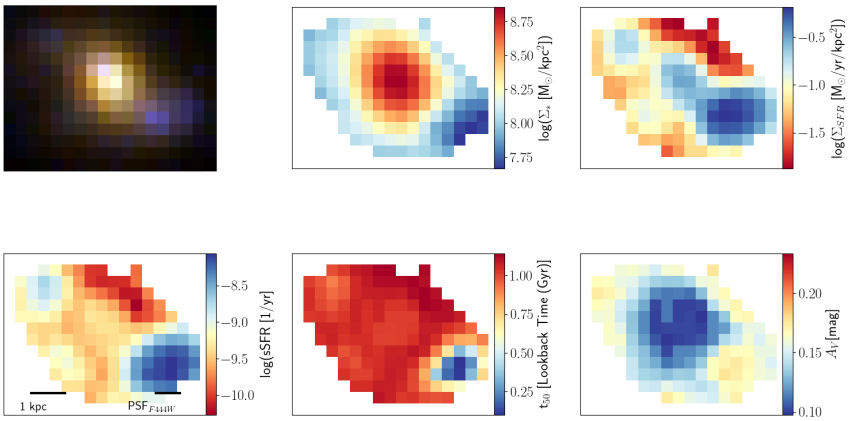

CANUCS - 4200074
$z = 2.54^{+0.07}_{-0.03}$
$\log(M_*/M_\odot) = 9.50^{+0.05}_{-0.06}$
$SFR_{100} = 2.35^{+0.90}_{-0.46}$ $M_\odot$/yr
$\log(sSFR/yr) = -9.13^{+0.09}_{-0.04}$
Δ MS = $-0.13^{+0.14}_{-0.10}$ dex
$t_{50} = 1.25^{+0.45}_{-0.67}$ Gyr
$SFR_{10}/SFR_{100} = 0.967^{+0.01}_{-0.03}$

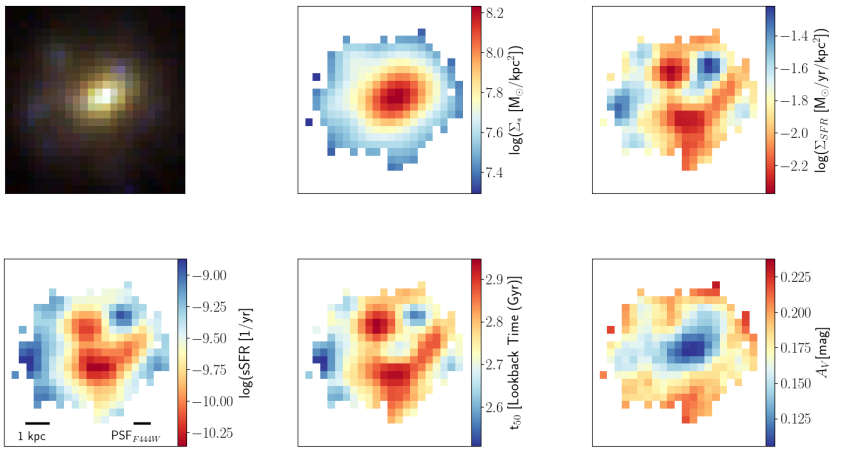

CANUCS - 4200110
$z = 0.87^{+0.05}_{-0.06}$
$\log(M_*/M_\odot) = 9.13^{+0.08}_{-0.10}$
$SFR_{100} = 0.39^{+0.16}_{-0.09}$ $M_\odot$/yr
$\log(sSFR/yr) = -9.54^{+0.08}_{-0.02}$
Δ MS = $0.04^{+0.16}_{-0.14}$ dex
$t_{50} = 3.01^{+1.11}_{-0.99}$ Gyr
$SFR_{10}/SFR_{100} = 0.991^{+0.01}_{-0.00}$

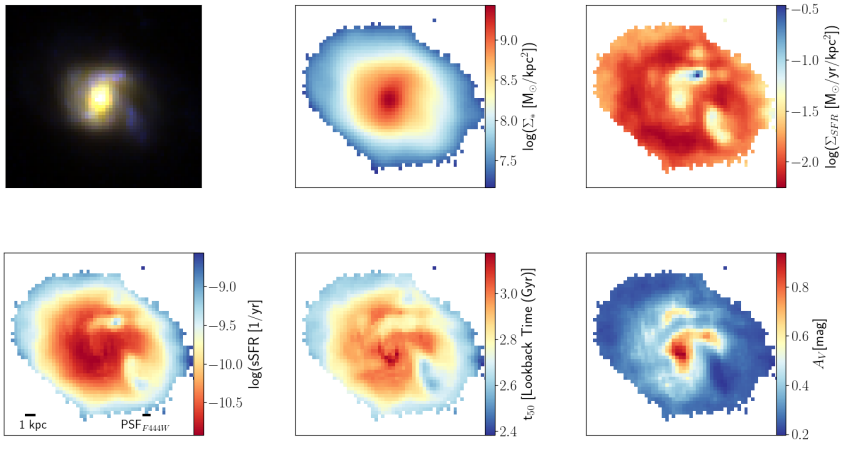

CANUCS - 4200116
$z = 1.01^{+0.03}_{-0.09}$
$\log(M_*/M_\odot) = 10.56^{+0.04}_{-0.06}$
$SFR_{100} = 2.58^{+1.54}_{-0.51}$ $M_\odot$/yr
$\log(sSFR/yr) = -10.15^{+0.16}_{-0.04}$
Δ MS = $-0.28^{+0.21}_{-0.10}$ dex
$t_{50} = 2.82^{+0.85}_{-0.02}$ Gyr
$SFR_{10}/SFR_{100} = 0.969^{+0.01}_{-0.01}$

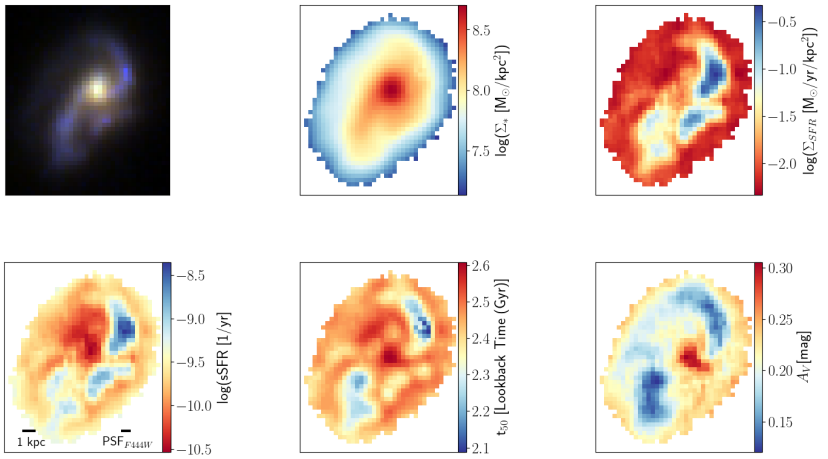

CANUCS - 4200119
$z = 1.13^{+0.07}_{-0.03}$
$\log(M_*/M_\odot) = 9.98^{+0.05}_{-0.05}$
$SFR_{100} = 3.45^{+0.86}_{-0.84}\ M_\odot/yr$
$\log(sSFR/yr) = -9.44^{+0.05}_{-0.07}$
$\Delta\ MS = 0.20^{+0.10}_{-0.13}$ dex
$t_{50} = 1.86^{+1.03}_{-0.48}$ Gyr
$SFR_{10}/SFR_{100} = 0.995^{+0.00}_{-0.00}$

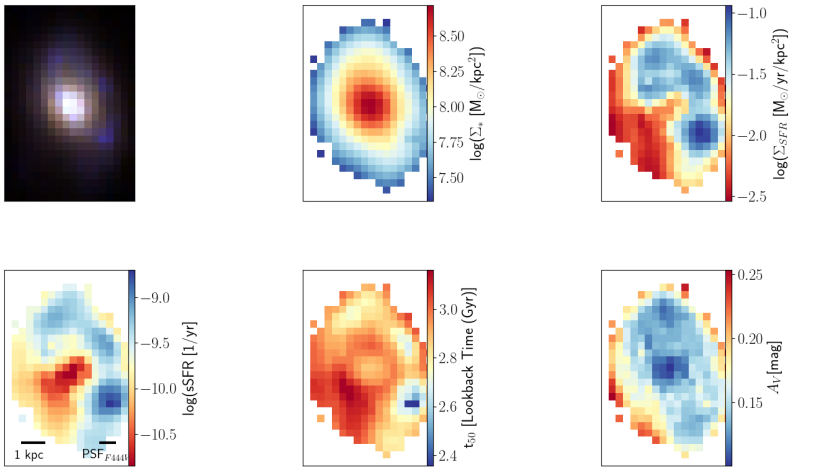

CANUCS - 4200132
$z = 0.78^{+0.06}_{-0.04}$
$\log(M_*/M_\odot) = 9.45^{+0.07}_{-0.08}$
$SFR_{100} = 0.67^{+0.13}_{-0.10}\ M_\odot/yr$
$\log(sSFR/yr) = -9.62^{+0.01}_{-0.02}$
$\Delta\ MS = 0.10^{+0.09}_{-0.09}$ dex
$t_{50} = 3.66^{+0.96}_{-1.02}$ Gyr
$SFR_{10}/SFR_{100} = 0.998^{+0.00}_{-0.00}$

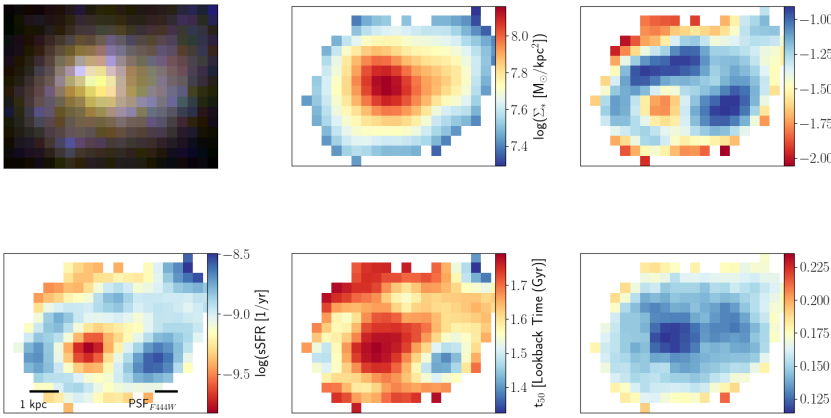

CANUCS - 4200162
$z = 1.53^{+0.02}_{-0.08}$
$\log(M_*/M_\odot) = 9.15^{+0.08}_{-0.11}$
$SFR_{100} = 1.36^{+0.35}_{-0.24}\ M_\odot/yr$
$\log(sSFR/yr) = -9.01^{+0.02}_{-0.02}$
$\Delta\ MS = 0.18^{+0.11}_{-0.11}$ dex
$t_{50} = 2.22^{+0.67}_{-0.66}$ Gyr
$SFR_{10}/SFR_{100} = 1.096^{+0.00}_{-0.05}$

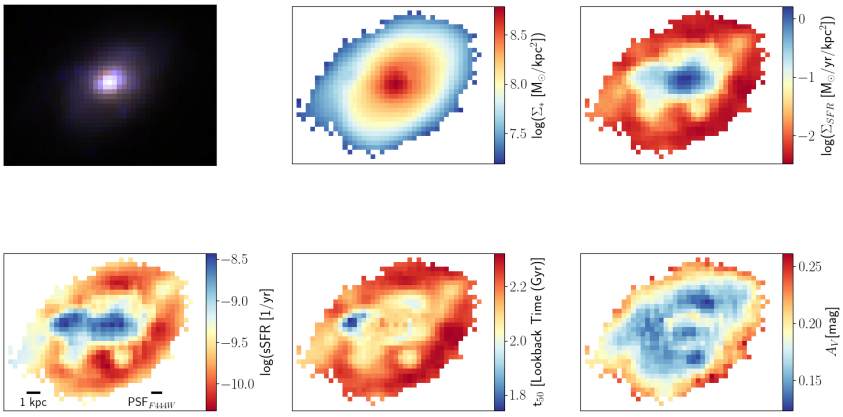

CANUCS - 4200210
$z = 1.24^{+0.03}_{-0.07}$
$\log(M_*/M_\odot) = 9.93^{+0.07}_{-0.01}$
$SFR_{100} = 6.94^{+0.25}_{-0.73}$ $M_\odot$/yr
$\log(sSFR/yr) = -9.09^{+0.05}_{-0.04}$
Δ MS $= 0.47^{+0.05}_{-0.05}$ dex
$t_{50} = 2.75^{+0.15}_{-1.41}$ Gyr
$SFR_{10}/SFR_{100} = 1.033^{+0.00}_{-0.00}$

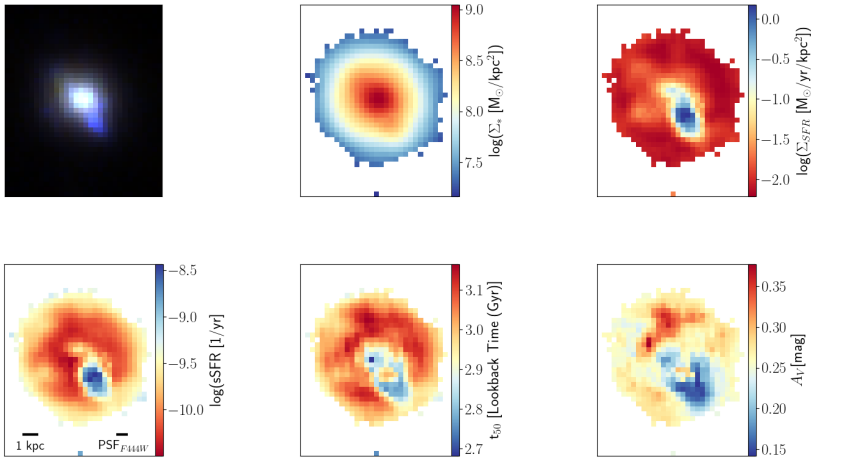

CANUCS - 4200212
$z = 0.87^{+0.07}_{-0.05}$
$\log(M_*/M_\odot) = 9.94^{+0.06}_{-0.09}$
$SFR_{100} = 2.67^{+0.43}_{-0.96}$ $M_\odot$/yr
$\log(sSFR/yr) = -9.51^{+0.01}_{-0.10}$
Δ MS $= 0.28^{+0.08}_{-0.21}$ dex
$t_{50} = 3.04^{+1.98}_{-1.04}$ Gyr
$SFR_{10}/SFR_{100} = 1.015^{+0.01}_{-0.01}$

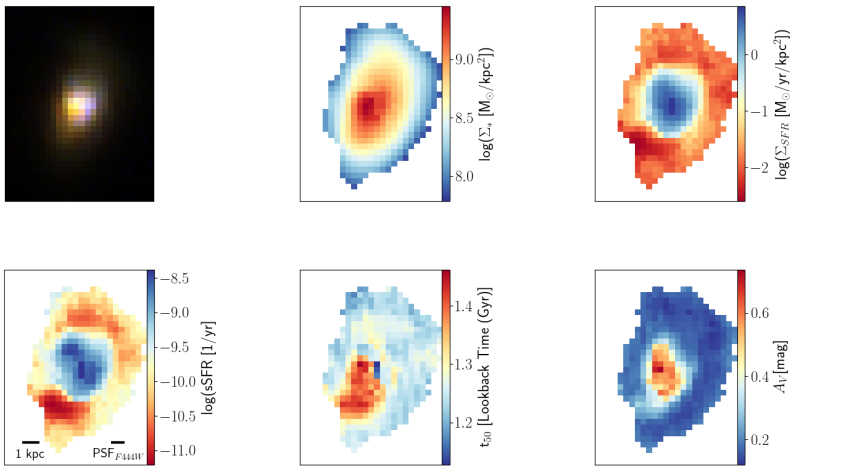

CANUCS - 4200219
$z = 2.35^{+0.01}_{-0.10}$
$\log(M_*/M_\odot) = 10.31^{+0.15}_{-0.09}$
$SFR_{100} = 18.32^{+2.09}_{-4.14}$ $M_\odot$/yr
$\log(sSFR/yr) = -9.04^{+0.11}_{-0.02}$
Δ MS $= 0.27^{+0.10}_{-0.12}$ dex
$t_{50} = 1.30^{+0.35}_{-0.17}$ Gyr
$SFR_{10}/SFR_{100} = 1.003^{+0.00}_{-0.00}$

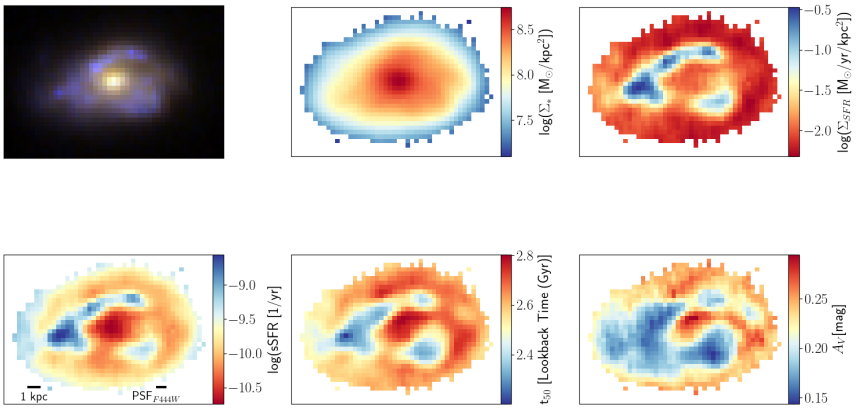

CANUCS - 4200264
$z = 1.03^{+0.02}_{-0.10}$
$\log(M_*/M_\odot) = 10.04^{+0.02}_{-0.03}$
$SFR_{100} = 2.65^{+0.85}_{-0.36}\ M_\odot/yr$
$\log(sSFR/yr) = -9.62^{+0.10}_{-0.03}$
Δ MS $= 0.10^{+0.12}_{-0.07}$ dex
$t_{50} = 1.80^{+1.22}_{-0.68}$ Gyr
$SFR_{10}/SFR_{100} = 0.954^{+0.00}_{-0.00}$

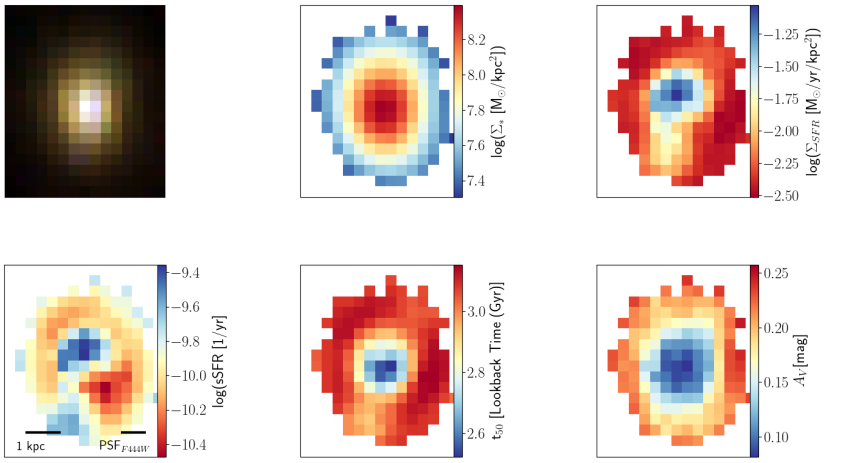

CANUCS - 4200270
$z = 0.79^{+0.09}_{-0.02}$
$\log(M_*/M_\odot) = 9.00^{+0.07}_{-0.05}$
$SFR_{100} = 0.14^{+0.12}_{-0.13}\ M_\odot/yr$
$\log(sSFR/yr) = -9.84^{+0.18}_{-1.07}$
Δ MS $= -0.25^{+0.26}_{-1.12}$ dex
$t_{50} = 2.62^{+1.47}_{-1.63}$ Gyr
$SFR_{10}/SFR_{100} = 0.986^{+0.00}_{-0.01}$

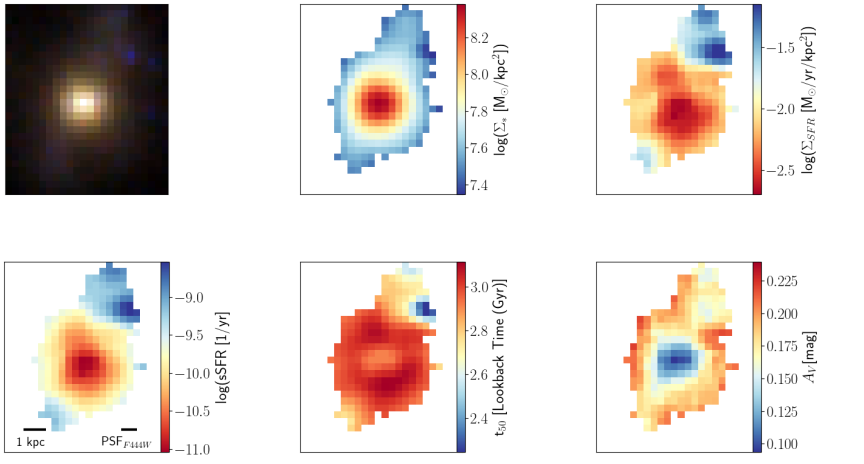

CANUCS - 4200278
$z = 0.83^{+0.07}_{-0.04}$
$\log(M_*/M_\odot) = 9.18^{+0.07}_{-0.08}$
$SFR_{100} = 0.29^{+0.07}_{-0.09}\ M_\odot/yr$
$\log(sSFR/yr) = -9.71^{+0.02}_{-0.08}$
Δ MS $= -0.09^{+0.10}_{-0.17}$ dex
$t_{50} = 2.70^{+1.38}_{-1.16}$ Gyr
$SFR_{10}/SFR_{100} = 0.999^{+0.00}_{-0.00}$

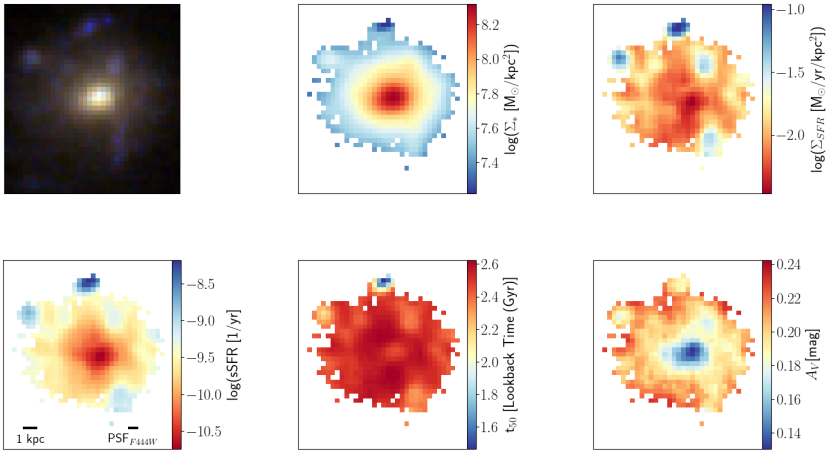

CANUCS - 4200294
$z = 1.03^{+0.03}_{-0.10}$
$\log(M_*/M_\odot) = 9.54^{+0.08}_{-0.05}$
$SFR_{100} = 0.89^{+0.35}_{-0.38}\ M_\odot/yr$
$\log(sSFR/yr) = -9.58^{+0.06}_{-0.19}$
$\Delta\ MS = 0.00^{+0.16}_{-0.24}$ dex
$t_{50} = 2.46^{+0.98}_{-1.30}$ Gyr
$SFR_{10}/SFR_{100} = 0.993^{+0.00}_{-0.00}$

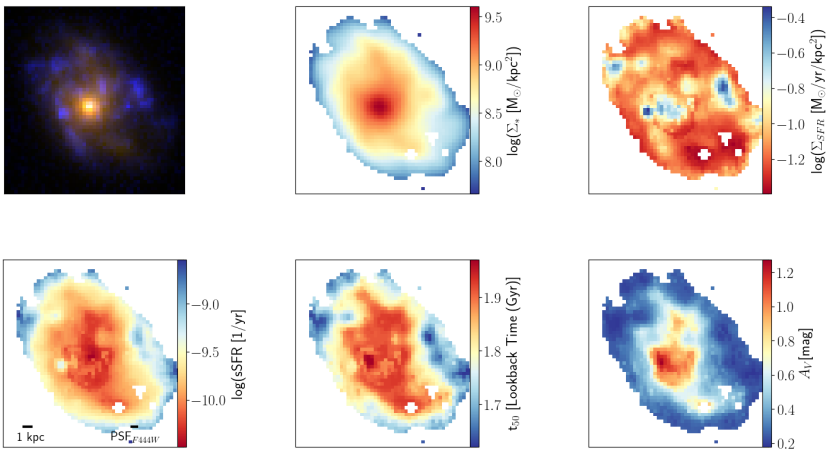

CANUCS - 4200319
$z = 1.82^{+0.05}_{-0.12}$
$\log(M_*/M_\odot) = 10.98^{+0.01}_{-0.07}$
$SFR_{100} = 15.09^{+3.98}_{-6.76}\ M_\odot/yr$
$\log(sSFR/yr) = -9.80^{+0.09}_{-0.19}$
$\Delta\ MS = -0.15^{+0.10}_{-0.26}$ dex
$t_{50} = 2.16^{+0.04}_{-0.31}$ Gyr
$SFR_{10}/SFR_{100} = 1.002^{+0.00}_{-0.00}$

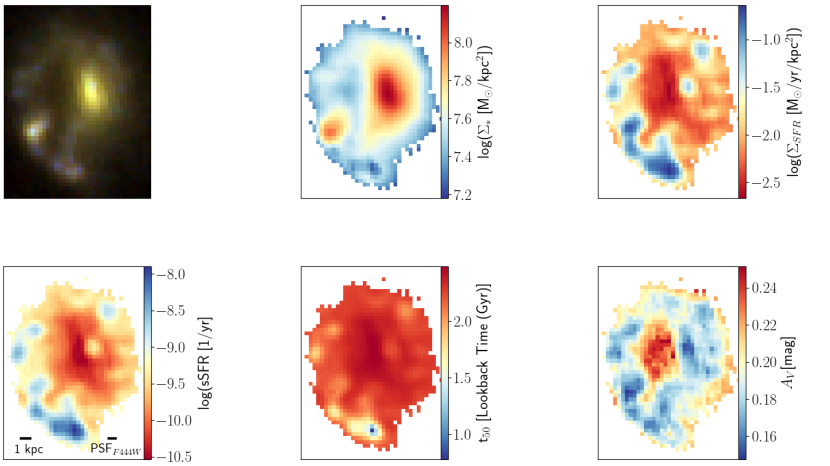

CANUCS - 4200326
$z = 1.18^{+0.05}_{-0.04}$
$\log(M_*/M_\odot) = 9.71^{+0.07}_{-0.05}$
$SFR_{100} = 2.64^{+0.56}_{-0.52}\ M_\odot/yr$
$\log(sSFR/yr) = -9.29^{+0.02}_{-0.04}$
$\Delta\ MS = 0.25^{+0.10}_{-0.10}$ dex
$t_{50} = 2.54^{+0.61}_{-0.80}$ Gyr
$SFR_{10}/SFR_{100} = 0.994^{+0.01}_{-0.00}$

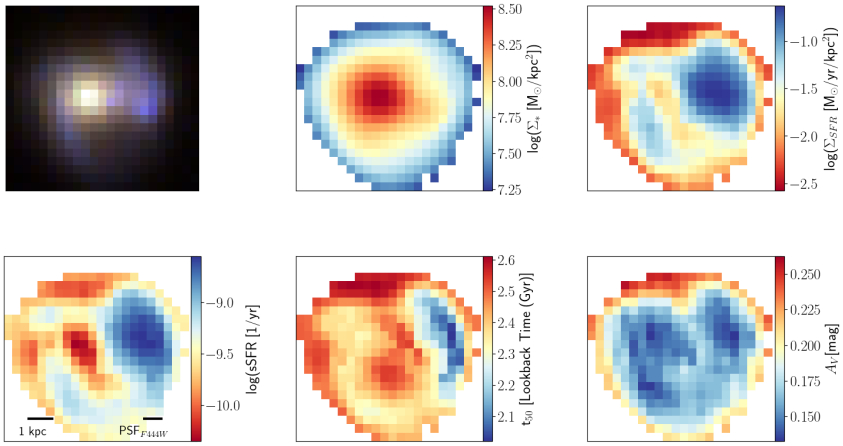

CANUCS - 4200333
$z = 1.05^{+0.05}_{-0.01}$
$\log(M_*/M_\odot) = 9.45^{+0.03}_{-0.04}$
$SFR_{100} = 1.59^{+0.22}_{-0.27}$ $M_\odot$/yr
$\log(sSFR/yr) = -9.25^{+0.03}_{-0.04}$
Δ MS $= 0.30^{+0.06}_{-0.09}$ dex
$t_{50} = 3.21^{+0.51}_{-1.07}$ Gyr
$SFR_{10}/SFR_{100} = 0.995^{+0.00}_{-0.00}$

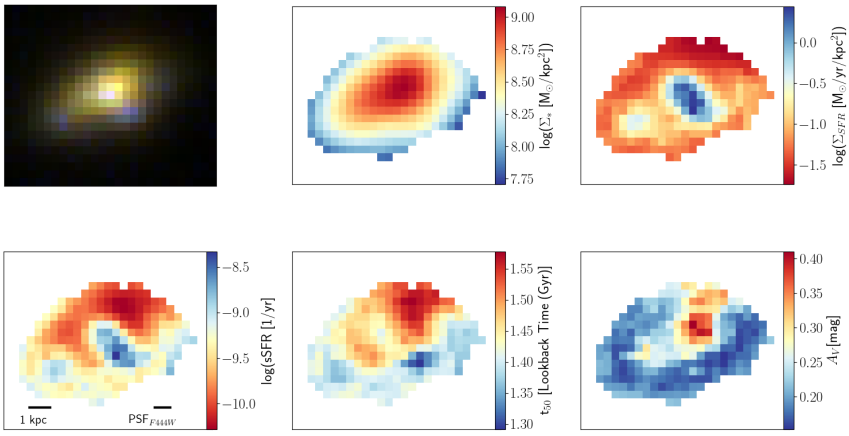

CANUCS - 4200366
$z = 2.13^{+0.09}_{-0.02}$
$\log(M_*/M_\odot) = 9.98^{+0.07}_{-0.04}$
$SFR_{100} = 5.53^{+0.90}_{-1.39}$ $M_\odot$/yr
$\log(sSFR/yr) = -9.24^{+0.00}_{-0.09}$
Δ MS $= -0.02^{+0.08}_{-0.13}$ dex
$t_{50} = 1.33^{+0.29}_{-0.24}$ Gyr
$SFR_{10}/SFR_{100} = 0.966^{+0.01}_{-0.06}$

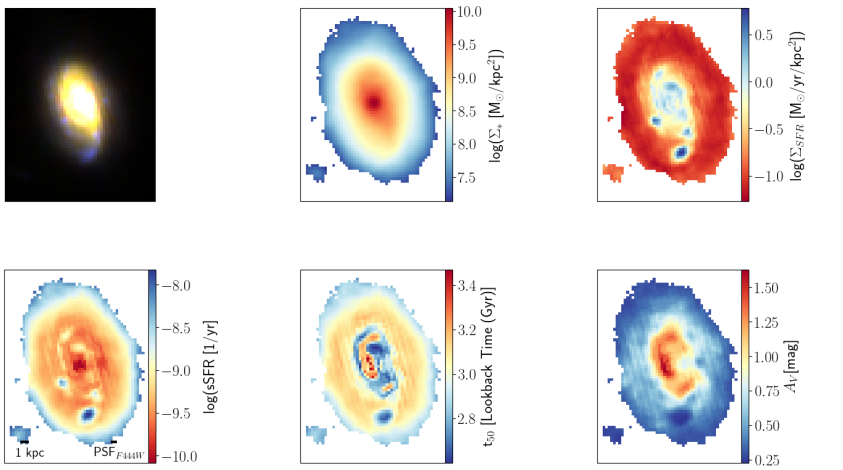

CANUCS - 4200394
$z = 0.94^{+0.08}_{-0.04}$
$\log(M_*/M_\odot) = 11.05^{+0.05}_{-0.00}$
$SFR_{100} = 55.63^{+30.10}_{-0.00}$ $M_\odot$/yr
$\log(sSFR/yr) = -9.31^{+0.14}_{-0.00}$
Δ MS $= 0.74^{+0.19}_{-0.00}$ dex
$t_{50} = 3.50^{+0.04}_{-0.00}$ Gyr
$SFR_{10}/SFR_{100} = 0.995^{+0.00}_{-0.00}$

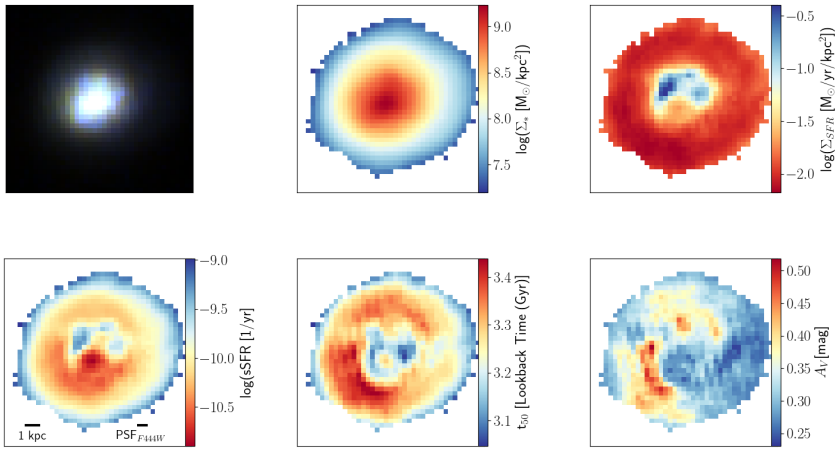

CANUCS - 4200404
$z = 0.82^{+0.05}_{-0.05}$
$\log(M_*/M_\odot) = 10.29^{+0.04}_{-0.08}$
$SFR_{100} = 1.96^{+1.62}_{-0.56}$ $M_\odot$/yr
$\log(sSFR/yr) = -9.99^{+0.22}_{-0.07}$
Δ MS $= -0.08^{+0.26}_{-0.16}$ dex
$t_{50} = 3.17^{+1.47}_{-1.15}$ Gyr
$SFR_{10}/SFR_{100} = 0.988^{+0.00}_{-0.00}$

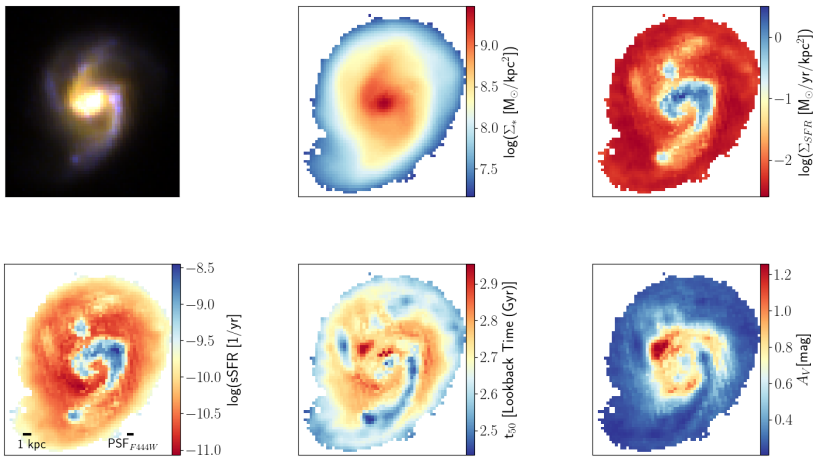

CANUCS - 4200419
$z = 1.10^{+0.03}_{-0.04}$
$\log(M_*/M_\odot) = 10.87^{+0.00}_{-0.00}$
$SFR_{100} = 17.82^{+0.13}_{-0.00}$ $M_\odot$/yr
$\log(sSFR/yr) = -9.62^{+0.00}_{-0.00}$
Δ MS $= 0.28^{+0.00}_{-0.00}$ dex
$t_{50} = 2.20^{+0.00}_{-0.01}$ Gyr
$SFR_{10}/SFR_{100} = 0.980^{+0.00}_{-0.00}$

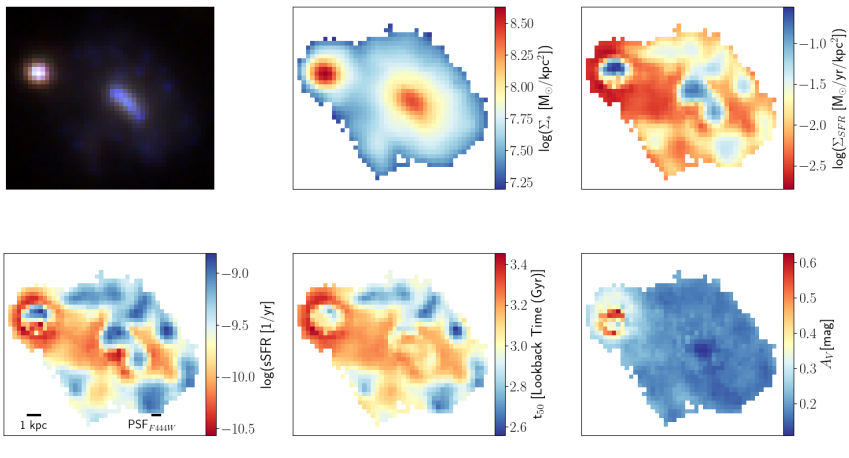

CANUCS - 4200427
$z = 0.74^{+0.09}_{-0.02}$
$\log(M_*/M_\odot) = 9.70^{+0.11}_{-0.02}$
$SFR_{100} = 1.62^{+0.59}_{-0.16}$ $M_\odot$/yr
$\log(sSFR/yr) = -9.49^{+0.03}_{-0.03}$
Δ MS $= 0.32^{+0.16}_{-0.05}$ dex
$t_{50} = 3.26^{+1.12}_{-0.23}$ Gyr
$SFR_{10}/SFR_{100} = 1.000^{+0.00}_{-0.00}$

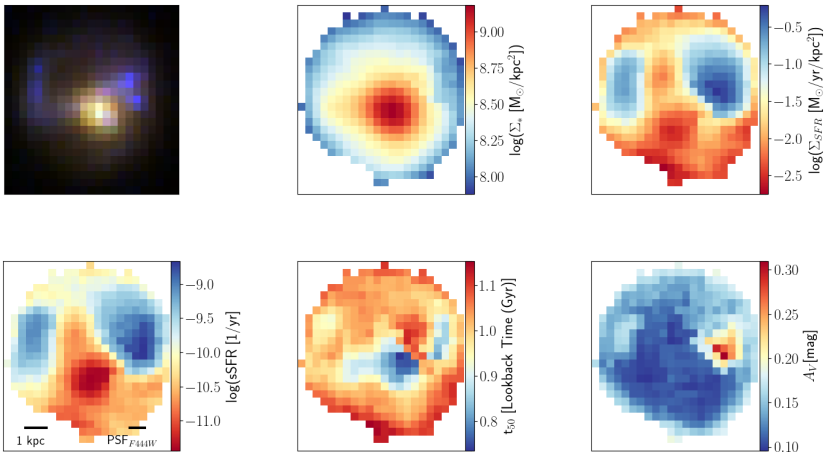

CANUCS - 4200437
$z = 2.60^{+0.02}_{-0.05}$
$\log(M_*/M_\odot) = 10.12^{+0.00}_{-0.06}$
$SFR_{100} = 2.54^{+0.13}_{-0.01}$ $M_\odot$/yr
$\log(sSFR/yr) = -9.71^{+0.02}_{-0.06}$
Δ MS $= -0.48^{+0.02}_{-0.04}$ dex
$t_{50} = 0.88^{+0.00}_{-0.54}$ Gyr
$SFR_{10}/SFR_{100} = 0.221^{+0.02}_{-0.00}$

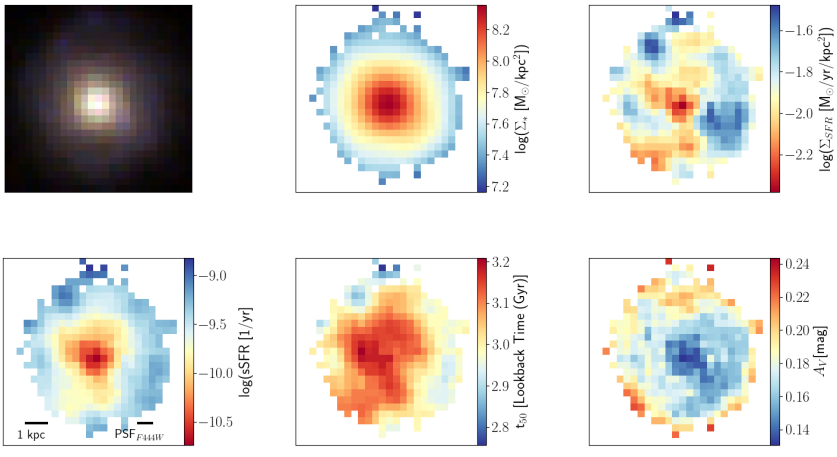

CANUCS - 4200448
$z = 0.79^{+0.08}_{-0.03}$
$\log(M_*/M_\odot) = 9.30^{+0.08}_{-0.06}$
$SFR_{100} = 0.46^{+0.11}_{-0.11}$ $M_\odot$/yr
$\log(sSFR/yr) = -9.64^{+0.01}_{-0.06}$
Δ MS $= 0.04^{+0.11}_{-0.13}$ dex
$t_{50} = 3.15^{+1.23}_{-1.22}$ Gyr
$SFR_{10}/SFR_{100} = 0.983^{+0.01}_{-0.00}$

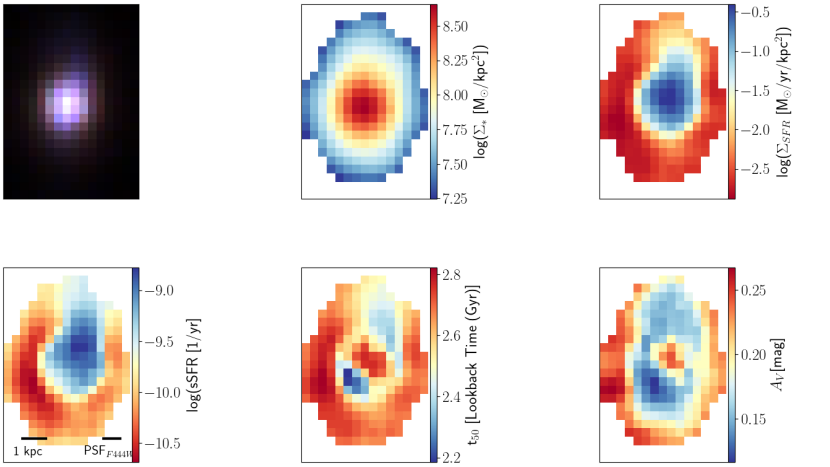

CANUCS - 4200565
$z = 0.99^{+0.02}_{-0.08}$
$\log(M_*/M_\odot) = 9.31^{+0.09}_{-0.07}$
$SFR_{100} = 0.93^{+0.47}_{-0.15}$ $M_\odot$/yr
$\log(sSFR/yr) = -9.34^{+0.09}_{-0.00}$
Δ MS $= 0.21^{+0.19}_{-0.10}$ dex
$t_{50} = 3.15^{+0.72}_{-1.44}$ Gyr
$SFR_{10}/SFR_{100} = 1.009^{+0.00}_{-0.01}$

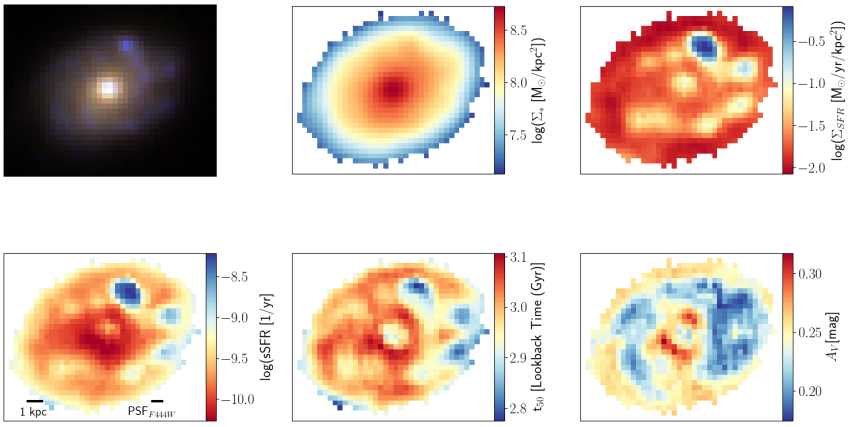

CANUCS - 4200569
$z = 0.87^{+0.04}_{-0.06}$
$\log\ (M_*/M_\odot) = 9.93^{+0.07}_{-0.05}$
$SFR_{100} = 3.04^{+0.31}_{-1.02}\ M_\odot/yr$
$\log(sSFR/yr) = -9.45^{+0.03}_{-0.13}$
$\Delta\ MS = 0.34^{+0.07}_{-0.18}$ dex
$t_{50} = 3.37^{+1.06}_{-1.36}$ Gyr
$SFR_{10}/SFR_{100} = 0.983^{+0.01}_{-0.01}$

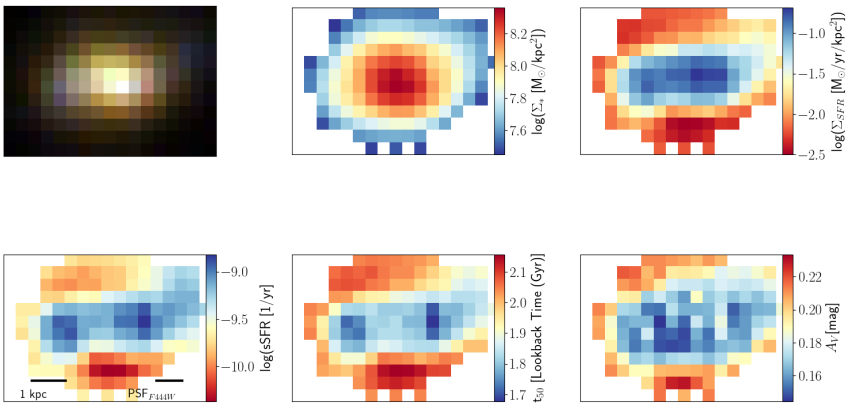

CANUCS - 4200575
$z = 1.36^{+0.06}_{-0.03}$
$\log\ (M_*/M_\odot) = 9.11^{+0.07}_{-0.11}$
$SFR_{100} = 0.65^{+0.32}_{-0.20}\ M_\odot/yr$
$\log(sSFR/yr) = -9.29^{+0.10}_{-0.05}$
$\Delta\ MS = -0.03^{+0.18}_{-0.17}$ dex
$t_{50} = 2.40^{+0.77}_{-0.96}$ Gyr
$SFR_{10}/SFR_{100} = 0.989^{+0.01}_{-0.01}$

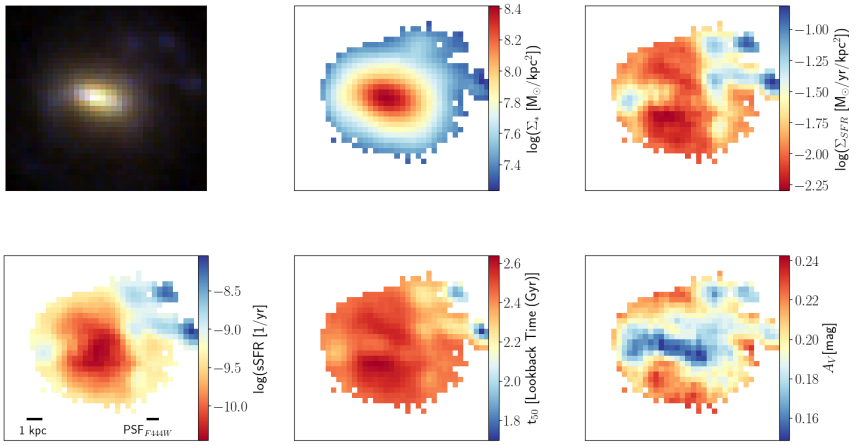

CANUCS - 4200613
$z = 1.10^{+0.03}_{-0.04}$
$\log\ (M_*/M_\odot) = 9.54^{+0.07}_{-0.07}$
$SFR_{100} = 1.29^{+0.32}_{-0.34}\ M_\odot/yr$
$\log(sSFR/yr) = -9.43^{+0.02}_{-0.06}$
$\Delta\ MS = 0.11^{+0.11}_{-0.14}$ dex
$t_{50} = 2.01^{+1.49}_{-1.06}$ Gyr
$SFR_{10}/SFR_{100} = 0.979^{+0.01}_{-0.01}$

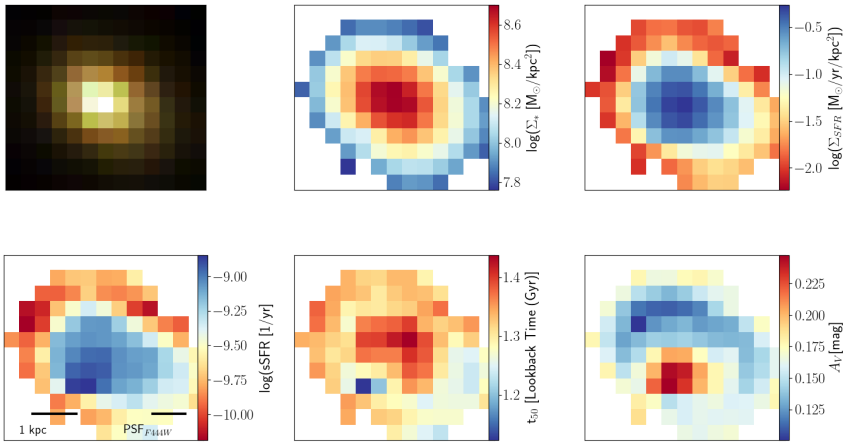

CANUCS - 4200637
$z = 2.04^{+0.01}_{-0.01}$
$\log(M_*/M_\odot) = 9.31^{+0.06}_{-0.03}$
$SFR_{100} = 1.22^{+0.41}_{-0.22}$ $M_\odot$/yr
$\log(sSFR/yr) = -9.22^{+0.06}_{-0.05}$
Δ MS = $-0.21^{+0.13}_{-0.09}$ dex
$t_{50} = 0.98^{+1.16}_{-0.36}$ Gyr
$SFR_{10}/SFR_{100} = 0.881^{+0.09}_{-0.05}$

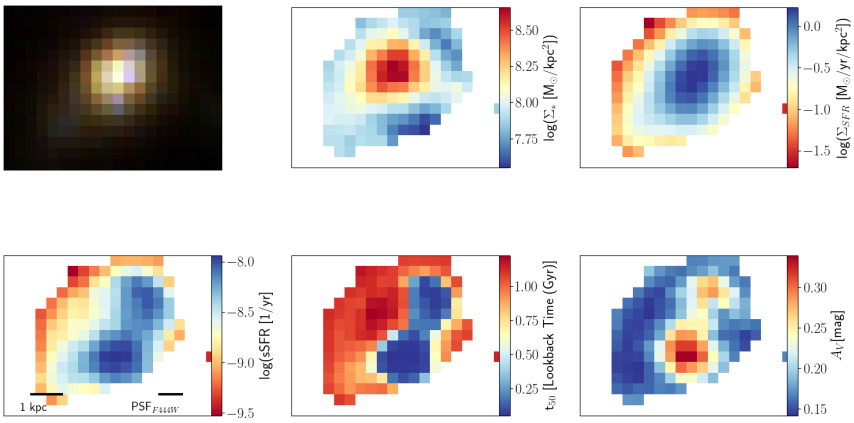

CANUCS - 4200641
$z = 2.35^{+0.01}_{-0.01}$
$\log(M_*/M_\odot) = 9.27^{+0.09}_{-0.02}$
$SFR_{100} = 6.76^{+0.32}_{-1.24}$ $M_\odot$/yr
$\log(sSFR/yr) = -8.44^{+0.07}_{-0.07}$
Δ MS = $0.47^{+0.06}_{-0.09}$ dex
$t_{50} = 1.19^{+0.33}_{-0.82}$ Gyr
$SFR_{10}/SFR_{100} = 1.155^{+0.00}_{-0.01}$

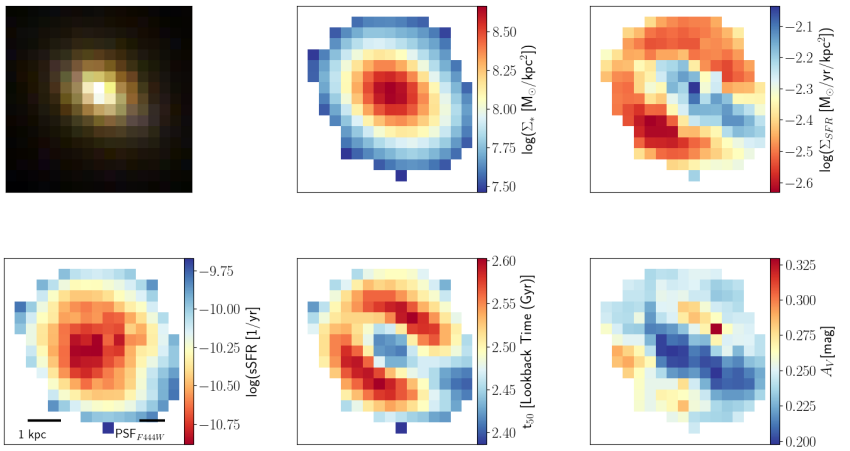

CANUCS - 4200642
$z = 1.15^{+0.05}_{-0.04}$
$\log(M_*/M_\odot) = 9.32^{+0.03}_{-0.06}$
$SFR_{100} = 0.08^{+0.27}_{-0.08}$ $M_\odot$/yr
$\log(sSFR/yr) = -10.43^{+0.62}_{-2.00}$
Δ MS = $-0.98^{+0.65}_{-2.06}$ dex
$t_{50} = 2.24^{+0.95}_{-0.91}$ Gyr
$SFR_{10}/SFR_{100} = 0.977^{+0.00}_{-0.01}$

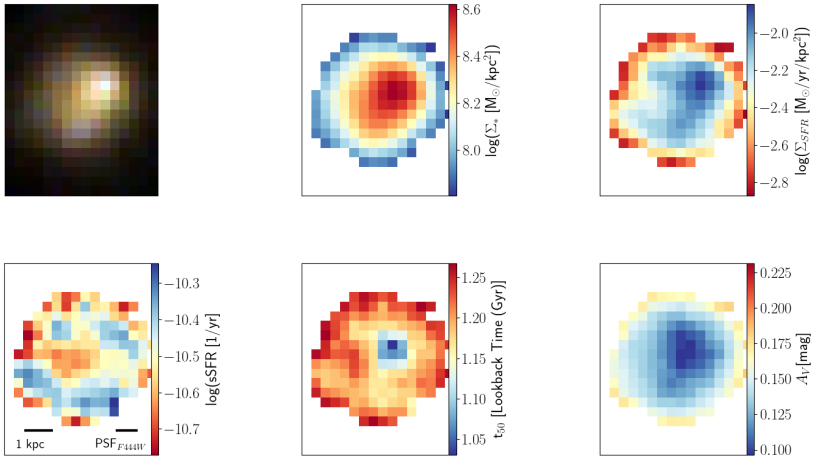

CANUCS - 4200651
$z = 2.18^{+0.02}_{-0.19}$
$\log(M_*/M_\odot) = 9.46^{+0.07}_{-0.05}$
$SFR_{100} = 0.09^{+0.73}_{-0.09}$ $M_\odot$/yr
$\log(sSFR/yr) = -10.49^{+0.88}_{-2.36}$
Δ MS = $-1.48^{+0.95}_{-2.41}$ dex
$t_{50} = 0.52^{+0.50}_{-0.17}$ Gyr
$SFR_{10}/SFR_{100} = 1.000^{+0.00}_{-0.00}$

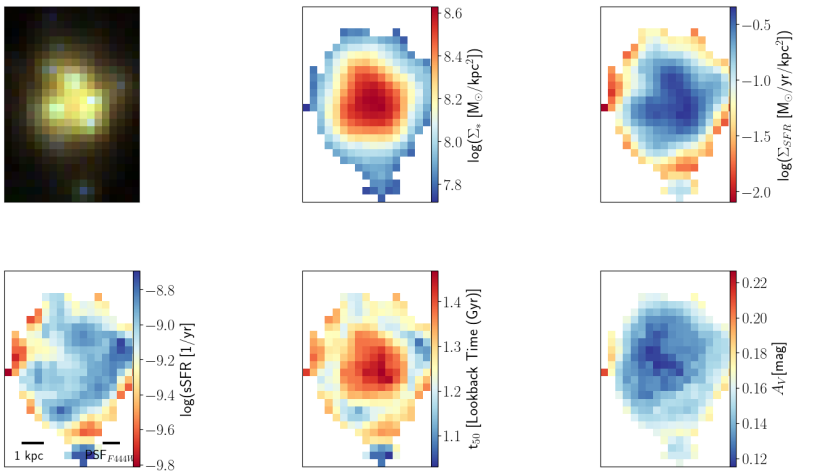

CANUCS - 4200654
$z = 2.00^{+0.49}_{-0.00}$
$\log(M_*/M_\odot) = 9.67^{+0.01}_{-0.01}$
$SFR_{100} = 4.42^{+0.59}_{-1.24}$ $M_\odot$/yr
$\log(sSFR/yr) = -9.02^{+0.04}_{-0.13}$
Δ MS = $0.13^{+0.06}_{-0.14}$ dex
$t_{50} = 1.50^{+0.43}_{-0.10}$ Gyr
$SFR_{10}/SFR_{100} = 1.009^{+0.11}_{-0.01}$

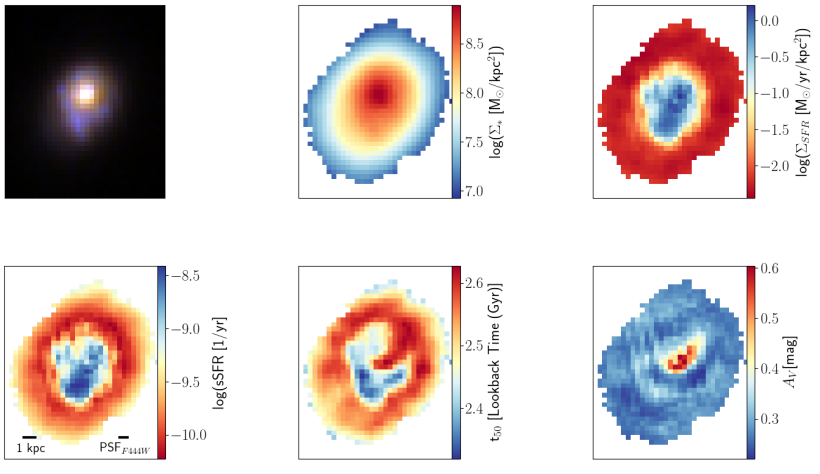

CANUCS - 4200658
$z = 1.17^{+0.05}_{-0.05}$
$\log(M_*/M_\odot) = 9.94^{+0.26}_{-0.00}$
$SFR_{100} = 7.40^{+0.58}_{-1.20}$ $M_\odot$/yr
$\log(sSFR/yr) = -9.07^{+0.22}_{-0.08}$
Δ MS = $0.54^{+0.19}_{-0.08}$ dex
$t_{50} = 3.79^{+0.01}_{-2.29}$ Gyr
$SFR_{10}/SFR_{100} = 0.916^{+0.02}_{-0.00}$

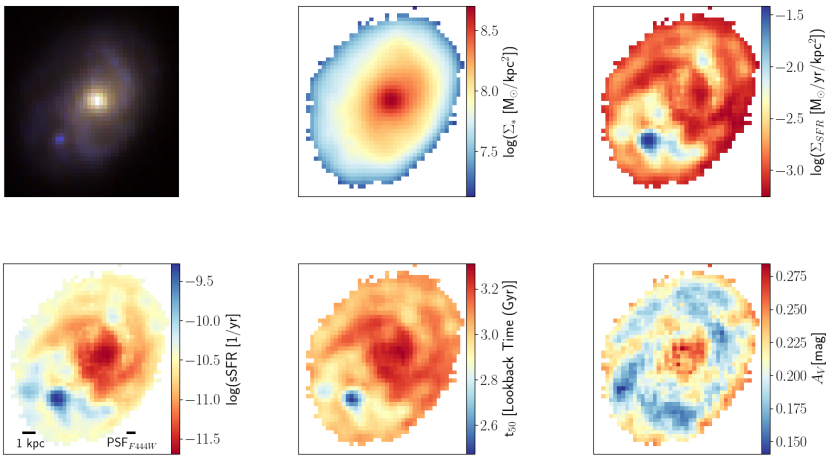

CANUCS - 4200809
$z = 0.81^{+0.09}_{-0.04}$
$\log(M_*/M_\odot) = 10.01^{+0.04}_{-0.07}$
$SFR_{100} = 0.27^{+1.25}_{-0.27}\ M_\odot/yr$
$\log(sSFR/yr) = -10.58^{+0.71}_{-1.63}$
$\Delta\ MS = -0.73^{+0.75}_{-1.70}$ dex
$t_{50} = 2.05^{+1.55}_{-1.10}$ Gyr
$SFR_{10}/SFR_{100} = 1.024^{+0.01}_{-0.01}$

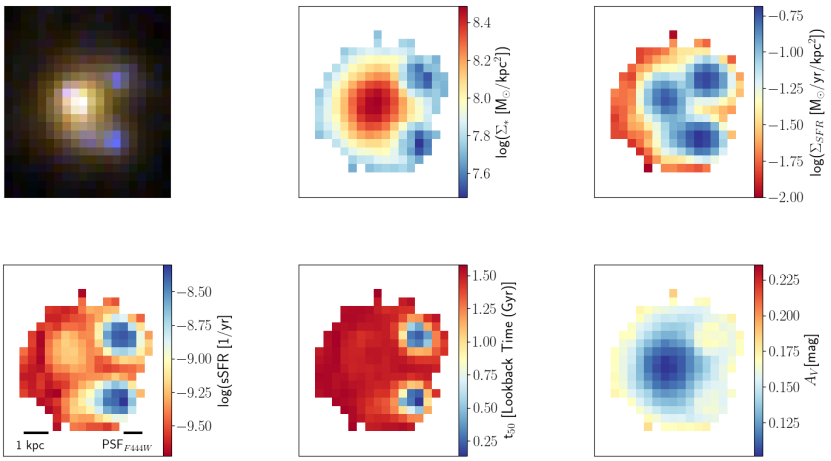

CANUCS - 4200830
$z = 1.73^{+0.11}_{-0.03}$
$\log(M_*/M_\odot) = 9.38^{+0.07}_{-0.05}$
$SFR_{100} = 1.55^{+0.38}_{-0.35}\ M_\odot/yr$
$\log(sSFR/yr) = -9.19^{+0.02}_{-0.06}$
$\Delta\ MS = -0.02^{+0.11}_{-0.12}$ dex
$t_{50} = 1.67^{+0.51}_{-0.51}$ Gyr
$SFR_{10}/SFR_{100} = 1.048^{+0.01}_{-0.01}$

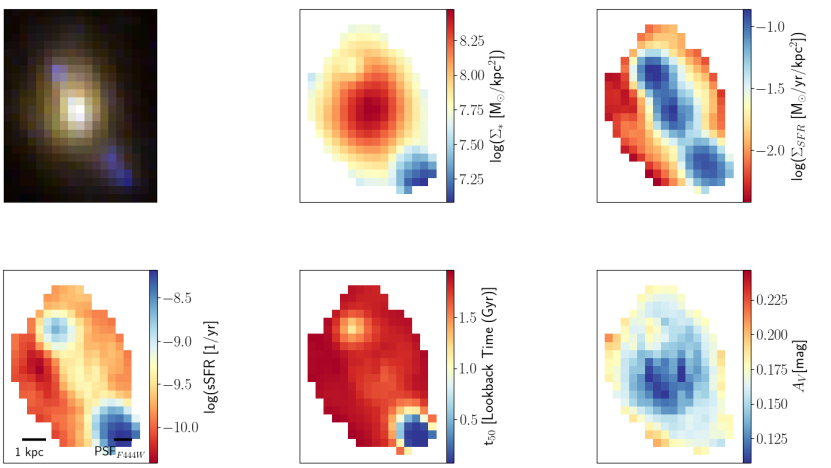

CANUCS - 4200837
$z = 1.44^{+0.08}_{-0.05}$
$\log(M_*/M_\odot) = 9.44^{+0.06}_{-0.07}$
$SFR_{100} = 1.02^{+0.32}_{-0.24}\ M_\odot/yr$
$\log(sSFR/yr) = -9.43^{+0.06}_{-0.05}$
$\Delta\ MS = -0.10^{+0.13}_{-0.13}$ dex
$t_{50} = 2.14^{+0.78}_{-0.73}$ Gyr
$SFR_{10}/SFR_{100} = 1.007^{+0.01}_{-0.02}$

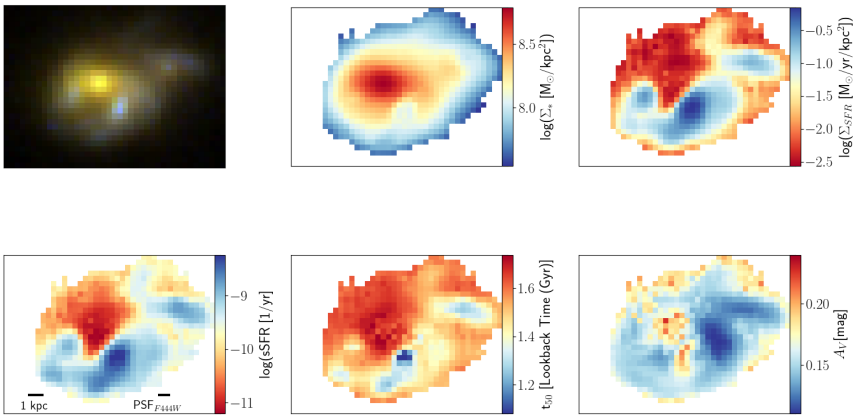

CANUCS - 4200849
$z = 1.77^{+0.10}_{-0.07}$
$\log\,(M_*/M_\odot) = 10.06^{+0.10}_{-0.06}$
$SFR_{100} = 5.19^{+0.70}_{-1.20}\ M_\odot/yr$
$\log(sSFR/yr) = -9.34^{+0.05}_{-0.06}$
Δ MS $= 0.02^{+0.09}_{-0.12}$ dex
$t_{50} = 1.78^{+0.57}_{-0.85}$ Gyr
$SFR_{10}/SFR_{100} = 0.996^{+0.00}_{-0.00}$

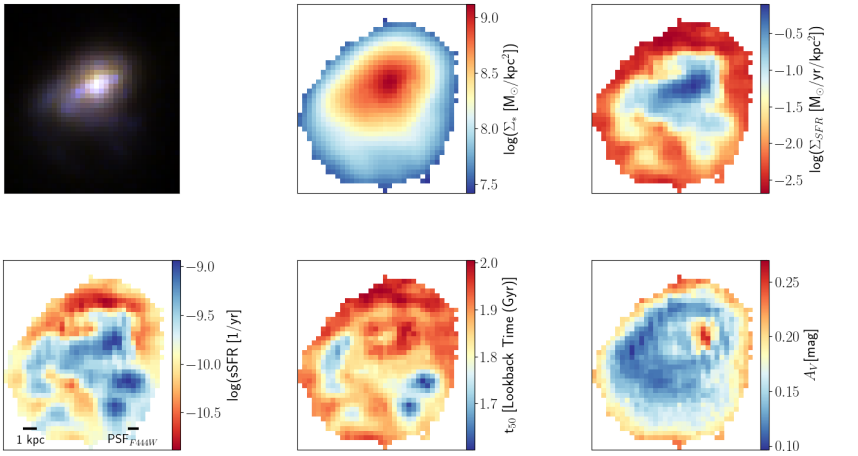

CANUCS - 4200856
$z = 1.47^{+0.05}_{-0.06}$
$\log\,(M_*/M_\odot) = 10.33^{+0.02}_{-0.03}$
$SFR_{100} = 6.20^{+1.81}_{-1.02}\ M_\odot/yr$
$\log(sSFR/yr) = -9.54^{+0.09}_{-0.05}$
Δ MS $= 0.04^{+0.11}_{-0.08}$ dex
$t_{50} = 2.34^{+1.03}_{-0.56}$ Gyr
$SFR_{10}/SFR_{100} = 1.001^{+0.00}_{-0.00}$

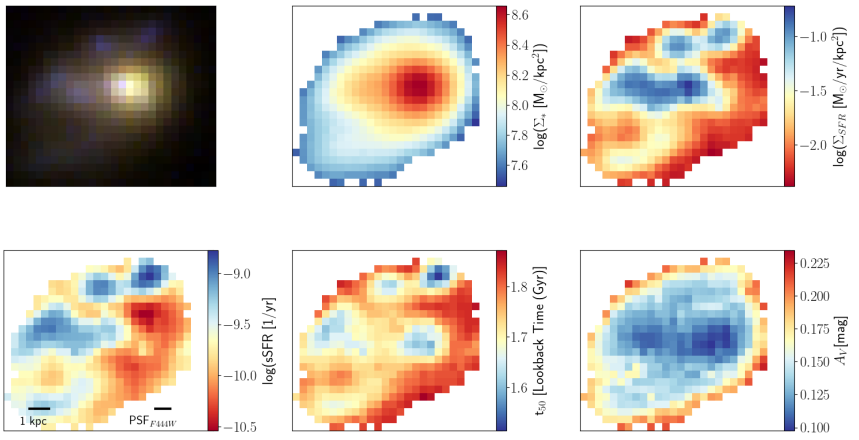

CANUCS - 4200859
$z = 1.56^{+0.03}_{-0.13}$
$\log\,(M_*/M_\odot) = 9.75^{+0.03}_{-0.05}$
$SFR_{100} = 1.51^{+0.31}_{-0.20}\ M_\odot/yr$
$\log(sSFR/yr) = -9.57^{+0.05}_{-0.01}$
Δ MS $= -0.21^{+0.08}_{-0.07}$ dex
$t_{50} = 2.23^{+0.81}_{-0.88}$ Gyr
$SFR_{10}/SFR_{100} = 0.993^{+0.00}_{-0.00}$

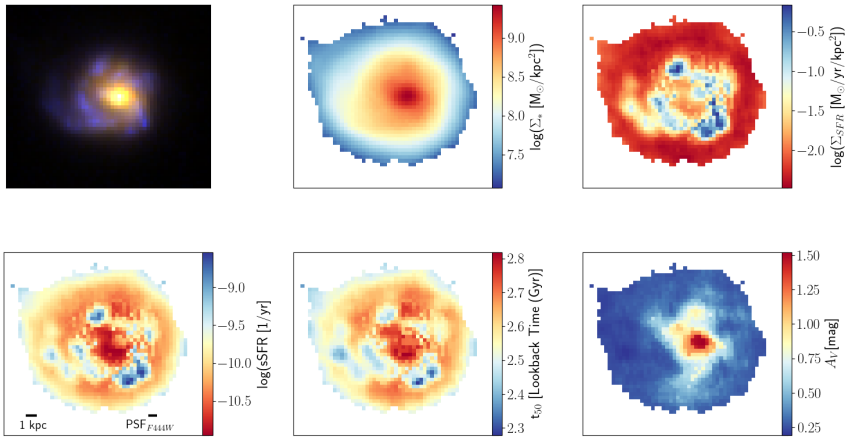

CANUCS - 4200930
$z = 1.15^{+0.08}_{-0.04}$
$\log(M_*/M_\odot) = 10.56^{+0.01}_{-0.00}$
$SFR_{100} = 5.30^{+0.02}_{-2.10}\ M_\odot/yr$
$\log(sSFR/yr) = -9.83^{+0.01}_{-0.22}$
$\Delta\ MS = -0.04^{+0.01}_{-0.22}$ dex
$t_{50} = 2.75^{+0.01}_{-0.30}$ Gyr
$SFR_{10}/SFR_{100} = 0.969^{+0.01}_{-0.00}$

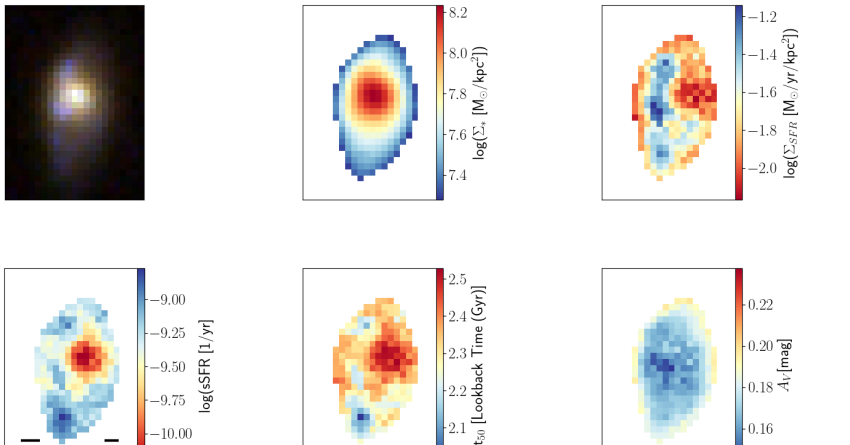

CANUCS - 5101044
$z = 1.02^{+0.04}_{-0.06}$
$\log(M_*/M_\odot) = 9.14^{+0.09}_{-0.07}$
$SFR_{100} = 0.57^{+0.41}_{-0.44}\ M_\odot/yr$
$\log(sSFR/yr) = -9.38^{+0.15}_{-0.57}$
$\Delta\ MS = 0.11^{+0.24}_{-0.64}$ dex
$t_{50} = 2.47^{+0.92}_{-1.77}$ Gyr
$SFR_{10}/SFR_{100} = 0.942^{+0.03}_{-0.03}$

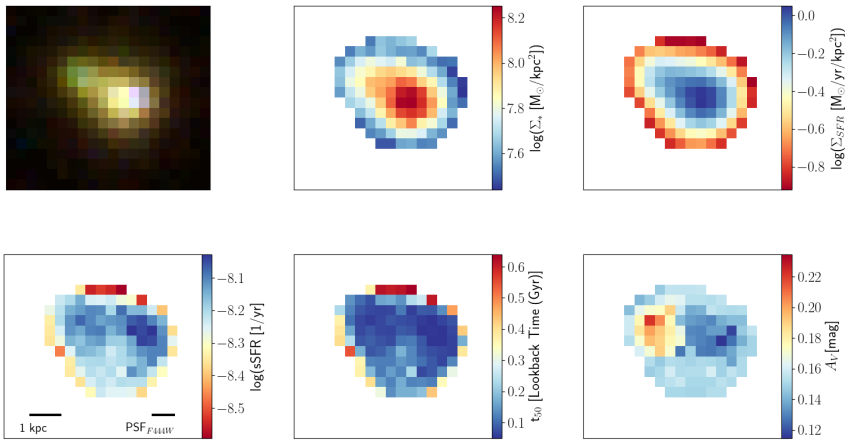

CANUCS - 5101623
$z = 2.68^{+0.43}_{-0.01}$
$\log(M_*/M_\odot) = 8.87^{+0.27}_{-0.21}$
$SFR_{100} = 4.86^{+1.07}_{-1.10}\ M_\odot/yr$
$\log(sSFR/yr) = -8.18^{+0.19}_{-0.10}$
$\Delta\ MS = 0.57^{+0.19}_{-0.17}$ dex
$t_{50} = 0.10^{+0.98}_{-0.07}$ Gyr
$SFR_{10}/SFR_{100} = 1.269^{+0.02}_{-0.02}$

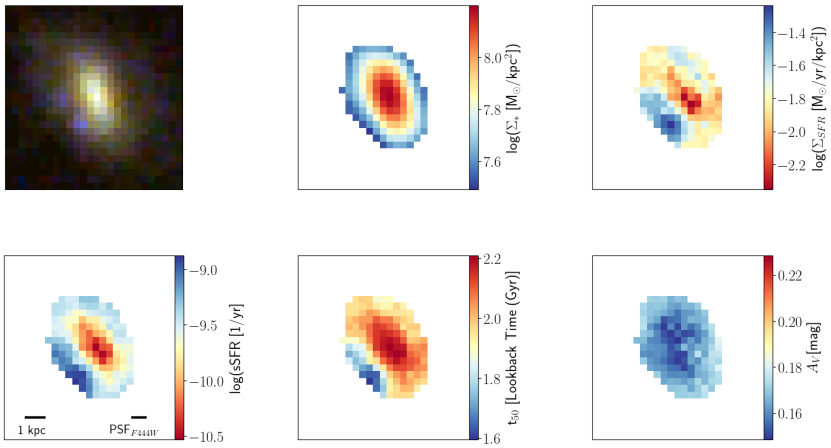

CANUCS - 5103079
z = $1.23^{+0.09}_{-0.08}$
log ($M_*/M_\odot$) = $9.06^{+0.10}_{-0.09}$
SFR_{100} = $0.30^{+0.29}_{-0.30}$ $M_\odot$/yr
log(sSFR/yr) = $-9.58^{+0.19}_{-1.90}$
Δ MS = $-0.25^{+0.30}_{-1.99}$ dex
t_{50} = $2.11^{+0.96}_{-1.19}$ Gyr
SFR_{10}/SFR_{100} = $0.991^{+0.02}_{-0.00}$

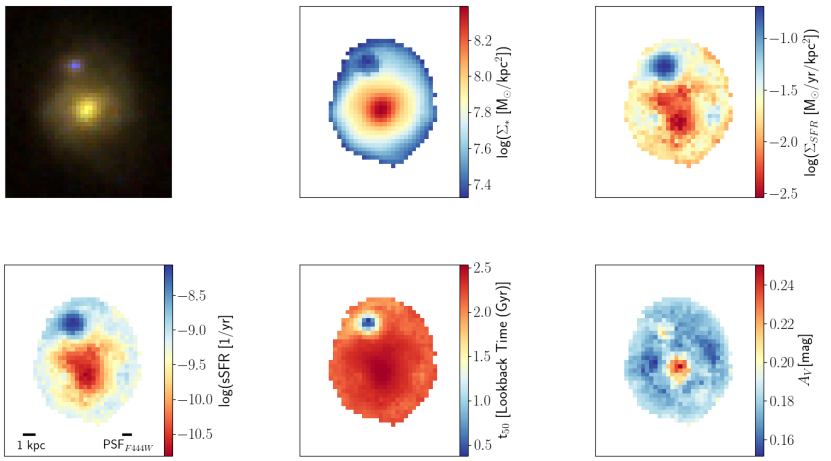

CANUCS - 5103162
z = $1.14^{+0.06}_{-0.05}$
log ($M_*/M_\odot$) = $9.60^{+0.06}_{-0.08}$
SFR_{100} = $1.72^{+0.62}_{-0.56}$ $M_\odot$/yr
log(sSFR/yr) = $-9.36^{+0.08}_{-0.10}$
Δ MS = $0.17^{+0.14}_{-0.18}$ dex
t_{50} = $2.29^{+0.93}_{-0.86}$ Gyr
SFR_{10}/SFR_{100} = $0.993^{+0.00}_{-0.00}$

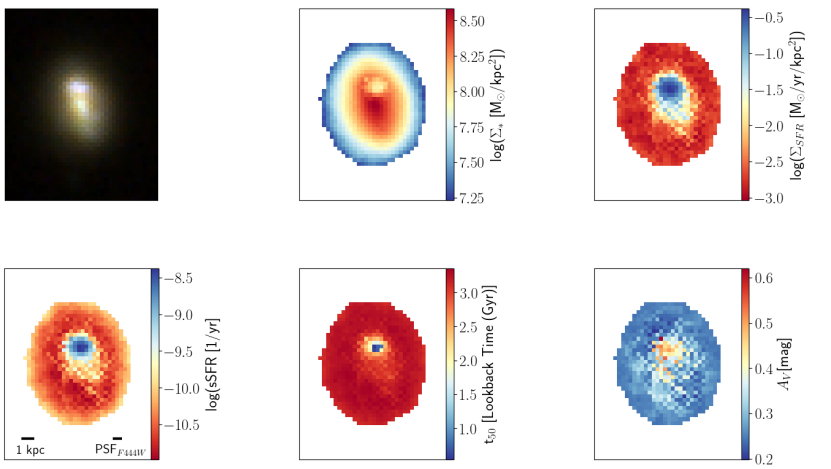

CANUCS - 5103479
z = $0.76^{+0.05}_{-0.04}$
log ($M_*/M_\odot$) = $9.76^{+0.06}_{-0.04}$
SFR_{100} = $1.02^{+0.42}_{-0.54}$ $M_\odot$/yr
log(sSFR/yr) = $-9.75^{+0.09}_{-0.29}$
Δ MS = $0.06^{+0.16}_{-0.33}$ dex
t_{50} = $3.18^{+1.48}_{-0.53}$ Gyr
SFR_{10}/SFR_{100} = $0.997^{+0.00}_{-0.00}$

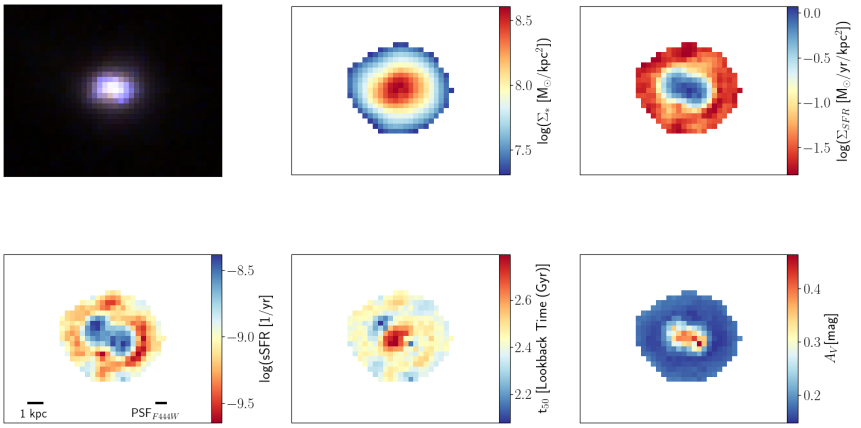

CANUCS - 5103949
$z = 0.97^{+0.00}_{-0.22}$
$\log(M_*/M_\odot) = 9.40^{+0.10}_{-0.00}$
$SFR_{100} = 3.96^{+0.02}_{-1.91}$ $M_\odot$/yr
$\log(sSFR/yr) = -8.81^{+0.10}_{-0.28}$
Δ MS $= 0.78^{+0.07}_{-0.29}$ dex
$t_{50} = 3.52^{+0.01}_{-0.86}$ Gyr
$SFR_{10}/SFR_{100} = 0.971^{+0.02}_{-0.01}$

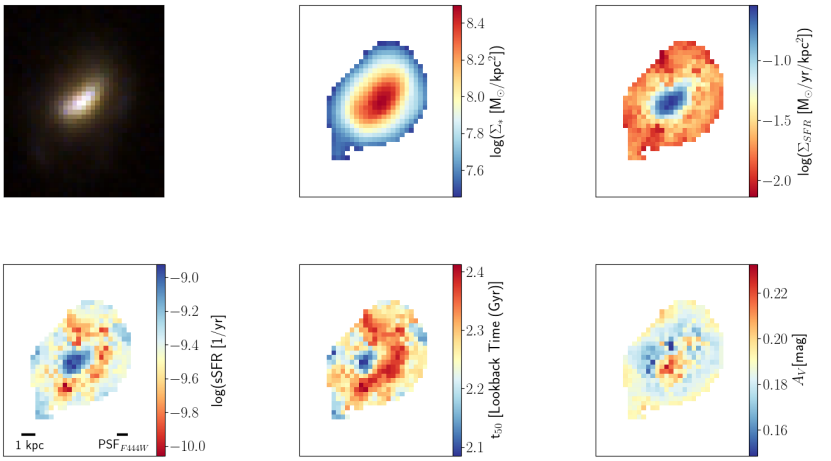

CANUCS - 5105044
z = $1.05^{+0.04}_{-0.07}$
log (M$_*$/M$_\odot$) = $9.58^{+0.09}_{-0.09}$
SFR$_{100}$ = $1.59^{+0.92}_{-0.36}$ M$_\odot$/yr
log(sSFR/yr) = $-9.38^{+0.11}_{-0.03}$
Δ MS = $0.21^{+0.21}_{-0.13}$ dex
t$_{50}$ = $2.62^{+0.97}_{-1.84}$ Gyr
SFR$_{10}$/SFR$_{100}$ = $0.995^{+0.00}_{-0.01}$

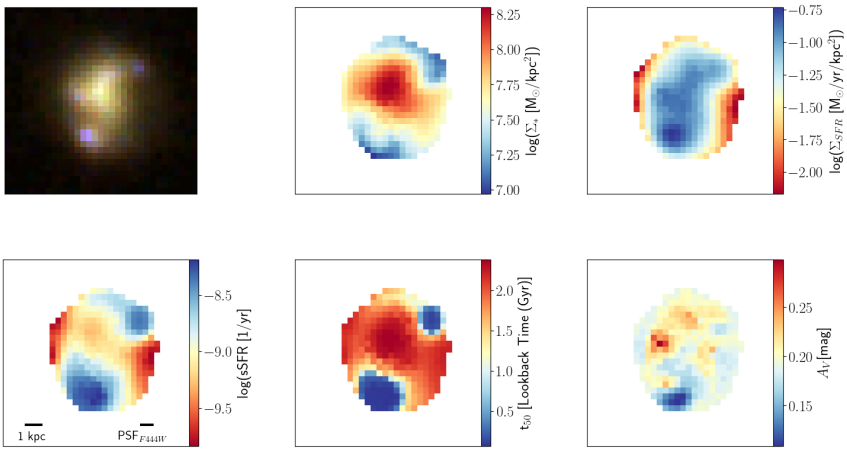

CANUCS - 5105148
z = $1.15^{+0.03}_{-0.01}$
log (M$_*$/M$_\odot$) = $9.32^{+0.03}_{-0.05}$
SFR$_{100}$ = $2.29^{+0.31}_{-0.14}$ M$_\odot$/yr
log(sSFR/yr) = $-8.96^{+0.02}_{-0.03}$
Δ MS = $0.49^{+0.06}_{-0.05}$ dex
t$_{50}$ = $2.24^{+0.71}_{-0.55}$ Gyr
SFR$_{10}$/SFR$_{100}$ = $1.062^{+0.00}_{-0.02}$

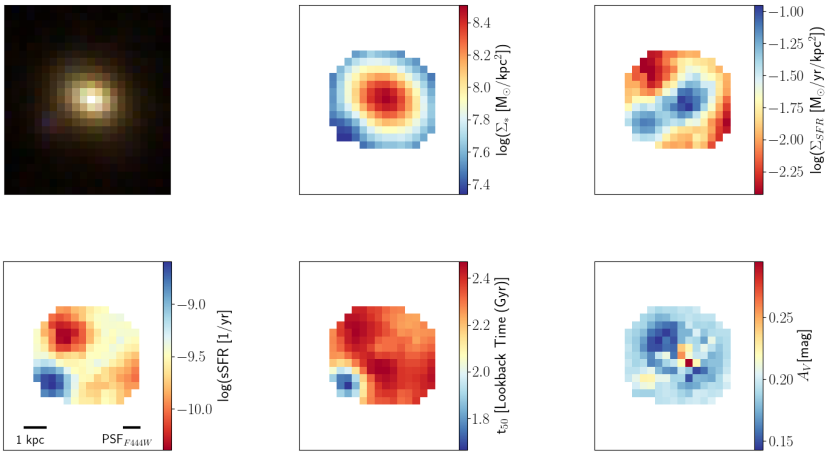

CANUCS - 5105244
z = $1.09^{+0.02}_{-0.04}$
log (M$_*$/M$_\odot$) = $9.19^{+0.08}_{-0.05}$
SFR$_{100}$ = $0.45^{+0.09}_{-0.10}$ M$_\odot$/yr
log(sSFR/yr) = $-9.54^{+0.00}_{-0.06}$
Δ MS = $-0.09^{+0.10}_{-0.12}$ dex
t$_{50}$ = $2.61^{+1.07}_{-0.72}$ Gyr
SFR$_{10}$/SFR$_{100}$ = $0.992^{+0.00}_{-0.00}$

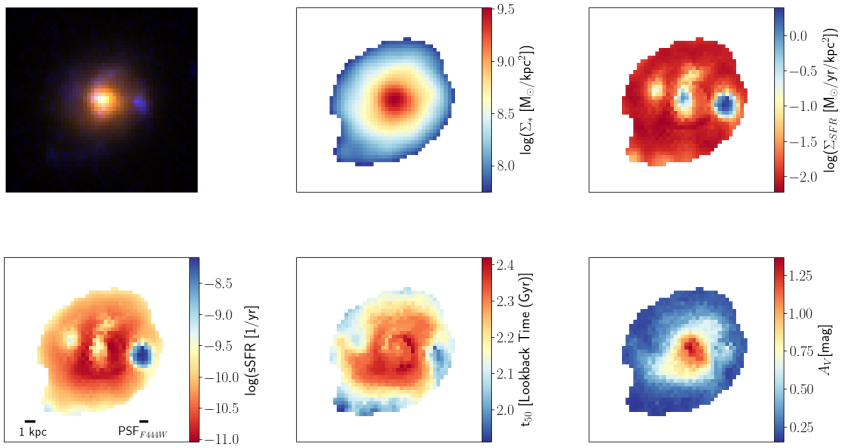

CANUCS - 5109174
$z = 1.44^{+0.03}_{-0.09}$
$\log(M_*/M_\odot) = 10.60^{+0.01}_{-0.02}$
$SFR_{100} = 6.08^{+2.02}_{-1.43}$ $M_\odot$/yr
$\log(sSFR/yr) = -9.82^{+0.11}_{-0.10}$
Δ MS = $-0.15^{+0.12}_{-0.12}$ dex
$t_{50} = 2.63^{+0.30}_{-0.39}$ Gyr
$SFR_{10}/SFR_{100} = 0.978^{+0.00}_{-0.00}$

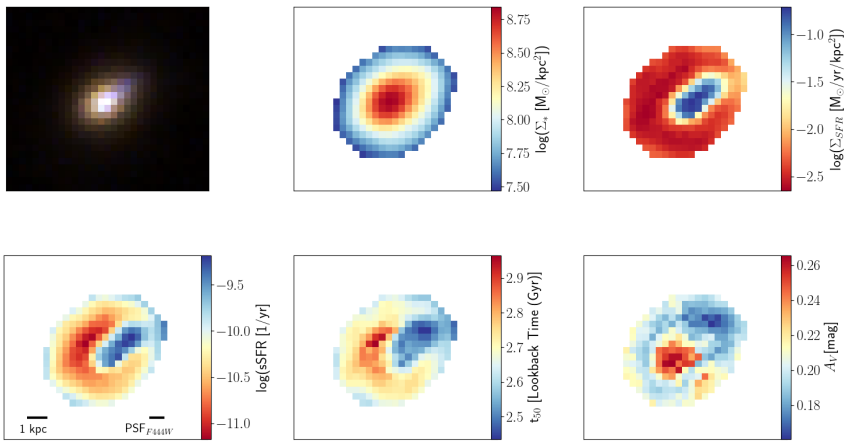

CANUCS - 5110077
$z = 1.01^{+0.02}_{-0.11}$
$\log(M_*/M_\odot) = 9.57^{+0.02}_{-0.06}$
$SFR_{100} = 0.44^{+0.24}_{-0.23}$ $M_\odot$/yr
$\log(sSFR/yr) = -9.92^{+0.16}_{-0.25}$
Δ MS = $-0.32^{+0.19}_{-0.32}$ dex
$t_{50} = 2.90^{+0.77}_{-0.63}$ Gyr
$SFR_{10}/SFR_{100} = 1.003^{+0.01}_{-0.00}$

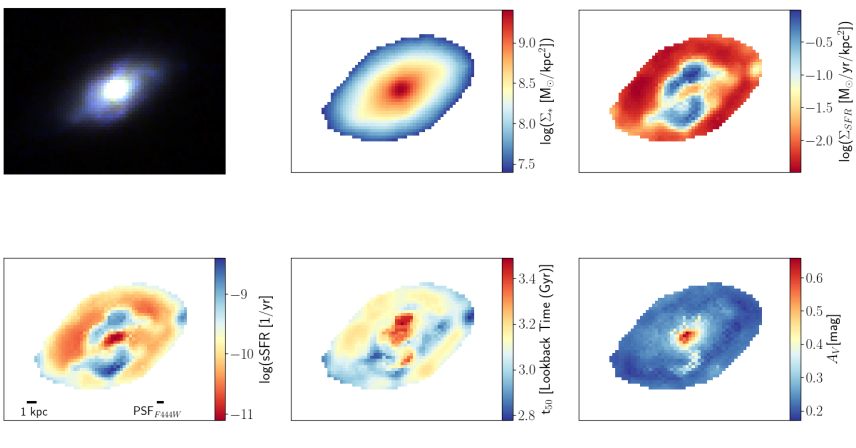

CANUCS - 5110956
$z = 0.85^{+0.04}_{-0.06}$
$\log(M_*/M_\odot) = 10.45^{+0.08}_{-0.04}$
$SFR_{100} = 7.85^{+0.95}_{-3.23}$ $M_\odot$/yr
$\log(sSFR/yr) = -9.55^{+0.03}_{-0.19}$
Δ MS = $0.39^{+0.08}_{-0.23}$ dex
$t_{50} = 3.59^{+0.98}_{-0.63}$ Gyr
$SFR_{10}/SFR_{100} = 0.979^{+0.00}_{-0.00}$

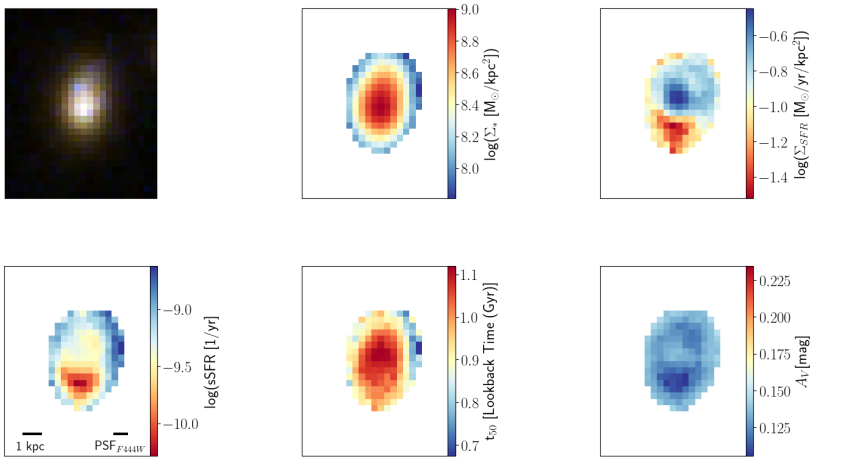

CANUCS - 5113258
$z = 2.45^{+0.10}_{-0.13}$
$\log(M_*/M_\odot) = 9.73^{+0.08}_{-0.11}$
$SFR_{100} = 2.30^{+1.15}_{-0.72}\ M_\odot/yr$
$\log(sSFR/yr) = -9.37^{+0.10}_{-0.05}$
Δ MS = $-0.28^{+0.18}_{-0.18}$ dex
$t_{50} = 1.15^{+0.59}_{-0.52}$ Gyr
$SFR_{10}/SFR_{100} = 0.995^{+0.04}_{-0.00}$

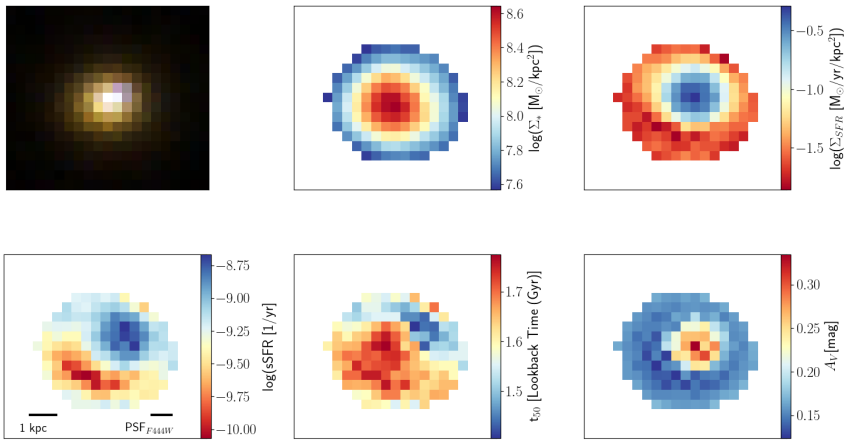

CANUCS - 5113387
$z = 1.52^{+0.01}_{-0.08}$
$\log(M_*/M_\odot) = 9.29^{+0.04}_{-0.08}$
$SFR_{100} = 1.32^{+0.68}_{-0.39}\ M_\odot/yr$
$\log(sSFR/yr) = -9.17^{+0.14}_{-0.07}$
Δ MS = $0.07^{+0.18}_{-0.16}$ dex
$t_{50} = 2.23^{+0.63}_{-0.84}$ Gyr
$SFR_{10}/SFR_{100} = 1.006^{+0.01}_{-0.00}$

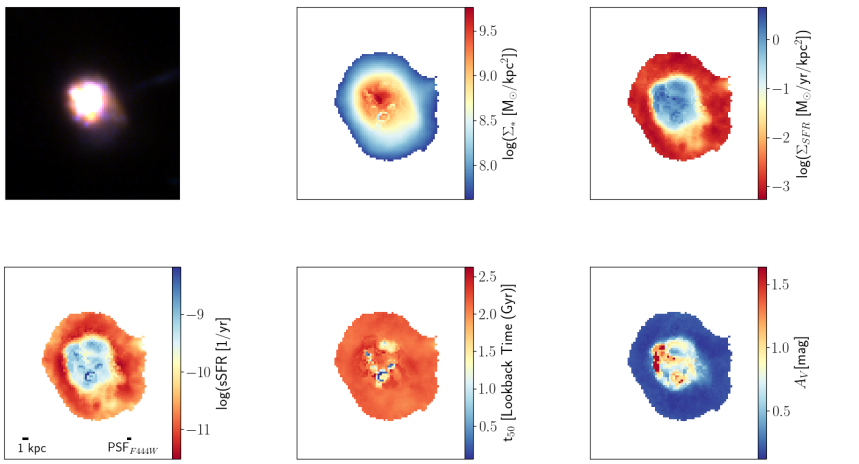

CANUCS - 5113897
$z = 1.31^{+0.08}_{-0.09}$
$\log(M_*/M_\odot) = 11.06^{+0.00}_{-0.05}$
$SFR_{100} = 43.23^{+16.12}_{-0.66}\ M_\odot/yr$
$\log(sSFR/yr) = -9.42^{+0.14}_{-0.04}$
Δ MS = $0.42^{+0.14}_{-0.04}$ dex
$t_{50} = 2.68^{+0.27}_{-0.02}$ Gyr
$SFR_{10}/SFR_{100} = 0.981^{+0.00}_{-0.02}$

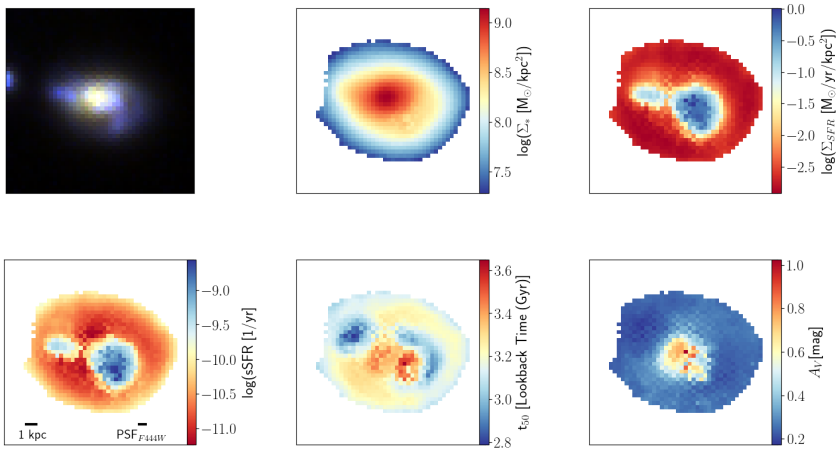

CANUCS - 5114014
$z = 0.85^{+0.05}_{-0.01}$
$\log(M_*/M_\odot) = 10.22^{+0.08}_{-0.07}$
$SFR_{100} = 3.71^{+0.66}_{-0.08}$ $M_\odot$/yr
$\log(sSFR/yr) = -9.65^{+0.01}_{-0.06}$
Δ MS $= 0.23^{+0.09}_{-0.05}$ dex
$t_{50} = 2.76^{+1.79}_{-0.26}$ Gyr
$SFR_{10}/SFR_{100} = 0.987^{+0.00}_{-0.02}$

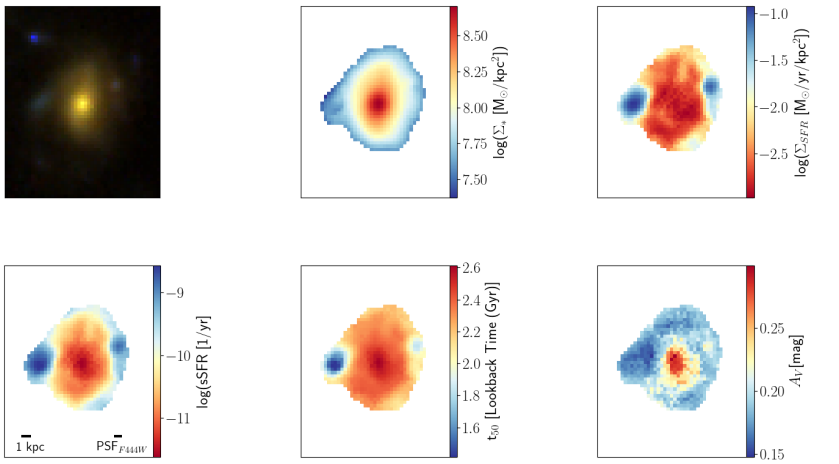

CANUCS - 5114207
$z = 1.22^{+0.07}_{-0.06}$
$\log(M_*/M_\odot) = 9.93^{+0.04}_{-0.07}$
$SFR_{100} = 0.92^{+0.55}_{-0.53}$ $M_\odot$/yr
$\log(sSFR/yr) = -9.96^{+0.16}_{-0.31}$
Δ MS $= -0.39^{+0.20}_{-0.38}$ dex
$t_{50} = 2.19^{+0.94}_{-0.77}$ Gyr
$SFR_{10}/SFR_{100} = 1.015^{+0.01}_{-0.03}$

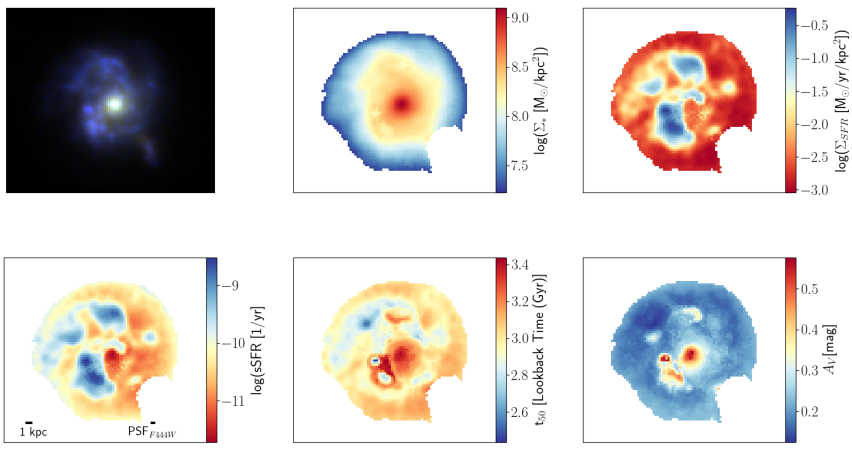

CANUCS - 5115603
$z = 0.85^{+0.04}_{-0.06}$
$\log(M_*/M_\odot) = 10.59^{+0.09}_{-0.00}$
$SFR_{100} = 7.51^{+3.08}_{-0.03}$ $M_\odot$/yr
$\log(sSFR/yr) = -9.72^{+0.06}_{-0.00}$
Δ MS $= 0.26^{+0.16}_{-0.00}$ dex
$t_{50} = 3.37^{+0.38}_{-0.13}$ Gyr
$SFR_{10}/SFR_{100} = 0.998^{+0.00}_{-0.00}$